Modeling Submillimetre Polarization of Molecular Cloud Cores Using Successive Parametrized Coordinate Transformations

by

Erica Franzmann

A Thesis submitted to the Faculty of Graduate Studies of

The University of Manitoba

in partial fulfilment of the requirements of the degree of

MASTER OF SCIENCE

Department of Physics and Astronomy

University of Manitoba

Winnipeg

Abstract

We present a novel new method for modelling magnetized molecular cloud cores using submillimetre linear polarization maps from thermal dust emission. Our PolCat modelling software builds a three-dimensional core model via the use of consecutive parametrized coordinate transformations, and produces simulated polarization maps to fit to observational datasets. We utilize the Ferret evolutionary optimizer to search the parameter space to simultaneously minimize χ^2 for the intensity and polarization position angle maps separately.

We have applied PolCat to multiple test problems and several datasets from the SCUPOL Legacy Catalogue. We find that PolCat is able to distinguish between maps of twisted and non-twisted field geometries and identify twist symmetry. Preliminary fits to several datasets show that the best potential field geometries to our sample cores contain field twists. Further research using a larger number of maps is required to determine if twisted fields are commonplace in cores.

Acknowledgements

First I would like to thank my supervisor, Dr. Jason Fiege, for not only taking me on as a graduate student, but also making himself frequently and consistently available for consultation. His advice is outstanding and I have learned a great deal with his guidance.

Many thanks to Dr. Brenda Matthews for providing the SCUPOL Legacy Catalogue, and for her speedy assistance and willingness to answer questions relating to its use.

I would also like to thank Dr. Jayanne English for lending both her artistic and scientific expertise at multiple points, especially with regards to her input on several figures.

Thanks to Susan Beshta, the department's Graduate Secretary, for cheerfully and patiently assisting me with the plethora of details surrounding the thesis submission process.

Thanks to Adam Rogers for volunteering his time to read through this thesis and provide extremely helpful comments, and also to my Aunt Susan Crawford-Young, and cousins Nancy and Janet Young for also undertaking to copyedit a draft of this document.

Thank you also to my parents, Alice Crawford and Michael Franzmann, and my brother Neale Franzmann, for their endless care, support, and lively banter. I couldn't have made it through without them.

This research was funded in part by an NSERC Canada Graduate Scholarship (Master's) and Dr. Fiege's NSERC Discovery Grant.

Contents

List of Figures

List of Tables

Chapter 1

Introduction

The process of star formation is one of the most important astrophysical processes in the universe; however, it is also one for which our understanding is incomplete. Stars form out of molecular clouds, which are enormous, gravitationally-bound clouds of gas and dust that are largely confined to the disc of the galaxy. Internally, they are clumpy, turbulent, and often filamentary structures, supported by magnetic fields and supersonic turbulence against self-gravity. Molecular clouds range greatly in size from small ($\sim$0.1 pc) isolated Bok globules, to 150 pc giant molecular cloud complexes (GMCs) (Bally, 1989). Molecular clouds appear dark against background starlight, largely due to the presence of absorbing dust, but can be traced by emission lines from carbon monoxide and other molecules, and thermal emission from dust grains embedded in the cloud.

Molecular clouds are shaped by a combination of self-gravity, turbulent motion, and magnetic fields. Thermal pressure plays only a minor role, except for within the darkest, coldest, most dense, and least turbulent regions near the centres of cores. Star formation begins when self-gravity overcomes turbulent and magnetic support in a dense clump within a cloud and collapse ensues. If gravity were the only force present, these clouds would undergo free-fall collapse and convert most of the material in a molecular cloud into stars in a time comparable to the freefall time (Binney and Tremaine, 1987; Carroll and Ostlie, 2007). Clouds are

usually in virial equilibrium, such that a combination of magnetic fields and turbulence, and, to a much lesser extent, thermal pressure, prevents overall collapse. Instead, the cloud fragments into clumps. Dense, gravitationally-bound, magnetohydrostatically supported cores may form within these clumps, and the eventual collapse of these cores leads to star formation. Powerful bipolar jets of gas and surrounding wide-angle winds, called bipolar outflows, are generated in the early stages of star formation. These outflows stir up the gas of the molecular cloud, contributing to the turbulence that provides most of the support against self-gravity.

Despite the supersonic turbulence that dominates the dynamics of a molecular cloud on large scales, ordered magnetic field structures have been observed in regions within molecular clouds. The size scale where magnetic turbulence gives way to organized magnetic structure is not entirely clear. On large scales, turbulence is expected to dominate, whereas on smaller scales such as clumps and cores, gravity is expected to dominate. However, the presence of the cloud's magnetic field will have an effect on the core shape.

Magnetic field geometries of molecular cloud cores are an important initial condition in the star-formation process, since molecular clouds and cloud cores are the initial states of star formation. An important question is the scales over which turbulent field components and ordered (gravitational) field components dominate. One goal of this thesis is to develop a general method to model magnetic fields in the hope that we may soon shed light on the roles of turbulence and ordered fields in molecular clouds, and to better understand the geometry of the field in ordered regions.

Perfect magnetohydrodynamics (MHD) is a good approximation for molecular clouds, since the magnetic Reynolds number tends to be on the order of $10^6 - 10^7$ (Hennebelle and Falgarone, 2012). That is, the magnetic field is effectively "locked-in" to the gas and so must move with the material, dragged along as the gas moves. However, the field also exerts a force on the gas moving at right angles to the field direction. The strength of the force depends on the field strength; strong magnetic fields exert a larger force on the material to

resist transverse motion. In practice, this would have the effect of providing support against gravitational collapse, although this is not necessarily true for a helical field, which is radially compressive if the toroidal component B_ϕ dominates (Fiege and Pudritz, 2000b).

Thermal emission from embedded spinning dust grains inside molecular clouds causes emission at submillimetre wavelengths, which allows us to trace the dust in the cloud. These grains tend to align, on average, with their long axis 90° to the local magnetic field (Greaves et al., 1999; Draine, 2003). As a result, this emission (and partially absorbed starlight from stars behind or embedded within the cloud) is significantly polarized. We focus on polarized thermal emission in this thesis, which allows us to trace the two-dimensional projection of the magnetic field on the plane of the sky. However, the maps produced are the effective average of all the grains along the line of sight to the region as this is a two-dimensional projection of a three-dimensional structure. There is no direct way to derive the magnetic field strength from these maps; however, we can use the statistical variation of the linear polarization to estimate direction of the field component in the plane of the sky to some extent (see §2.5).

We have developed a molecular cloud modelling package called PolCat, which generates models of magnetized molecular cloud cores via the application of a series of parametrized coordinate transformations under conditions of perfect MHD. The coordinate transformations deform the simulated cloud, generally starting from a uniform distribution and rearranging the gas into a density profile that matches observations. The advantages of this coordinate transformation technique are two-fold: first, the list of transformations suggests a possible (though non-unique) history of gas motions in the cloud, and second, as the gas in the cloud is rearranged via the transformations, the magnetic field is dragged naturally into the corresponding configuration. By applying a sequence of several simple geometric transformations, we can produce models with quite complex fields. This coordinate transformation technique, first presented in Fiege et al. (2004) and Fiege (2005), is a new approach to modelling molecular clouds, although a similar technique known as "transformation optics" is used to design

complex optical systems (see §2.7).

PolCat uses the technique of Fiege and Pudritz (2000a) to "observe" the model and generate simulated polarization maps to compare to observational data. The models are highly degenerate; astronomical observations of linear polarization are two-dimensional, representing a projection of the three-dimensional region along the line of sight. Since this is a three-dimensional problem reduced to two dimensions, many different field patterns can produce very similar polarization maps. Effectively, we may be able to rule out particular model geometries, but it is not generally possible to confirm any particular model as "correct."

We utilize Ferret, a powerful multi-objective genetic algorithm (Fiege, 2010) to produce an optimal set of models. As polarization maps are characterized by at least two functions (intensity and position angle of polarization) calculated from the Stokes vectors, to properly judge fitness we need to minimize fitness to the intensity and polarization objectives simultaneously. However, we cannot combine the intensity and polarization objectives into a single objective due to the signal-to-noise of the intensity having a much larger magnitude than Stokes Q and U. This causes their chi-squared fitness (χ^2) values to have different orders of magnitude (§4.1.5). A combined χ^2, formed by summing a χ^2 from the intensity map with one derived from the polarization, would be completely dominated by the intensity component and the polarization signal would be lost. Such models provide excellent fits to the intensity data, but provide no reliable insight into the field configuration. Therefore, we take a multi-objective approach to this problem (§3.2) which does not combine the χ^2 values.

We have tested PolCat extensively using simulated datasets. We then applied the code to several real datasets from the SCUPOL Legacy Catalogue (Matthews et al., 2009), which is a large, uniformly reprocessed archive of 850 μm data from the SCUPOL polarimeter at the James Clerk Maxwell Telescope (JCMT). We apply our technique to several regions found in this important data archive, as a preliminary attempt to understand the three-dimensional structure of magnetic fields in star-forming regions. This thesis documents numerical ex-

periments used to develop our method, and paves the way for broader application to other data sets. Eventually, we hope to answer several important questions in star-formation research, such as the following. How ubiquitous are ordered fields? What is the minimal set of transformations needed to model magnetic fields in cores? What field geometries are allowed by the data? PolCat's model-building technique allows for exploration of a large range of potential field geometries.

The following is a brief roadmap of the thesis. Chapter 2 presents a background summary of molecular cloud properties, in addition to some discussion of current models of molecular clouds. Chapter 3 explains the concept of optimization and the basics of multi-objective optimization, along with some background information on genetic algorithms. We discuss PolCat in Chapter 4, summarizing its methods, code structure, and available transformations. In Chapter 5 we discuss the SCUPOL Legacy catalogue and provide background information on each of the three cores selected for analysis. We present the results of PolCat fits to both simulated and real data in Chapter 6, and conclusions on both the results of the PolCat fits and the effectiveness and characteristics PolCat's current modelling techniques in Chapter 7. We have included a glossary of symbols in Appendix C.

Chapter 2

Molecular Clouds

Molecular clouds refer to a class of objects in interstellar space composed of gas and grains of dust. Studying these structures is important, as it is from molecular clouds that stars form. Eventually, the higher-mass stars will return their mass to the interstellar medium (ISM) through stellar winds, supernova explosions and planetary nebulae, enriching the ISM with heavier elements. To understand the process of star formation it is important to study the conditions inside molecular clouds to observe the initial conditions in the regions where stars form. This chapter describes the composition and physical conditions inside molecular clouds, and discusses the measurement techniques used to deduce the cloud properties, in addition to providing a brief discussion of current cloud models.

2.1 Cloud Structure and Equilibrium

Giant molecular clouds (GMCs) are massive, clumpy complexes encompassing collections of smaller molecular cloud classes. There are differing theories as to how these structures form. The "top-down" model suggests the clouds formed out of the ISM due to large scale thermal, gravitational, and magnetic instabilities, whereas the "bottom-up" model posits the clouds form via collisions of cool HI clouds, with self-gravitating GMCs slowly built up by collecting mass (Bally, 1989; McKee and Ostriker, 2007; Poidevin et al., 2013).

2.1.1 Jeans' Instability

GMCs are highly textured; the gas and dust inside the clouds clump together into smaller cores and filaments. Some of these structures contain substructures, such as smaller clumps, protostars, and young stars. The classic Jeans instability assumes clouds are only subject to gravitational attraction and internal gas pressure. Under this assumption we would expect the cloud to collapse into a protostar quite easily. This can be seen by the following argument based on the virial theorem, which states that for gravitationally bound systems in equilibrium, the total energy of the system is equal to one-half of the system's gravitational potential energy such that

$$-2\mathcal{T} = \mathcal{W}, \tag{2.1}$$

where $\mathcal{T}$ and $\mathcal{W}$ represent the time-averaged kinetic and potential gravitational energy of the system. The cloud will begin to collapse under the condition where gravitational potential exceeds the kinetic terms, i.e. $2\mathcal{T} < |\mathcal{W}|$. A derivation based on the virial theorem will lead to approximately the correct answer (Carroll and Ostlie, 2007). However a more accurate approach is to treat the problem as the propagation of sound waves modified by self-gravity propagating through a uniform medium (Binney and Tremaine, 1987).

Sir James Jeans derived the minimum criteria for a uniform isothermal sphere of density ρ and sound speed c_s to spontaneously collapse by examining small perturbations from equilibrium. The wavelength of the perturbation which will cause the cloud to collapse under these conditions is the Jeans Length:

$$\lambda_J = \sqrt{\frac{\pi c_s^2}{G\rho}}, \tag{2.2}$$

where G is the gravitational constant. The mass contained within a sphere of diameter λ_J is the Jeans Mass

$$M_J = \frac{1}{6}\pi\rho\left(\frac{\pi c_s^2}{G\rho}\right)^{3/2} \tag{2.3}$$

(Binney and Tremaine, 1987; McKee and Ostriker, 2007). Calculating λ_J and M_J, considering only thermal support, with c_s=0.23 km s^{-1} (characteristic of gas at a temperature of 15K) and a cloud density of 1000 cm^{-3} we obtain λ_J=0.84 pc, and M_J=17.2 M$_\odot$ (solar masses). As most molecular clouds typically contain thousands of solar masses, one would expect that most molecular clouds would be fragmenting into hundreds of self-gravitating clumps that would rapidly collapse to form stars. The fallacy in this argument is the assumption that thermal pressure is the chief support against gravitational contraction is incorrect.

2.1.2 Turbulence and Larson's Laws

Molecular clouds have a non-thermal supersonic turbulent component to their internal motions in addition to thermal pressure (McKee and Ostriker, 2007; Hennebelle and Falgarone, 2012). As such, the cloud's one-dimensional velocity dispersion σ, which combines thermal (c_s) and non-thermal particle motions $\sigma = \sqrt{c_s^2 + \sigma_{nt}^2}$, is a better velocity scale for the cloud as a whole. If we account for turbulent support in the Jeans calculations by substituting a velocity dispersion of σ=1 km s^{-1} for the sound speed, we obtain λ_J=3.6 pc and M_J=1400 M$_\odot$, which are more typical of molecular cloud cores. Fragmentation, therefore, occurs on much larger scales than with purely thermal support, and gas is converted into stars less efficiently than the Jeans assumption would allow. The Jeans calculation is overly simplistic. It does not account for the presence of a magnetized and clumpy medium, using turbulent σ in the Jeans equations does not truly account for turbulence correctly, and Jeans neglected surface pressure when solving Poisson's equation and solved for the potential due to an infinite medium, which is non-unique. This situation is often called the Jeans Fudge, or Jeans Swindle (Binney and Tremaine, 1987). Nevertheless, the Jeans' mass and length scales are frequently used as convenient measures to predict when objects are close to gravitational equilibrium or at risk of fragmentation or collapse.

Larson (1981) studied a large sample of molecular clouds with known masses to examine how the internal supersonic motions relate to cloud size and mass. He discovered three

power-law relations, which have been colloquially called "Larson's Laws", that relate velocity dispersion to cloud mass, size, and density. His findings can be summarized as

1. Velocity dispersion σ is proportional to region size L: $\sigma(\text{km s}^{-1}) = 1.1L(\text{pc})^{0.38}$.

2. Velocity dispersion is proportional to mass: $\sigma(\text{km s}^{-1}) = 0.42M(\text{M}_\odot)^{0.20}$.

3. Number density of a uniform sphere of mass M and size L is inversely proportional to region size: $\langle n(\text{H}_2)\rangle(\text{cm}^{-3}) = 3400L(\text{pc})^{-1.10}$.

Larson applied (1) to not only the main clouds in his sample, but also plotted relations for clumps embedded within larger clouds, finding the same power-law dependence throughout. Larson's virial analysis of the cores in his sample, performed by logarithmically plotting $2GM/\sigma^2 L$ vs physical size L, led him to conclude that the cores were gravitationally bound (Larson, 1981). He concluded that supersonic turbulence plays an important role in cloud structure and formation, based on the universality of (1) and its agreement with turbulence theories. These results have been extended to a variety of molecular clouds and traces, and (1) is currently found to be $\sigma(\text{km s}^{-1}) = 1L(\text{pc})^{0.5}$ (Hennebelle and Falgarone, 2012).

2.1.3 The Magnetic Virial Theorem

Computing the equilibrium conditions for molecular clouds and their cores becomes more complex when rotation, supersonic internal motion, and the presence of magnetic fields are accounted for (though rotation is not usually significant within cloud cores (Myers and Goodman, 1988)). A more complete form of the virial theorem that takes these factors into account is given by

$$\frac{1}{2}\ddot{I} = 2(\mathcal{T} - \mathcal{T}_s) + \mathcal{B} + \mathcal{W} \tag{2.4}$$

(McKee and Ostriker, 2007). Here $\mathcal{T}$ is the total internal kinetic energy, both thermal and non-thermal, and $\mathcal{T}_s = \oint P_{th}\mathbf{r}\cdot\mathbf{dS}$ is the surface kinetic term. The moment of inertia I is

constant for cores in equilibrium, so that $\ddot{I} = 0$. The net magnetic energy, $\mathcal{B}$ is expressed

$$\mathcal{B} = \frac{1}{8\pi}\int_{V_{\rm cl}} B^2 dV + \frac{1}{4\pi}\oint \mathbf{r}\cdot\left(\mathbf{BB} - \frac{1}{2}B^2\mathbf{I}\right)\cdot\mathbf{dS} \tag{2.5}$$

where $V_{\rm cl}$ represents the cloud volume (McKee and Ostriker, 2007). Clearly, the surface terms of the magnetic term are complicated to calculate. However, they are responsible for interesting effects such as the magnetic "hoop stress" due to the B_ϕ field component that was much discussed by Fiege and Pudritz (Fiege and Pudritz, 2000b,d).

Magnetic fields add additional complications to the structure of molecular clouds and their cores. Due to the presence of free ions, the gas effectively acts as an infinitely conductive fluid, and so the gas is subject to the conditions of perfect magnetohydrodynamics (MHD). Despite the population of ions being much smaller than that of the neutral material in the cloud, the ions and neutral gas are coupled together through collisions (Hennebelle and Falgarone, 2012). This collisional coupling causes the magnetic field to influence the neutral material as well, effectively "locking" the magnetic field into the gas. The gas is able to drag the magnetic field with it as it moves, but the magnetic field will exert force on the material when it moves perpendicular to the field direction. In the magnetically regulated model of star-formation, a contracting cloud reaches a state where pressure from the compressed magnetic field balances gravity and halts the contraction. Such cores are magnetically subcritical. This state persists until the neutrals and ions begin to slip past each other (ambipolar diffusion), gradually increasing the core mass and weakening the magnetic field (Mestel and Spitzer Jr., 1956; McKee et al., 1993). For a cloud in virial equilibrium, the ambipolar diffusion timescale is approximately eight times the free-fall timescale, showing that ambipolar diffusion can substantially extend the time for the cloud to contract (Hennebelle and Falgarone, 2012). Once the field has been appreciably weakened, gravity once again dominates and collapse is possible.

2.2 Observational Considerations

Molecular clouds are composed largely of atomic and molecular gas, with embedded dust grains on the order of 10^{-7}–10^{-5} cm in size (Dyson and Williams, 1997). The dust grains will absorb light most efficiently at wavelengths on the order of, or smaller than, their characteristic size (Binney and Merrifield, 1998). The dust therefore preferentially absorbs and scatters short-wavelength (blue) light, limiting useful observations of molecular clouds to the longer-wavelength bands, such as IR and submillimetre.

Neutral atomic and ionized hydrogen dominate the composition of the interstellar medium (ISM), which is characterized by the property that self-gravity is relatively unimportant. Molecular hydrogen requires shielding against external radiation, as the H-H bond is fragile and is easily broken by interstellar UV radiation. However, dark, dusty, self-gravitating molecular clouds can coalesce within the ISM, where the compression due to self-gravity increases the density and pressure of the gas, and the temperature drops to approximately 10–20 K due to radiative processes. Under these conditions, the gas becomes self-shielding against external radiation and molecular hydrogen (H_2) can readily form and stay bound (Binney and Merrifield, 1998; Dyson and Williams, 1997). It has long been thought that molecular cloud complexes are typically surrounded by a layer of atomic hydrogen gas, which helps shield the cloud from incoming radiation. Current theory holds that the presence of dust not only shields the cloud from UV radiation, but also aids the formation of H_2 molecules by providing sites for H-atoms to meet (Binney and Merrifield, 1998; Dyson and Williams, 1997). Detecting H_2 is much more difficult than atomic hydrogen as its emission lines typically lie in the UV bands, and as the molecules only exist in the UV-shielded "dark" areas of the clouds, they are not easily detectable. As such, to estimate the amount of molecular hydrogen we conventionally rely on information gleaned from studying other tracer molecules present in the cloud (Binney and Merrifield, 1998).

The most common molecules used to estimate the amount of H_2 and to map its structure are isotopomers of the CO (carbon monoxide) molecule. Carbon monoxide works as a tracer

due to its relatively high abundance (typically 10^{-4} H_2 (Carroll and Ostlie, 2007)) and ease of excitation. Spectral lines from CO emission are generally from collisional excitation of $^{12}C^{16}O$ (^{12}CO in shorthand), $^{13}C^{16}O$ (^{13}CO) and $^{12}C^{18}O$ ($C^{18}O$) which radiate at characteristic wavelengths of 1.3 and 2.6 mm. Other molecules, including CS, NH_3, and others, are used to probe the coldest and densest regions within molecular cloud cores.

Molecular lines are often used to derive the one-dimensional, line of sight velocity dispersion σ. Moving gas causes Doppler shifts in the spectral lines, and, as the gas is not moving uniformly in any one direction, the cumulative Doppler shifts cause the spectral lines to broaden. If we assume Gaussian spectral lines, it is trivial to derive the relation of the velocity dispersion σ to the full-width-at-half-maximum (FWHM) of the profile:

$$\sigma = \frac{FWHM}{2\sqrt{2\ln 2}}. \tag{2.6}$$

2.3 Dust Properties

There is some debate over the exact composition of dust grains. Evidence points toward a significant component of the composition being a silicate material, but the amount of observed emission seems to indicate the presence of another component substance (Lee and Draine, 1985). Examination of extinction features points towards a combination of silicate material, graphite, and ice, likely with the ice existing as a coating on the silicate and graphite grains (Lee and Draine, 1985). Each grain type has different emission/absorption properties, making it difficult to derive a unified emission model that accounts for contributions from all species.

Dust grains along the line of sight to an object absorb incoming emission, quantitatively described by the difference between expected magnitude and observed magnitude of a background source. The amount of extinction naturally increases with the amount of dust, and therefore density, along the line of sight. Dust grains preferentially absorb and scatter

emission on wavelengths of comparable size or smaller (Binney and Merrifield, 1998). As a result, the dust preferentially absorbs emission from the blue end of the spectrum, "reddening" it by robbing the emission of short-wavelength photons. UV emission is therefore absorbed most efficiently, while far infrared suffers less absorption. Reddening as a quantity is the difference between the observed "colour" (difference between magnitudes at different wavelengths) and the expected colour. Other photons are absorbed, converted into heat, and re-emitted in the infrared (Binney and Merrifield, 1998). Absorption of starlight tends to maintain grain temperatures between 15–20 K, although dark, dense cloud interiors are typically colder (Draine, 2003).

2.3.1 Polarization and Grain Alignment

Further investigation of background starlight passing through molecular cloud regions reveals the emission to be partially polarized, indicating that the dust grains are non-spherical and act as a polarizing filter on the incoming radiation. Polarization is possible because grains are preferentially aligned with their long axes orthogonal to the magnetic field. The dust grains rotate with their axis of rotation 90° to their long axis (the axis with the greatest moment of inertia). This axis of rotation shows a tendency to align, on average, with the magnetic field. There are a number of different theories as to what mechanisms provide the aligning torque, dependent on whether the grains exhibit thermal rotation $\omega_T \approx (kT_{gas})^{1/2}/(\rho_{grain}a_{grain}^5)^{1/2}$ or suprathermal rotation caused by H_2 formation or radiation torques (Lazarian et al., 1997). Current theories suggest that the alignment is caused by some combination of paramagnetic relaxation, radiative torques, interaction with gaseous flows such as those caused by Alfvén waves, and magnetic alignment of ferromagnetic grains. The net result is the grains tend to align with their long axis perpendicular to the magnetic field, producing thermal emission with the same orientation. Emission polarization can therefore be used as an effective tool to map magnetic fields in molecular clouds.

In addition to absorption polarization, these dust grains emit partially-polarized light

at far-IR and (sub)millimetre wavelengths (Lazarian et al., 1997; Weintraub et al., 2000; Lee and Draine, 1985). As tracing background starlight polarization is only effective for conditions where background stars may be observed, NIR background starlight polarimetry is insensitive to the conditions in the interiors of dark molecular clouds (Lazarian et al., 1997; Weintraub et al., 2000). However, the same grains that absorb starlight also emit light at submillimetre wavelengths, and therefore the same potential alignment mechanisms apply for emission polarimetry.

Observers have noted an interesting effect known as the "polarization hole" effect, where the degree of polarization is diminished in dense regions. This could be caused by conditions favouring the formation of spherical grains in dense regions, which produce no polarization, or collisions within the clouds that cause temporary misalignment (Clark et al., 2000; Curran and Chrysostomou, 2007; Matthews et al., 2009).

2.4 Magnetic Field Strength Measurements

It is difficult to obtain the total magnetic field strength from dust polarization. Weak magnetic fields can still align dust grains, therefore even if we obtain the strength of the polarized emission, it does not directly correlate to the magnetic field strength (Heiles and Crutcher, 2005). However, Chandrasekhar and Fermi (1953) developed a technique to estimate the magnitude of the field component in the plane of the sky using the disorder in the field vectors caused by turbulence. An alternate technique for estimating the field strength of the line-of-sight component requires circular polarization data of spectral lines that are sensitive to the Zeeman Effect. Zeeman measurements are notoriously difficult to obtain and are correspondingly rare in the literature. Both techniques are discussed here for completeness. However, we do not directly utilize these observational constraints, as the strength of the magnetic field can be scaled arbitrarily in our model.

2.4.1 Zeeman Observations

Observations of the 21-cm line of HI, the 18 cm and 2 cm lines of OH, the 1.3 cm H_2O maser line and the 3 mm line of CN are sensitive to the Zeeman effect. The Zeeman effect arises from the coupling of the magnetic moment of an atom or molecule with the magnetic field of the cloud (Heiles et al., 1993). For degenerate energy states with non-zero angular momentum, the Zeeman effect splits them into a number of polarized frequencies with the frequency separation ν_Z dependent on the field strength (Heiles et al., 1993; Crutcher et al., 2003). As such, Zeeman measurements are the most important direct measurement of field strengths in dense regions of the ISM (McKee and Ostriker, 2007). The polarization of the Zeeman components vary depending on orientation of the emission with respect to the magnetic field direction. For a magnetic field in the plane of the sky, the polarization is linear (Heiles et al., 1993), and for a magnetic field pointing along the line of sight we observe circular polarization, with the direction dependent on whether the frequency is above or below the line frequency.

The frequency separation ν_Z is proportional to the total magnetic field strength as $\nu_Z = B \times Z$, where Z is the "Zeeman sensitivity" in Hz/μG. When this separation is on the order of the line width (or larger), the Zeeman components are clearly separated and B can be derived. However, ν_Z is usually much smaller than the line width, so deriving the full field strength is not possible. In practical terms, this means that the linear polarization dependent on the plane-of-sky component of the magnetic field is too weak to discern the magnetic field strength component in the plane of the sky, but the circular polarization component proportional to the line-of-sight field is strong enough to calculate the magnetic field strength of the line of sight (Crutcher et al., 2003; Heiles and Crutcher, 2005). Instrumental polarization must be carefully removed from observations to obtain the astronomical signal. This work is difficult and such measurements are rare.

The usefulness of an atom or molecule to this measurement depends on the strength of the atom or molecule's magnetic moment. Species used for Zeeman measurements generally

have magnetic moments on the order of the Bohr magneton (Heiles et al., 1993; Crutcher et al., 2003). Zeeman splitting shows up as a pattern in the Stokes V spectrum, produced by subtracting the right circular polarization from the left. The amplitude of the "Zeeman pattern" depends on the line-of-sight magnetic field component. Based on a large sample of clouds with random field orientations, a general statistically valid estimate of the total field strength is found to be approximately twice that of the component along the line of sight (Crutcher et al., 2003).

2.4.2 Chandrasekhar-Fermi Method

The Chandrasekhar-Fermi method (Chandrasekhar and Fermi, 1953) of estimating plane-of-sky field strengths is based on the fact that strong magnetic fields are less susceptible to deformation by turbulence. While material can move freely along magnetic field lines, the magnetic field resists transverse motion. However, if the field is weak the transverse motion is able to drag the field lines along with the material more easily. Assuming a regular, uniform, zeroth order magnetic field with an irregular magnetohydrodynamic wave component, we can use the irregularity observed in the polarization maps to determine $B_\perp$, the field component in the plane of the sky, by comparing fluctuations in position angle of polarization with the direction of the velocity field (Chandrasekhar and Fermi, 1953; Crutcher et al., 2003; Heiles and Crutcher, 2005; McKee and Ostriker, 2007). Using the Alfvén velocity $V_A = B/\sqrt{4\pi\rho}$, with ρ consisting of gas and dust mass density, perturbations in the velocity field δV are therefore related to magnetic field perturbation δB via $\delta V = \delta B/\sqrt{4\pi\rho}$ for incompressible turbulence (Crutcher et al., 2003). $B_\perp$ is therefore given by

$$B_\perp = Q\sqrt{4\pi\rho}\frac{\delta V}{\delta\phi} \tag{2.7}$$

with $\delta\phi = \delta B/B_\perp$ being the position angle dispersion, and Q being a factor of order 1 (Crutcher et al., 2003; Heiles and Crutcher, 2005).

One problem with this technique is that it requires the velocity dispersion in the plane of the sky, but we can only measure the line-of-sight velocity dispersion. A calibrated estimate of $Q \approx 0.5$ has been obtained through "observing" linear polarization from simulations of MHD turbulence (Ostriker et al., 2001). The calibrated estimate of Q accounts for some of the effect of smoothing which can lead to an over-estimate of $B_\perp$, although this effect can be minimized by acquiring maps at high resolution (Heiles and Crutcher, 2005). Another problem is the assumption that the unperturbed magnetic field is straight. With this assumption, any possible ordered geometrical structure, such as an hourglass configuration, would be included in the turbulent field component, causing the strength of the field to be underestimated.

2.5 Polarization Map Simulation

Accurately simulating the emission and polarization properties of dust in molecular clouds is a complex problem, because they include many different types of dust species in different populations with different emission and alignment properties, and many grain properties are unknown. Lee and Draine (1985) presented a method to calculate polarization and extinction properties of partially aligned spheroidal dust grains. However, their method requires detailed knowledge of highly uncertain dust properties. Wardle and Konigl (1990) derived a technique to generate integrated Stokes parameters from dust emission as part of modelling the magnetic field at the Galactic centre. Further work by Fiege and Pudritz (2000a) showed that the unknown grain parameters could be grouped into a single unknown parameter, the value of which can be estimated from observation. This modified technique reduces the computation of model polarization maps to functions that depend only on the mass density and magnetic field direction of the simulated cloud. We follow this technique for computing our models' polarization maps, with some small modifications to be discussed in Section 4.1.4. Here we go through the work presented in Fiege and Pudritz (2000a) with

some further explanation from Lee and Draine (1985) and Wardle and Konigl (1990).

The polarized emission is considered to be due to contributions along the line of sight from a group of aligned grain species indexed by subscript j. Thermal emission is assumed to be optically thin, and we can neglect the effects of absorption and scattering in this analysis since we are working in submillimetre wavelengths greater than 100 μm (Fiege and Pudritz, 2000a). We assume that the grains are all either oblate or prolate spheroids, each with absorption cross-sections $C_{\perp,j}$ perpendicular, and $C_{\parallel,j}$ parallel to the grain's axis of symmetry. The thermal emission is only polarized if the grains are not spheroidal, such that $C_{\perp,j} \neq C_{\parallel,j}$ (Lee and Draine, 1985; Wardle and Konigl, 1990; Fiege and Pudritz, 2000a). The effective polarization cross-section for grain species j is given in Lee and Draine (1985) as

$$C_{\mathrm{pol},j} = \begin{cases} C_{\perp,j} - C_{\parallel,j} & \text{(oblate grains)} \\ C_{\parallel,j}/2 - C_{\perp,j} & \text{(prolate grains)} \end{cases} . \tag{2.8}$$

We can define the polarization reduction factor Φ_j as

$$\Phi_j = R_j F_j \cos^2 \gamma_B, \tag{2.9}$$

where R_j is the Rayleigh reduction factor, which characterizes the degree of alignment with the local magnetic field (Lee and Draine, 1985) and F_j represents reduction in alignment due to a turbulent magnetic field component, both assumed constant for each dust species. Angle γ_B is the angle $\mathbf{B}$ makes with the plane of the sky. The effective polarization cross-section of the grain species is $C_{\mathrm{pol},j}\Phi_j$.

Each species of dust is also assumed to have constant temperature T_j, and number density proportional to total mass density as $n_j = c_j\rho$. The effective extinction cross-section is defined by Lee and Draine (1985) and simplified as

$$C_{\mathrm{ext},j} = C_{+,j}\left[1 - \alpha_j\left(\frac{\cos^2\gamma_B}{2} - \frac{1}{3}\right)\right], \tag{2.10}$$

where

$$C_{+,j} = \frac{2C_{\perp,j} + C_{\parallel,j}}{3} \tag{2.11}$$

and

$$\alpha_j = \frac{C_{\mathrm{pol},j} R_j F_j}{C_{+,j}}. \tag{2.12}$$

Contributions from each grain species need to be summed and integrated along the line of sight to obtain the Stokes parameters I, Q, and U for the model. Following Fiege and Pudritz (2000a) the equations for I, Q, and U are given by

$$I = \sum_j C_{+,j} B_\nu(T_j) c_j (\Sigma - \alpha_j \Sigma_2), \tag{2.13}$$

$$Q = \sum_j C_{+,j} B_\nu(T_j) c_j \alpha_j q, \quad \text{and} \tag{2.14}$$

$$U = \sum_j C_{+,j} B_\nu(T_j) c_j \alpha_j u, \tag{2.15}$$

where $B_\nu(T_j)$ is the Planck function; and Σ, Σ_2, q, and u are quantities integrated along the line of sight, dependent only on the density and magnetic field geometry and not on the grain ensemble properties:

$$\Sigma = \int \rho \; ds \tag{2.16}$$

$$\Sigma_2 = \int \rho \left(\frac{\cos^2 \gamma_B}{2} - \frac{1}{3} \right) \; ds \tag{2.17}$$

$$q = \int \rho \cos(2\psi_B) \cos^2 \gamma_B \; ds \tag{2.18}$$

$$u = \int \rho \sin(2\psi_B) \cos^2 \gamma_B \; ds. \tag{2.19}$$

Angle ψ_B represents the angle between north on the sky and the projection of the magnetic field in the plane of the sky, and varies along the line of sight as the magnetic field direction varies.

The polarization position angle of the electric field vector χ_{pol} can thus be calculated by

the equation

$$\tan(2\chi_{pol}) = \frac{U}{Q} = \frac{u}{q}. \tag{2.20}$$

We note that χ_{pol} is dependent on the density and magnetic field properties alone. Correspondingly the fraction of polarized emission is given by

$$P_{frac} = \frac{\sqrt{Q^2+U^2}}{I} \tag{2.21}$$

$$= \frac{\sum_j C_{+,j} B_\nu(T_j) c_j \alpha_j \sqrt{q^2+u^2}}{\sum_j C_{+,j} B_\nu(T_j) c_j \left(\Sigma - \frac{\sum_j C_{+,j} B_\nu(T_j) c_j \alpha_j}{\sum_j C_{+,j} B_\nu(T_j) c_j} \Sigma_2\right)} \tag{2.22}$$

$$= \langle\alpha\rangle \frac{\sqrt{q^2+u^2}}{\Sigma - \langle\alpha\rangle\Sigma_2}, \tag{2.23}$$

where $\langle\alpha\rangle$ is the ratio of the two sums in equation (2.22) and can be thought of as a weighted mean of α_j, which effectively absorbs all unknown grain properties:

$$\langle\alpha\rangle = \frac{\sum_j C_{+,j} B_\nu(T_j) c_j \alpha_j}{\sum_j C_{+,j} B_\nu(T_j) c_j}. \tag{2.24}$$

Therefore, all of the dust properties are encapsulated in a single constant $\langle\alpha\rangle$. Fiege and Pudritz (2000a) find that observational values for $\langle\alpha\rangle$ are typically around 10%, although they caution that $\langle\alpha\rangle$ could vary between clouds, or with position within a cloud, which could affect polarization profiles. We attempt to take this into account in our models by assuming a possible spatial dependence of $\langle\alpha\rangle$ on ρ, which we will discuss in §4.1.4

2.5.1 Mathematical Degeneracy: Limitations of Modelling Polarization

We note that models of polarization are highly degenerate. Observational polarization maps are essentially a weighted sum of polarization contributions along the line of sight, and as

such, our simulated model observations are as well. Any spatial variation along the line of sight is lost in projection and cannot be exactly reproduced. As such, any method for modelling polarization will necessarily contain mathematical degeneracy, as many three-dimensional configurations of density and field may produce identical polarization patterns. Therefore, our analysis assumes specific, physically-motivated and parametrically-defined field structures that we compare to data. In effect, we expect to be able to rule out broad classes of models representing particular geometries, but it is not generally possible to firmly confirm any particular model as correct.

2.6 Equilibrium Models of Molecular Clouds

This section briefly introduces equilibrium models of molecular clouds. We note that our models are not detailed equilibrium magnetic models, since such models are generally too slow to compute. However, we include this discussion to introduce polytropes, which are central to our method, and in the hopes that true magnetic equilibrium models may eventually be included within the PolCat framework.

2.6.1 Polytrope

A simple model often utilized when modelling molecular clouds is that of a non-magnetized polytrope, which obeys the equation of state

$$P = K\rho^{\gamma}. \tag{2.25}$$

Here P is pressure, ρ is the density, and K is a constant. The coefficient γ is the "polytropic index" and is sometimes expressed as $\gamma = (n+1)/n$. These are calculated in the absence of a magnetic field, and so the equation of hydrostatic equilibrium takes the form

$$\rho\nabla\Phi + \nabla P = 0 \tag{2.26}$$

where Φ represents the cloud's gravitational potential. For a spherical symmetry

$$\nabla\Phi = \frac{-GM(r)}{r^2}. \tag{2.27}$$

We note that closed-form solutions to (2.26) and (2.27) do not exist for arbitrary γ.

2.6.2 Bonnor-Ebert Sphere

The equilibrium of a sphere of isothermal gas in hydrostatic equilibrium between gravitation, thermal pressure, and external pressure is known as a Bonnor-Ebert sphere (Bonnor, 1956). An isothermal gas has equation of state

$$P = c_s^2\rho, \tag{2.28}$$

which is a special case of the polytropic equation of state (2.25) where $\gamma \mapsto 1$ and $K \mapsto c_s^2$, the square of the (constant) sound speed. Thus, the Bonnor-Ebert sphere may be viewed as a special case of a polytrope model.

The Bonnor-Ebert sphere has its own critical mass based on the surface pressure $P_{ext} = \rho_s c_s^2$, the Bonnor-Ebert mass

$$M_{BE} = 1.182\frac{c_s^4}{(G^3P_{ext})^{1/2}}, \tag{2.29}$$

which defines the maximum mass allowed for a non-magnetized core subject to external pressure P_{ext}. (Bonnor, 1956; McKee and Ostriker, 2007). However, this picture is still incomplete; as it still assumes thermal internal velocities and neglects the effects of magnetic fields.

2.6.3 Singular Isothermal Sphere (SIS)

A closed-form singular solution exists for the isothermal model, which is referred to as the SIS solution. This is defined by the density profile

$$\rho = \frac{c_s^2}{2\pi G r^2} \tag{2.30}$$

(Shu, 1977). We note that the SIS model was used as a core density model in the Pol2007 code that predated PolCat (Chapter 4)

2.6.4 Ostriker Model

Ostriker (1964) studied the case of infinite, self-gravitating, non-magnetized cylinders with a polytropic equation of state, with γ in equation (2.25) taking the form $\gamma = 1 + 1/n$. The isothermal case has an exact density solution of

$$\rho = \frac{\rho_c}{[1 + r^2/8r_0^2]^2} \tag{2.31}$$

where ρ_c represents the central density of the profile. However, for large radii, this profile falls off as $\sim r^{-4}$, whereas observed filaments show $\sim r^{-2}$ (McKee and Ostriker, 2007).

2.6.5 Fiege & Pudritz Models

The Fiege & Pudritz model (Fiege and Pudritz, 2000b) models are of infinite, magnetized, isothermal cylinders threaded by a helical magnetic field. However, the isothermal equation of state in this case uses the full velocity dispersion with both thermal and non-thermal components. They found that, while the poloidal (z-direction) field component supported the cloud against gravitational contraction, the toroidal component works with gravity to compress the filament.

2.6.6 Self-Consistent Field Models

Due to the complex nature of the magnetohydrostatic equilibrium equation (equation (2.4) with magnetic terms (2.5)), no closed-form solutions exist. Constructing the simulation requires simultaneous evaluation of three linked differential equations: the Poisson equation for gravitation, Ampère's law, and the magnetohydrodynamic equilibrium equation (equation (2.4), differential form). Mouschovias (1976) developed a numerical technique called the self-consistent field method, by which these equations can be iteratively solved such that the solutions evolve towards stability.

Tomisaka, Ikeuchi, and Nakamura (1988a) apply self-consistent field method to model the equilibrium structure of a self-gravitating, isothermal, magnetized, rotating molecular cloud embedded in a stationary medium (Tomisaka et al., 1988a,b, 1989, 1990; Tomisaka, 1991). Fiege and Pudritz (2000d) expanded on this method to find prolate equilibrium models of cores that are dominated by a toroidal field component (B_ϕ).

Magnetic Equilibrium models have generally been too slow for the massive scale parameters search employed by PolCat. However, this may change as computational speeds continue to improve and new modelling techniques become available. Indeed, we are investigating a promising new method for the fast calculation of magnetic equilibrium models, which would make such models feasible for use with PolCat.

2.7 Flux Freezing and Coordinate Transformation

Under conditions of flux-freezing, the magnetic field is dragged along into a new configuration consistent with the change in position of the gas as it fragments to form cores and filaments. It follows that we can deform the simulated cloud from an assumed initial state to construct a model with a field consistent with the new configuration.

The behaviour of electric and magnetic fields is governed by Maxwell's equations

$$\nabla \times \mathbf{H} = \boldsymbol{\varepsilon}\frac{\partial \mathbf{E}}{\partial t} + \mathbf{J}, \tag{2.32}$$

$$\nabla \times \mathbf{E} = -\boldsymbol{\mu}\frac{\partial \mathbf{H}}{\partial t}, \tag{2.33}$$

$$\nabla \cdot (\boldsymbol{\varepsilon}\mathbf{E}) = \rho_{charge}, \quad \text{and} \tag{2.34}$$

$$\nabla \cdot (\boldsymbol{\mu}\mathbf{H}) = 0, \tag{2.35}$$

where $\mathbf{J}$ represents the current density, ρ_{charge} the charge density, $\mathbf{E}$ the electric field, and $\mathbf{B} = \boldsymbol{\mu}\mathbf{H}$. One important property to note is that the form of Maxwell's equations is invariant under coordinate transformations. Therefore, if we treat our cloud deformations as parametrized coordinate transformations, we can then apply multiple transformations in succession to deform our initial uniform magnetized cloud into the more complex geometry representing the final state. The invariance of Maxwell's equations keeps the magnetic field consistent to the new configuration. This method is similar to a technique called "transformation optics" employed to simplify computation of light propagation through non-homogeneous media and to design complex optical components such as invisibility cloaks (Ward and Pendry, 1996; Pendry et al., 2006). The initial formalism was first derived by Ward and Pendry (1996), although more recent publications utilizing this technique such as Tomisaka et al. (1988a,b, 1989, 1990); Tomisaka (1991) adopt a tensor-based approach. The exact formalism that we use is taken from lecture notes by Steven G. Johnson at MIT (Johnson, 2007), freely available over the internet at `http://math.mit.edu/~stevenj/18.369/coordinate-transform.pdf`.

The field transformations required for Maxwell's equations to take the same form across the coordinate systems from $\boldsymbol{r} \rightarrow \boldsymbol{r'}$ are expressed in terms of the Jacobian matrix $\boldsymbol{\mathcal{J}} =$

$\partial(x_i', ..x_n')/\partial(x_i, ...x_n)$ of the transformation as

$$\mathbf{E}' = (\boldsymbol{\mathcal{J}}^T)^{-1}\mathbf{E} \tag{2.36}$$

$$\mathbf{H}' = (\boldsymbol{\mathcal{J}}^T)^{-1}\mathbf{H} \tag{2.37}$$

$$\boldsymbol{\varepsilon}' = \frac{\boldsymbol{\mathcal{J}}\boldsymbol{\varepsilon}\boldsymbol{\mathcal{J}}^T}{\det \boldsymbol{\mathcal{J}}} \tag{2.38}$$

$$\boldsymbol{\mu}' = \frac{\boldsymbol{\mathcal{J}}\boldsymbol{\mu}\boldsymbol{\mathcal{J}}^T}{\det \boldsymbol{\mathcal{J}}} \tag{2.39}$$

$$\mathbf{J}' = \frac{\boldsymbol{\mathcal{J}}\mathbf{J}}{\det \boldsymbol{\mathcal{J}}} \tag{2.40}$$

$$\rho'_{charge} = \frac{\rho_{charge}}{\det \boldsymbol{\mathcal{J}}}. \tag{2.41}$$

We note that these equations are proven in Appendix A.

To apply the transformation technique to the problem of a magnetized molecular cloud, we assume that charge density is directly proportional to mass density, which is justified if the density of ions and neutrals are proportional in the initial state, since they can only slip past each other on the ambipolar diffusion timescale (see §2.1), which is much larger than the dynamical timescales in the molecular cloud core. Under this assumption, the coordinate transformation for mass density takes the identical form to equation (2.41)

$$\rho' = \frac{\rho}{\det \boldsymbol{\mathcal{J}}}. \tag{2.42}$$

To obtain the corresponding magnetic field transformation, we take $\mathbf{B} = \boldsymbol{\mu}\mathbf{H}$ to obtain

$$\mathbf{B}' = \frac{\boldsymbol{\mathcal{J}}\boldsymbol{\mu}\boldsymbol{\mathcal{J}}^T(\boldsymbol{\mathcal{J}}^T)^{-1}\boldsymbol{H}}{\det \boldsymbol{\mathcal{J}}} = \frac{\boldsymbol{\mathcal{J}}}{\det \boldsymbol{\mathcal{J}}} \cdot \boldsymbol{\mu}\boldsymbol{H} \tag{2.43}$$

$$= \frac{\boldsymbol{\mathcal{J}}}{\det \boldsymbol{\mathcal{J}}} \cdot \mathbf{B} \tag{2.44}$$

Following this logic, we can begin with a simple initial density and field configuration and apply a series of parameterized coordinate transformations to create a more complex core model. This approach has several notable advantages, including the ability to easily create a

complex, three-dimensional model of a core or filament with a "natural" field resulting from the gas motions, and the series of transformations suggests a possible (though non-unique) history of gas motions of the cloud. Moreover, since the transformations are parameterized, the method lends itself to methods designed for the efficient exploration of large parameter spaces. Fiege (2005) was the first to apply this technique to modelling a molecular cloud, transforming a uniform distribution into a selected density configuration by assuming mass conservation. The resulting field is assumed to have been dragged along with the gas into the new configuration, simulating the effect of flux-freezing (Fiege, 2005). We shall discuss the detailed mechanics of this technique in §4.1.3.

Chapter 3

Optimization and Genetic Algorithms

Our overall objective with this project was to create a modelling package that attempts to generate a parametric model of the intensity and polarization structure of molecular cloud cores that are well-constrained by observational data. We argued at the end of the previous section that this can be accomplished using techniques to explore a large parameter space encoding our coordinate transformations by optimizing functions representing the goodness of fit to observational data. In this section, we discuss the genetic algorithm that we used for this purpose.

3.1 Optimization, Parameter Search, and Optimizers

We consider a bounded optimization problem, in which we scale to minimize $f(x_i, ...x_n)$ by varying each x_i over its range $x_i \in [x_{i,\min}, x_{i,\max}]$.[1] In general, we will attempt to minimize a function representing the residuals between the data and the model.

For the case of comparing a parametric model $X_i(x_i, ..., x_n)$ to a target dataset with corresponding values D_i, we require an objective function that minimizes the difference between X_i and D_i to determine the model's "goodness-of-fit." The standard objective

[1]Note that there is no loss of generality in discussing minimization, since any maximization problem can be trivially converted into a minimization problem by minimizing its negative.

function for this case is the χ^2 test:

$$\chi^2 = \sum_i^N \frac{(X_i - D_i)^2}{\sigma_i^2} \tag{3.1}$$

for N points with uncertainties σ_i.[2]

The heart of an optimizer is the method by which it explores the parameter space, and there are many different approaches. A variety of simple techniques involve measuring the change in the objective function over the local search area. These algorithms essentially find the direction in the parameter space where the objective function is decreasing and direct their search in that direction. The advantages of these techniques lie in that many of them are very quick at finding solutions with only a small number of function evaluations. However, these optimizers rely on a good starting point to evade local minima, often require gradient information, and are most effective in small search spaces. A poorly chosen initial point is likely to cause the algorithm to become trapped in a local minimum, leaving the global minimum undiscovered. A good general overview of computational optimization techniques can be found in Press et al. (2007).

In general, thorough exploration of the parameter space is required to uncover the global solution, but this can be computationally expensive. A good global optimizer is designed to search through large parameters spaces efficiently, to discover the global solution. However, this process is always more costly than local optimization.

3.2 Multi-Objective Optimization

Many problems in science and engineering are characterized by multiple criteria $f_1, \cdots, f_N$ which need to be optimized simultaneously. For example, the manufacturing problem of maximizing the quality of a product whilst simultaneously minimizing production cost (Fiege,

[2]In the context of optimization and the data itself, σ_i is understood to refer to uncertainty in the data, as opposed to the velocity dispersion in discussion of molecular clouds.

2010). Another example is our own situation, which requires simultaneous optimization of intensity and polarization parameters. Theoretically these objectives can be combined to create a single-objective problem, but often these objectives are characterized by mathematically independent functions which are often in conflict with each other. In most cases, a feasible solution that minimizes all of the conflicting objectives simultaneously does not exist. In this case, we aim to discover the Pareto front, or trade-off surface, such that it is not possible to improve any one objective without degrading at least one other.

It is useful to visualize each solution F^α as a vector in "fitness-space" with coordinates $(f_1^\alpha, ..., f_N^\alpha)$. For a solution F^β to dominate $F^{\alpha,}$ each fitness value of F^β must not be greater than the corresponding fitness value of F^α and must also have at least one value that is smaller than its F^α counterpart, that is,

$$\forall i \in \{1, \cdots, N\}, \quad f_i^\beta \leq f_i^\alpha, \quad \text{and} \quad \exists\, i \in \{1, \cdots, N\} : f_i^\beta < f_i^\alpha \tag{3.2}$$

(Goldberg, 1989; Fonseca and Fleming, 1993; Yu and Gen, 2010). Correspondingly, in this case F^α is said to be inferior to F^β. The set of all solutions that are inferior to no other solution (including those in the set) is said to be non-inferior or non-dominated. This set forms what is called the "Pareto-optimal" set or "trade-off surface", upon which no objective f_i can be improved for any solution without degrading the values of other objectives (Fonseca and Fleming, 1993, 1998; Yu and Gen, 2010). In an objective sense, all solutions on the trade-off surface are equally "good", although any one solution in the set may be poor for a specific objective. For example, a solution with good fitness in f_1 will often have relatively poor fitness in $f_2 ... f_N$, but will still be Pareto-optimal because it is non-dominated. However, it will be a very poor solution in the context of our whole problem. Many dual objective problems are characterized by a sharp bend (i.e. a significant change in curvature) in the curve, generally referred to as the "knee", where the solutions are considered balanced. However, such balanced solutions do not always occur. They are not preferred

over other solutions by the Pareto-optimality condition, but they are often preferred due to their balanced nature.

GAs are especially well-suited to multi-objective optimization, but some modifications are required. A common strategy is to rank the solutions based on Pareto-optimality. A solution's rank is defined by p_i, the number of solutions that dominate it such that

$$\text{rank}_i = 1 + p_i. \tag{3.3}$$

(Fonseca and Fleming, 1993). Naturally, solutions along the trade-off surface, being non-dominated, are all of rank 1. The rank is used in place of fitness during tournament selection. Niching is essential for a successful multi-objective GA, since all non-dominated solutions have rank 1 and are therefore all equally good. A niched code allows the population to spread out over the current non-dominated set, which gradually converges toward the Pareto front.

3.3 Genetic Algorithms

Genetic algorithms (GAs) are global search algorithms that optimize a collection of solutions by simulating the biological evolution of a population of individuals, taking advantage of the natural way organisms evolve to suit their environment. In the original Holland-style GA (Holland, 1975), each individual solution coded by a string of binary bits, where the sequence of bits may represent a set of real-valued parameters or other attributes of the model. The bit sequence in a Holland-style GA is referred to as the "genotype," which must be decoded into a "phenotype" to express the model and evaluate its fitness.

The basic genetic algorithm first put forward by Holland (1975) generally follows this approach:

1. An initial population of individual solutions is generated as a random bit sequence.

2. Bit sequences are decoded into parameters and the models are generated, which are

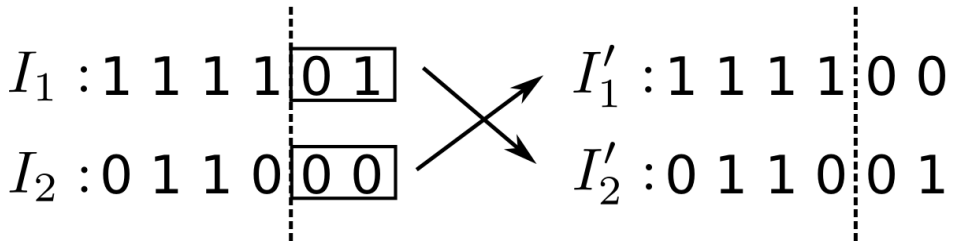

Figure 3.1: Holland-Style Crossover.

judged according to some objective function, f, which acts as the arbiter of natural selection for the population.

3. A selection operator is applied, in which poor solutions are "killed off" and replaced with copies of good solutions.

4. A crossover operator is applied, which mixes information present in the population. In the most basic case of a string of bits, two solutions are paired and a random number representing a parameter index is selected. The two parent solutions swap their bits for all parameters to the right of this index as a block, and create two new child individuals. (For an illustration of this process, see Figure 3.1).

5. A mutation operator is applied to a small fraction of the population, in which (usually) a single bit is flipped ($0 \leftrightarrow 1$) has a small probability of changing value at random. This allows some ability for parameter space exploration, even as the population converges on the ideal solution.

6. Steps 3 to 5 are iterated until the population converges on an ideal solution to the problem represented by f.

In this basic GA, information is transferred as a block. Eventually, as evolution proceeds patterns will emerge in the individual strings as the population gets closer to the optimal value, e.g. the individuals 1100010 and 0110011 share the pattern *1**01*. It is apparent that this pattern has a high chance of being split during crossover. However, the pattern ****01* is more likely to survive intact to the next generation due to its compactness. These

little packets are referred to as building blocks. The well-known schema theorem shows that the enrichment of building blocks via genetic operators is a powerful search of the solution space and global optimization.

The Holland-style GA described above is only the simplest form of genetic algorithm, and is rarely used today. Modern implementations usually bypass the bit string encoding entirely, encoding parameters directly as real numbers. this is more convenient for parametric problems, but also allows more general evolution operators based on geometry in a space of real-valued parameters.

Genetic algorithms here have the advantage that they are extremely robust, require no derivations, and have an excellent capability of exploring the parameter space efficiently. They are naturally parallelizable, since each solution can be evaluated independently.

Many optimization problems admit multiple solutions that are equally good. There may be multiple islands of solutions or continuous sets spanning some region of the parameter space. A good example is a χ^2 minimization problem, in which one ideally wants to find the true minimum plus all solutions within some confidence interval. A "niched" GA can be used for this purpose.

3.3.1 Niching

A "niche" is an organism's role in its environment (Goldberg, 1989). Applying niching to a population causes it to break into several subpopulations optimized for different areas of the solution space. The size of the subpopulations is generally determined by some sort of shared cost. This assists in effectively searching the parameter space, as each of the subpopulations maps out an optimal area and can explore it without the entire population converging on one apparently optimal region when there may be several regions equally as good at face value. This is especially helpful for small population sizes, which might not effectively sample large spaces otherwise.

There are several methods available to encourage niches. One example is the "pre-

selection" technique, where the offspring replaces the inferior parent. This ensures that solutions only replace similar solutions in the next generation. Another technique is to assign a "shared fitness" to each member of a subpopulation, where the individual's fitness value f_i is modified by a "sharing function", which penalizes solutions that are very close together. This method reduces the "benefits" conferred by its own value as though there are finite rewards in its local area and it is forced to share them among its local population (Goldberg, 1989). Another common strategy (and the one that we employ), is to calculate a weighted evaluation ("niche count") of the number of close neighbours within some radius r_{share}. The weighting operates such that identical solutions (distance=0) have a weighting of 1, and this falls off to zero as distance goes to r_{share}. If two solutions are judged to be equally (or nearly as) good (i.e. χ^2 differing by less than some $\Delta\chi^2$), then the winner in tournament selection is declared to be the solution with the lower niche count, thereby encouraging the population to explore less well-explored parts of the parameter space (Fiege, 2010).

3.4 Ferret

Ferret is a powerful multi-objective genetic optimizer which is a part of the Qubist optimization toolbox for MATLAB developed by Jason Fiege. Qubist also contains four other optimizers, including Locust, multi-objective a particle swarm optimizer, and Anvil, a simulated annealing optimizer. Ferret has been in development for over decade and is distributed by nQube Technical Computing Corporation (`www.nqube.ca`). Moreover, it has been used extensively at the University of Manitoba in the department of Physics and Astronomy. It has been applied to the problem of modelling gravitational lensing (Rogers and Fiege, 2011), and is the optimizer for PARETO, a modelling package for intensity-modulated radiation therapy planning (Fiege et al., 2011), and GalAPAGOS, a modelling package for generating models of warped rotating galaxy disks (English et al., 2010).

Ferret is loosely based on the multi-objective GA paradigm described above, but also

employs some techniques borrowed from Evolution Strategies (Yu and Gen, 2010), such as self-optimization of control parameters. Other features are entirely unique to this software. Some relevant features include the following:

- multi-objective parameter space mapping, allowing us to model intensity and polarization simultaneously;
- built-in parallelization, which greatly decreases the overall runtime by splitting the calculations over multiple processors;
- automatic zooming, where the code automatically contracts its search limits as the solution evolves towards the global optimum;
- Linkage-Learning, which seeks out connections between parameters and breaks large problems down into smaller sub-problems when it can.
- strategy auto-adaptation, a process that adapts its own control parameters as needed as the run progresses.
- integrated visualization, which allows easy conceptualization of the solution space and views of the solutions, as well as efficiently allowing interfacing with user-defined graphics functions.

These are only some of the features Ferret has to offer; we have listed only the features we have applied to our problem. An exhaustive discussion of the code is provided in Fiege (2010).

Parameters in Ferret are real-valued and form vectors in the solution space. The crossover operator (referred to in the manual as "X-type crossover") draws a line connecting the two solutions and selects an offspring off that line. A number generated randomly from a Gaussian distribution determines where the offspring falls on that line, with a value of 0.5 picking the offspring off the midpoint. It also has an additional crossover operator, which behaves similarly to the traditional GA crossover in that it is a direct swapping of parameters.

However, it differs in that it swaps building blocks comprised of linked real-valued parameters instead of the string after an arbitrary index. This building-block crossover is controlled by Ferret's linkage-learning system and aids convergence.

Niching can be performed either in parameter space ("X-niching"), or fitness space ("F-niching"). We have used both "X-niching" and "F-niching" modes for our work. F-niching promotes mapping of the fitness space, producing well-mapped tradeoff surfaces, whereas X-niching promotes parameter space exploration. Our strategy is to combine the results of two separate runs performed with each type of niching, so as to gain the advantages of both.

It is important to note that PolCat and Ferret are separate software packages that work together at arms length. PolCat is a self-contained model-building package that uses Ferret as an optimizer, but is not a GA in itself. Rather, PolCat defines the parameter space, and Ferret searches it for combinations of parameters and uses PolCat to judge fitness between the models in its solution set and the input dataset. As the size of PolCat's parameter space is large – typically on the order of about 15 parameters for the primary models discussed in this work – Ferret's ability to handle large multi-objective data-modelling problems is crucial.

Chapter 4

PolCat

The PolCat framework began as "Pol2007": a basic, transformation-based modelling package developed by Jason Fiege and Lee Ferchoff in 2007. We first began work on development of this code in 2009, after which the code was renamed from "Pol2007" to "PolCat." The name is intended as a play on PolCat's polarization modelling capabilities and use of the Ferret optimizer (as polecats and ferrets are close relatives). The approach utilized by both versions of the software builds a three-dimensional model of a molecular cloud core by applying a series of parametrized coordinate transformations to a cloud with uniform density and magnetic field via the method of §2.7. Each coordinate transformation is defined by an independent set of adjustable parameters. PolCat uses Ferret to find an optimal combination of model parameters by comparing the data's polarization maps to those of a model generated by each Ferret parameter combination. The model maps are generated via the technique of Fiege and Pudritz (2000a), outlined in §2.5, with some minor modifications outlined in §4.1.4.

In its basic form, Pol2007 had a range of geometrical transformations, including one that transformed a uniform density and field into a singular isothermal sphere (SIS) density. This was used as the primary density model, as it was reasonable and the coordinate transformation could be computed analytically. Pol2007's transformations also included transformation components that could scale the spherical core into a spheroid or triaxial ellipsoid, twist the

magnetic field, orient the core axes with respect to the line of sight, and shift the position of the core from the centre of the grid to position $(\Delta x, \Delta z)$ in the plane of the sky. Due to the singular nature of the SIS model, the resultant model polarization maps had a large Gaussian blur applied to make the core appear extended. To prevent the blurred model polarization maps from being reduced in size, the Gaussian convolution was accomplished by first padding the array with zeros, causing the intensity and polarization to be artificially reduced at the edges. Additionally, Pol2007 fit the input dataset to a dimensionless model; that is, the code would attempt to generate a model that reproduced the intensity and polarization vectors, without taking into account physical scales.

A summary of our contributions to PolCat includes:

- The development of a technique to generate semi-analytic coordinate transformations based on a numerical radial density solution when an analytic expression does not exist (see §4.1.3).

- Correctly scaling our density models and simulated data into physical units for direct comparison to data.

- Modifications to the code structure to make it more organized, flexible, and easily extensible for future development.

- Numerous improvements to graphics and graphical user interfaces.

- Thorough testing and code validation.

- Application to real astrophysical data.

The remainder of this chapter gives a thorough overview of PolCat's features.

4.1 Methods

PolCat uses several adaptations of techniques described in the following sections in the process of building a model. Here we outline the exact formulations we use to generate our models and compare them to data.

4.1.1 Dimensional Scaling

For convenience in computation, we descale the coordinate grids and compute the models in dimensionless units, which are rescaled prior to polarization map simulation. We take this approach to avoid having to deal with physical constants during the actual computation, simplifying the problem to its essentials. As the dimensional scaling involves only constants, it is trivial to convert a dimensionless model to a physical one.

We have defined the dimensional units (r) as related to the dimensionless units ($\tilde{r}$) in the following way:

$$r = r_0 \tilde{r} \tag{4.1}$$

$$\rho = \rho_0 \tilde{\rho}. \tag{4.2}$$

We do not require a magnetic field scale, as the simulated polarization maps depend only on the direction of the magnetic field and not its magnitude.

As a convenient radial normalization, we choose the scaling required to cancel the constants for the Bonnor-Ebert problem (§2.6.2), obtained by solving Poisson's law for gravitation $\nabla^2\Phi = 4\pi G\rho$ and the hydrostatic equilibrium equation for a gravitationally bound, non-rotating, isothermal gas $\rho\nabla\Phi + \sigma_0^2\nabla\rho = 0$ self-consistently. Treating gravitational potential Φ as we have treated r and ρ above, we obtain

$$\frac{\Phi_0}{r_0^2} = 4\pi G\rho_0 \text{ , and} \tag{4.3}$$

$$\frac{\rho_0\Phi_0}{r_0} = \frac{\sigma_0^2\rho_0}{r_0}. \tag{4.4}$$

By rearranging and solving for r_0, we define the radial scale as

$$r_0 = \sqrt{\frac{\sigma_0^2}{4\pi G \rho_0}} \tag{4.5}$$

with ρ_0 and σ_0 — defined for our model's purposes as the cloud's initial density and velocity dispersion — as parameters in the model. Since the Jacobian is dimensionless, the model can be computed in dimensionless units and scaled back into physical units at the end of the calculation for the purpose of calculating dimensional polarization maps in Jy beam^{-1}.

4.1.2 Model Building

PolCat uses polarization maps generated from the Stokes I, Q, and U maps of an observational polarization data cube to determine the goodness of fit of a particular model, and so we require the polarization map of the model to have the same dimensions as the input dataset. To simplify ray-tracing of the three-dimensional model, we require the final grid to be rectangular, with the x–z plane of the grid having the dimensions of the input polarization map. We therefore begin with the uniform, rectangular grid, which we define by convention to be the "final" or "most-primed" system of coordinates ($\mathbf{r}^{(n)}$ for n transformations). We apply the inverse of each coordinate transformation in reverse order to the grid to take it into the "initial" or "unprimed" system of coordinates ($\mathbf{r}^{(0)}$), onto which the initial density $\rho^{(0)}$ and field configuration $\mathbf{B}^{(0)}$ are defined. The density and magnetic field of the core are then transformed forward according to

$$\mathbf{B}^{(n)} = \frac{\boldsymbol{\mathcal{J}}^{(n)} \boldsymbol{\mathcal{J}}^{(n-1)} \cdots \boldsymbol{\mathcal{J}}^{(1)}}{\det \boldsymbol{\mathcal{J}}^{(n)} \det \boldsymbol{\mathcal{J}}^{(n-1)} \cdots \det \boldsymbol{\mathcal{J}}^{(1)}} \cdot \mathbf{B}^{(0)} \tag{4.6}$$

and

$$\rho^{(n)} = \frac{\rho^{(0)}}{\det \boldsymbol{\mathcal{J}}^{(n)} \det \boldsymbol{\mathcal{J}}^{(n-1)} \cdots \det \boldsymbol{\mathcal{J}}^{(1)}} \tag{4.7}$$

for n transformations, where each $\boldsymbol{\mathcal{J}}^{(k)}$ is the 3x3 Jacobian matrix of the kth coordinate transformation with elements

$$\mathcal{J}_{ij}^{(k)} = \frac{\partial x_i^{(k)}}{\partial x_j^{(k-1)}}. \tag{4.8}$$

Figure 4.1 shows an example of this process. We then project the model to create a simulated polarization map according to the technique of Fiege and Pudritz (2000a), with modifications described in §4.1.4.

4.1.3 Semi-analytic coordinate transformation

For each model, the initial state of the cloud is assumed to be a uniform density and magnetic field. For the initial field, there are two possible geometric configurations: a constant field aligned with the z-axis of the core, or a constant field at polar angles (ϕ, θ) to core-z.

To compute a coordinate transformation that transforms a uniform density into a specified profile, we can use the principle of conservation of mass to link the two coordinate systems. This enforces the criterion that mass enclosed inside a radius of r' must be identical to that enclosed within a sphere of $r(r')$. This "moves" the gas in such a way that simulates contraction into a denser sphere (or expansion into a bubble if that is the desired density profile). Assuming spherical symmetry with co-linear axes between the two coordinate systems, the coordinate transformation behaves like a "stretch" on the spherical radius. Thus the coordinate transformation can be expressed as

$$x'_i = \frac{r'}{r} x_i, \tag{4.9}$$

with r' mapped to r (or vice versa) via mass conservation

$$dM = 4\pi\rho r^2 dr = 4\pi\rho' r'^2 dr'. \tag{4.10}$$

To calculate the least-primed radius r as a function of r' we can simply integrate (4.10) on

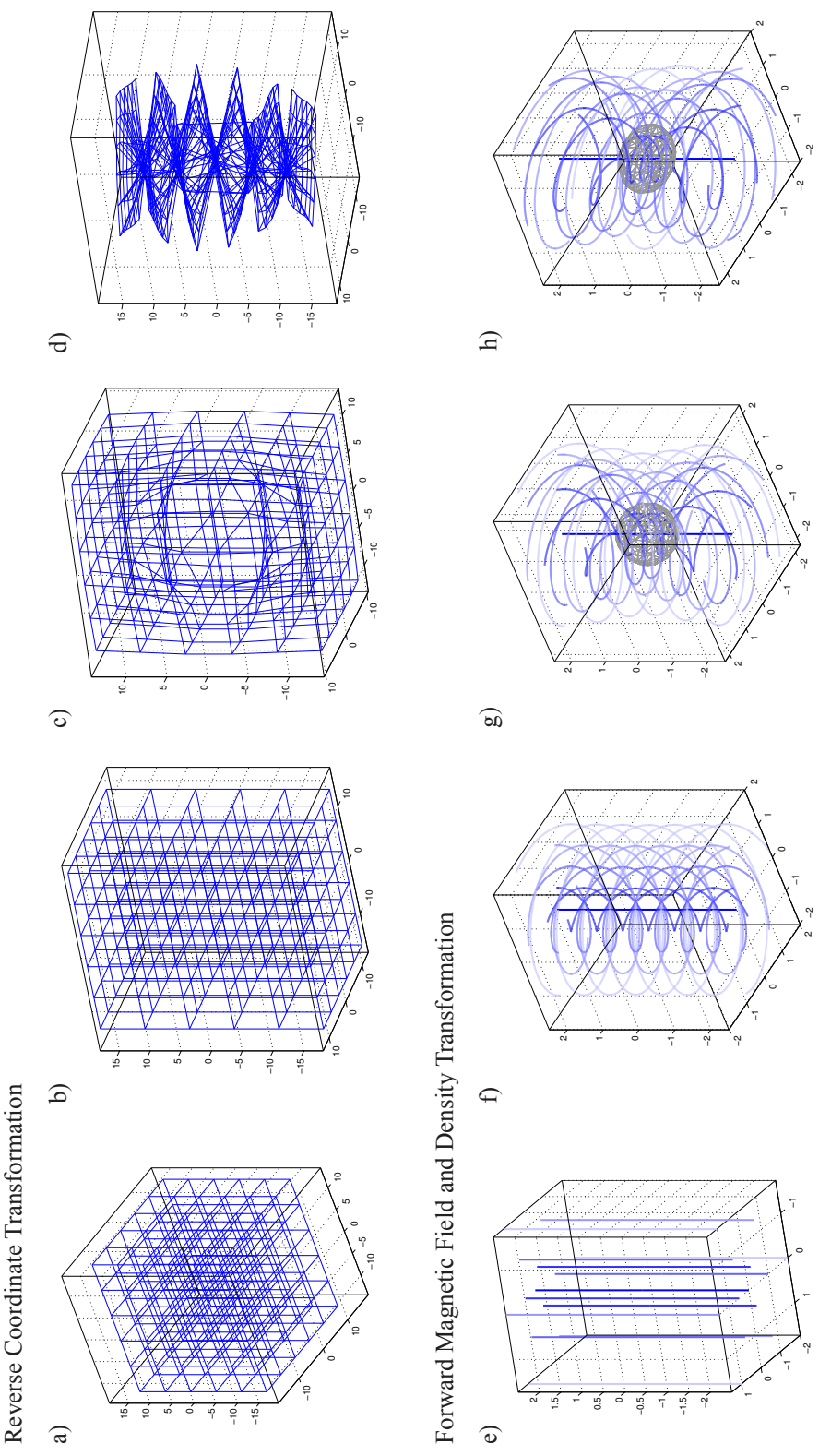

Figure 4.1: PolCat Model Building Process. Process for a 3-component model consisting of the transformations LinearTwistA, POLY, and Scale, in order of operation, a)-d) show the reverse coordinate transformation, starting with (a) the most-primed rectangular grid, through (b) scale, (c) polytrope, and (d) twist. In the bottom row, (e) starts with a uniform field and density defined on the transformed coordinates, then applies the forward transformations for the (f) twist, (g) POLY, and (h) Scale.

both sides of the equation, obtaining for a uniform less-primed density:

$$r = \left(3 \int r'^2 \frac{\rho'}{\rho} dr'\right)^{1/3}. \tag{4.11}$$

For the case of a singular isothermal sphere (§2.6.3), where the density profile is proportional to $1/r^2$, the result of (4.11) is a simple analytic equation. However, this model is not ideal, as it is unphysical due to the singularity at the centre of the sphere. Attempting to use more realistic density profiles creates an additional complication, as these profiles can often only be expressed with numerical solutions to a series of differential equations. While one may generate analytic approximations to these numerical solutions, the result of using them in (4.11) is often so complicated that the relation is either impractical or impossible to use.

We have therefore developed a technique by which we may calculate a coordinate and field transformation to transform a uniform density and field to that of a specified numerical density distribution. To compute the coordinate transformation itself, we we can rearrange (4.10) to obtain the differential equation

$$\frac{dr}{dr'} = \frac{\rho' r'^2}{\rho r^2}. \tag{4.12}$$

If the density profile is computed via a series of linked differential equations, (4.12) can be added to the list and computed simultaneously.

The Jacobian of a coordinate transformation is dependent on the derivative of the coordinates of one system with respect to another. For the case of a numerical density distribution, this would lead to taking numerical derivatives, which are performed by literally computing $\Delta f/\Delta x$. That is, for the components of the Jacobian matrix, we would literally be computing $(x_{i,n}^{(k)} - x_{i,n-1}^{(k)})/(x_{i,n}^{(k-1)} - x_{i,n-1}^{(k-1)})$, which is too crude and introduces error into the result. To avoid this, we require an alternate method to compute the components of the Jacobian. Taking the expression for an element of the Jacobian matrix (4.8) and substituting

in equation (4.9) yields

$$\mathcal{J}_{ij} = \frac{\partial x'_i}{\partial x_j} = \frac{\partial (r'/r \cdot x_i)}{\partial x_i}. \tag{4.13}$$

However, if we expand this expression via product rule and chain rule we obtain

$$\mathcal{J}_{ij} = \frac{x_i}{r}\frac{\partial r'}{\partial r}\frac{\partial r}{\partial x_j} + r' x_i \frac{\partial (r^{-1})}{\partial x_j} + \frac{r'}{r}\frac{\partial x_i}{\partial x_j} \tag{4.14}$$

$$= \frac{x_i}{r}\frac{\partial r'}{\partial r}\left(\frac{x_j}{r}\right) + r' x_i \left(-\frac{1}{r^2}\cdot\frac{x_j}{r}\right) + \frac{r'}{r}\delta_{ij} \tag{4.15}$$

where δ_{ij} is the Kronecker delta. Substituting in (4.12) yields the final form:

$$\mathcal{J}_{ij} = \frac{\rho r^2}{\rho' r'^2}\frac{x_i x_j}{r^2} - \frac{r'}{r}\left(\frac{x_i x_j}{r^2}\right) + \frac{r'}{r}\delta_{ij}. \tag{4.16}$$

This allows the elements and determinant of the Jacobian to be computed quickly and efficiently using known numerical quantities without introducing error from numerical derivatives.

As a proof-of-concept, we shall explore the case of a transformation from a uniform density ($\rho = 1$) and field to singular isothermal sphere (SIS); a problem that can be computed independently of the above expansion. The SIS profile has the equation

$$\rho' = \frac{c_s^2}{2\pi G r^2} \longmapsto \rho' = \frac{2}{r'^2} \text{ (dimensionless)} \tag{4.17}$$

and using (4.10) we obtain the dimensionless radial ratio with corresponding coordinate transformation

$$\frac{r'}{r} = \frac{r^2}{6} = \frac{1}{6}(x_i^2 + x_j^2 + x_k^2), \tag{4.18}$$

and

$$x'_i = \frac{r'}{r}x_i = \frac{r^2}{6}x_i = \frac{1}{6}(x_i^3 + x_i x_j^2 + x_i x_k^2). \tag{4.19}$$

Computing the Jacobian elements directly using (4.8) we obtain

$$\mathcal{J}_{ij} = \frac{1}{3}x_i x_j + \frac{1}{6}(x_i^2 + x_j^2 + x_k^2)\delta_{ij}. \tag{4.20}$$

Using (4.16), we obtain

$$\mathcal{J}_{ij} = \frac{r^2}{2}\frac{x_i x_j}{r^2} - \frac{r^2}{6}\frac{x_i x_j}{r^2} + \frac{r^2}{6}\delta_{ij} \tag{4.21}$$

$$= \frac{1}{3}x_i x_j + \frac{1}{6}(x_i^2 + x_j^2 + x_k^2)\delta_{ij}, \tag{4.22}$$

identical to (4.20). This transformation has been previously implemented, for a description, see §4.3.1.

This semi-analytic technique can also be applied to systems with cylindrical symmetry under the assumption that $z' = z$ between coordinate transformations. This has not been implemented at PolCat's current state of development, but we intend to add the capability for cylindrical models as a priority for future development. These modifications will allow us to model long filaments without stretching a spherical distribution, as is the current approach.

4.1.4 Polarization Map Simulation

Calculation of the simulated polarization follows the formulation of Fiege and Pudritz (2000a) as discussed in §2.5, with the addition of a grain alignment function, $g(\rho)$ to simulate the reduction of polarization observed in denser regions and provide an additional control on polarization intensity and fraction. We choose our empirical grain alignment equation to be

$$g(\rho) = \left(1 + \gamma_g \frac{\rho}{\rho_{\max}}\right)^{\beta_g}, \tag{4.23}$$

with $\gamma_g \in [0, 1]$ and β_g parameters fit by Ferret. Inclusion of these parameters in Ferret's search is optional, and the user can eliminate the effect of $g(\rho)$ from the polarization maps

entirely by setting either γ_g or β_g equal to zero in the `setupPol` file (see §4.2). As the default ranges for these parameters include zero, solutions without depolarization are always contained within the parameter ranges that are searched.

We integrate $g(\rho)$ into the polarization map calculation, with equations (2.18) and (2.19) now taking the form

$$q = \int \rho \; g(\rho) \cos(2\psi_B) \cos^2(\gamma_B) dy \tag{4.24}$$

$$u = \int \rho \; g(\rho) \sin(2\psi_B) \cos^2(\gamma_B) dy \tag{4.25}$$

and,

$$I = \int \rho \; dy + \langle \alpha \rangle \int \rho \; g(\rho) \left(\frac{\cos^2(\gamma_B)}{2} - \frac{1}{3} \right) dy. \tag{4.26}$$

The intensity maps created with the effective Stokes vectors are of integrated surface density in units of g cm^{-2} instead of Jy beam^{-1}, so we require additional scaling to properly fit the maps to the data. Equation (2.13) can be expressed

$$I = (\Sigma - \langle \alpha \rangle \Sigma_2) \sum_j C_{+,j} B_\nu(T_j) c_j, \tag{4.27}$$

We can treat the summation term as a constant, C_{flux} ("flux conversion") scale in units of Jy beam^{-1} g^{-1} cm^2, with which we can scale the maps into Jy beam^{-1}. Johnstone et al. (2003) and Fiege et al. (2004) estimated that the inverse of this factor (defined in Fiege et al. (2004) as "FCF" which is C_{flux}^{-1} in our definition) using observed dust temperature T_d and emissivity at 850 μm κ_{850} via

$$FCF = 0.13 \left(\frac{\kappa_{850}}{0.02 \text{ cm}^2 \text{ g}^{-1}} \right)^{-1} \times \left[\exp \left(\frac{17 \text{ K}}{T_d} \right) - 1 \right] \text{ Jy}^{-1} \text{ beam g cm}^2 \tag{4.28}$$

(Johnstone et al., 2003). Fiege et al. (2004) included a similar scaling constant as a parameter in their model, using this equation to estimate the bounds. With a dust temperature range of

8–15 K and estimated κ_{850} range of 0.01–0.02 cm^2 g^{-1}, they determined bounds of 0.27–1.92 g cm^{-2} Jy^{-1} beam on FCF. We have adopted a slightly wider range in the default fitting parameters for our C_{flux}, taking into account that we have defined our scaling constant as the inverse of the parameter in Fiege et al. (2004) for convenience in our code.

In addition to this conversion factor, we also include an intensity offset C_{shift}. This parameter is required due to the JCMT measurements being the difference between chop positions rather than directly measuring the absolute intensity, and so there is no absolute zero point on the intensity maps (Fiege et al., 2004).

Effective Stokes q and u are adequate for computing map vector position angles χ_{pol} and fractional polarization P_{frac}. Since both maps are dependent on ratios, C_{flux} has no bearing on these quantities. However, both the intensity map and the polarized intensity $P_{flux} = \sqrt{Q^2 + U^2}$ require C_{flux} to be expressed in Jy beam^{-1}.

After we have generated the Stokes maps, we convolve them with a Gaussian with a FWHM equal to the beam size of the observing instrument. Prior to the convolution, the maps are padded on all sides to a size of $(X + 2N) \times (Z + 2N)$ where our Gaussian mask is size $N \times N$. The padding is performed by reflecting the map at the edges so as to create a continuous edge. We have adopted this reflecting approach as padding the maps with zeros has a non-negligible effect on the maps as a whole; most notably artificially lowering the model values on the edges. The maps are then cropped back to the original size and used to calculate position angle (χ_{pol}), polarized intensity (P_{flux}), and fractional polarization (P_{frac}) maps via

$$\chi_{pol} = \tan^{-1}\left(\frac{U}{Q}\right), \tag{4.29}$$

$$P_{flux} = \sqrt{Q^2 + U^2}, \text{ and} \tag{4.30}$$

$$P_{frac} = \frac{\sqrt{Q^2 + U^2}}{I} \tag{4.31}$$

This map is used to determine the fitness values. For an in-depth description of our fitness

function, see section 4.1.5.

4.1.5 Fitness Function

As Ferret searches the parameter space for combinations of parameters to build core models, it requires a function to assess the quality of the models produced. PolCat's fitness function outputs fitness values dependent on the residuals of the data with the model. Since we judge fitness based on polarization maps, there are seven potential objectives associated with this problem: the Stokes vectors, polarized intensity, position angle of the polarization vectors, and fractional polarized intensity. Potentially, we could treat this as a single-objective problem by adding the fitness functions for each objective into a single quantity to minimize. However, the intensity has a much higher signal-to-noise ratio ($\sim I/\sigma_I$) than the other potential polarization objectives, and so has a much larger reduced χ^2 value. This value is large enough that the intensity fitness would completely dominate and the polarization signal would be lost in the noise. This would prevent us from obtaining the best possible fits to the polarization objectives. Instead, we opt for a multi-objective approach, such that each objective can be minimized separately while still contributing to the fit significantly.

The code is set up for two fitness modes: Stokes and Pol. Stokes mode is a three-objective fit using Stokes vectors I, Q, and U as the fitness objectives, whereas Pol mode uses I, χ_{pol}, P_{frac}, and polarized intensity $P_{flux} = \sqrt{Q^2 + U^2}$). Any of the four objectives in Pol mode can be turned "on" or "off" for a given run. For a typical run, we use only two objectives in Pol mode for reasons discussed in §6.

Although we wish to have the best possible simultaneous fit to both intensity and polarization, we argue that the fit to the intensity map must be prioritized over that of the polarization (although not to the extent that combining the parameters into a single-objective problem would produce). The model polarization vectors tend to be highly degenerate for a variety of different intensity maps, and often the solutions with good polarization fitness after the knee in the trade-off surface will not have intensity maps that match the data at all.

An adequate model must fit well in intensity since the density structure contributes more strongly to the intensity map than the magnetic field.

When choosing our fitness function, we find that fitting in Stokes mode, where the second and third objectives are the Stokes parameters Q and U, is problematic. We are mainly interested in the position angle and polarized intensity, and we find that Stokes mode is not effective at producing optimal polarization maps. The position angles calculated from these fits are extremely poor matches to the observed polarization patterns of the data outside the immediate knee region of the tradeoff curve. As a result, the Stokes mode fitness function is largely deprecated, although it remains as part of PolCat's infrastructure.

As an additional hurdle, 3-objective Pol mode fits using I, χ_{pol}, and P_{flux} to judge fitness are also problematic, due to two of these three fitness objectives being highly dependent on Q and U. This causes the optimizer to prioritize fits to the polarization objectives over the intensity, which tends to degrade the quality of the intensity fits. By this logic, using fractional polarization as a third objective would seem to be a solution to this problem, as it is calculated based on all three Stokes vectors and depends only on the integrated model functions independent of the scaling conversion constants. However, we find that similar issues arise, as the fractional polarization's inverse dependence on intensity has a tendency to prioritize the fidelity of fit towards fainter areas of the map.

All objectives except intensity are fit for a dataset of N non-masked pixels for a run of ν parameters using a reduced chi-squared function

$$\chi^2_\nu = \frac{1}{N-1-\nu} \sum_{i=1}^{N} \frac{(X_i - D_i)^2}{\sigma_i^2} \tag{4.32}$$

with X_i representing model map values and D_i and σ_i^2 the corresponding data and variance values. As χ_{pol} is defined as the angle the polarization vectors make with the vertical, the data and model χ_{pol} values are adjusted such that all angles are between 0 and π (a simple 180° rotation is applied if the angle falls outside this range) before computing the χ^2_ν value.

We use a different function to determine goodness-of-fit for the intensity map. Attempting a reduced chi-squared fit on the intensity data results in a χ^2_ν values somewhere around 10^4, which does not necessarily represent the quality of the model as we find that often the deviation between model and data values are around 20% or less. A thorough examination of the data reveals that the intensity variance itself is very small; typically the error in the intensity is on the order of 1% of the intensity root mean square (RMS) value. Since the uncertainty is so small, this causes the intensity χ^2 value to be very large, despite reasonable residuals.

Instead of the reduced χ^2 function, we use

$$F_I = 100 \times \frac{\frac{1}{N_I}\sum_{i=1}^{N_I} |I_i^{model} - I_i^{data}|}{\bar{I}^{data}} \tag{4.33}$$

where N_I is the number of non-masked points in the map and $\bar{I}^{data}$ is the average data value. This expression describes the average absolute deviation as a percentage of average data intensity. It is important to note that N_I and the number of non-masked data pixels may occasionally differ due to occasional (rare) NaNs due to small MATLAB calculation errors in the model map, which reduces the number of points available for comparison. We therefore calculate $\bar{I}^{data}$ based on the available non-masked pixels in the dataset, such that $\bar{I}^{data}$ remains a fixed, constant value for each run.

In addition to the base fitness values, we have applied a penalty for the shift parameters centring the model core in areas where the data has been cropped (or "masked out"), as sometimes positioning the core at the edges of the map can produce a good fit to the polarization objectives despite being a terrible fit for intensity. As the model is not optimal if the resulting intensity map does not coincide with the data, applying this penalty prevents Ferret from wasting time on these models. This penalty function only applies to models whose shift parameters Δx and Δz lie on masked pixels, and it scales linearly with distance

from the nearest non-masked pixel as

$$\mathrm{P_{dist}} = 100 \times (1 + \min(\sqrt{(X - \Delta x)^2 + (Z - \Delta z)^2})) \tag{4.34}$$

where X and Z are the coordinates of all non-masked pixels.

We apply a second penalty, $\mathrm{P_{fit}}$, to the fitness value to better populate the trade-off surface in the knee region. The penalty acts as a threshold on the fitness value, with $\mathrm{P_{fit}}$ having the largest value when both F values are outside the allowed range, and reducing to zero when both F values are inside the range as

$$\mathrm{P_{fit}} = 100 \sum_{i=1}^{n} F_i^{max} \times w_i + (F_i - F_i^{max}) \times w_i \tag{4.35}$$

where w_i is 0 if F_i is under the threshold F_i^{max}, and 1 if it is over.

Occasionally, PolCat has a tendency to select a population of elongated solutions with their major axes closely aligned to the line of sight. Due to projection effects, this particular geometry allows a great deal of control over the intensity and polarization vectors and so these solutions tend to fit exceptionally well to the data. While these solutions are a valid possible geometry, it is unlikely in the extreme that many cores are at that particular orientation, and conflicts with previous findings on the objects in question. Additionally, due to the numerical nature of our simulations, it is inadvisable to accept solutions where the "surface" of the core intersects with the "front" and/or "back" x–z planes of our coordinate grid. We define this "intersection" penalty as follows: for N voxels at $y = y_{min}$ and M voxels at $y = y_{max}$ where $\rho > \rho_s$,

$$\mathrm{P_{int}} = C \times (N + M) \tag{4.36}$$

where C represents a scaling constant. Tests with this function show a scaling factor of 5 is adequate. This penalty is not calculated for non-truncated polytropes, as there is no "surface" and therefore no sudden change in density to intersect with the front and back

edges of the grid.

We apply these penalties to each fitness value, such that an improvement in any of the penalty functions show an equal improvement over all objectives. This aids the algorithm in its search by clearly indicating which areas of the solution space are undesirable in the context of our problem.

4.2 Code Structure

Figure 4.2 summarizes PolCat's main functions and how those functions interface with Ferret. The initialization file, `init`, loads the specified dataset. The `setupPol` file is intended for user edits in order to enable or disable PolCat-specific model features, such as initial field configuration or polarization parameters. The function `makeModel` is PolCat's core: the main model-generation function. Given a set of model parameters and the output of `setupPol`, `makeModel` will generate a three-dimensional density and field model and the corresponding model polarization maps. Ferret interfaces with PolCat by calling `init` and `FerretSetup` to define the parameters for the fit, then calls the specified fitness function to find the fitness value. The fitness function calls the function `X2Par` to encode the Ferret parameters back into the transformation structures, generates a model with corresponding polarization maps for each solution, and computes the fitness values for each target objective.

This procedure remains largely unchanged between the two versions of the code; the basic model-building framework and the functions required to interface with Ferret were in place in Pol2007. However, the code was not flexible; changing to a different model required simultaneous manual edits to `init`, `setupPol`, `FerretSetup`, and `X2Par`. The general process of changing the model entailed:

1. editing `init` to change the dataset name;

2. editing `setupPol` to not only specify each model component, but also to properly initialize each transformation structure with placeholder parameters (see Figure 4.3

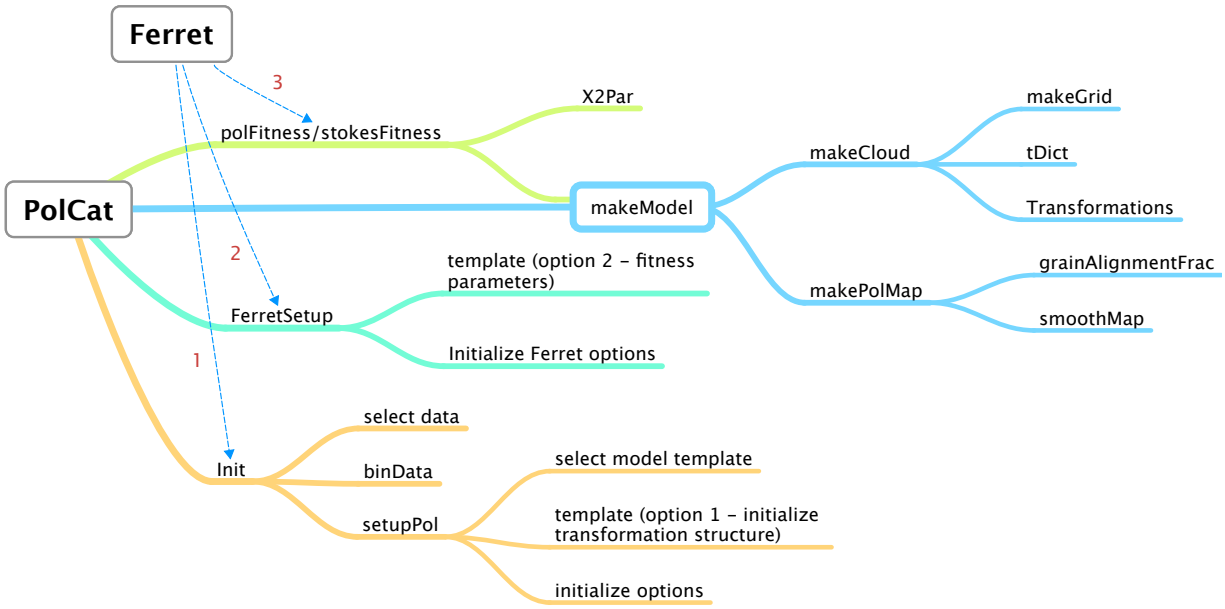

Figure 4.2: Illustrated PolCat File Structure.

for graphical representation of the `trans` structure);

3. manually editing the minimum and maximum limit arrays, parameter names, and cyclic parameters; and

4. editing `X2Par` to assign each element in the array of Ferret parameters to their proper place in the transformation structure.

Of particular note is step 3. This step was the most prone to error, as the order of parameters in the Ferret lists was assigned manually by the user in `FerretSetup`, which led to some confusion when changing the model components. Special attention needed to be paid when editing `X2Par` to ensure the parameters from the Ferret array were encoded properly into the model-building framework.

For PolCat, we have largely automated this process such that in most cases the only manual edits required are minor adjustments to `setupPol` and `FerretSetup` to edit polarization or Ferret options. Transformation component setup is now handled automatically through the use of user-defined templates. The model templates only require the user to define the

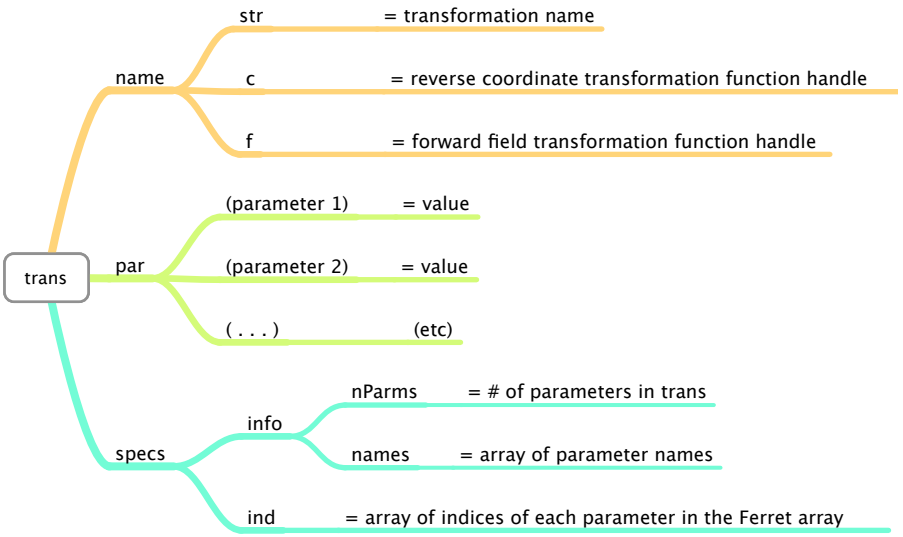

Figure 4.3: Illustrated Transformation ("trans") Data Structure.

names of the transformations to be used and the order in which they are to be performed. Optionally, the user may define any parameter to be logarithmic (such that $X \rightarrow \log_{10}(X)$), freeze any parameter to a given value to exclude it from the fit, and set custom fitness limits for any parameter. The template then automatically generates the output directory names, initializes the transformation structures, and generates the limit lists for `FerretSetup`. The template also assigns default values to the parameters where no custom limits are defined. This system has the benefit that a specific set of transformation settings can be applied to multiple datasets quickly and efficiently.

4.3 Transformations

This section lists the coordinate transformations in the library and their effects on the model structure. The singular isothermal sphere transformation (§4.3.1) and the transformations described in sections 4.3.3 to 4.3.9 were developed in 2007 by Jason Fiege and Lee Ferchoff. We have made minor alterations to several of these to improve flexibility and make them consistent with our improved infrastructure.

In addition to the parameters governing the coordinate transformations, there are op-

tional parameters relating to the initial cloud conditions and grain physics that the user can enable or disable for a particular run. This includes the grain alignment parameters, C_{flux} and C_{shift} discussed in §4.1.4 and the initial density and velocity dispersion discussed in section §4.1.1, although fitting r_0 and σ_0 is currently mandatory. In addition, if the user chooses to have the initial magnetic field to be misaligned with the z-axis of the core by polar angles (ϕ, θ), these angles are added to the PolCat parameter list.

A PolCat model consists of a list of transformations in a custom template. In this template, the user also has the option to define whether certain parameters are to be fit logarithmically or assigned a set value and excluded from the fit, and set custom limits for their choice of parameters. Each model should include scale, rotation, and shift transformations to properly shape, orient, and position the core with respect to our line of sight, in addition to whatever density setup and field transformations chosen for a particular model. The basic "default" model contains 5 transformation components (in order): Asymmetric Linear Twist (§4.3.6), Polytrope Density (§4.3.2), Scale (§4.3.4), Astronomical Rotation (§4.3.3), and Shift (§4.3.5). In this model, Twist parameter c_{twist} and POLY's dimensionless scaling constant K are fit logarithmically. A more thorough summary of this template and the other commonly-used templates for this work are located in Section 4.4.

4.3.1 SIS - Singular Isothermal Sphere Density

The singular isothermal sphere model was PolCat's original density setup, implemented by Lee Ferchoff. SIS transforms a uniform field and density into that of a non-truncated singular isothermal sphere (SIS), with the results shown in Figure 4.4. This model has no free parameters other than σ_0, one of the scaling constants, and has largely been abandoned in favour of the semi-analytic numerical models created by the technique of section 4.1.3. The derivation for this transformation may be found as a proof of concept of the technique of that section. However, we summarize the results here for completeness.

The dimensional SIS profile has the equation

$$\rho' = \frac{\sigma_0^2}{2\pi G r'^2} \tag{4.37}$$

which reduces to

$$\rho' = \frac{2}{r'^2} \tag{4.38}$$

in dimensionless coordinates. This results in the coordinate transformation

$$x_i' = \frac{1}{6} r^2 x_i = \frac{1}{6}(x_i^3 + x_i x_j^2 + x_i x_k^2) \tag{4.39}$$

which is simply and analytically reversible. The Jacobian operator therefore has diagonal terms

$$\mathcal{J}_{ii} = \frac{1}{2} x_i^2 + \frac{1}{6}(x_j^2 + x_k^2) \tag{4.40}$$

and off-diagonal terms

$$\mathcal{J}_{ij} = \frac{1}{3} x_i x_j. \tag{4.41}$$

4.3.2 POLY - Polytrope density transformation

POLY calculates and applies a coordinate transformation that takes an initial uniform density configuration and transforms it into a truncated polytropic sphere embedded in a uniform, isothermal medium with density ρ'_{out} and pressure P'_{out}, via the technique of §4.1.3. The coordinates and fields relating to the polytrope transformation are expressed in "primed" coordinates. The equation of state of the polytrope inside the truncation radius r'_s is given by the expression

$$P' = K \rho'^{\gamma} \tag{4.42}$$

with P' being the pressure, γ being the polytropic index, and K representing a scaling constant. The density profile in this region is obtained by solving Poisson's equation for

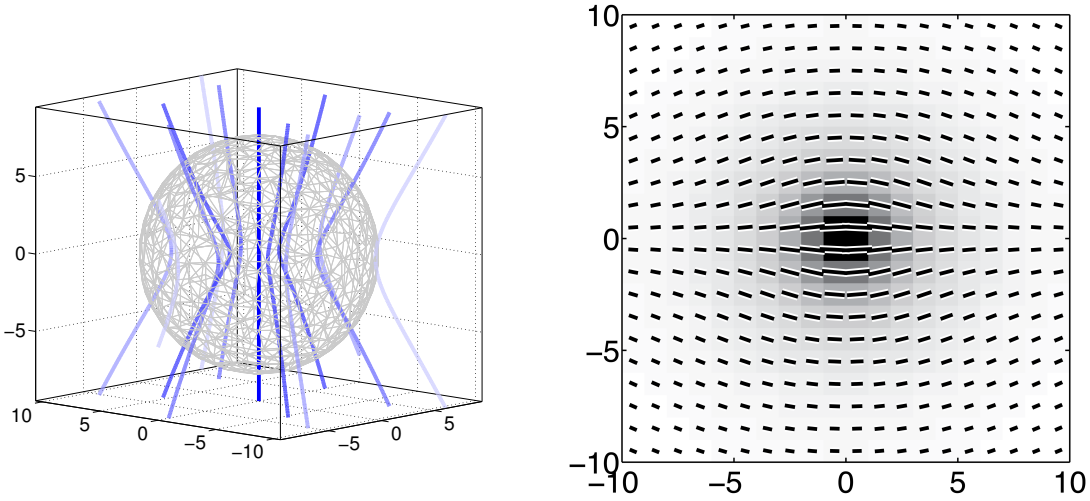

Figure 4.4: SIS Transformation. The model generated via applying the SIS transformation to a uniform field and density. The figure on the left is a stream plot of the magnetic field lines with the core represented by a density isosurface. The figure on the right is the simulated polarization map with the vectors scaled by $\sqrt{P_{flux}}$.

gravitation

$$\nabla'^2\Phi' = 4\pi G\rho' \tag{4.43}$$

where Φ' represents gravitational potential, in conjunction with the equation for hydrostatic equilibrium (non-magnetic case)

$$\rho'\nabla'\Phi' + \nabla'P' = 0. \tag{4.44}$$

Since these solutions are radially symmetric, the gradient reduces to $\nabla' = d/dr'\hat{r}$ and we obtain the linked differential equations

$$\frac{d\Phi'}{dr'} = g' \tag{4.45}$$

$$\frac{dg'}{dr'} = 4\pi G\rho' - \frac{2}{r'}g' \tag{4.46}$$

$$\frac{d\rho'}{dr'} = -\frac{g'}{\gamma K\rho'^{\gamma-2}} \tag{4.47}$$

where $g' = d\Phi'/dr'$ is a variable introduced to reduce the problem to a set of first-order differential equations. These equations can be written in dimensionless form using the scaling constants from section 4.1.1 in addition to

$$P_0' = \sigma_0^2 \rho_0 \tag{4.48}$$

$$K_0 = \frac{\sigma_0^2}{\rho_0^{\gamma-1}} \tag{4.49}$$

$$\Phi_0' = K_0 \rho_0^{\gamma-1} r_0^2 = 4\pi G \rho_0 r_0^2 = \sigma_0^2 \tag{4.50}$$

$$g_0' = \Phi_0 / r_0. \tag{4.51}$$

This results in the final set of equations

$$\frac{d\tilde{\Phi}'}{d\tilde{r}'} = \tilde{g}', \tag{4.52}$$

$$\frac{d\tilde{g}'}{d\tilde{r}'} = \tilde{\rho}' - \frac{2}{\tilde{r}'}\tilde{g}', \text{ and} \tag{4.53}$$

$$\frac{d\tilde{\rho}'}{d\tilde{r}'} = -\frac{\tilde{g}'}{\gamma \tilde{K} \tilde{\rho}'^{\gamma-2}}. \tag{4.54}$$

With the initial values at the origin $\tilde{\Phi}'(0) = 0$, $\tilde{g}'(0) = 0$, and $\tilde{\rho}'(0) = \rho_c$, with ρ_c defined as the dimensionless central density $\rho(0)/\rho_0$.

The model parameters of this transformation are therefore $\tilde{K}$, γ, and ρ_c, the density at the centre of the core. As we are also truncating where equation (4.42) is equal to the pressure of the external medium P_{out}, we also include the parameters $\tilde{P}_{out}$ and ρ_{out} in the fit. To prevent the density outside the core from being larger than that at the edge, ρ_{out} is defined as a fraction of the density at the surface ($\tilde{\rho}_s$) such that

$$\tilde{\rho}_{out} = \tilde{\rho}_s \rho_{out}. \tag{4.55}$$

Figure 4.5 shows example 1-D polytrope profiles generated with varying parameters. We find that, as ρ_c serves as the control on the height of the profile, K controls its spatial

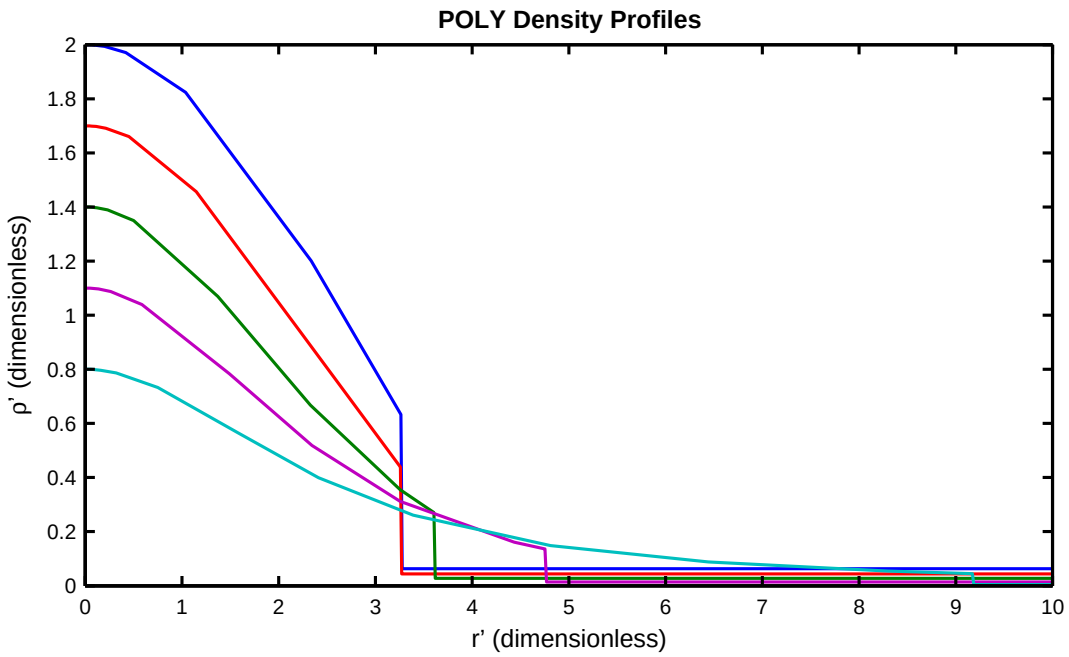

Figure 4.5: Polytrope Density Profiles. Plotted as a function of r', set for $\gamma = \rho_c$, $K = 0.5$, ρ_{out} and $P_{out} = 0.01$.

extent; reducing K while keeping other parameters constant results in a narrower profile, while increasing K results in a wider profile.

After experimenting with computing r by inserting equation (4.12) into the integrator as part of the (4.52)–(4.54) set and solving for r using trapezoidal integration after the computation, we find that the differences between the two are negligible on the order of the peak density. Therefore, we choose to compute the transformation equations via trapezoid integration for simplicity.

With no other transformations applied, a model consisting of only POLY transforms the uniform cloud to the truncated polytrope with an hourglass magnetic field arising naturally from the transformation (see Figure 4.6). The discontinuity in density at the truncation radius is also expressed on the field lines, which appear "kinked" at the core surface. However, the code has the option to eliminate the truncation entirely; if core pressure never falls below P_{out}, the core is not truncated. For $\gamma > 1$, the cores are self-truncating and therefore always fall below P_{out} at or near this radius of self-truncation.

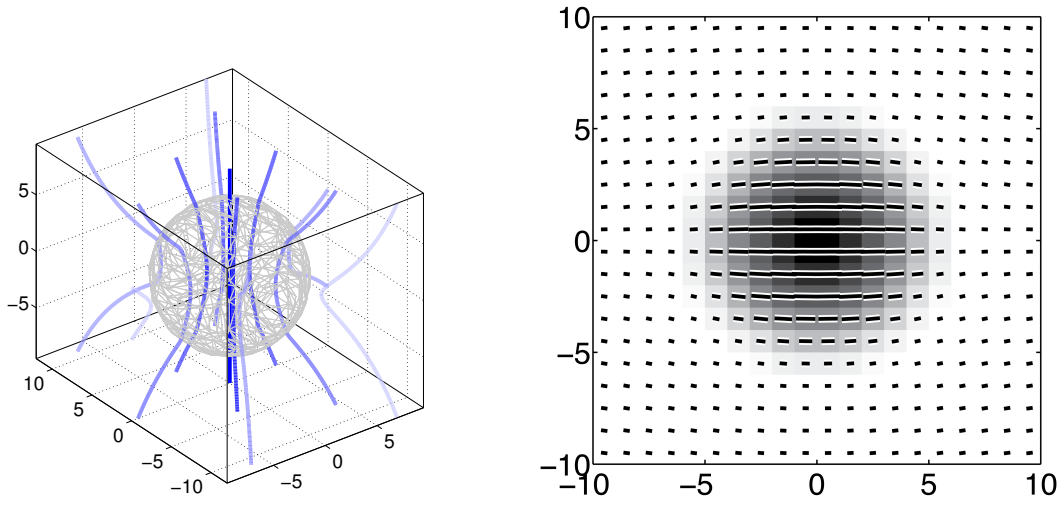

Figure 4.6: POLY Transformation. The results of the POLY transformation on a uniform medium. The figure on the left is the resultant magnetic field lines, with the density isosurface plotted at the truncation density ρ_s. The figure on the right is the simulated polarization map with the vectors scaled by the square root of the polarized intensity.

We note that this model is computed for non-magnetized hydrostatic equilibrium; the presence of the magnetic field means that cores generated with this transformation are generally not in equilibrium. We note that including the cloud's magnetic field into the equilibrium equations adds several magnetic terms to the conditions for hydrostatic equilibrium (equation (4.44)), which require the use of self-consistent field method to solve. As this technique is computationally expensive, it is not feasible to use at this time. However, we do not rule out the possible inclusion of such models in a future iteration of the code.

4.3.3 RotateA

This transformation performs a three-dimensional rotation consisting of:

1. A rotation about the positive z-axis by angle ϕ

2. A rotation about the positive x-axis by angle i

3. A rotation about the positive y-axis by angle PA.

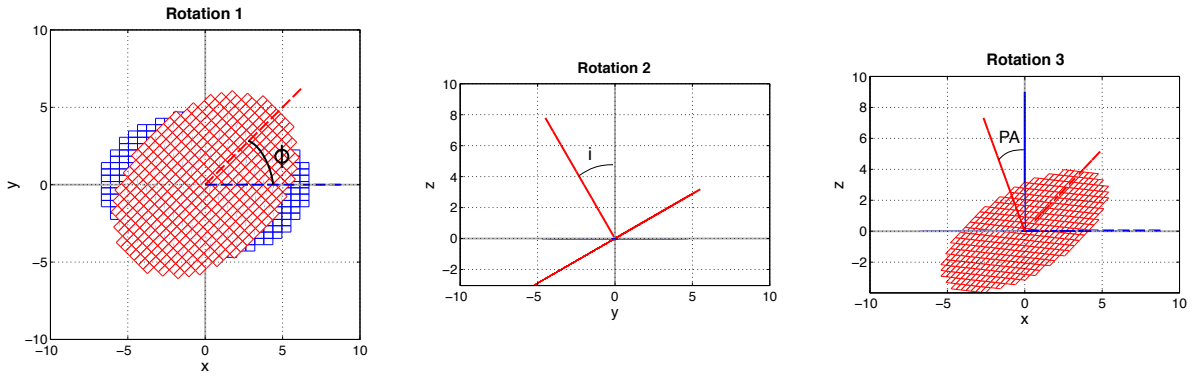

Figure 4.7: RotateA Transformation. The three steps of RotateA

The end result has the z-axis of the rotated system at inclination angle i to the line of sight and position angle PA to the z'-axis (for a visual representation of the RotateA orientation angles see Figure 4.7). This model uses all three angles as its parameters.

4.3.4 Scale

Scale transforms a sphere in the less primed coordinate system into a triaxial ellipsoid, as shown in Figure 4.8. The coordinate transformation itself is defined

$$x' = ax, \tag{4.56}$$

$$y' = by, \tag{4.57}$$

$$z' = \frac{z}{ab}, \tag{4.58}$$

where a and b are the model parameters. Defining the stretch on z to be equal to $c = (ab)^{-1}$ results in the determinant of the Jacobian being unity, preserving volume between the two coordinate systems.

As we have defined c dependent on a and b, it is difficult to determine the overall shape of the core from the two-dimensional parameter plot. As such, we have developed a useful plot to identify the specific shape of a core model at a glance. Since we have defined $c = (ab)^{-1}$, we can analytically determine the regions of the (a, b) parameter space where the triaxial

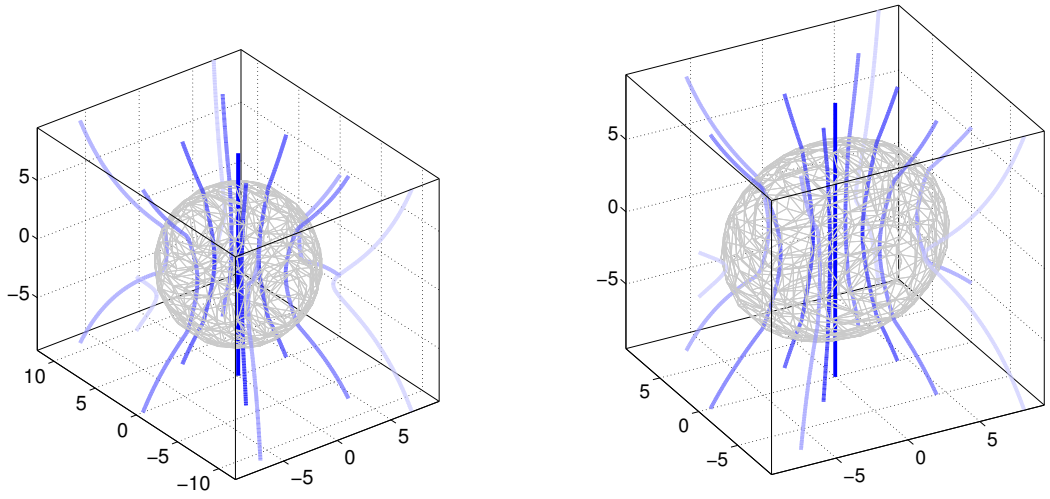

Figure 4.8: Scale Transformation. The polytrope core shown in Figure 4.6 (left) is transformed via Scale to produce the field and density shown on the right.

core is "oblate" ($c < a\&b$) and "prolate" ($c > a\&b$). These areas are the shaded regions of Figure 4.9, where the darker grey region is the "oblate" region, and the white area is the "prolate" region. The two light grey "wings" represent cores where $a < c < b$ (top) and $b < c < a$ (bottom). The diagonal line represents "true" spheroids, where $a = b$, and the two curves represent $a = c$ and $b = c$ respectively. The point at $a = 1$, $b = 1$ where the curves and line intersect represent spherical solutions.

4.3.5 Shift

Shift is a trivial transformation that offsets the centre of the projected core from (0,0) on the polarization map. In the three-dimensional model space, this transformation only operates on the x- and z-directions, so the coordinate transformation is given by

$$x' = x + \Delta x \tag{4.59}$$

$$y' = y \tag{4.60}$$

$$z' = z + \Delta z. \tag{4.61}$$

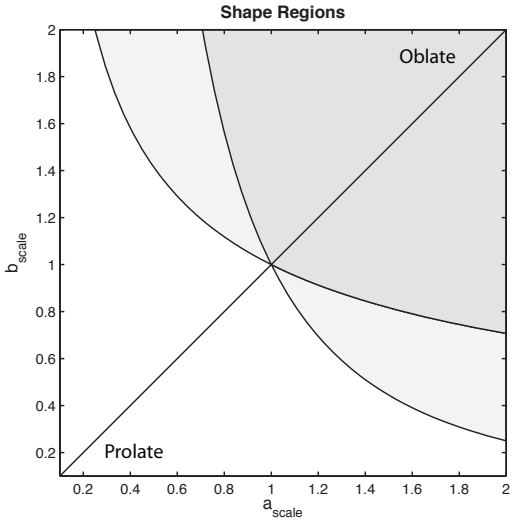

Figure 4.9: Shape Map Example. The shape map using default PolCat limits for scale parameters a and b. Oblate region ($c < a\&b$) in darker grey, prolate ($c > a\&b$) in white.

The Jacobian of this transformation is the identity matrix, and so has no effect on the geometry of the density and field. The transformation only affects the coordinates of the centre of the core.

4.3.6 LinearTwistA

This transformation applies an asymmetric linear twist about the z-axis, which is the axis of symmetry for symmetric models. The equations governing this transformation (in cylindrical coordinates) are

$$\phi' = \phi + c_{twist} z, \tag{4.62}$$

$$r' = r, \tag{4.63}$$

$$z' = z. \tag{4.64}$$

The only model parameter, c_{twist}, determines the amount of twist. This twists the field around the coordinate system's z-axis, creating a helical magnetic field shape (see Figure

4.10). If the z-axis is aligned with the axis of symmetry, the transformation does not affect the density of the core and only affects the magnetic field.

It would appear on the surface, that a simple way to produce a helical filament, such as the "pigtail" filament presented in Matsumura et al. (2012), would be to offset the core centre from the z-axis before applying the twist. However, it should be noted that attempting to apply this transformation to a shifted core does not result in a helix with circular density cross-section. In this case, the transformation behaves like a "coin shift", creating a flattened helix with a thin ellipsoidal cross-section. Two examples are shown in Figure 4.11.

4.3.7 LinearTwistS

This transformation behaves in a similar fashion to LinearTwistA, with the exception that the twist is symmetric about the x–y plane. The coordinate transformation is described in cylindrical coordinates by

$$\phi' = \phi + c_{twist}|z|, \tag{4.65}$$

$$r' = r, \quad \text{and} \tag{4.66}$$

$$z' = z \tag{4.67}$$

where c_{twist} is again a constant controlling the amount of twist. The field produced appears as though the centre (through the x–y plane) has been held fixed while the field lines are twisted counter-clockwise (see Figure 4.12). Creating polarization maps of models using this transformation often results in an overall 'S' shape to the E-field vectors.

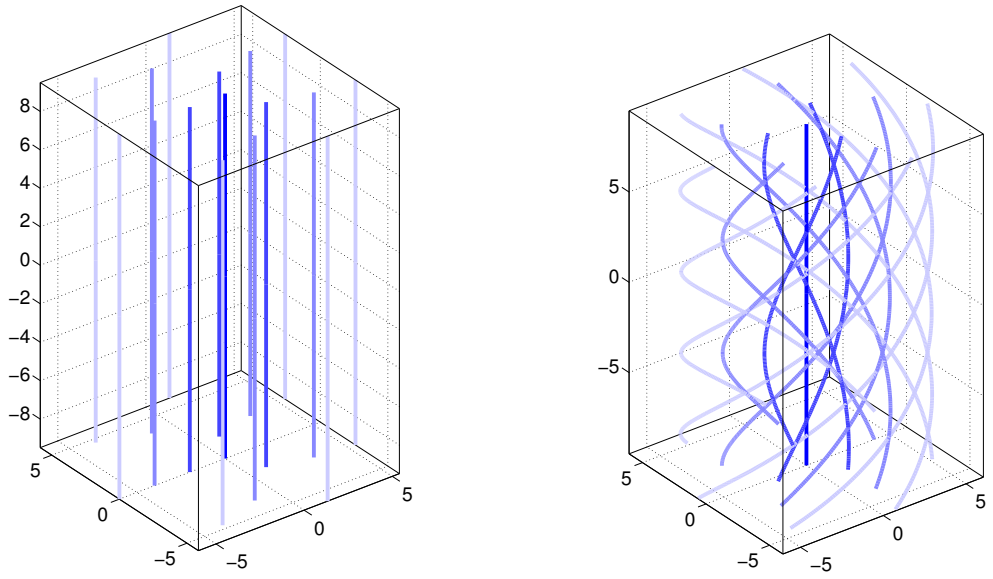

Figure 4.10: LinearTwistA Transformation. The effect of an asymmetric linear twist on a uniform magnetic field. LinearTwistA transforms the field on the left into the field on the right.

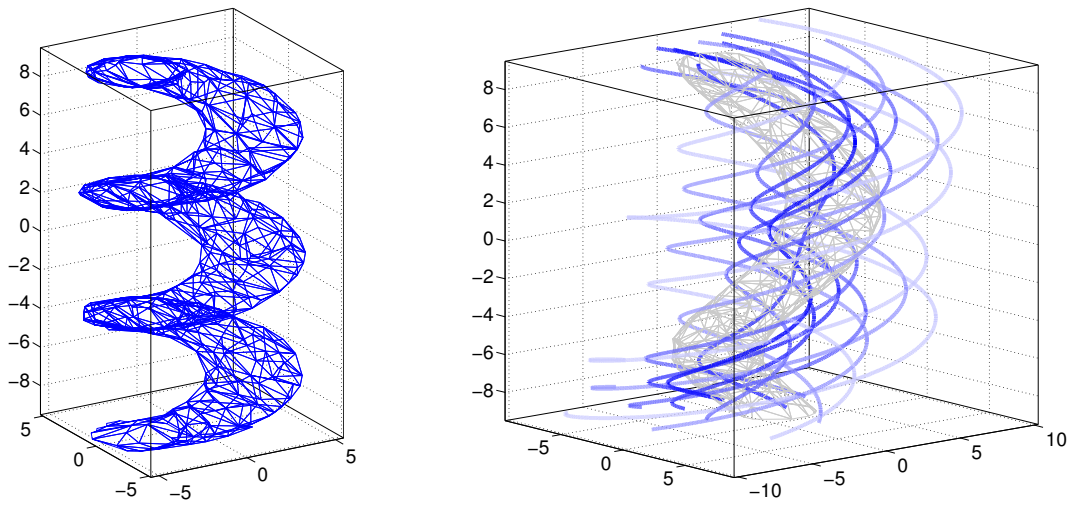

Figure 4.11: Helical Core Example. Models with a LinearTwistA applied post-shift. The image on the left is a surface density plot of a rather extreme twist; the image on the right has somewhat less extreme LinearTwistA transformations applied both before and after the shift. Note the change to cross-section.

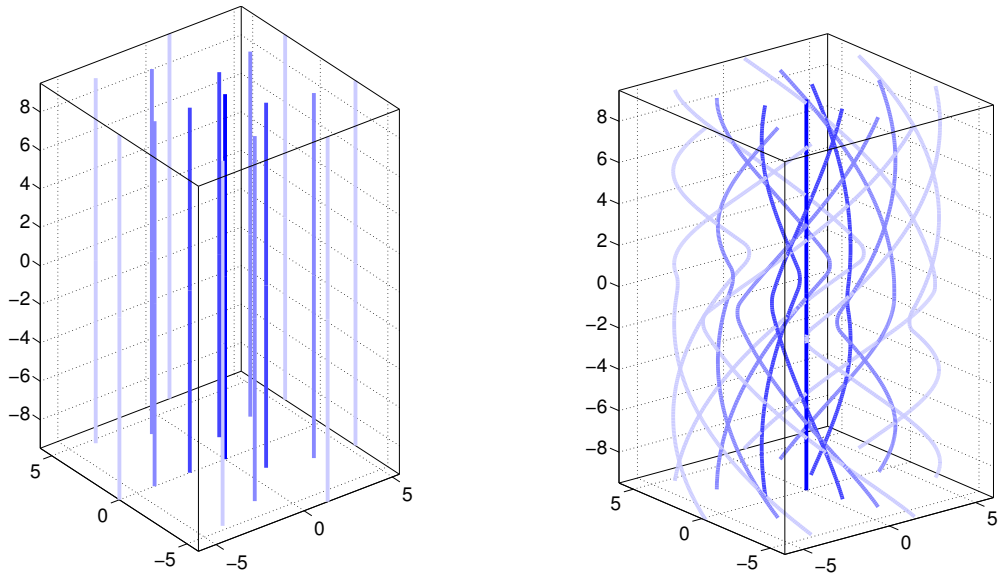

Figure 4.12: LinearTwistS Transformation. The effect of a symmetric linear twist on uniform magnetic field lines. The field on the left is transformed into the field on the right via this transformation.

4.3.8 PowerTwistA

This transformation describes an asymmetric twist that increases as a power law of $|z|$, governed by

$$\phi' = \phi + c_{twist} z |z|^{m_{twist}-1} \tag{4.68}$$

$$r' = r \tag{4.69}$$

$$z' = z \tag{4.70}$$

where the scaling parameter c_{twist} functions in the same capacity as LinearTwistA and S, and m_{twist} controls the extent of the twist. Figure 4.13 shows two examples of the resulting field geometry. As in LinearTwistA, the twist is antisymmetric across the $x - y$ plane.

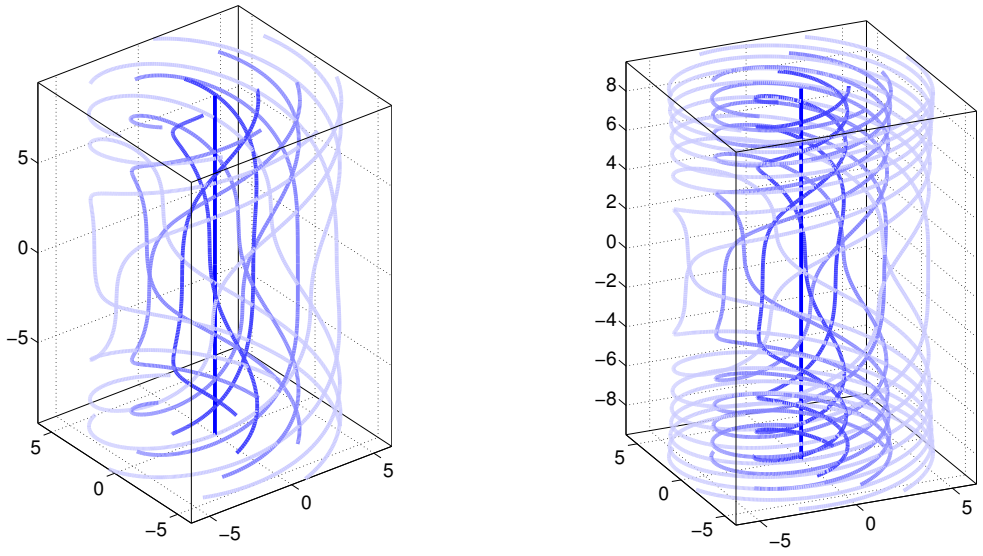

Figure 4.13: PowerTwistA Transformation. Two examples of fields produced by a the PowerTwistA transformation with different values of c_{twist} and m_{twist}.

4.3.9 PowerTwistS

PowerTwistS is a symmetric twist, similar to LinearTwistS, with a power law increase in twist with increasing z in the fashion of PowerTwistA. The coordinate transformation is given by

$$\phi' = \phi + c_{twist}|z|^{m}_{twist} \tag{4.71}$$

$$r' = r \tag{4.72}$$

$$z' = z. \tag{4.73}$$

The parameters c_{twist} and m_{twist} serve the same function as the two parameters in PowerTwistA. The resulting field geometry is shown in Figure 4.14.

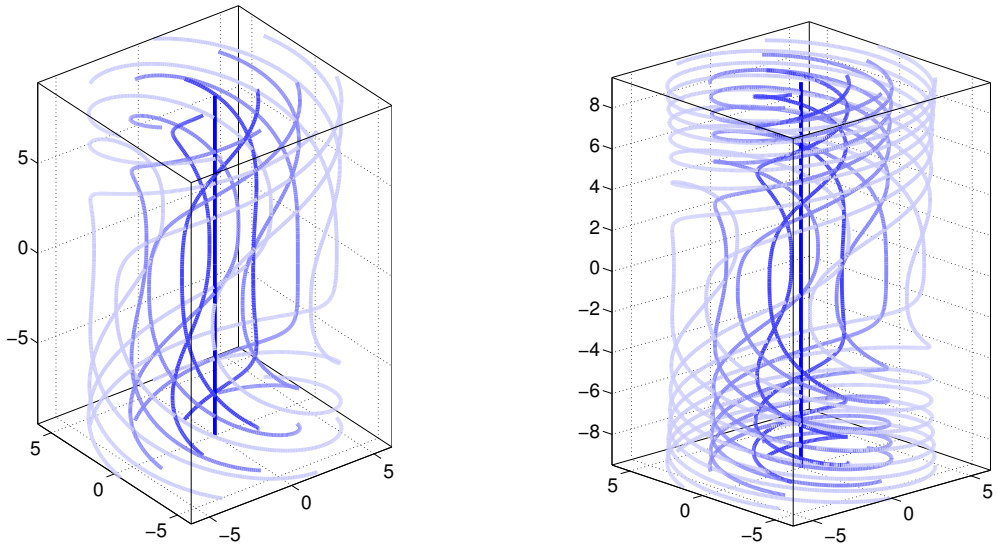

Figure 4.14: PowerTwistS Transformation. Two examples of the PowerTwistS transformation. The values of c_{twist} and m_{twist} are the same as the corresponding models from Figure 4.13

4.3.10 Bend

The Bend transformation bends lines of constant x such that the segments between $z = z_0$ and $z = z_0 + \alpha r_0$ are mapped to circular arcs of angular size α. We achieve this by first rotating the coordinate system such that the plane parallel to the z-axis containing the point (r_0, ϕ, z_0) lies along the x-axis (Figure 4.15a), performing the bend, and then rotating the system back to the original orientation.

We first perform a clockwise rotation about the z-axis of the less-primed system by angle ϕ to align the point (r_0, ϕ, z_0) with the x-axis, expressed by the rotation matrix

$$\begin{bmatrix} \cos(\phi) & \sin(\phi) & 0 \\ -\sin(\phi) & \cos(\phi) & 0 \\ 0 & 0 & 1 \end{bmatrix}. \tag{4.74}$$

The Jacobian for this incidental transformation is identical to (4.74), and so this trans-

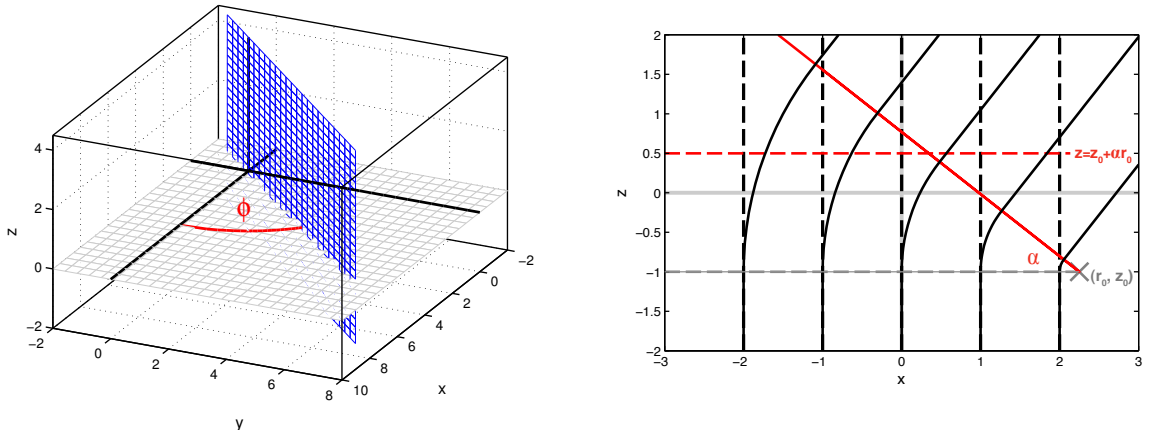

(a) Step 1: Initial Rotation

(b) Step 2: Bend

Figure 4.15: Bend Transformation Process. (a) Step 1: Rotate the system such that the plane parallel to the z-axis at angle ϕ to the x-axis (blue) lies along the x–z plane. (b) Step 2: Bend. Dotted lines correspond to solid (bent) lines before the transformation. Note that the transformation itself places the point of bend (r_0, z_0) outside of the grid.

formation is also applied to properly align the fields with the rotated coordinate system. As the transformation is planar, we can reduce the calculation in the rotated system to a two-dimensional problem, replicated down the rotated y-axis.

The coordinate transformation is piecewise, defined in three separate regions along the z-axis:

1. $z < z_0$, which is unaffected by the transformation (below horizontal dotted grey line in Figure 4.15b),

2. $z_0 \leq z \leq z_0 + \alpha r_0$, the "bend" region (between horizontal dotted grey and red lines in Figure 4.15b), and

3. $z > z_0 + \alpha r_0$, which is rotated by angle α and shifted such that there is no discontinuity at $z = z_0 + \alpha r_0$.

By convention, we define coordinates in this split space with a subscript 1–3 corresponding to the region in which they belong, i.e. coordinates in region 2 are designated (x_2, y_2, z_2) and so on. We perform the bend in region 2 by mapping each z_2 to an angle of arc of a circle

centred on (r_0, z_0) with radius of curvature $r = r_0 - x_2$ via

$$\theta = \frac{z_2 - z_0}{r_0}. \tag{4.75}$$

Angle α is therefore the angle of maximum bend, and length is conserved along the centre of the filament. The coordinates in region 3 continue as before, rotated by α. Note that this transformation is continuous; the sections are rejoined such that transforming any line parallel to the z-axis in the original space is a continuous curve in the transformed space.

We derive the transformation equations in regions 2 and 3 via inspecting the geometry of the system. In region 2, we approach the transformation as an offset, such that $x' = x + \Delta x$ and $z' = z_0 + \Delta z$. As each line of constant x in region 2 is mapped to the arc of a circle of angular size θ and radius r, we can see from Figure 4.15 that

$$\Delta x = r - r\cos(\theta), \text{ and} \tag{4.76}$$

$$\Delta z = r\sin(\theta). \tag{4.77}$$

The forward transformation in this region is therefore

$$x_2' = x_2 + (r_0 - x_2)\left[1 - \cos\left(\frac{z_2 - z_0}{r_0}\right)\right] \tag{4.78}$$

$$y_2' = y_2 \tag{4.79}$$

$$z_2' = z_0 + (r_0 - x_2)\sin\left(\frac{z - z_0}{r_0}\right). \tag{4.80}$$

Therefore, planes of constant z inside this region are mapped to a plane passing through point (r_0, z_0) at angle θ to the x-axis. This gives the Jacobian array

$$\begin{bmatrix} \cos(\frac{z_2-z_0}{r_0}) & 0 & \frac{r_0-x_2}{r_0}\sin(\frac{z_2-z_0}{r_0}) \\ 0 & 1 & 0 \\ -\sin(\frac{z-z_0}{r_0}) & 0 & \frac{r}{r_0}\cos(\frac{z-z_0}{r_0}) \end{bmatrix}. \tag{4.81}$$

The coordinate transformation inside region 3 takes the form of a rotation by angle α and a shift to align the coordinates properly with region 2. As the coordinates are continuous across the three regions, the coordinates in this region are transformed via

$$x_3' = x_3 + (r_0 - x_3)(1 - \cos\alpha) + [z_3 - (z_0 + r_0\alpha)]\sin\alpha \tag{4.82}$$

$$y_3' = y_3 \tag{4.83}$$

$$z_3' = z_0 + (r_0 - x_3)\sin\alpha + [z_3 - (z_0 + r_0\alpha)]\cos\alpha, \tag{4.84}$$

yielding a Jacobian matrix of

$$\begin{bmatrix} \cos(\alpha) & 0 & \sin(\alpha) \\ 0 & 1 & 0 \\ -\sin(\alpha) & 0 & \cos(\alpha) \end{bmatrix}. \tag{4.85}$$

After we have performed the transformations on each region, the regions are recombined and rotated back to the original orientation by applying the inverse of (4.74) to both the coordinates and fields. An example of the resulting model and polarization map is shown in Figure 4.16.

This results in the gas experiencing extension between $\infty < x < 0$ and compression in the region $0 < x < r_0$, creating a singularity at $x = r_0$. We note that along the $x = 0$ line, the gas experiences no compression (arc length is conserved). Therefore, the model parameters that define Bend are: ϕ, α, z_0, and Δr_0, where $r_0 = r_{\max} + \Delta r_0$. We define Δr_0 in this fashion to ensure that the centre of curvature, and thus the compression singularity, is located outside of the grid. Additionally, the range of angles α is permitted to take must be less than $\pi/2$ to ensure a reversible transformation.

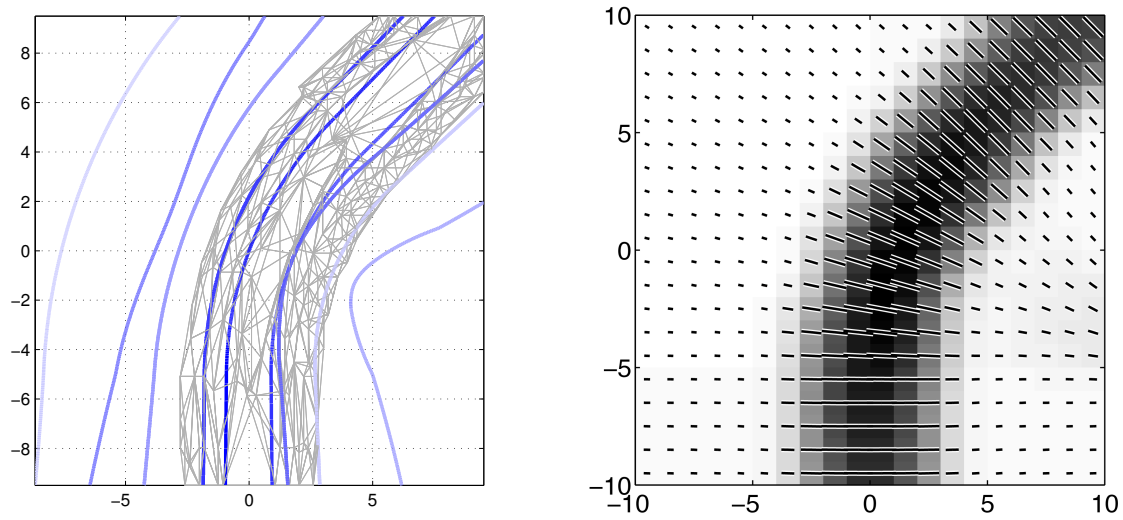

Figure 4.16: Bend Transformation Results. The three-dimensional structure (left) and corresponding polarization map (right) of a bent core with $\alpha = \pi/4$. Note that the density isosurface in the three-dimensional figure shows a discontinuity due to the compressive effect of the bend.

4.3.11 Sinebend

The "Sinebend" transformation maps the z-axis of the least-primed system to a sine wave. This transformation operates in a similar fashion to the Bend transformation of Section 4.3.10, rotating planes of constant z by an amount determined by the curvature of the "spine." However, this transformation is not defined to conserve length along the spine, as the computation for arc length along sine waves is complicated to compute. As this transformation is also planar, we take an approach similar to Bend, first performing a rotation of angle ϕ using equation (4.74) to align the plane of the transformation with the x-axis before we perform the bend, and rotate it back into place after.

In the x–z plane of the rotated system, we transform the line $x = 0$ to take the form of a sine wave. The equation governing the transformation we define to be

$$x'(0, z) = A \sin[B(z + z_0)] \tag{4.86}$$

$$z'(0, z) = z \tag{4.87}$$

where A and B are scaling parameters, and z_0 is a coordinate offset. As this is a bend and not a shear transformation, we use x'(0,z) to bend the core such that lines of constant z are kept perpendicular to $x'(0,z)$ in the new system. For each line of constant z we perform a rotation about the y-axis through a point on $x'(0,z)$ by z-dependent angle θ. The angle θ is derived from the observation that a tangent line to the $x'(0,z)$ curve at any z is at angle θ to the z'-axis. Therefore

$$\tan\theta = \frac{dx'(0,z)}{dz'} = AB\cos(B(z+z_0). \tag{4.88}$$

The coordinate transformations therefore take the form

$$x' = A\sin(B(z+z_0) + x\cos(\theta) \tag{4.89}$$

$$z' = z + x\sin(\theta). \tag{4.90}$$

However, this transformation is not analytically reversible. In order to calculate the reverse coordinate transformation we must perform the forward transformation onto a reference grid. We can then use the original reference grid and the transformed reference grid to perform a scattered interpolation. We currently use MATLAB's `triScatteredInterp` function to interpolate the proper less-primed coordinates. Unfortunately, this transformation has very high memory requirements, and so is only feasible for runs with much smaller genetic algorithm population sizes than we typically use for a production run of the code. However, Mathworks is phasing out `triScatteredInterp` in favour of `scatteredInterpolant`, which may compute more efficiently.

4.4 Model Summary

For the purposes of this work, we have applied at minimum two basic model templates, noTwistPoly and basic5Component, to each of the example datasets. However, we also cre-

ated core-specific templates using these as a base if we suspected some particular parameters needed to be adjusted from the template defaults. For each model we have restricted our analysis to the case where the magnetic field is aligned with the z-axis of the core.

The initial density ρ_0 and velocity dispersion σ_0 are not able to be excluded from the fit at this time. The initial density scale is fit logarithmically as a power of ten and has limits set from 10^{-22}–10^{-12} g cm^{-3}. Initial limits on σ_0 were set to 0.4–1.2 km s^{-1}.

We have found that including the grain alignment parameters γ and β and the offset C_{shift} in the fit create too much degeneracy in the models. As the grain alignment parameters have the greatest effect on polarization fraction and intensity, and we are performing fits in the two-objective Intensity/Polarization Angle mode, it will have a minimal effect on the fit and can be disabled. In particular, C_{shift} tended to lock onto an offset values far smaller than the smallest intensity values in the image, not contributing significantly to our model results.

The following subsections summarize the main attributes of each primary template used in our analysis. Tables 4.1, 4.2, 4.3, and 4.4 present this information in tabulated form.

4.4.1 noTwistPoly

This is a four-component model, containing the transformations POLY, Scale, RotateA, and Shift. It is the most basic reasonable model, as it contains a density setup (POLY), allows for spherical or triaxial cores (Scale), orients the core with respect to the line of sight (RotateA), and allows the core to be offset from the centre of the polarization map (Shift). Parameter limits are set to the PolCat defaults.

4.4.2 basic5Component

The basic5Component model is considered the default, and contains the components (in order) LinearTwistA, POLY, Scale, RotateA, and Shift. All parameters are set to PolCat defaults with the exception of LinearTwistA's twist constant c_{twist}, which is fit as a power of 10 (i.e. $c_{twist} = 10^X$ where X is the corresponding Ferret Parameter) with parameter limits

Transformation	Parameter	Linear Fit	Min	Max
POLY	K	no	10^{-2}	$10^{1.5}$
	γ_{poly}	yes	0.1	5
	ρ_c	yes	1	10
	ρ_{out}	yes	0.001	1
	P_{out}	yes	0.01	0.75
Scale	a_{scale}	yes	0.1	2
	b_{scale}	yes	0.1	2
RotateA	ϕ	yes	0	2π
	i	yes	$-\pi$	π
	PA	yes	0	2π
Shift	Δx	yes	grid minimum (x)	grid maximum (x)
	Δz	yes	grid minimum (z)	grid maximum (z)

Table 4.1: Parameter Setup for the noTwistPoly Template. Limits of logarithmic parameters are presented as 10^X, where X is the parameter value.

10^{-2}–10^2. This is the model currently set as the default in PolCat's code. This template produces a model with a helical magnetic field.

4.4.3 basic5wLinTwistS

The basic5wLinTwistS template substitutes the LinearTwistA transformation with a LinearTwistS transformation in basic5Component with no alteration to parameter limits.

4.4.4 basic5Component_MOD1

This model contains the same transformation components as basic5Component, but changes how some of the parameters are handled by Ferret. This particular model was developed through experimentation on OMC 1. As a result, the model template itself was designated "omc1_2a." However, we will refer to it as basic5Component_MOD1 to prevent confusion.

This model differs from basic5Component in that 1) LinearTwistA parameter c_{twist} is fit linearly from [0,100], 2) POLY parameter ρ_c has limits loosened from [1,10] to [1,320], and 3) POLY parameters ρ_{out} and P_{out} are fit logarithmically with limits [-5,0].

Transformation	Parameter	Linear Fit	Min	Max
LinearTwistA	c_{twist}	no	10^{-2}	10^{2}
POLY	K	no	10^{-2}	$10^{1.5}$
	γ_{poly}	yes	0.1	5
	ρ_c	yes	1	10
	ρ_{out}	yes	0.001	1
	P_{out}	yes	0.01	0.75
Scale	a_{scale}	yes	0.1	2
	b_{scale}	yes	0.1	2
RotateA	ϕ	yes	0	2π
	i	yes	$-\pi$	π
	PA	yes	0	2π
Shift	Δx	yes	grid minimum (x)	grid maximum (x)
	Δz	yes	grid minimum (z)	grid maximum (z)

Table 4.2: Parameter Setup for the basic5Component Template. Limits of logarithmic parameters are presented as 10^X, where X is the parameter value.

Transformation	Parameter	Linear Fit	Min	Max
LinearTwistS	c_{twist}	no	10^{-2}	10^{2}
POLY	K	no	10^{-2}	$10^{1.5}$
	γ_{poly}	yes	0.1	5
	ρ_c	yes	1	10
	ρ_{out}	yes	0.001	1
	P_{out}	yes	0.01	0.75
Scale	a_{scale}	yes	0.1	2
	b_{scale}	yes	0.1	2
RotateA	ϕ	yes	0	2π
	i	yes	$-\pi$	π
	PA	yes	0	2π
Shift	Δx	yes	grid minimum (x)	grid maximum (x)
	Δz	yes	grid minimum (z)	grid maximum (z)

Table 4.3: Parameter Setup for the basic5wLinTwistS Template. Limits of logarithmic parameters are presented as 10^X, where X is the parameter value.

Transformation	Parameter	Linear Fit	Min	Max
LinearTwistA	c_{twist}	yes	0	100
POLY	K	no	10^{-2}	$10^{1.5}$
	γ_{poly}	yes	0.1	5
	ρ_c	yes	1	320
	ρ_{out}	no	10^{-5}	10^{0}
	P_{out}	no	10^{-5}	10^{0}
Scale	a_{scale}	yes	0.1	2
	b_{scale}	yes	0.1	2
RotateA	ϕ	yes	0	2π
	i	yes	$-\pi$	π
	PA	yes	0	2π
Shift	Δx	yes	grid minimum (x)	grid maximum (x)
	Δz	yes	grid minimum (z)	grid maximum (z)

Table 4.4: Parameter Setup for the basic5Component_MOD1 Template. Limits of logarithmic parameters are presented as 10^X, where X is the parameter value.

Chapter 5

Data

The primary source of data for this work is the SCUPOL legacy catalogue, a collection of uniformly-processed 850 μm polarization data from the entire run of the now decommissioned Submillimetre Common-User Bolometer Array (SCUBA) at James Clerk Maxwell telescope (JCMT) (Matthews et al., 2009). Distance references to the object used for determining the physical pixel scales are drawn from Table 5 in Matthews et al. (2009). In the case of a dispute between the recorded distance in (Matthews et al., 2009) and other object studies, we chose the value recorded in Matthews et al. (2009).

SCUBA consisted of two arrays, a 91-pixel short-wavelength array optimized for 450 μm and a 37-pixel long-wavelength array optimized for 850 μm. These particular wavelengths are chosen based on limits of observing through Earth's atmosphere, which is only transparent to certain wavelength "windows" which extend from 350 μm to 850 μm. The array is also able to observe in the windows at 350 μm and 750 μm, with observations at either 450/850 μm and 350/750 μm, although only the former mode saw active use. This range of wavelengths made SCUBA suited to detect thermal emission from dust grains at temperatures of 3-30 K and synchrotron emission from extragalactic sources (Holland et al., 1999).

The SCUPOL polarimeter consisted of rotating half-waveplates and an analyzer, with measurements taken either at specific waveplate positions or in "continuous spinning" mode.

This process created a modulated sinusoidal signal which was used to determine the intensity of polarized emission and the position angle. The waveplates were optimized for 450 and 850 μm (Murray et al., 1997).

For targets smaller than the SCUBA field of view, such as most cores, the data was generally collected in "jiggle-mapping" mode (Holland et al., 1999; Matthews et al., 2009). The telescope was moved in a 16-point pattern (64-point pattern for dual-wavelength observations) in order to fully sample the source. To remove the effect of sky noise, "chopping and nodding" techniques were employed. Chopping refers a technique where the instrument is moved on- and off- source to sample the sky background, and nodding refers to switching source position in the chop-pattern, sampling both sides of the source. Subtracting these signals allowed effective removal of the sky signal. As this final result is a differential signal, it did not measure the absolute zero point. This difference manifested as an unknown DC offset (Fiege et al., 2004), which we have tried to account for in our code by using the parameter C_{shift} discussed in section 4.1.4.

Matthews et al. (2009) have reprocessed the entire run of 850 μm SCUPOL observations obtained in "jiggle-mapping" mode. Although SCUPOL was also able to obtain polarization for 450 μm, there were far less usable observations than the 850 μm data since 450 μm observations are more sensitive to weather effects. The reprocessing resulted in an effective beam width FWHM of 20$''$ (Matthews et al., 2009), and so we apply a Gaussian convolution of equivalent size to our model polarization maps to model the beam.

Since the SCUPOL Legacy catalogue compiles datasets for each core from multiple observations, Matthews et al. (2009) opted to combine maps in raw voltages instead of first converting to Jy beam^{-1} through each observation's flux conversion factor (FCF). Matthews et al. (2009) argued that combining results, often from multiple observing sessions, to produce flux-calibrated maps would introduce larger uncertainty into the results than using a fiducial value after the merge. Nevertheless, we apply an approximate (and admittedly imperfect) flux calibration to the data so that we can obtain physical densities and core masses

from our models. Averaging the historical SCUBA flux conversion factors compiled at (`http://www.jach.hawaii.edu/JCMT/continuum/calibration/sens/gains.html`, (Joint Astronomy Centre, 2005)), we obtain a fiducial FCF of 0.88 Jy arcsecond^{-2}. As the effective beam of the maps is $20''$, this results in a correction factor of FCF^*=200 Jy beam^{-1} Volt^{-1}.

We initially misinterpreted the units of the observational datasets, believing that they were in Jy beam^{-1} when they were actually in volts. This meant that the intensity values of the observational maps used by PolCat were too low in magnitude by a factor equal to the numerical value of FCF^*. Since the surface density to Jy beam^{-1} conversion factor C_{flux} is primarily set by cloud temperature, the discrepancy in the intensity values would be absorbed into the model density scale ρ_0. Since we treat our models as dimensionless until the final step, we can correct our model, without introducing any error, by absorbing the conversion factor into ρ_0 as $\rho_0^* = \rho_0 \times FCF^*/(\text{Jy beam}^{-1}\ \text{V}^{-1})$. We note that all quantities in PolCat are converted into dimensionless quantities internally, therefore this correction can be viewed as rescaling an already dimensionless model. Appendix B provides a brief derivation to demonstrate the validity of this correction.

Variance maps for each Stokes vector are included in the dataset, with the variance in P_{frac}, PA, and P_{flux} calculated via

$$\sigma^2_{P_{flux}} = \frac{Q^2\sigma_Q^2 + U^2\sigma_U^2}{(Q^2+U^2)} \tag{5.1}$$

$$\sigma^2_{P_{frac}} = \frac{Q^2\sigma_Q^2 + U^2\sigma_U^2}{(Q^2+U^2)I^2} \tag{5.2}$$

$$\sigma^2_{PA}(rad) = \frac{1}{4}\frac{U^2\sigma_Q^2 + Q^2\sigma_U^2}{(Q^2+U^2)^2}. \tag{5.3}$$

The expression for each variance term was determined via standard error propagation from equations (4.29)–(4.31). The σ_I term in equation (5.2) has been neglected due to being much smaller than the σ_Q and σ_U terms. We note that variance in position angle is usually taken to be $0.25 \times \sigma^2_{P_{flux}}/P^2_{flux}$, which assumes that $\sigma_Q \approx \sigma_U$. However, it is unnecessary to make

this approximation because variance maps for Q and U are available.

5.1 Data Pre-Processing

We have developed an arrangement of tools that are used to package catalogue data in FITS format into a form that PolCat can easily parse. FITS (Flexible Image Transport System) files consist of a primary header unit (HDU), other optional HDUs, and optional special records. The HDUs contain the data array and a "header", which lists relevant information about the observation. This typically includes image coordinates and pixel-to-sky conversion factors, in addition to processing notes and telescope conditions. A thorough description of the FITS file structure and keywords can be found in Pence et al. (2010), which is the definitive reference on the FITS format.

FITS files in the SCUPOL Legacy catalogue are packaged with each I, Q, and U map contained in a data cube in the primary HDU. The variance maps for each Stokes component are stored in their own data cube in a separate, secondary HDU in the same file. We have developed PolCat's framework with this packaged data structure in mind. However, due to our future involvement with CARMA, we have also added a packaging tool that groups separate I, Q, and U maps into a format our processing tool will recognize.

As some of the regions contain multiple objects and many have complex background morphology, the first step we perform is cropping external regions from the image. We developed a tool called `plotPolGUI` to crop the data and save it into a PolCat readable data structure in MATLAB's ".mat" format.

In Pol2007 there was a tool called `plotPol` that fulfilled the same purpose. It loaded a specified fits cube and generated an interactive contour plot of the Stokes I map. The user could left-click to select a particular contour, click the figure at several points to create an additional polygon, and then right-click to crop the figure. The area enclosed by both the selected contour and the polygon would be the area remaining after cropping.

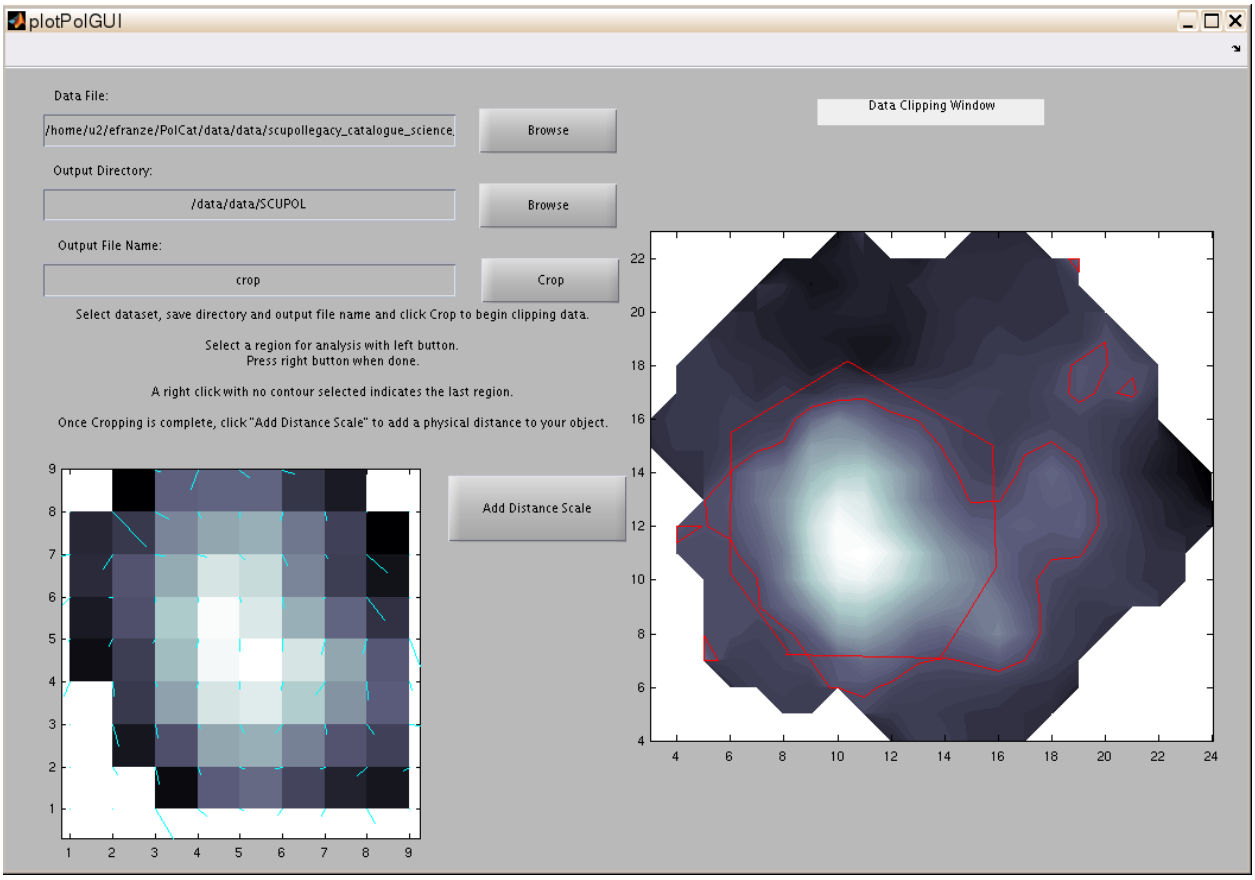

Figure 5.1: The `plotPolGUI` Interface. The large plot on the right is the cropping window. The original `plotPol` tool only consisted of the cropping window.

While functional, `plotPol` was inconvenient and inefficient to use, as once the cropping was complete the user would need to use a second function to view the result. If the result were deemed inadequate, the user would have to repeat the procedure until the cropping was satisfactory. We proceeded to develop `plotPolGUI` by fitting `plotPol` into a graphical interface (see Figure 5.1). The `plotPolGUI` interface allows the user to choose the source dataset and output directory via either entering the file manually in the text field or by browsing the file system using a graphical interface. A custom output name is then entered, and the cropping process initialized by clicking "crop."

The large plot on the right side of the interface in Figure 5.1 is the original figure generated by `plotPol`, with an identical cropping process. When cropping is complete, the cropped set is saved and the result is displayed in the smaller plot on the bottom right of the

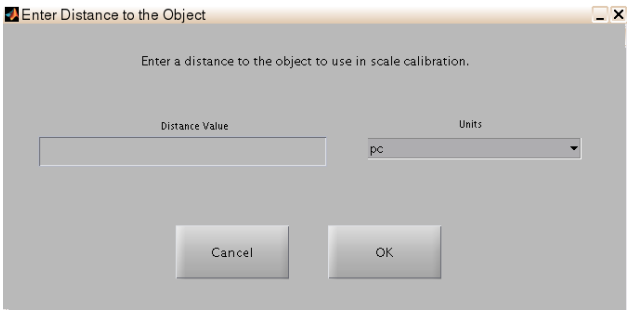

Figure 5.2: The `addDistanceScale` Dialog.

interface. If the cropping is unsatisfactory the user can click "crop" again without having to go through the process of reloading the dataset. This step of the code also searches through the header and preserves the "CDELT#" keywords, which define image scale, in addition to the "CRPIX#" and "CRVAL#" keywords, which define the position of the reference pixel in both image and sky coordinates. The image coordinates of the reference pixel are adjusted to reference the proper pixel in the cropped image. The latter keywords are preserved so as to properly translate the data and model images into right ascension and declination, although this has yet to be implemented in the code. The image scale keywords are required to properly scale the model into physical coordinates.

When clipping, we require the final result to contain the target core with a small amount of the background region for context. Care must be taken when clipping, as including too much of the background regions can include regions outside the main influence of the core where the field tends to be more disordered. There is also the additional consideration that too many points outside the region of interest can cause these external points to weight too heavily when optimizing the fitness function. Plotting residual maps in these cases show a clear pattern of the fractional intensity residuals being higher value in the core area. Conversely, clipping too severely can cause the program to have difficulty finding an edge if using an edged density model.

Once the cropping is satisfactory, the user can add the physical distance to object into the data structure by clicking the button labelled "add distance scale." This opens an additional

GUI that allows the user to enter a physical distance to the object in units selected from the drop down menu (see Figure 5.2). This step is required in order to translate image pixels into a physical size. This dialog is treated as a separate function, such that if the user forgets to perform this step or enters an incorrect value, they can run `addDistanceScale` on their cropped data outside `plotPolGUI` without having to re-crop the dataset.

For datasets stored as separate fits files, we have also created a tool that packages all of these separate files into a PolCat- and `plotPolGUI`-readable .mat file with all the necessary keywords preserved from the headers. In this package is also the option to use a user-defined value, such as the RMS variance, to generate flat variance maps for cases where no variance maps exist. In future, we expect to handle data from the TADPOL survey (Hull et al., 2014), which packages data in this fashion.

The output of `plotPolGUI` is a MATLAB structure called "pol", which contains the fields "header", containing the header information and distance scale; "fields", containing the Stokes vectors and computed PA, PFlux, and PPercent; and "variance", containing the variance maps.

Changes to MATLAB's fits framework between MATLAB versions have caused a problem when using MATLAB function `fitsread` to load rectangular (as opposed to square) fits images. The array returned is improperly indexed due to the row and column dimensions being switched. To prevent this, we implement a workaround that uses `fitsinfo`, which returns a structure containing the header and other information about the cube. We then swap the row and column sizes in the array containing the dimensions for the Primary and Image HDUs and feed the modified info structure back into `fitsread` when loading the data file. The most recent version of MATLAB has corrected this problem, but the workaround has no effect on the results when used with the newest version.

5.2 Selected Cores

The SCUPOL legacy catalogue contains a large sample of objects, including some that are irrelevant to PolCat's focus, such as galaxies, supernova remnants, and planetary nebulae. However, even discounting those targets, a total of 56 relevant observations remain. Due to the current limitations of the model, we have chosen the sample of cores preferentially to be spatially well-defined and isolated, as well as large enough that masking out background structure produced a dataset more than 4-5 pixels on each side. This tended to select single-core datasets, since regions with multiple cores usually contain some faint background structure which would be difficult to exclude without cropping too severely around the core. For the purposes of this work, we have chosen three cores for analysis: DR21-Main, OMC1 (KL), and R Coronae Australis.

5.2.1 DR21-Main

The DR21 complex is a star-forming region in Cygnus located approximately 3 kpc from the Sun (Matthews et al., 2009; Kirby, 2009). The parts of this complex of particular interest are the Main region in the south, and the brighter OH region to the north. The SCUPOL Legacy dataset for DR21 contains the northern DR21 (OH) region in addition to the DR21-Main region. However, we have opted not to cover this region in this study due to the fact that it is more complex than DR21-Main, and would require more in-depth modelling than the relatively simple analysis that we are providing here. Although the neighbouring region DR21(OH) is more widely studied, the southernmost component, DR21-Main, is an ideal candidate for this analysis due to its regular shape and ordered magnetic field. Figure 5.3 shows the southern half of the SCUPOL Legacy Catalogue dataset for the DR21, showing DR21-M alone.

Kirby (2009) has previously modelled the flux and magnetic field and found the field direction to be in good agreement with an hourglass field. Mass estimates within 1 pc from

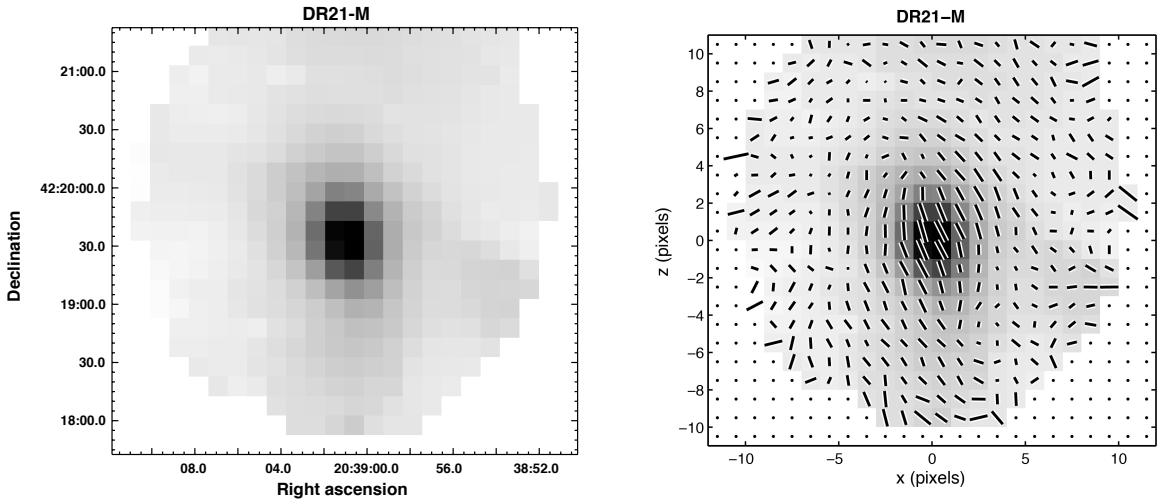

Figure 5.3: DR21-M SCUPOL Legacy Data. SCUPOL Legacy Catalogue intensity map with (α, δ) coordinates (left) and map with vectors (right). The map shows the southern half of the dataset; it has been cropped to show the DR21-M core alone. Polarization vectors are E-field, scaled by $\sqrt{P_{flux}}$.

Richardson et al. (1989) and Kirby (2009) are 20 000 and 25 000 $M_\odot$ respectively.

5.2.2 OMC1

The Orion Nebula complex is a large, heavily studied region of intense star formation. At a distance of ∼414 pc this also makes it the one of the nearest star formation regions to us (Coppin et al., 2000). The OMC1 region, located in the integral-shaped filament, is immediately behind the main nebula complex (Menten et al., 2007; Bally et al., 2011), and is the site of some of the youngest stars in the nebula (Menten et al., 2007). The OMC1 region itself contains two bright cores, the brightest of which is generally referred to as the Becklin-Neugebauer/Kleinman-Low (BN/KL) region. A simple analysis by Coppin et al. (2000) suggests that the field is mostly linear, consistent with a flattened ridge created by rapid collapse along field lines. Figure 5.4 shows the SCUPOL Legacy Catalogue data for this region.

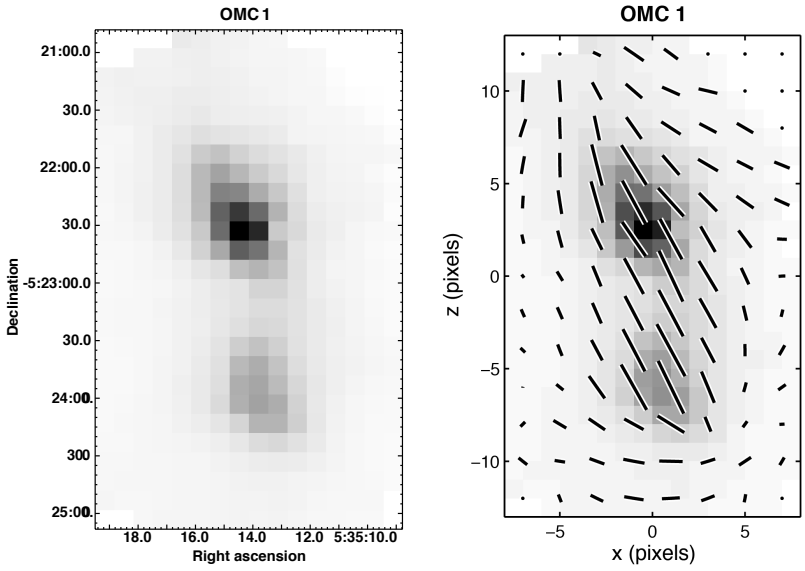

Figure 5.4: OMC1 SCUPOL Legacy Data. SCUPOL Legacy Catalogue intensity map with (α, δ) coordinates (left.) and map with vectors (right). The map has been cropped to eliminate empty space. Polarization vectors are E-field, scaled by $\sqrt{P_{flux}}$ and binned by 2.

5.2.3 RCrA

The R Coronae Australis dark cloud is located at a distance of 130 pc (Curran and Chrysostomou, 2007) or 170 pc (Nutter et al., 2005) from the Sun. The SCUPOL legacy catalogue contains data for the brightest object in this region, located between Herbig Ae/Be stars RCr A and TCr A. Nutter et al. (2005) labelled this region SMM 1, and determined it to be composed of three individual sources using Gaussian fitting. Curran and Chrysostomou (2007) noted that the field morphology may indicate the presence of ambipolar diffusion, and cite a temperature of 20 K. In the SCUBA polarization maps, the polarization pattern follows an intriguing S-shape, which motivated its selection for this study. The SCUPOL Legacy Catalogue dataset for this region is shown in Figure 5.5. Future discussion of the R Coronae Australis dark cloud will use the abbreviation RCrA.

We note that there is some disagreement to the actual distance to the cloud by approximately 50 pc. Knude and Høg (1998) reestimated distances to the RCrA dark cloud and three other star forming regions using Hipparcos and Tycho catalogue data and found a distance of 170 pc. However, we default to the 130 pc distance cited in Clark et al. (2000);

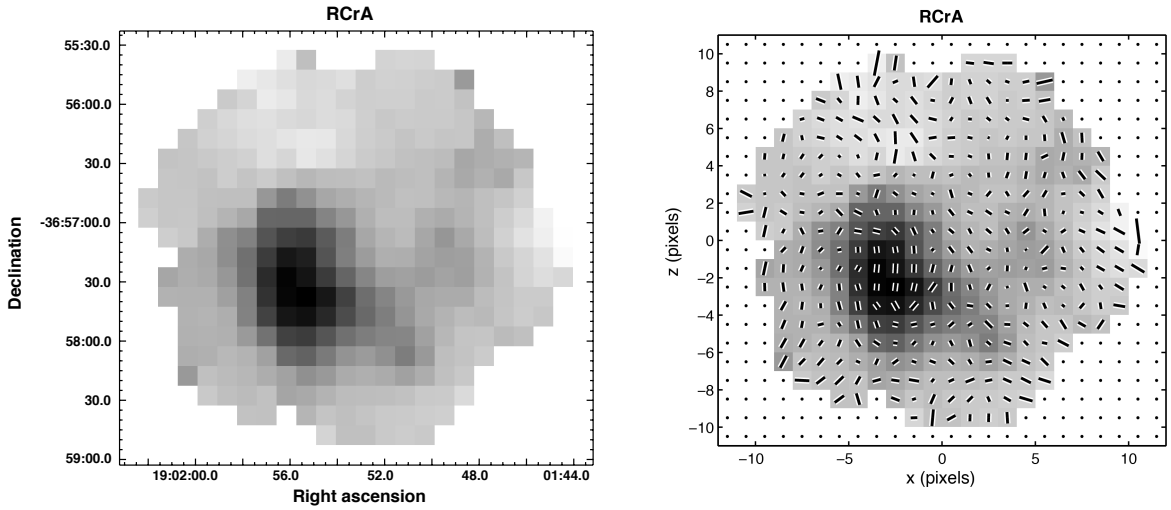

Figure 5.5: RCrA SCUPOL Legacy Data. SCUPOL Legacy Catalogue intensity map with (α, δ) coordinates (right) and map with vectors (right). Polarization vectors are E-field, scaled by $\sqrt{P_{flux}}$.

Curran and Chrysostomou (2007); Matthews et al. (2009).

Chapter 6

Analysis and Discussion

In polarization mode, we generally use F_I (F1) and F_{PA} (F2) as the fitness objectives, with the option of using either $F_{P_{frac}}$ or $F_{P_{flux}}$ as a third objective. A significant lesson learned from conducting multiple runs with and without the third objective function is that using the third objective tends to degrade the quality of the solutions slightly. We find that a model that yields a good fitness value for either or both of $F_{P_{frac}}$ and $F_{P_{flux}}$ is usually not a good fit in intensity and position angle. In addition, fitting for polarization fraction has a tendency to give precedence to areas of the map with fainter overall intensity, neglecting fitness at the core centre.

In a similar fashion, fitting in Stokes mode is less reliable than polarization mode. Fits to Q and U produce good results in fitness value, but the resulting field vectors tend to be in poor agreement with the data due to the position angle being very sensitive to the ratio of U to Q. The position angle of the polarization vectors naturally arises from the field direction, whereas Q and U are more abstract polarization quantities. As such, we do not include discussion of Stokes mode results.

Due to these uncertain factors, we favour results obtained from two-objective Intensity-χ_{pol} fits performed in polarization mode. In an attempt to generate a fully populated fitness curve, we take multiple runs of each model, half with X-niching and half with F-niching as

described in §3.4.

We have performed fits to all data with the default basic 5-component model template described in Section 4.4.2, as well as the 4-component noTwistPoly template described in Section §4.4.1. We have also determined other models to apply to each object on a case-by-case basis depending on intensity map and overall E-vector shape. We have limited our analysis to models with the magnetic field aligned to the z-axis of the core.

We note the polarization position angle abbreviation "PA" has a similar name to the RotateA transformation parameter PA. *To make a distinction between the two in the forthcoming analysis and discussion, we will use the abbreviation PA for the RotateA parameter exclusively. Polarization position angle will either be stated in full or as χ_{pol}, with fitness "F2." Correspondingly, we will typically refer to intensity fitness as "F1" for brevity.* All polarization vectors in figures are E-field vectors scaled by $\sqrt{P_{flux}}$.

6.1 Tests with Artificial Data

As a general test of PolCat's effectiveness, we generated polarization maps of several simple models to use as "test data" and attempted to reproduce the input parameters with PolCat. For simplicity, we have set the "physical distance" to the test core to 414 pc, that of OMC1.

To make our test datasets simulate the SCUPOL legacy data as closely as possible, we generated variance maps for each simulated I, Q, and U map. As a variance model, we took

$$\sigma_I^2 = c_I I \tag{6.1}$$

$$\sigma_Q^2 = c_Q P_{flux} \tag{6.2}$$

$$\sigma_U^2 = c_U P_{flux}, \tag{6.3}$$

with each c_X computed by averaging the median values of σ_X^2/X (where $X = I, Q$ or U respectively) from each dataset studied in this thesis.

Once we computed the variance maps, we added Gaussian noise to the I, Q, and U maps via

$$X' = X + \sigma_X \times \texttt{randn}(\texttt{size}(X)) \tag{6.4}$$

where $\texttt{randn}(\texttt{size}(X))$ is a random array generated from a Gaussian distribution in the same dimensions as X.

We note that the c_X values used to generate our test data were computed prior to the discovery of the data unit misinterpretation (§5). However, the signal-to-noise of the test data maps are on-par with the data. The main side-effect of the misinterpretation is that the simulated data is a factor of $FCF^*/(1\ \mathrm{Jy\ beam^{-1}\ V^{-1}})$ smaller than the typical scales of our selected data maps, as we used a typical PolCat density scale for the OMC1 region as the ρ_0 seed parameter. However, as our main motivation for fitting to generated test data is to explore PolCat's ability to reproduce the core parameters and geometry when the "true" structure is known, post-process scaling is unnecessary for this portion of the analysis.

We make a distinction between the original, noiseless model used to generate the test data and the test data itself. In the forthcoming analysis, we will refer to the model generated from the base parameters (with noiseless polarization maps) as the *seed model*, and the seed model polarization maps with added noise as the *test data*. The seed model parameters used to generate the test datasets are summarized in Table 6.1. *We note that when we present our tabulated results in the following sections, we provide computed F1, F2, χ^2_I and χ^2_{PA} values for the seed model in brackets for comparison, which are computed between the original seed model maps and the test data.*

6.1.1 Test Core 1: Bonnor-Ebert Sphere

The first test core (Core 1) was a simple Bonnor-Ebert sphere threaded by a weak hour-glass field, such that the resulting model is spherical. We generated the dataset with the "noTwistPoly" template. Our input parameters for the 4-component Bonnor-Ebert sphere

	Core 1 noTwist	Core 2 noTwist	Core 3 basic5	Core 4 basic5 (TwistS)
ρ_0 (g cm^{-3})	1×10^{-20}	1×10^{-20}	1×10^{-20}	1×10^{-20}
σ_0 (km s^{-1})	0.8	0.8	0.8	0.8
c_{twist}	–	–	10	10
K	0.1	0.1	0.1	0.1
γ_{poly}	1	1	1	1
ρ_c	5	5	5	5
ρ_{out}	0.1	0.1	0.1	0.1
P_{out}	0.35	0.35	0.35	0.35
a_{scale}	1	1	1	0.8
b_{scale}	1	1.2	1.2	1
ϕ	0°	45°	45°	45°
i	0°	30°	30°	30°
PA	0°	20°	20°	20°
Δx	0	0	0	0
Δz	0	0	0	0
C_{flux}[†]	1	1	1	1

Table 6.1: Test Core Seed Model Parameters
[†]Jy beam^{-1} g^{-1} cm^2

test dataset are summarized in Table 6.1. This generated a truncated core with central density $\rho_c = 5 \times 10^{-20}$ g cm^{-3}, with the initial magnetic field direction perpendicular to the line of sight. Figure 6.1 shows the resulting polarization map, Figure 6.2 shows the "residuals" between the test data and the generating seed model, and Figure 6.3 shows the seed model's three-dimensional structure.

This highly symmetric model serves as a barometer of PolCat's ability to replicate core orientation from the polarization position angle, as the circular profile in the intensity map is perfectly symmetrical and provides no clues as to spatial orientation.

6.1.1.1 Scenario 1A: Basic Fit (noTwistPoly)

In this test, we fit the test dataset to the noTwistPoly model with all transformation parameters free to vary, and with C_{flux} fitting enabled. This configuration is how we would apply this model to an actual observational dataset. The resulting tradeoff surface (Figure 6.4)

Test Core 1 Seed Model Summary

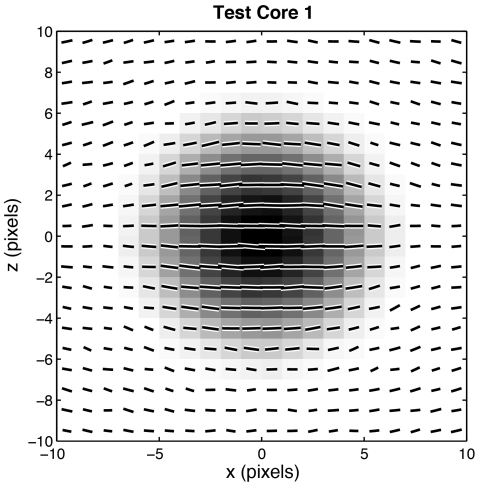

Figure 6.1: Test Core 1 Polarization Map. Includes noise. Vectors are scaled by $\sqrt{P_{flux}}$.

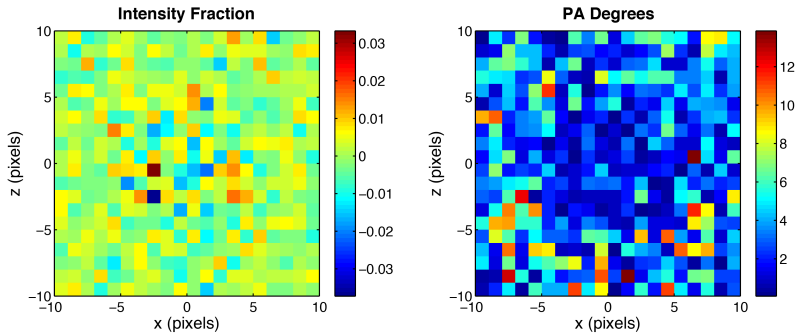

Figure 6.2: Test Core 1 Seed Model Residuals. Residuals between the seed model and the test data map (Figure 6.1). Intensity residuals are expressed as a fraction of $\bar{I}_{data} = 7.6\times10^{-3}$ Jy beam^{-1}.

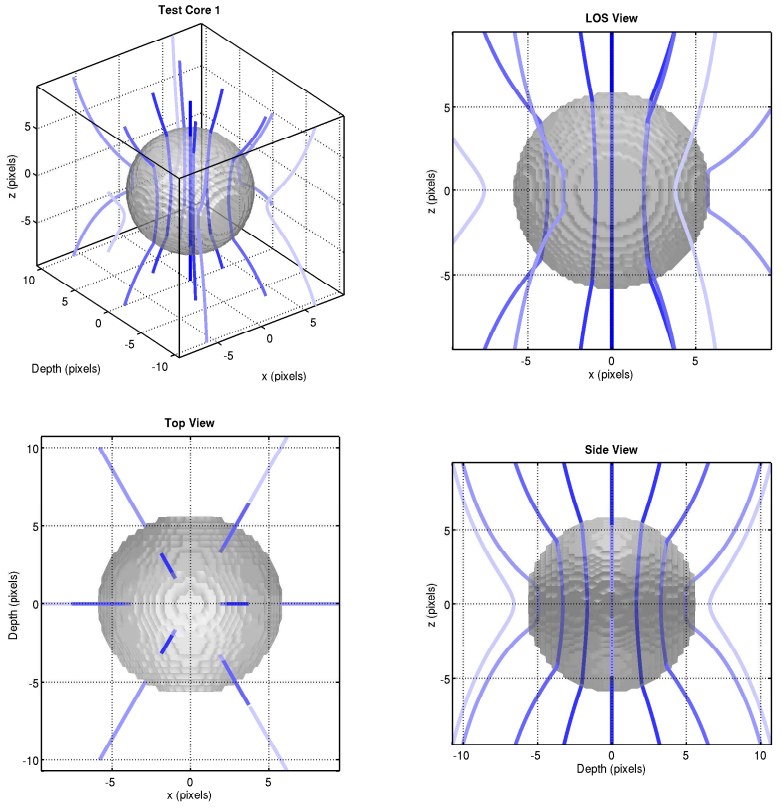

Figure 6.3: Three-Dimensional Structure of the Test Core 1 Seed Model.

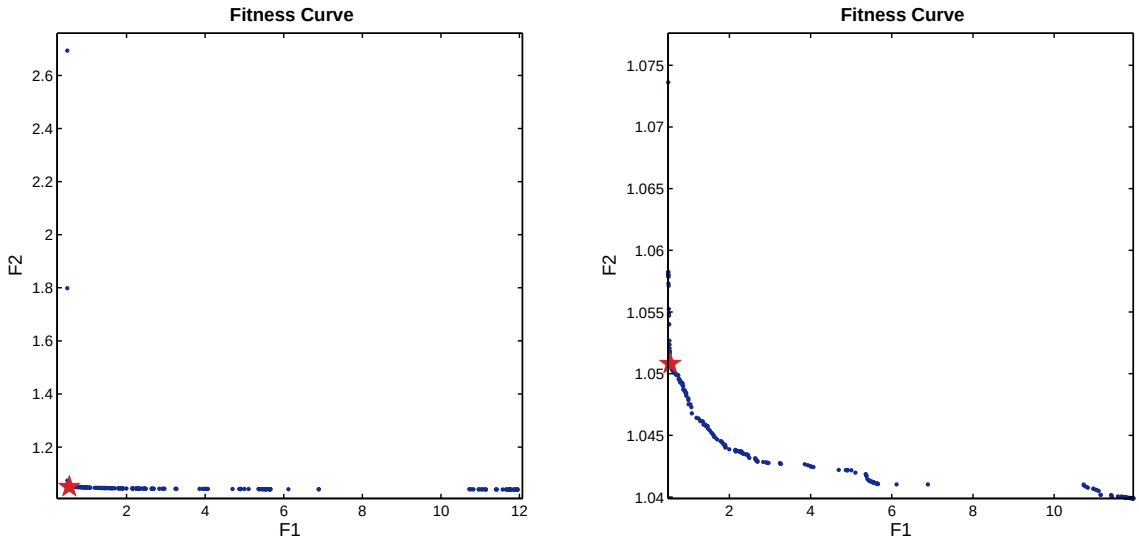

Figure 6.4: Test Core 1 Scenario A Trade-off Surface. Full merged fitness curve from all eight runs (left, right zoomed) with Solution 120 indicated by the red star.

falls almost straight downward before sharply changing direction 90° almost instantaneously at the knee and proceeding straight. In fact, the F2 (polarization position angle fitness) value falls so swiftly that there are two large gaps in the fitness curve along the y-axis before the change of direction. Zooming on the area of the curve after the second large gap (Figure 6.4, right) shows much wider curvature at the knee region, with what would appear to be the "knee" of the curve zoomed out fully appears to be only the top of the knee region. However, as the F1 value changes much more quickly than the F2 value at this resolution, choosing the analysis solution from the centre of the zoomed region sacrifices too much of the intensity fitness for a negligible improvement in position angle, and so we choose Solution 120 at the point of initial change of curvature as representative of a "balanced" solution, and summarize its parameters in Table 6.2 with the seed model parameters and the results of Scenarios 1B (§6.1.1.2) and 1C (§6.1.1.3).

Solution 120's polarization map with data vectors plotted for comparison is displayed in Figure 6.5. The vectors of Solution 120 show very good agreement with the original polarization map. The residuals for intensity (Figure 6.6, left) show little overall structure, although the largest magnitude residuals appear to be confined mostly to the central region,

and the outer environs confined mostly between $\pm 0.01\ \bar{I}_{data}$. However, the spatial distribution is consistent with the residuals displayed between the generated "data" and the seed model (Figure 6.2). There is no observable difference between the position angle residuals (Figure 6.6, right) for Solution 120 and those of the seed model.

From Table 6.2, we can see that PolCat was able to discern the core's proper spherical shape and position on the x–z plane. As such, the rotation angle ϕ has little or no bearing on the results and is largely unconstrained between runs. Rotation position angle PA is highly degenerate, as PolCat produced values at approximately 0°, 180°, and 360° for these angles for every solution in the set. As these are equivalent states for this parameter, in this case PolCat was successful in reproducing the input value. However, it was much less successful at reproducing inclination angle i, with the knee solution having a value of approximately -13° (field at 77° to the line of sight), as can be seen from the three-dimensional plot of Solution 120 (Figure 6.7). Additionally, the solution with the nearest-to-true inclination angle of approximately 5° actually had a slightly worse F2 value.

The density scale ρ_0 and the velocity dispersion σ_0 are poorly constrained. Although the ρ_0 and σ_0 values at the knee are reasonably close to the seed values, the parameters themselves are somewhat poorly constrained. Density scale ρ_c settled into the range 0.8–1.7×10^{-20} g cm^{-3}, σ_0 into the range 0.55–0.8 km s^{-1}. However, for σ_0 the majority of the merged set tended to select values lower than the seed value of 0.8, with the only solution in the merged set that reproduced σ_0 accurately having a F1 value of $\sim$4. There appears to be little or no correlation between the two scaling quantities from their distribution in the parameter space. The other scaling constant, C_{flux}, is also not well-constrained, taking values between 0.6 and 1.4; equally split to either side of the seed value of 1.

Although Solution 120 hit the K, ρ_c, and ρ_{out} values reasonably well, it failed to reproduce γ and P_{out} choosing a γ of approximately 1.22 and a P_{out} of approximately 0.25. However, if we plot Solution 120's density profile against that of the seed model (Figure 6.8, left), we see that, although the ρ_0 value causes the central peak to be too high, the core truncates at

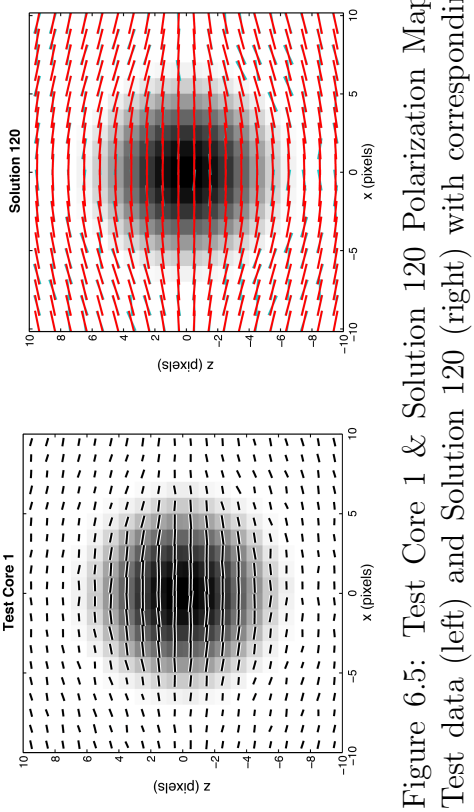

Figure 6.5: Test Core 1 & Solution 120 Polarization Maps. Test data (left) and Solution 120 (right) with corresponding polarization vectors (red) overlain on the test data vectors (blue).

Figure 6.6: Solution 120 Residuals. Intensity (left) and χ_{pol} (right). Intensity residuals are presented as a fraction of $\bar{I}_{data} = 7.6 \times 10^{-3}$ Jy beam^{-1}.

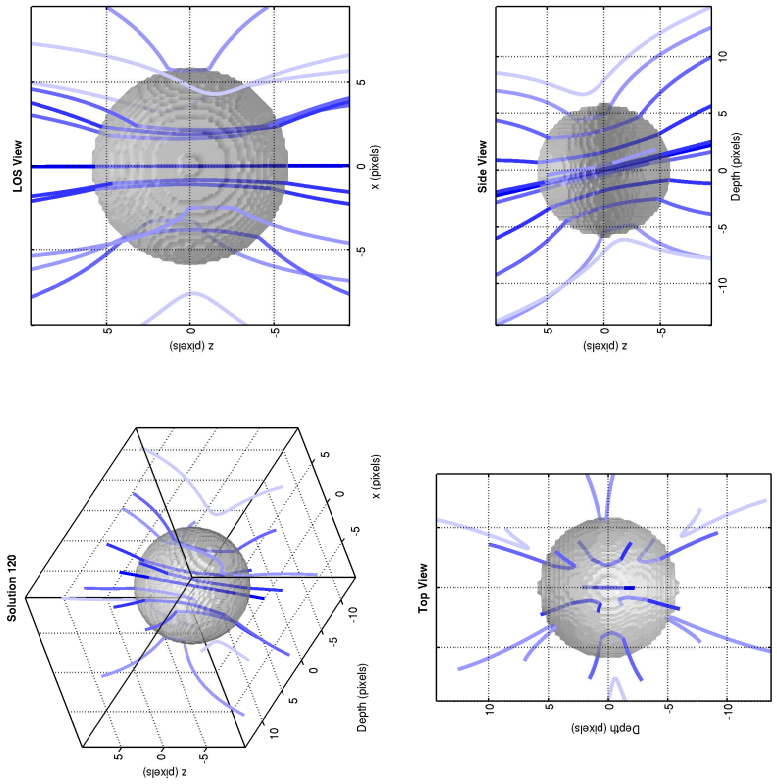

Figure 6.7: Three-Dimensional Structure of Solution 120.

Scenario 1A - noTwistPoly Solution 120

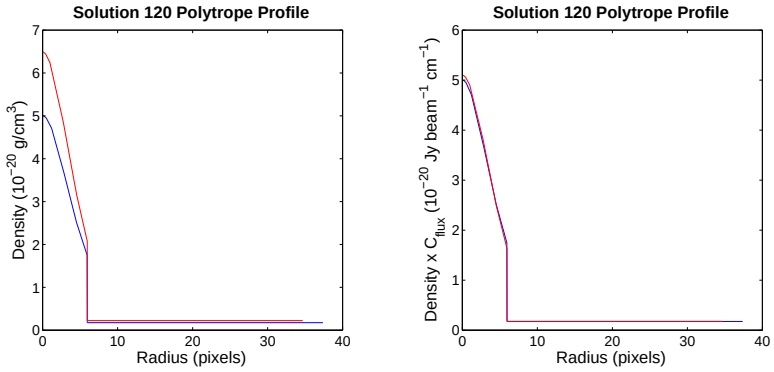

Figure 6.8: Solution 120 Polytrope Density Profiles. Scaled density profiles from Solution 120 (red) and the seed model (blue) POLY transformations.

exactly the same pixel radius.

We note that the simulated intensity (and Q and U) maps are calculated by integrating functions proportional to the density distribution ρ along the line of sight, and then scaling the resultant map by C_{flux}. Therefore, the magnitude scale of the peak intensity is determined by $\rho_{\max} \times C_{flux}$. If we scale the polytrope density profiles by C_{flux} (Figure 6.8, right), the profiles line up, and are nearly indistinguishable despite having different γ. *Observationally, these cores would be identical due to their C_{flux} values despite their differing densities.*

For the set as a whole, the parameters K and ρ_c are poorly constrained, with K between 0.05 and 0.55 and ρ_c taking a range of values between 3–7.

6.1.1.2 Scenario 1B: Frozen γ

For this test we ran the same model as Scenario 1A, but froze γ to the isothermal case $\gamma = 1$ to test whether the fit to the other parameters would be improved. Henceforth we shall refer to the template of this model as "noTwistBE" (noTwist Bonnor-Ebert).

As with Scenario 1A, the knee of the fitness curve (Figure 6.9) is a very sharp bend where the curve is nearly vertical before sharply changing direction almost 90° at the knee and proceeding horizontal. Zooming in on the lower part of the curve shows that the "knee solution" (Solution 152) is actually at the top of a shallow bend, after which the curve is

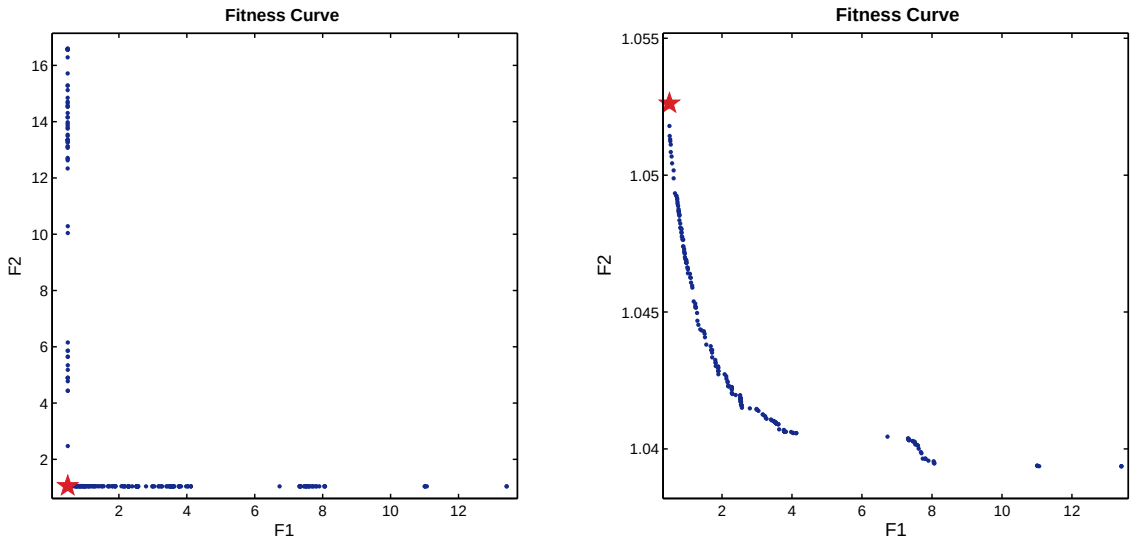

Figure 6.9: Test Core 1 Scenario B Trade-off Surface. Trade-off surface for the merged solution set (left, right zoomed). The red star indicates Solution 152.

truly flat. However, this part of the curve is very shallow, as in example in Scenario 1A, and the F2 value only improves by less than 0.01 while F1 degrades to a value of 1 from 0.5. This trades a barely legible difference in polarization angle for a large degradation in intensity. We therefore continue with our selection of Solution 152, which is at the point of the change of curvature.

Figure 6.10 shows the Core 1 map (left) next to the Solution 152 map (right). Vectors in the Solution 152 map are unscaled and plotted in red, with the unscaled data vectors plotted underneath in blue for comparison. Vectors from Solution 152 show good agreement with the data, and the corresponding residuals (Figure 6.11, right) show the same pattern and maximum angle of deviation as those of the seed model (Figure 6.2, right). Intensity residuals are also in good agreement, although the range of values is slightly wider than the seed map. There is no significant change in either of the residual patterns from Scenario 1A.

As with Scenario 1A, PolCat was unable to reproduce the inclination angle. The solution with the closest inclination angle to the seed value was approximately -8° for the set. Solution 152 locked in at an inclination angle of approximately -14°. We do note that there was far more variation in selected position angle in this set than in Scenario 1A, with clusters of

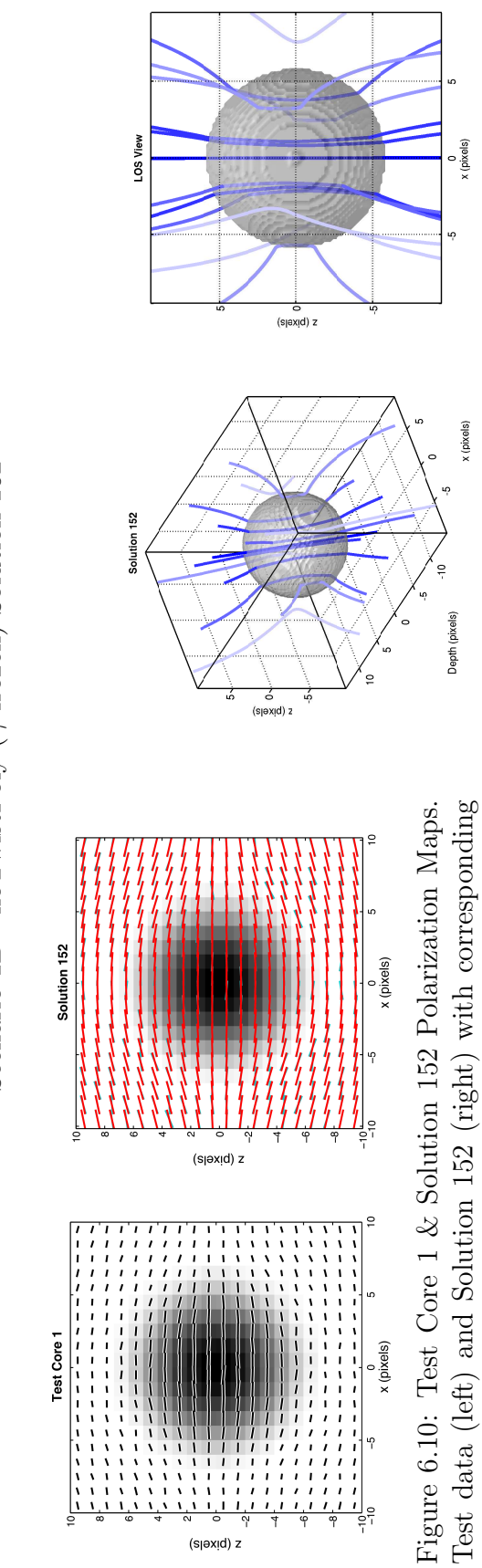

Figure 6.10: Test Core 1 & Solution 152 Polarization Maps. Test data (left) and Solution 152 (right) with corresponding polarization vectors (red) overlain on the test data vectors (blue).

Figure 6.11: Solution 152 Residuals. Intensity (left) and χ_{pol} (right). Intensity residuals are presented as a fraction of $\bar{I}_{data} = 7.6 \times 10^{-3}$ Jy beam^{-1}.

Figure 6.12: Three-Dimensional Structure of Solution 152.

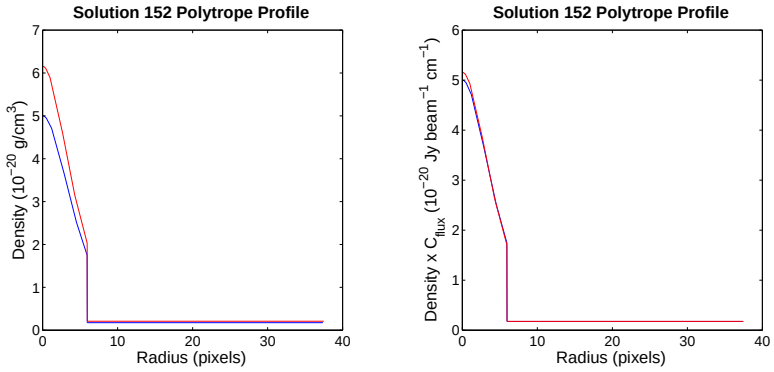

Figure 6.13: Solution 152 Polytrope Density Profiles. Scaled density profiles from Solution 152 (red) and the seed model (blue) POLY transformations.

solutions at points other than the usual symmetry angles of 0°, 180°, and 360°. However, we find that these solutions correspond to the "best" intensity fitness but a poor polarization χ_{pol} fit, with F2 values greater than 4, and an approximately uniform choice of inclination angle at approximately -20°. The bottom of the curve, including the knee region, is populated entirely by solutions clustered about angles symmetrically equivalent to the seed model orientation.

Solution 152 managed a slight improvement over Solution 120 in Scenario 1A in the density scale and velocity dispersion. The merged set from this template had approximately the same range of solution values for ρ_0, but the σ_0 range widened slightly and shifted upward to the range 0.6–0.9 km s^{-1}, with most of the solutions clustered between 0.7–0.8 km s^{-1}.

The knee solution for this set was slightly better at reproducing the external pressure and density POLY parameters, but failed to accurately reproduce the central density ρ_c. This parameter was as poorly constrained as Scenario 1A, showing the same range of values. Despite the minor discrepancy in ρ_c and C_{flux}, Figure 6.13 shows that once the density profiles are scaled by the C_{flux} as though replicating the step before line-of-sight integration, the profile matches almost perfectly to the corresponding seed model profile, as is the case in Scenario 1A results.

With the exception of the central density, the POLY parameters as a whole showed better constraint than with Scenario 1A. The knee model's K parameter is slightly larger, but truncation pressure P_{out} and external density ρ_{out} are reproduced reasonably well. The

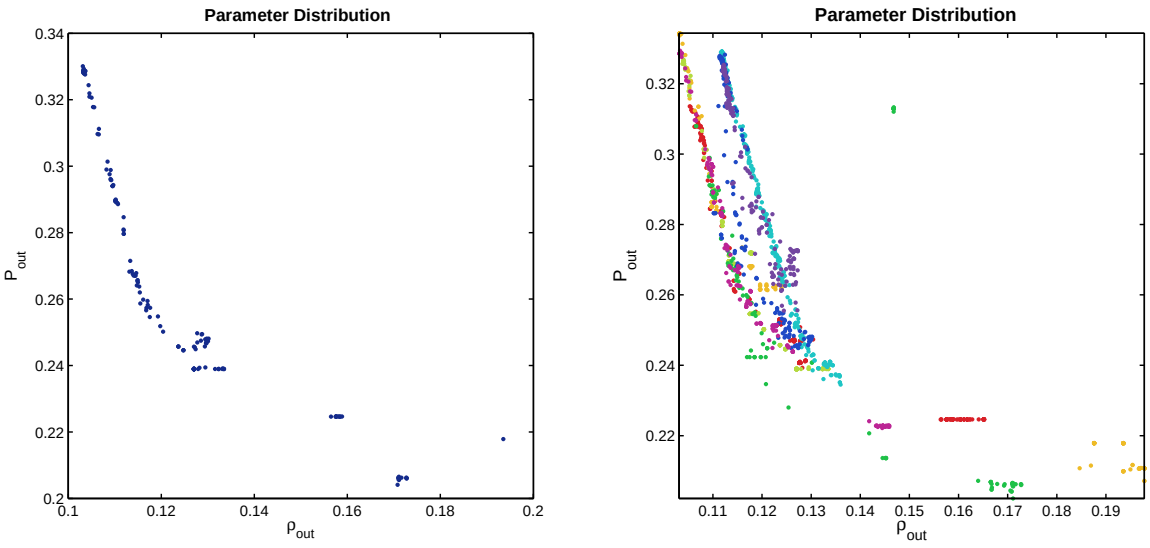

Figure 6.14: Parameter Distribution for POLY ρ_{out} vs P_{out}. Merged set (left) and its component runs (right).

parameter distribution for truncation pressure showed a slight correlation with external density for the merged set, which was also reflected in all of the runs (shown in Figure 6.14).

6.1.1.3 Scenario 1C: Frozen C_{flux}

In this scenario, we used the same noTwistBE model as in Scenario 1B, but edited the `setupPol` settings to freeze C_{flux} to the seed model value of 1. Again, we wished to see whether reducing the size of the parameter space would improve the fit for the rest of the parameters.

The appearance of the fitness curve (Figure 6.15) is similar to the last two scenarios, with the knee indicated from a sharp, almost instantaneous 90° bend in the curve. We have identified Solution 19 as the solution closest to the knee, with its parameters summarized in Table 6.2, with polarization maps, residual maps, and three-dimensional representation displayed in Figures 6.16 to 6.18.

Overall, this setup did not show much improvement over Scenario 1B. Improvement in intensity fitness was marginal and there was almost no improvement in χ_{pol} fitness. While the knee solution was very slightly closer to the seed model value, the merged solution set

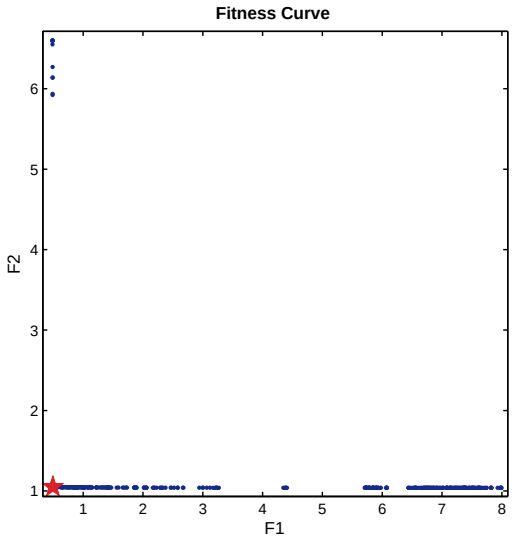

Figure 6.15: Test Core 1 Scenario C Trade-off Surface. Solution 19 marked by a red star.

as a whole showed an equivalent spread of inclination angle values as the merged set from Scenario 1B. Rotation PA showed a the usual symmetry angles in addition to two clusters at about 20° above the $PA = 0$ and 180° points, both with inclination angles of about 12°, that correspond to the lowest F1/highest F2 solutions as in Scenario 1B.

As in the previous two scenarios, core shape and shift parameters have also been replicated faithfully, confirmed by the three-dimensional plot of the core (Figure 6.18).

Exploring the POLY parameters shows that they are better constrained than in both the previous scenarios, although the knee model's central density is still high. Since the C_{flux} was frozen to a value of 1, the scaled density profile (Figure 6.19) for Solution 19 is a close match, even although the dimensionless polytrope profile is a relatively poor match in magnitude. In this case the density scale ρ_0 has compensated for the high ρ_c value. The truncation radius is duplicated exactly.

6.1.1.4 General Observations

The numbers in brackets in the Seed column of Table 6.2 represent the "fitness" and reduced χ^2 values between the generated polarization maps (with noise) and the seed model used to

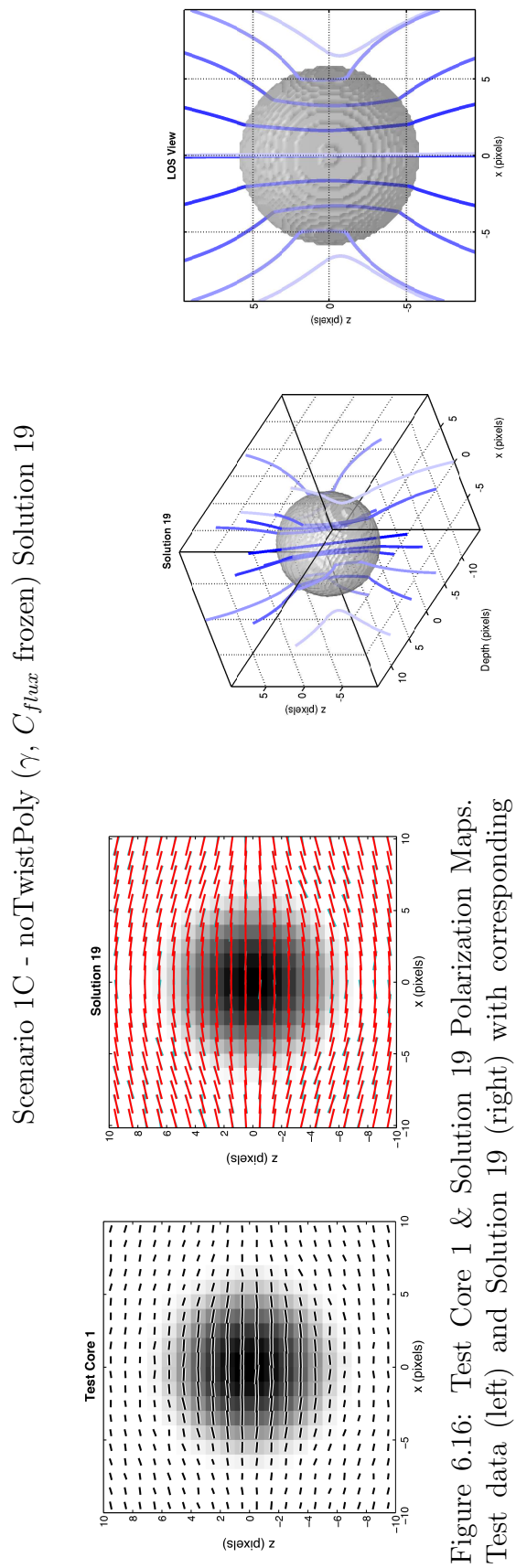

Figure 6.16: Test Core 1 & Solution 19 Polarization Maps. Test data (left) and Solution 19 (right) with corresponding polarization vectors (red) overlain on the test data vectors (blue).

Figure 6.17: Solution 19 Residuals. Intensity (left) and χ_{pol} (right). Intensity residuals are presented as a fraction of $\bar{I}_{data} = 7.6 \times 10^{-3}$ Jy beam^{-1}.

Figure 6.18: Three-Dimensional Structure of Solution 19.

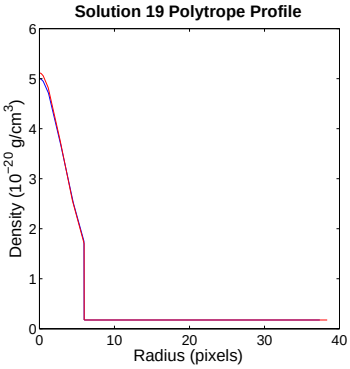

Figure 6.19: Solution 19 Polytrope Density Profile. Scaled density profiles from Solution 19 (red) and the seed model (blue) POLY transformations.

	Seed	Scenario A	Scenario B	Scenario C
	–	# 120	# 152	# 19
F1	(0.49)	0.54	0.50	0.49
F2	(1.06)	1.05	1.05	1.05
χ^2_I	(1.05)	1.34	1.12	1.11
χ^2_{PA}	(1.12)	1.10	1.11	1.11
ρ_0 (g cm^{-3})	1×10^{-20}	1.29×10^{-20}	9.25×10^{-21}	8.87×10^{-21}
σ_0 (km s^{-1})	0.8	0.74	0.78	0.81
K	0.1	0.09	0.12	0.09
γ_{poly}	1	1.22	1*	1*
ρ_c	5	5.03	6.65	5.77
ρ_{out}	0.1	0.11	0.10	0.10
P_{out}	0.35	0.25	0.33	0.33
a_{scale}	1	1.00	1.00	1.01
b_{scale}	1	1.01	1.00	1.00
ϕ	0°	184.4°	4.4°	270.3°
i	0°	13.2°	-13.6°	-10.3 °
PA	0°	179.8°	179.9°	179.8°
Δx (pix)	0	0.00	0.00	0.00
Δz (pix)	0	0.00	0.00	0.00
C_{flux}[†]	1	0.79	0.84	1*

Table 6.2: Test Core 1 Results
*Parameter is frozen to value
[†]Jy beam^{-1} g cm^{-1}

generate them (without noise). These values are generated using the noTwistPoly template used to originally generate the core. However, when these values were computed with the models from Scenarios 1B and 1C, we found that the variation in the values was less than 0.01 between all three, and so have recorded them to two decimal places.

The shared shape of the trade-off surfaces between runs with their sharp knees is generally expected from fits to generated data, as the generated data is free of any of the fine structure which may be present in actual molecular cloud cores.

The difficulty pinning down the inclination angle may be due to the amount of noise in the generated dataset. The added noise may have produced polarization vectors more typical of a magnetic field tilted slightly from the vertical. An observation that perhaps validates this assessment is the "seed model fitness" values. The fitness values of the seed model with respect to the test data are F1=0.49 and F2=1.06; the F2 value is slightly worse than that of Solution 120 at the knee of the Scenario 1A fitness curve. The same behaviour is displayed between the reduced χ^2 values are computed. Therefore, it appears the models computed in Scenarios 1A–1C represent a "better" fit to the magnetic field from the polarization of the Core 1 map than the seed model does. However, these models do not show improvement on the intensity map. These results suggest that, in cases of high symmetry where the intensity map offers no clues to the core orientation, the polarization vectors constrain i within the limits of the noise. The polarization vectors also constrain PA as well, but with much more fidelity.

Overall, the knee model in each scenario was able to reproduce the intensity residuals reasonably well, with the absolute values of the residuals being within the range of the residuals between the Core 1 maps and the seed model (Figure 6.2). Removing γ and C_{flux} from the fit only showed marginal improvement in parameter value over Scenario 1A. However, fixing γ caused the code to reproduce the value of the truncation pressure P_{out}. We suggest that the code's motivation for selecting a particular value of P_{out} may be motivated by the choice of the polytropic index γ.

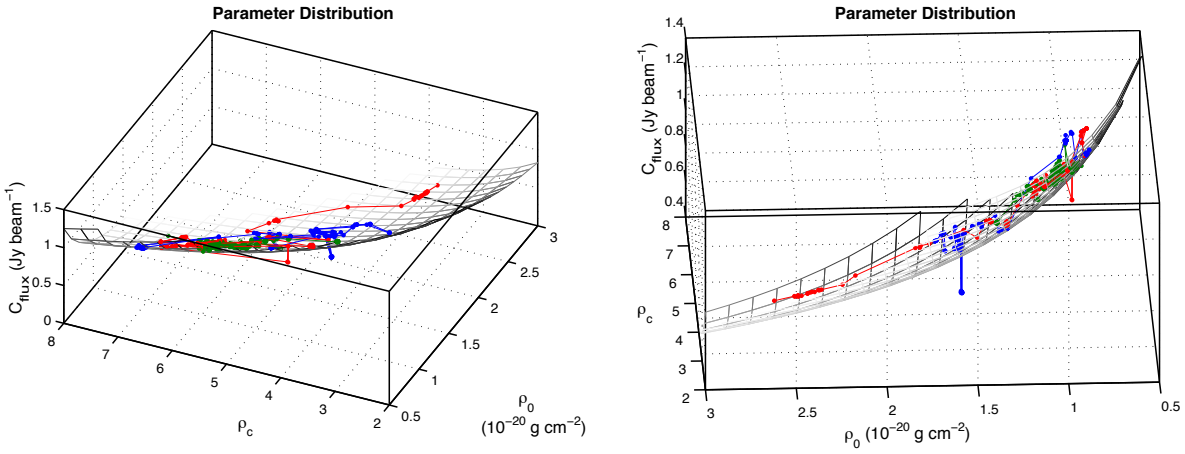

Figure 6.20: C_{flux} vs ρ_0 vs ρ_c For All Three Scenarios. Surface represents $C_{flux} \times \rho_0 \times \rho_c = 5 \times 10^{-20}$ Jy beam^{-1} cm^{-1}.

As a trend for all three scenarios, the quantities ρ_0, ρ_c, and C_{flux} are not well-constrained. However, as the quantity $C_{flux} \times \rho_0 \times \rho_c$ controls the peak intensity, it is possible that this quantity is better constrained than the individual parameters are. For the seed model, the value of the previous expression is 5×10^{-20} Jy beam^{-1} cm^{-1}, and for each of the three scenarios we obtain knee values of A) 5.10×10^{-20}, B) 5.19×10^{-20}, and C) 5.11×10^{-20} Jy beam^{-1} cm^{-1}. Figure 6.20 shows the solutions plotted by the three previously mentioned parameters for each merged set, along with on the surface defined by $C_{flux} \times \rho_0 \times \rho_c = 5 \times 10^{-20}$ Jy beam^{-1} cm^{-1}. While not precisely confined to that surface, the solutions appear to be approximately correlated with it.

6.1.2 Test Core 2: Oblate Triaxial Bonnor-Ebert Profile

The parameters for the second test core are summarized in Table 6.1. The second test core consisted of a polytrope profile identical to Test Core 1 (§6.1.1), but where Test Core 1 was a non-rotated sphere, Test Core 2 is scaled into a triaxial ellipsoid with non-zero rotation angles. In this particular test case we have chosen the a and b values so as to produce an "oblate" core flattened along the magnetic field direction. Test core parameters are summarized in Table 6.1, with resulting data map, seed model residuals, and three-

dimensional structure shown in Figures 6.21–6.23 respectively. Using a triaxial core set at a non-zero angle serves as a better test of the code's ability to discern proper shape and orientation angle. The Test Core 1 results showed that, in the spherical case, the orientation angle was governed by the magnetic field alone. Test Core 2 gives a further constraint by giving the core different symmetry along each axis, which may constrain the rotation parameters better than the spherical case.

6.1.2.1 Scenario 2A: Basic Fit (noTwistPoly)

This test was a basic fit with the noTwistPoly model. The trade-off surface (Figure 6.24) shows a sharp bend at approximately (0.56, 1.0). As such, we select Solution 22 for analysis. The parameters for Solution 22 are summarized in Table 6.3 along with the results from Scenario 2B.

The polarization map of Solution 22 with comparison data vectors is shown in Figure 6.25 alongside the Test Core 2 "data" (left) Comparing the intensity residuals of Solution 22 (Figure 6.26) to those of the seed model (Figure 6.22), we can see there is some slight correspondence between the areas of maximum and minimum deviation, although these areas are much smaller in the seed model result. The polarization position angle residuals are virtually identical to those of the seed model.

The parameters for the set as a whole showed a tendency to group themselves into tightly-packed clusters in the parameter space. The shape parameters are reasonably well-constrained, with the majority of solutions clustered around the same area of the parameter space. One lone solution lies on the opposite side of the $a = b$ line in the corresponding area to the majority. The solutions in the mirrored areas are equivalent, as the orientation of a and b to the line of sight can be changed easily with the rotation transformation. Solution 22's values of $a = 1.20$ and $b = 1.02$ have therefore reproduced the core shape accurately.

We can see from Figures 6.23 and 6.27 that, although the magnetic field in the seed model is tilted away from us, Solution 22's field is tilted towards us. The inclination angle

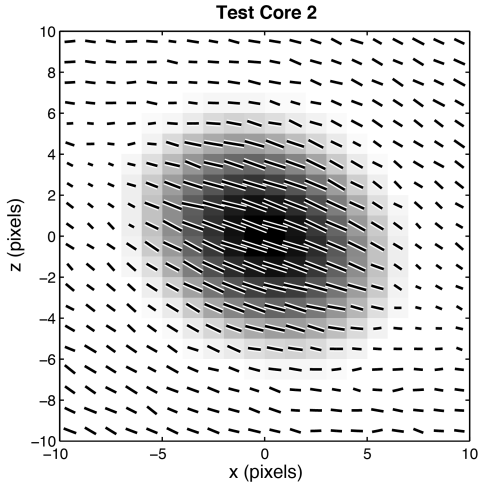

Figure 6.21: Test Core 2 Polarization Map. Includes noise. Vectors are scaled by $\sqrt{P_{flux}}$.

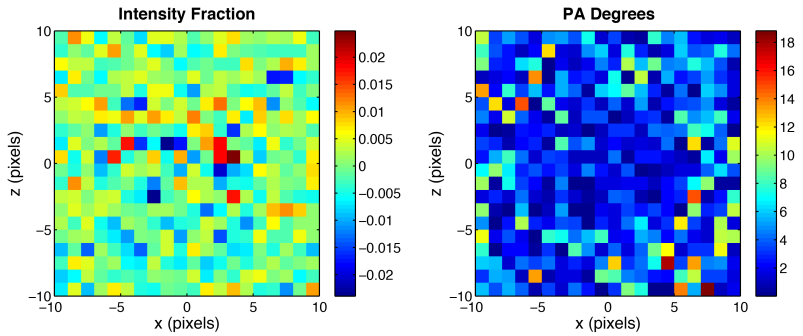

Figure 6.22: Test Core 2 Seed Model Residuals. Residuals between the seed model and the test data map (Figure 6.21). Intensity residuals are presented as a fraction of $\bar{I}_{data}$=7.46 × 10^{-3} Jy beam^{-1}

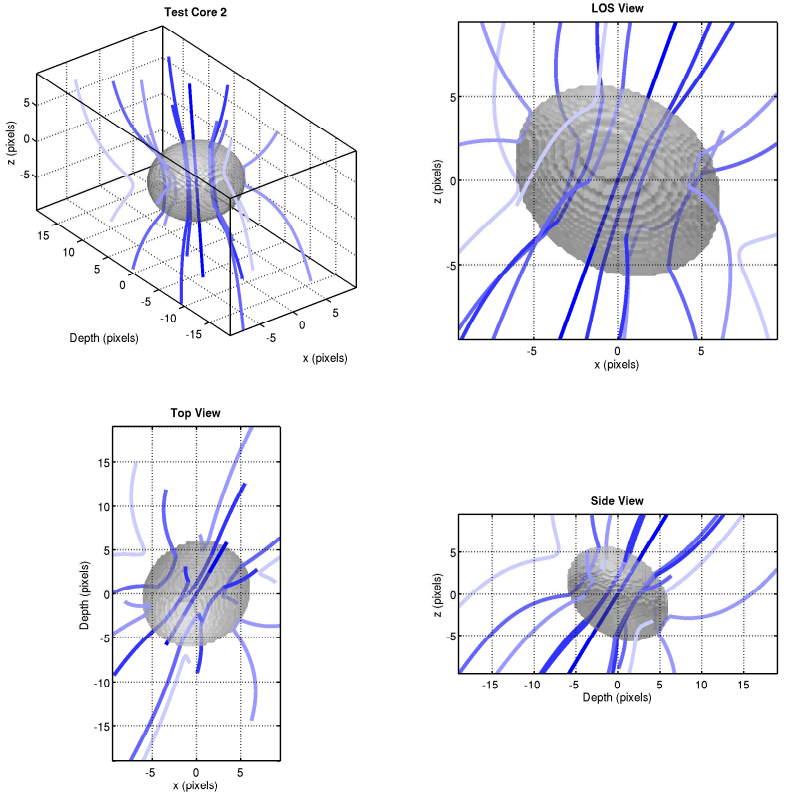

Figure 6.23: Three-Dimensional Structure of the Test Core 2 Seed Model.

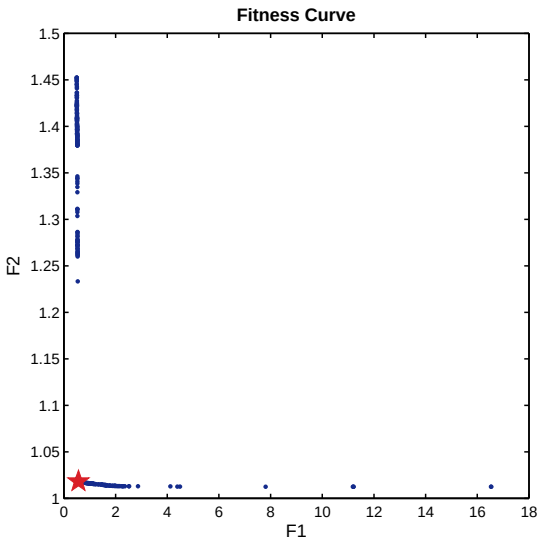

Figure 6.24: Test Core 2 Scenario A Trade-off Surface. Solution 22 indicated by a red star.

for Solution 22 is reported as i=-150° to the seed value of 30°. These angles are 180° apart, meaning that, in terms of and x–z projection, these models are equivalent. The change in tilt between the seed model and Solution 22 is likely due to PA having a value of 20° + 180°. As the PA rotation is applied last, this would cause the "top" of the core after the i rotation to be flipped to the bottom when RotateA completed.

Figures 6.28a and 6.28b plot RotateA's i and PA parameters. At a glance, the inclination angle seems well-constrained, with the merged set having selected values clustered around +30° and ±150°. Close inspection on the clusters in Figure 6.28 shows that the spread of values in the inclination angle is approximately 5° wide, closer to the seed model inclination than the models of Test Core 1. Rotation PA shows a similar behaviour, with clusters at 20° and 200°, with the 20° clusters having split into a smaller subgroup with PA ∼25°.

As the core is not radially symmetric, we find that the azimuthal rotation angle ϕ is better constrained than in the Test Core 1 results, as expected. The degenerate symmetry angles appear to be ϕ, 180°-ϕ, ϕ +180°, and 360° - ϕ (45°, 135°, 225°, and 315° respectively). However, although the knee solution selected a value within 4° of the seed value, most of the solutions either skewed high or were spread out over an area 10° wide.

Scenario 2A - noTwistPoly Solution 22

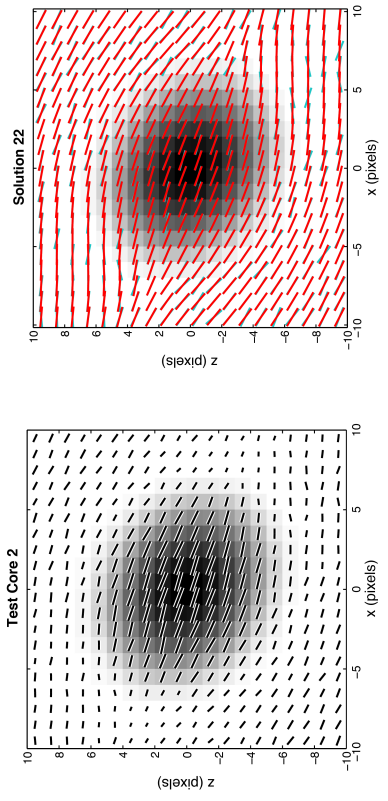

Figure 6.25: Test Core 2 & Solution 22 Polarization Maps. Test data (left) and Solution 22 (right) with corresponding polarization vectors (red) overlain on the test data vectors (blue).

Figure 6.26: Solution 22 Residuals. Intensity (left) and χ_{pol} (right). Intensity residuals are presented as a fraction of $\bar{I}_{data}$=7.46 $\times 10^{-3}$ Jy beam^{-1}.

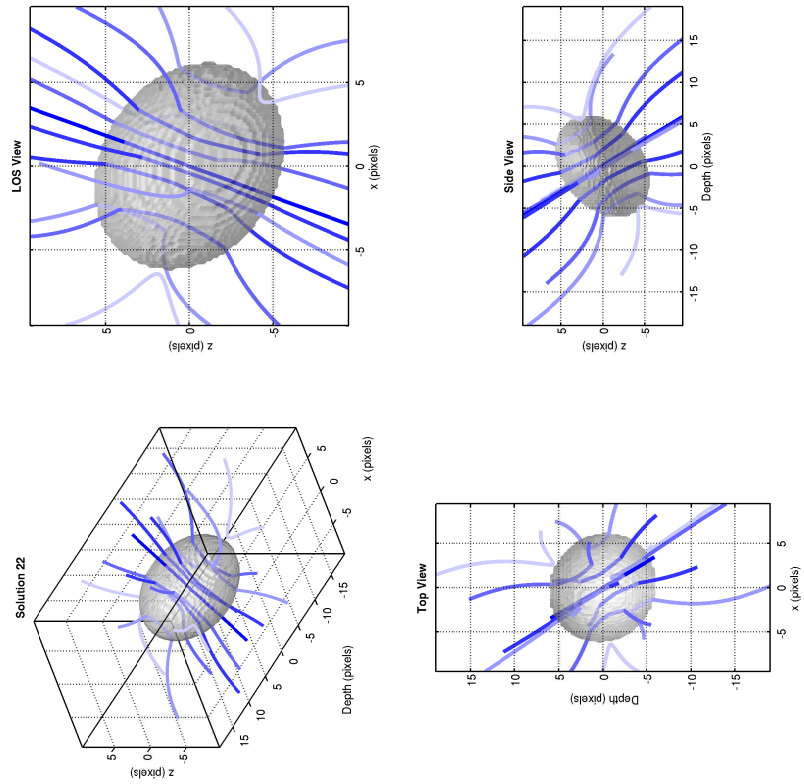

Figure 6.27: Three-Dimensional Structure of Solution 22.

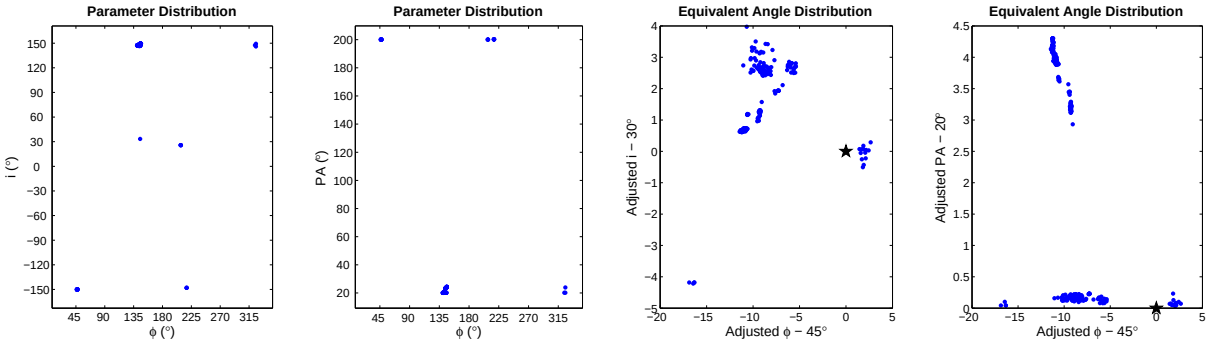

(a) (b) (c) (d)

Figure 6.28: Scenario 2A Rotation Transformation Angles. Parameter distribution of rotation angles for the merged set ((a) and (b)). Plots (c) and (d) show the angles adjusted to equivalents 0–90° with seed values subtracted (star indicates seed value position).

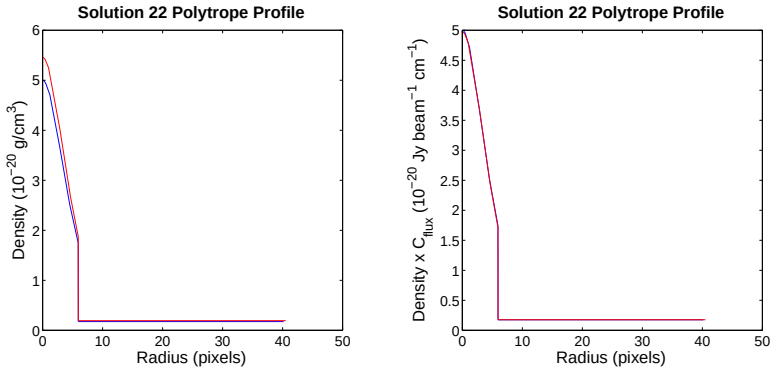

Figure 6.29: Solution 22 Polytrope Density Profiles. Scaled density profiles from Solution 22 (red) and the seed model (blue) POLY transformations.

Adjusting the rotation angles to their equivalents between 0 and 90° (Figures 6.28c and 6.28d) better demonstrates the spread in the angles. This adjustment was made by accounting for how the angles would project along the line of sight. Figures 6.28c and 6.28d show the distribution of angles after this adjustment, showing majority of solutions to have ϕ clustering between -5° to -10° from the seed value. Figure 6.28c shows the majority of solutions have inclination angles clustered between -1 to 4° from the seed value, with a tiny population at around -4°. PA is well constrained, with the majority of the merged solution set falling within 0.5° of the seed value with a small population at +3.5° (Figure 6.28d).

Density scale ρ_0 and velocity dispersion σ_0 showed a tendency clump in the parameter space. Overall there were three preferred values for ρ_0: approximately 0.8, 0.9 and 1.4×10^{-20}

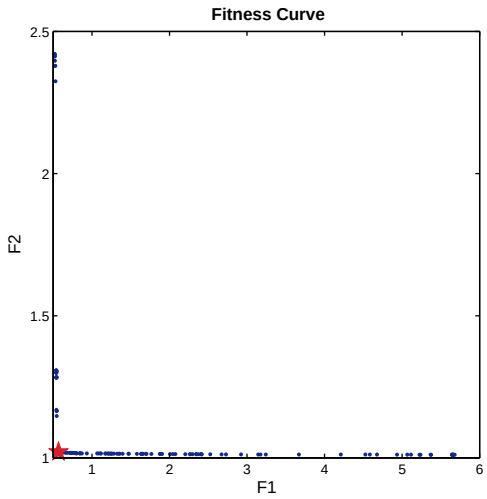

Figure 6.30: Test Core 2 Scenario B Trade-off Surface. The red star represents Solution 64

g cm^{-3}, with the latter being the preferred value over the majority of the set. The velocity dispersion showed preference for values at approximately 0.66, 0.72, and 0.88 km s^{-1} with the latter value being preferred by the majority of the solution set. Solution 22 itself selected values of 0.818×10^{-20} g cm^{-3} and 0.72 km s^{-1}.

Examination of the polytrope profile for Solution 22 (Figure 6.29) shows the same behavioural relationship between ρ_0, ρ_c, and C_{flux} exhibited by the Test Core 1 scenarios, where scaling the density profile into Jy beam^{-1} cm^{-1} causes the profiles to match. The polytrope parameters, with the exception of central density ρ_c were reproduced reasonably well in the knee model. The solution set as a whole placed γ typically within $\sim$0.1 of the true value. The parameter distribution of ρ_{out} relative to P_{out} did not show the same relationship as the Test Core 1 runs (see Figure 6.14).

6.1.2.2 Scenario 2B: Frozen γ

Scenario 2B tests the fit when the polytropic index γ is frozen to the seed value. The fitness curve shows the same sharp bend as the other test results. We have selected Solution 64 at the knee of the curve (indicated by the red star in Figure 6.30). Figures 6.31–6.33 show the resulting polarization map, residuals, and views of the model in three dimensions.

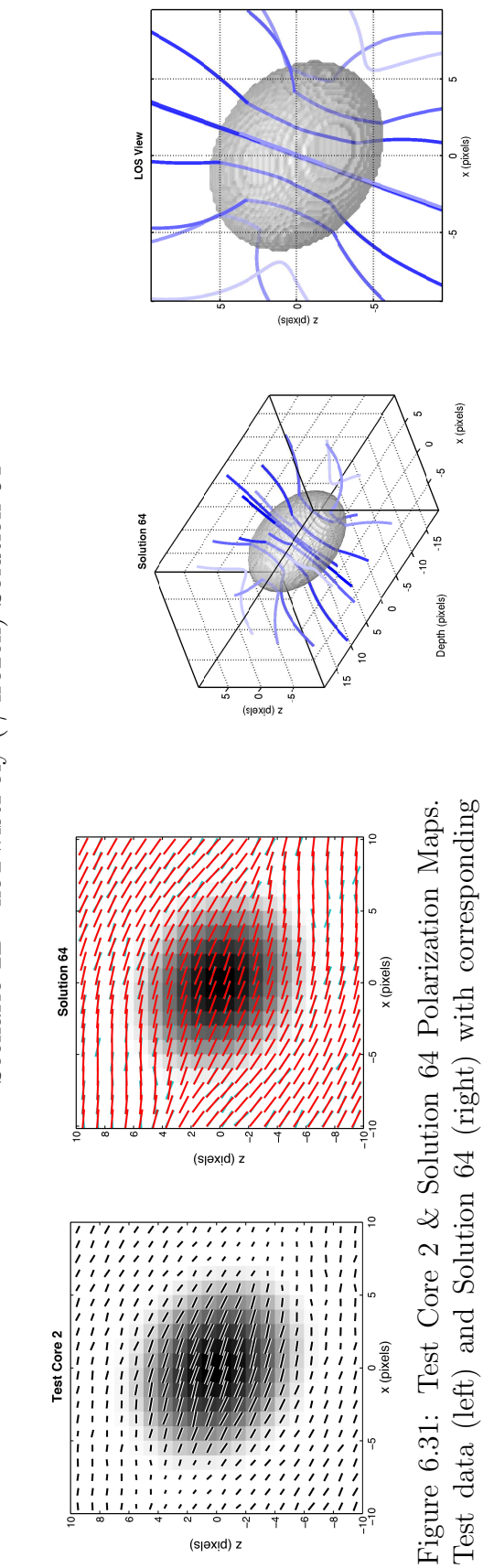

Figure 6.31: Test Core 2 & Solution 64 Polarization Maps. Test data (left) and Solution 64 (right) with corresponding polarization vectors (red) overlain on the test data vectors (blue).

Figure 6.32: Solution 64 Residuals. Intensity (left) and χ_{pol} (right). Intensity residuals are presented as a fraction of $\bar{I}_{data}$=7.46 $\times 10^{-3}$ Jy beam^{-1}.

Figure 6.33: Three-Dimensional Structure of Solution 64.

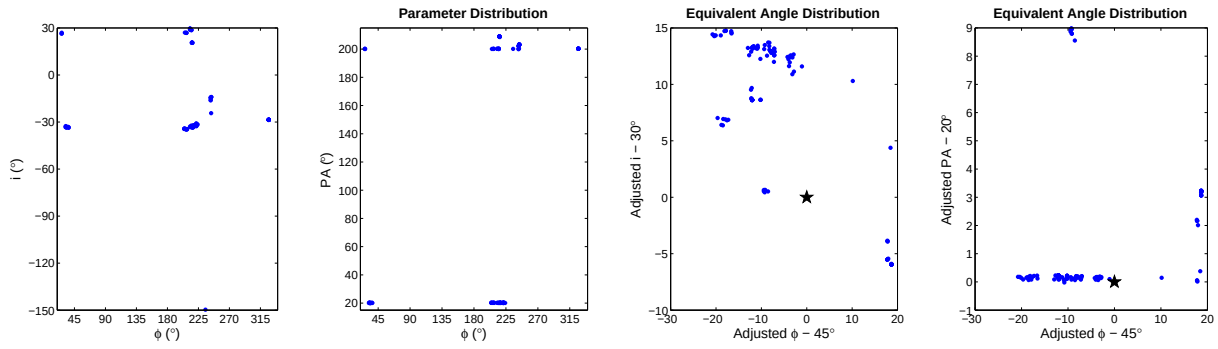

(a) (b) (c) (d)

Figure 6.34: Scenario 2B Rotation Transformation Angles. Parameter distribution of rotation angles for the merged set ((a) and (b)). Plots (c) and (d) show the angles adjusted to equivalents 0–90° with seed values subtracted (star indicates seed value position).

The Solution 64 intensity residuals (Figure 6.32) show a similar distribution and range to those of Solution 22 in Scenario 2A. The polarization position angle residuals are again virtually indistinguishable from those of the seed model.

Overall, the parameter distributions for Scenario 2B did not show the preference for clustering that the Scenario 2A solutions did; the parameter distributions tended to be spread out over the parameter space. In some cases the range of values the parameters took was even larger than the Scenario 2A ranges.

The knee solution selected a core shape with a similar a value to the seed model. However, the b value was larger by $\sim$0.07, resulting in a core that was slightly flattened compared to the original, with a visibly wider profile in the Side View of Figure 6.33. Despite this slight elongation, the shape of the Test Core 2 seed model core and Solution 64 projected along the line of sight view are identical.

The distribution of i and PA angles in the solution set is, if anything, less constrained than the Scenario 2A runs. Both parameters showed the same degeneracy in value as in Scenario 2A (Figures 6.34a and 6.34b), although once the individual runs were merged, the set only showed i values at $\pm$30° and -150°. The maximum deviation from the seed value for i was about 15° with most solutions falling between 30° + 5–15°. The majority of PA values fell within 0.5° of the seed values, as with Scenario 2A, but the solutions with equivalent PA

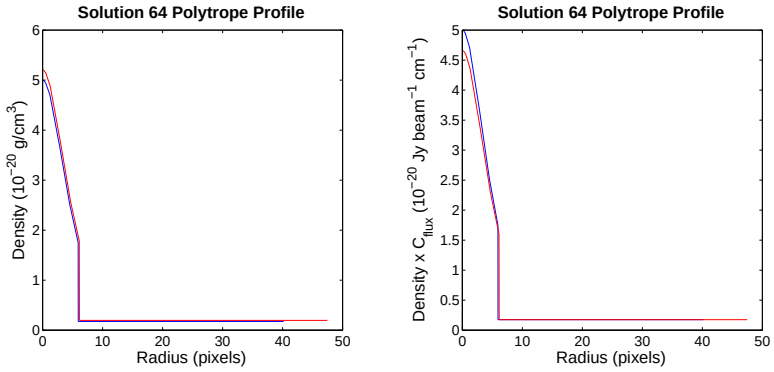

Figure 6.35: Solution 64 Polytrope Density Profiles. Scaled density profiles from Solution 64 (red) and the seed model (blue) POLY transformations.

greater than ∼20.5° showed a wider spread in values.

The knee model itself locked on $\phi = 205.3°$ which is equivalent to approximately 25°: 20° from the seed value. The i and PA values were closer, taking values of approximately 27.0° for i and 200.1° (equivalent to 20.1°) for PA.

Solutions in the Scenario 2B ρ_0 versus σ_0 parameter distribution were not as tightly clustered as those in Scenario 2A, although they were distributed over an equivalent range of values. Despite some solutions having values very close to the seed σ_0 value of 0.8 km s^{-1}, they did not get any closer to the seed density value than any of the Scenario 2A solutions. The knee value selected a low density scale value of 0.690×10^{-20} g cm^{-3} and a high velocity dispersion value of 0.94 km s^{-1}. However, it also selected a central density value of $\rho_c = 7.54$, giving the physical density at the core centre a value of 5.20×10^{-20} g cm^{-3}. The polytrope density plot (Figure 6.35) showed better congruence with the seed model than the density $\times$ C_{flux} profile, with the scaled profile underestimating the emission by $\sim 0.3 \times 10^{-20}$ Jy beam^{-1}cm^{-1}.

6.1.2.3 General Observations

A common thread between the two scenarios was that PolCat could not distinguish between positive and negative angles of inclination. That is, the model is insensitive to whether the core magnetic field is tilted towards or away from us; cores with an inclination of $i \pm$

	Seed	Scenario A	Scenario B
	–	# 22	# 64
F1	(0.47)	0.56	0.57
F2	(1.02)	1.02	1.02
χ^2_I	(1.02)	1.35	1.33
χ^2_{PA}	(1.04)	1.04	1.04
ρ_0 (g cm^{-3})	1×10^{-20}	8.18×10^{-21}	6.90×10^{-21}
σ_0 (km s^{-1})	0.8	0.72	0.94
K	0.1	0.10	0.08
γ_{poly}	1	1.12	1*
ρ_c	5	6.67	7.54
ρ_{out}	0.1	0.10	0.11
P_{out}	0.35	0.30	0.34
a_{scale}	1	1.20	1.03
b_{scale}	1.2	1.02	1.27
ϕ	45°	47.7°	205.3°
i	30°	-149.7°	27.0°
PA	20°	200.1°	200.1°
Δx (pix)	0	0.00	-0.01
Δz (pix)	0	0.00	-0.01
C_{flux}[†]	1	0.91	0.90

Table 6.3: Test Core 2 Results
*Frozen to value
[†]Jy beam^{-1} g^{-1} cm^2

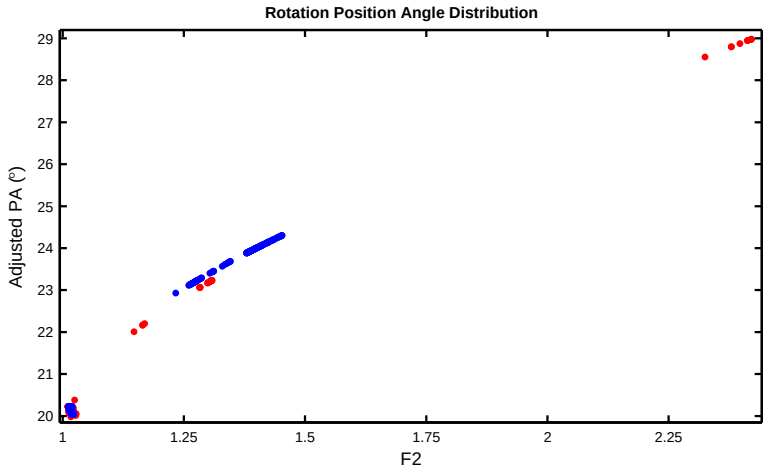

Figure 6.36: Scenario 2A & 2B Adjusted PA vs. F2. Scenario 2A results in blue and Scenario 2B results in red.

180° are equivalent. As expected, a similar degeneracy exists in the rotation PA, although the distribution of values was better confined. In both scenarios, the model managed to reproduce the approximate shape of the seed model.

When we take the PA values for each solution and confine the angles to values less than 180° (i.e. `PA(PA > pi)= PA(PA > pi)− pi`), we find that the solutions with the best F2 are confined to values within 0.05° of the seed value of 20° (see Figure 6.36). All adjusted PA values outside of this range correspond to solutions with the highest F2 and the lowest F1. Indeed, the gap in F2 value before the knee region in Figures 6.24 and 6.30 acts as a separator between these solutions and the 20° ± 0.5° solutions. This result appears to imply that the polarization position angle (F2 objective) works to tightly constrain the RotateA PA parameter. In all cases, the LOS view of the three-dimensional model (Figures 6.23, 6.27, and 6.33) were identical, despite minor differences in shape and orientation.

6.1.3 Test Core 3: Oblate Triaxial Bonnor-Ebert Profile with a Twist

This core is identical to Test Core 2, with the addition of an asymmetric linear twist (LinearTwist A) to create a helical field. We used the basic5Component model to generate the

test data, and we have summarized the seed parameters in Table 6.1. Figures 6.37–6.39 show the test data polarization maps, the seed model residuals, and the three-dimensional model.

Primarily, we will be testing not only PolCat's ability to replicate a core with a twisted field, but also how a non-twisted model would behave when applied to a core with twisted field geometry.

6.1.3.1 Scenario 3A: Basic Fit (basic5Component)

Scenario 3A is a basic fit with the basic5Component template (seed template). The merged trade-off surface for all eight runs (Figure 6.40) shows a smooth bend at the knee region, rather than the sharp, almost instantaneous bend resulting from the other Test Cores. The fitness values are also restricted to a narrower range of values than the previous tests. We select Solution 38 from the centre of the bend to discuss for analysis. Solution 38's parameters are summarized in Table 6.4, and its resulting polarization maps, residuals, and three-dimensional model are shown in Figures 6.41–6.43.

The resulting polarization map of Solution 38 (Figure 6.41) shows that the intensity map appears to reproduce the shape of the emission, although the fractional intensity residuals (Figure 6.42, left) show that the emission along the top right edge is slightly enhanced relative to the initial distribution, and does not match the seed model intensity residuals (Figure 6.38, left). The polarization position angles are a better match, with the corresponding residuals (Figure 6.42, right) closely matching the corresponding seed model residuals.

The three-dimensional core structure is shown in Figure 6.43. The knee model reproduced the core shape, swapping the a and b values relative to the seed model. The orientation angles for i and PA for the knee model are within less than 1° of their corresponding seed values, with ϕ at 133.0°: within 2° of its 180°-ϕ = 135° degenerate value. However, as we chose ϕ=45° for the seed model, the knee value for ϕ also corresponds to ϕ + 90°, accounting for the shape parameters a and b swapping values. The merged solution set as a whole shows PA constrained from 0.4°–1° from the seed value, and i constrained between approximately

Test Core 3 Seed Model Summary

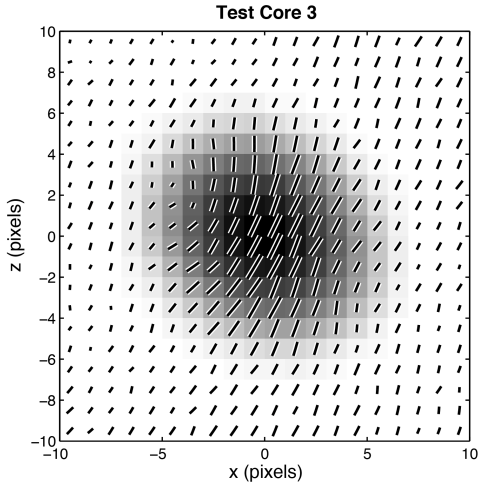

Figure 6.37: Test Core 3 Polarization Map. Includes noise. Vectors are scaled by $\sqrt{P_{flux}}$.

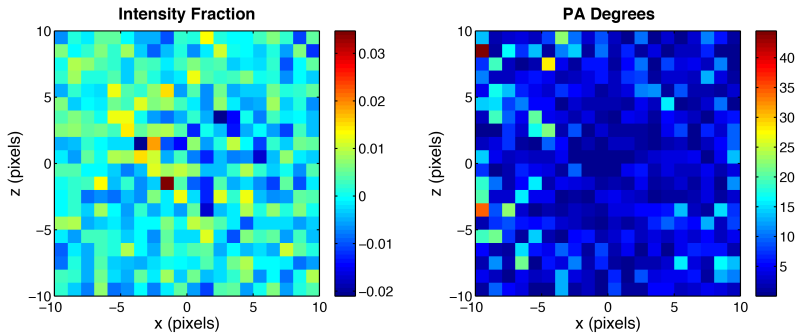

Figure 6.38: Test Core 1 Seed Model Residuals. Residuals between the seed model and the test data map (Figure 6.37). Intensity residuals are presented as a fraction of $\bar{I}_{data}$=7.46 × 10^{-3} Jy beam^{-1}.

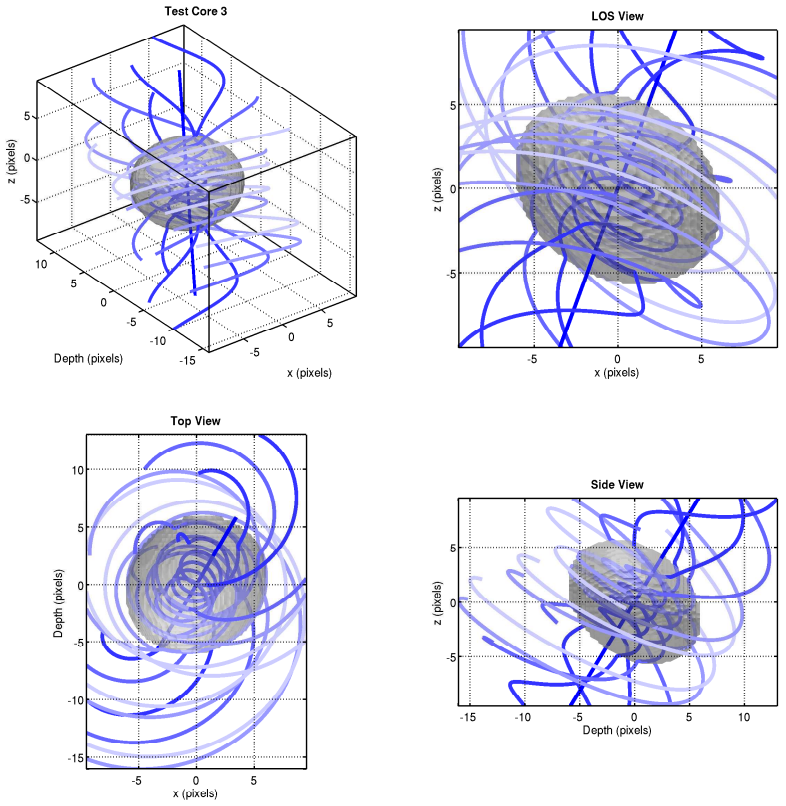

Figure 6.39: Three-Dimensional Structure of the Test Core 3 Seed Model.

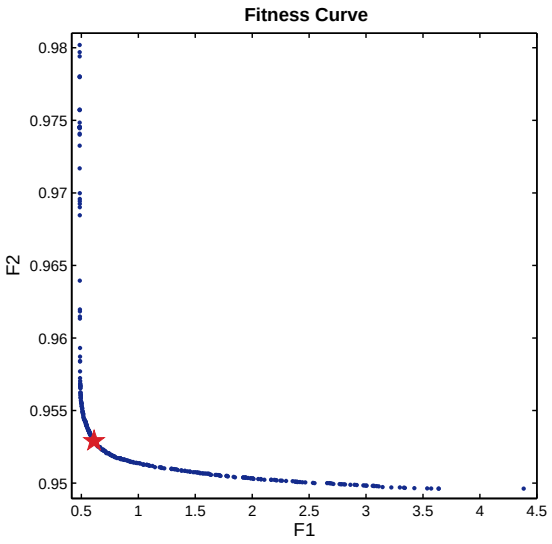

Figure 6.40: Test Core 3 Scenario A Trade-off Surface. The red star indicates Solution 38.

-0.6°–+0.2° of the seed value. The ϕ values range between approximately -2.5°–+0.6° of the 135° degenerate value.

Solution 38 had a c_{twist} parameter of 8.45, reasonably close to the seed value. While examination of Figures 6.39 and 6.43 shows that Solution 38's magnetic field lines are perhaps very slightly less twisted than the seed model's. However, the difference in appearance between the two is almost negligible.

Solution 38 has a ρ_0 value of 1.39×10^{-20} g cm^{-3}, which is high. The velocity dispersion σ_0 locked in at a value of 0.745 km s^{-1}, which is reasonable. The solution set as a whole collected into a single cluster in the parameter space, with ρ_0 values between 1.388–1.404 $\times$ 10^{-20} g cm^{-3} and σ_0 between 0.736–0.746 km s^{-1}. The C_{flux} value locked in at 0.88 for the knee, with the majority of the solution set clustered between 0.88–0.91 Jy beam^{-1} g^{-1} cm^2, with a few scattered solutions between 0.91–0.95 Jy beam^{-1} g^{-1} cm^2.

The knee solution's poly parameters were reasonably well fit to the seed model, with the polytropic index within 0.05 of the Bonnor-Ebert value of 1. The K, ρ_{out}, and P_{out} parameters were very close to their corresponding seed model values, with a less than 0.03 difference for K and P_{out}, and a less than 0.004 difference in ρ_{out}. As has been the trend with

Scenario 3A - basic5Component Solution 38

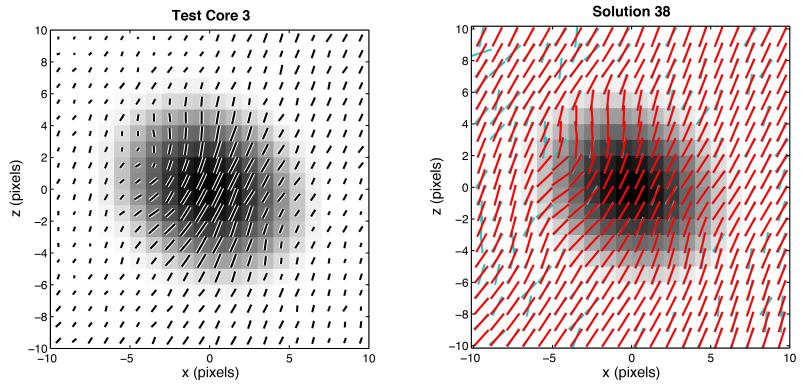

Figure 6.41: Test Core 3 & Solution 38 Polarization Maps. Test data (left) and Solution 38 (right) with corresponding polarization vectors (red) overlain on the test data vectors (blue).

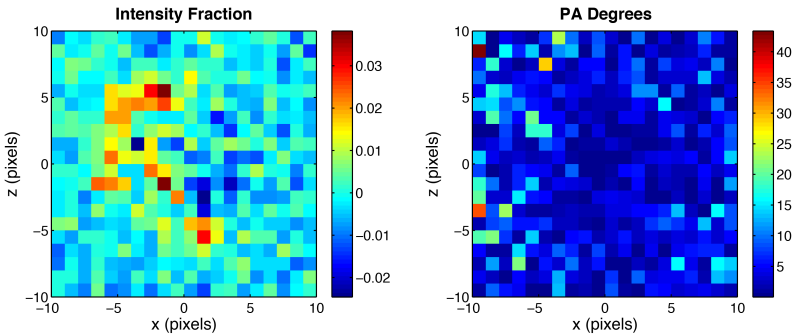

Figure 6.42: Solution 38 Residuals. Intensity (left) and χ_{pol} (right). Intensity residuals are presented as a fraction of $\bar{I}_{data}$=7.46 $\times$ 10^{-3} Jy beam^{-1}.

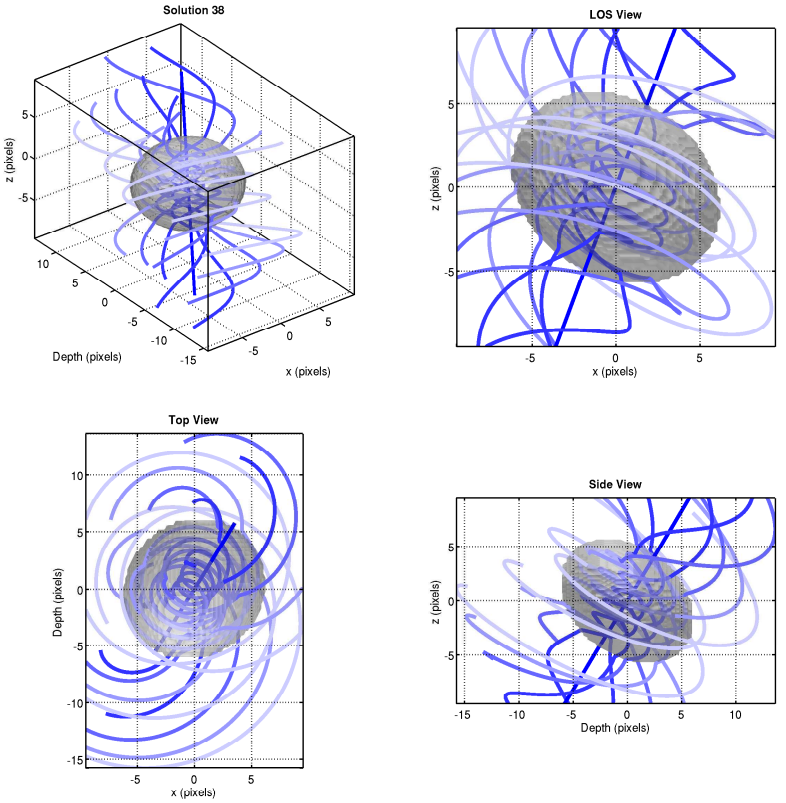

Figure 6.43: Three-Dimensional Structure of Solution 38

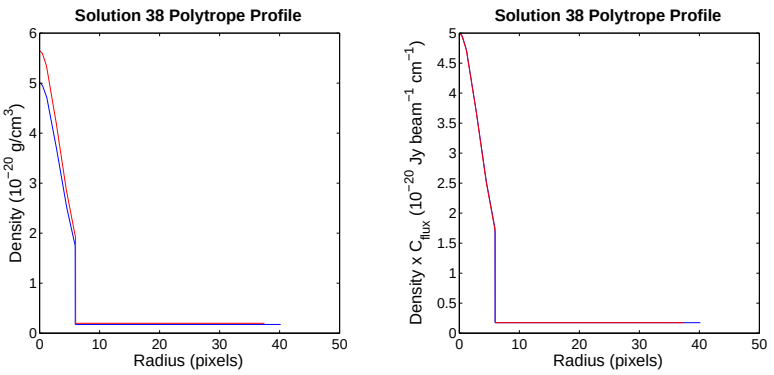

Figure 6.44: Solution 38 Polytrope Density Profiles. Scaled density profiles from Solution 38 (red) and the seed model (blue) POLY transformations.

the test fits, the central density ratio ρ_c had the largest discrepancy. Nevertheless, when the polytrope profile was scaled into Jy beam^{-1}cm^{-1} the profiles matched (Figure 6.44).

6.1.3.2 Scenario 3B: noTwist Fit

Scenario 3B fit Test Core 3 with a noTwistPoly model to observe the effect that attempting to fit a non-twisted model to a twisted field would have on the results, i.e. applying a model that we know is wrong for the system. We opted to apply the noTwistPoly template over the noTwistBE template to test what effect neglecting the twist component would have on all parameters, including the polytropic index. Figure 6.45 shows the resulting merged trade-off surface. As we can see, the fitness curve is far more sparsely populated, with the obvious knee region located at approximately $(4.0, 2.25)$. Solution 246 is located at this point, and we have summarized its parameters in Table 6.4, and have displayed its polarization maps, residuals, and three-dimensional representation in Figures 6.46–6.48.

While the intensity distribution appears to be adequate in the solution's intensity map (Figure 6.46), examination of the fractional intensity residuals (Figure 6.47, left) shows that Solution 246 is a poor fit to the intensity, as the residuals have structure at a larger magnitude to the noise. Solution 246 is too bright on the left and right edges, and too faint on the top and bottom edges and in the centre.

As we can see from Figure 6.46, the position angles of the field vectors are nearly uniform,

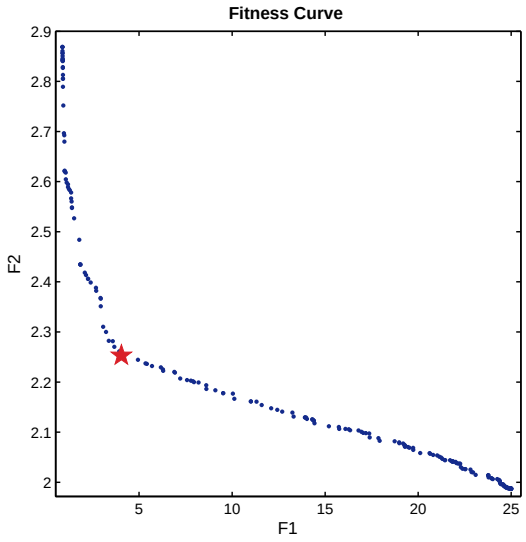

Figure 6.45: Test Core 3 Scenario B Trade-off Surface. Knee Solution 246 is indicated by a red star.

with no change in direction across the map. The model cannot account for the position angles produced by the twist in the field, most notably, the change in direction the vectors make at the top left of the core, as shown by the polarization position angle residuals. Figure 6.47 (right) shows the residuals in that area of the map to be between ∼25°–35° of the Test Core 3 map vectors.

The three-dimensional structure of Solution 246 (Figure 6.48) shows a core very different from the seed model. The core is disk-like, with the magnetic field lying parallel to the plane of the disk. If this were an observational dataset, we would rule out this geometry as the degree of contraction perpendicular to the magnetic field direction contradicts what we would expect from magnetic field pressure in the absence of a field twist.

Examination of the Shape Map for the entire solution set (Figure 6.49, right) shows the majority of the solutions clustered in the "prolate" region of the plot; where the z-stretch (c) is larger than the other two directions ($c > a, b$). The left side of Figure 6.49 is the fitness curve with each solution coloured according to c value. The colourmap reveals that the solutions with the smallest c value are the best for intensity, and increases over low to high F1, resulting in the highest c solutions having the best field vectors, but the worst intensity

Scenario 3B - noTwistPoly Solution 246

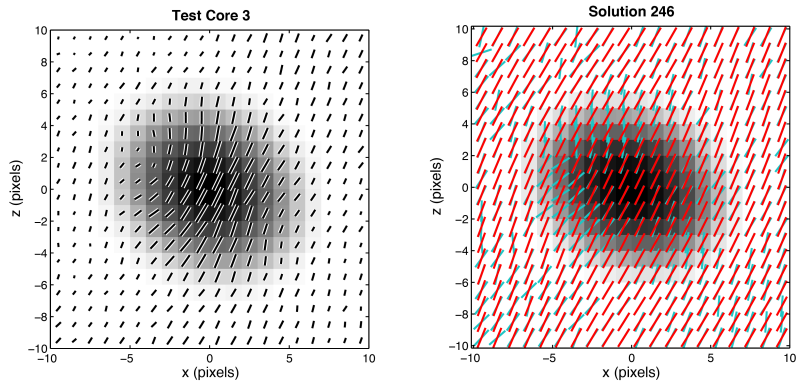

Figure 6.46: Test Core 3 & Solution 246 Polarization Maps. Test data (left) and Solution 246 (right) with corresponding polarization vectors (red) overlain on the test data vectors (blue).

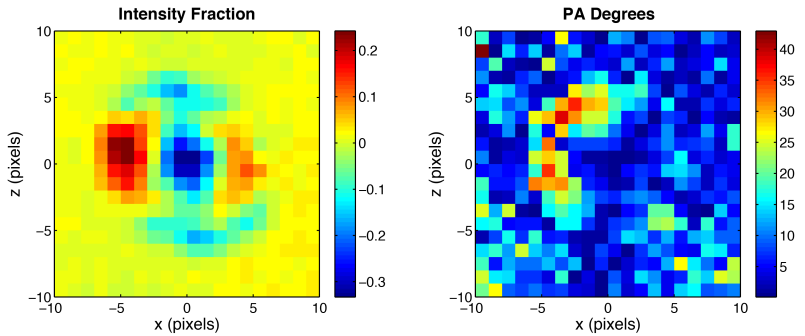

Figure 6.47: Solution 246 Residuals. Intensity (left) and χ_{pol} (right). Intensity residuals are presented as a fraction of $\bar{I}_{data}$=7.46 $\times$ 10^{-3} Jy beam^{-1}.

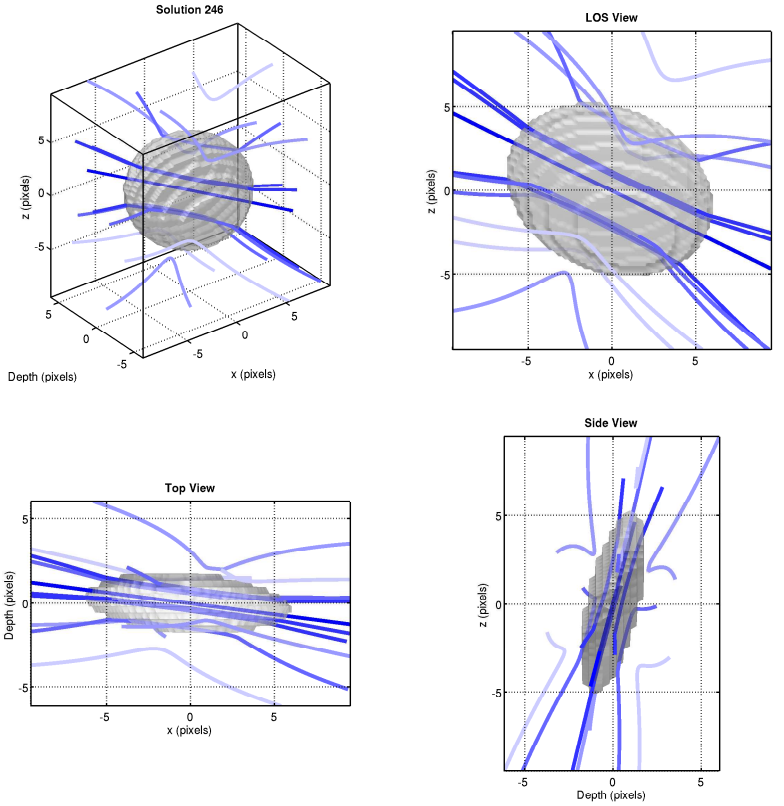

Figure 6.48: Three-Dimensional Structure of Solution 246.

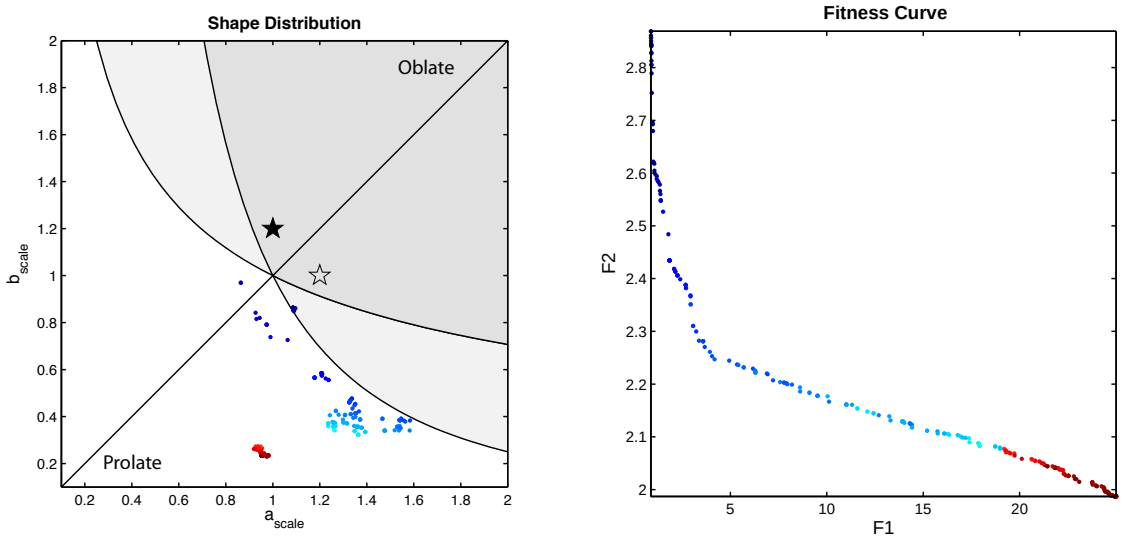

Figure 6.49: Scenario 3B Shape Map. Each solution coloured by $c = (ab)^{-1}$ value. (For a thorough explanation of this figure, see §4.3.4). The black star represents the a & b seed model values, with the symmetrically equivalent solution marked by the white star.

fitness. The seed model has (a, b, c)=$(1, 1.2, 0.833)$, which results in a rounded, slightly flattened core. The best F1 core lies in the small cluster slightly inside the lower wing, where $b < c < a$. Examination of the values shows that the core has (a, b, c)=$(1.09, 0.862, 1.06)$, which is very near the same shape as the original core, rotated 90° relative to the magnetic field. The best F2 model has the most flattened shape of the set, and still fails to account for the pattern of Test Core 3's polarization vectors. In fact, the polarization vectors show little difference than those of Solution 246.

While the RotateA parameters were (naturally) not consistent with the seed model values, we found that ϕ and i were largely unconstrained, yet PA was again tightly constrained between two equivalent angles. A comparison between the LOS views in Figures 6.39 and 6.48 shows the PA orientations for the seed model and Scenario 3B Solution 246 to be ∼90° to each other.

The density scale for Solution 246 was about five times the seed value, whereas the velocity dispersion produced a value of 0.84 km s^{-1}, reasonably close to the seed value. The polytropic profiles do not match even when scaled into Jy beam^{-1} cm^{-1}. The relationship between ρ_{out}

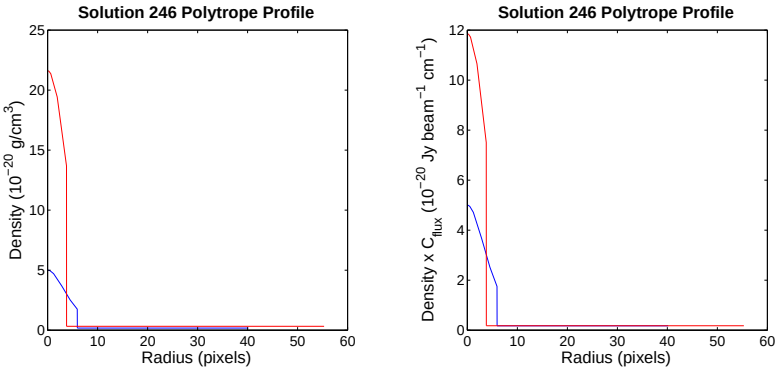

Figure 6.50: Solution 246 Polytrope Density Profiles. Scaled density profiles from Solution 246 (red) and the seed model (blue) POLY transformations.

and P_{out} observed in fits to non-twisted fields was evident in this Scenario. Examination of the best intensity solution, however, showed reasonable fits to all five polytrope parameters, ρ_0, σ_0 and C_{flux}, producing polytrope profiles that were a reasonable approximation to the seed model (Figure 6.50).

6.1.3.3 General Observations

Fitting the core with the appropriate model managed to produce a core with the appropriate amount of field twist. Additionally, the presence of the twist appeared to constrain the RotateA i and PA parameters better than the non-twisted geometries of Sections 6.1.1 and 6.1.2.

Fitting the core with the wrong field model showed that the solution set failed to reproduce the polarization pattern. However, solution with the best intensity fitness in the set managed to reproduce a core of the approximate shape, with the core's z-symmetry axis (and therefore initial field direction) rotated 90° relative to the Test Core 3 geometry.

It appears that PolCat is capable of detecting twisted field geometries, and ruling out non-twisted models in the presence of a twisted field.

	Seed	Scenario A	Scenario B
	–	# 38	# 246
F1	(0.496)	0.611	4.05
F2	(0.959)	0.953	2.25
χ^2_I	(1.02)	1.66	65.4
χ^2_{PA}	(0.920)	0.908	5.08
ρ_0 (g cm^{-3})	1×10^{-20}	1.39×10^{-20}	4.80×10^{-20}
σ_0 (km s^{-1})	0.8	0.745	0.832
c_{twist}	10	8.49	–
K	0.1	0.118	0.047
γ_{poly}	1	1.04	2.18
ρ_c	5	4.05	4.51
ρ_{out}	0.1	0.103	0.023
P_{out}	0.35	0.324	0.370
a_{scale}	1	1.21	1.34
b_{scale}	1.2	1.01	0.434
ϕ	45°	133.0°	10.2°
i	30°	29.6°	-6.7°
PA	20°	20.6°	116.1°
Δx (pix)	0	-0.009	-0.14
Δz (pix)	0	0.003	0.052
$C_{flux}{}^{\dagger}$	1	0.884	0.548

Table 6.4: Test Core 3 Results
†Jy beam^{-1} g^{-1} cm^2

6.1.4 Test Core 4: Prolate Triaxial Bonnor-Ebert Profile with LinearTwistS Field

Test Core 4 is generated with the basic5wLinTwistS template, which has the LinearTwistS transformation in place of LinearTwistA. The seed c_{twist} parameter is the same as for Test Core 3, and the Scale parameters have been changed to generate a "prolate" geometry in the direction of the magnetic field ($a = 0.8, b = 1$). Figures 6.51–6.53 show the test data polarization maps, seed residuals, and three-dimensional structure of the core. For this core, we wish to test: A) how well PolCat can reproduce the initial parameters, B) whether the core can be described adequately without the twist, and C) whether this pattern can be adequately reproduced with an asymmetric twist.

6.1.4.1 Scenario 4A: Basic Fit (basic5wLinTwistS)

Scenario 4A is the basic fit with the original generating template, in this case basic5wLinTwistS. The resulting merged trade-off surface is displayed in Figure 6.54. The fitness curve appears to be mostly confined between the F1 values 0.5 and 3, with one single solution out at F1=12.4. The outlying solution does not appear to have any significant advantage in F2 over the second-largest F1 value at F1=2.4. When we observe slices of the parameter space, we find that in most projections the merged solution set clusters into three groupings, two of which correspond to high F1 value. We select Solution 116 for analysis, and display its polarization maps, residuals, and three-dimensional views in Figures 6.55 – 6.57.

At a glance, the intensity map for Solution 116 (Figure 6.55, right) appears to match reasonably well with the Test Core 4 dataset. Examination of the fractional intensity residuals (Figure 6.56, left) seems to show a thin, faint ring of negative residuals corresponding to the core edges, in addition to a small cluster of negative residuals near the centre of the core. While the distribution of positive and negative residuals inside the core proper do not precisely match those of Test Core 4 in relation to its seed model (Figure 6.52), the overall background noise levels do fall into approximately the same range. The overall pattern of

Test Core 4 Seed Model Summary

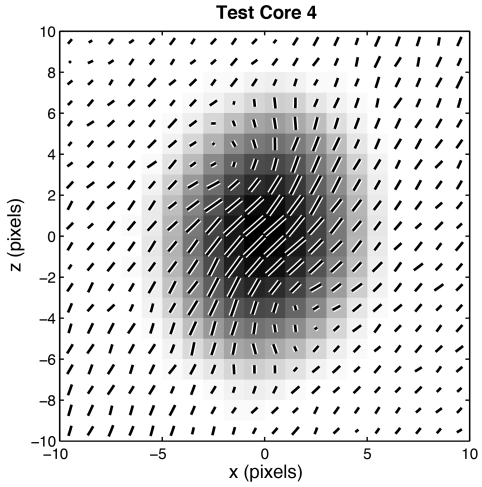

Figure 6.51: Test Core 4 Polarization Map. Includes noise. Vectors are scaled by $\sqrt{P_{flux}}$.

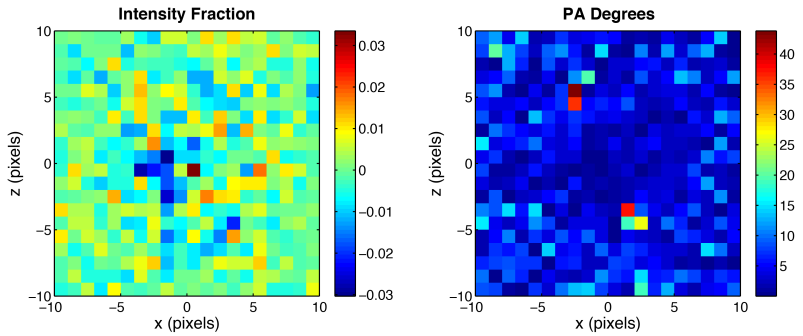

Figure 6.52: Test Core 4 seed Model Residuals. Residuals between the seed model and the test data map (Figure 6.51). Intensity residuals are presented as a fraction of $\bar{I}_{data}$=7.44 × 10^{-3} Jy beam^{-1}

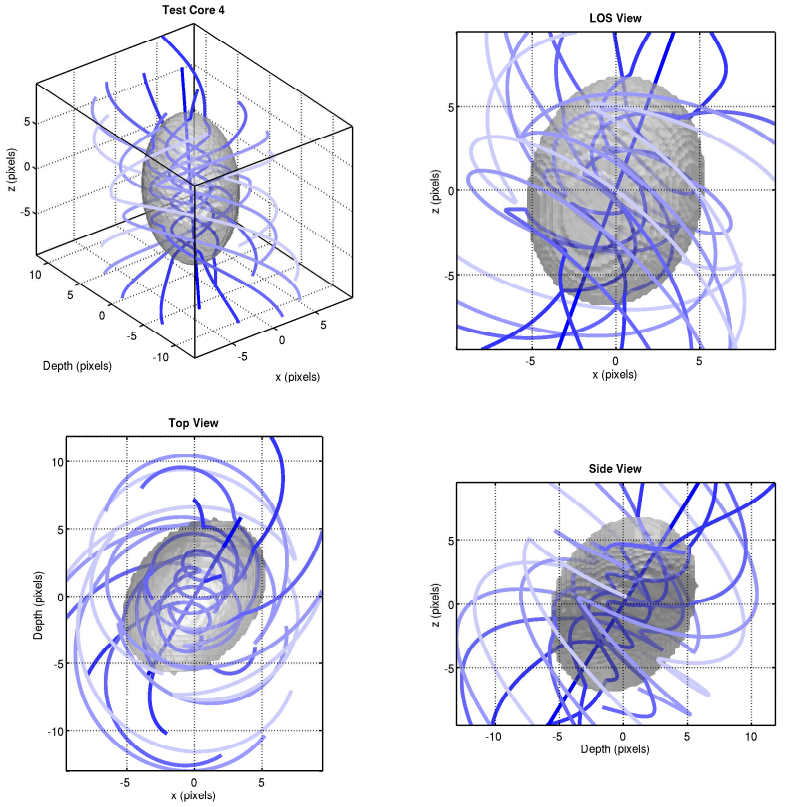

Figure 6.53: Three-Dimensional Structure of the Test Core 4 Seed Model.

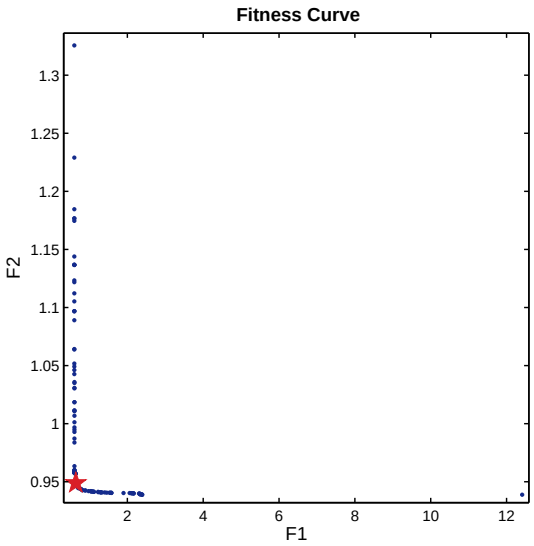

Figure 6.54: Test Core 4 Scenario A Trade-off Surface. The location of Solution 116 is indicated with a red star.

the polarization position angle residuals (Figure 6.56), is virtually indistinguishable from the corresponding Test Core 4 residual map, although one or two pixels in the enhancements at the top left and bottom right of the cores appear to have slightly smaller differences in angle than the Test Core.

The solution with the best c_{twist} value appears to have the worst polarization position angle fitness. The knee model itself selected a value of 7.58, although a comparison of Figures 6.57 and 6.53, shows that the appearance of the field lines does not appear much different in Solution 116 than in the seed model.

The density scale values for the set as a whole are high, with the smallest ρ_0 value at approximately 1.8×10^{-20} g cm^{-3}. The knee solution selected a value of 2.44×10^{-20} g cm^{-3}, more than double the seed value. The majority of the solutions selected values around the knee model value; interestingly these solutions are also tightly clustered around σ_0=0.8 km s^{-1}, whereas the rest of the solution set clustered around 0.5 and 0.76 km s^{-1}.

Figure 6.58 shows the polytrope profiles of the seed model and Solution 116. Scaling the polytrope density profiles into Jy beam^{-1} cm^{-1} lines up the edges of Solutions 116 and the seed model. However, the seed model profile has a slightly smaller central value than

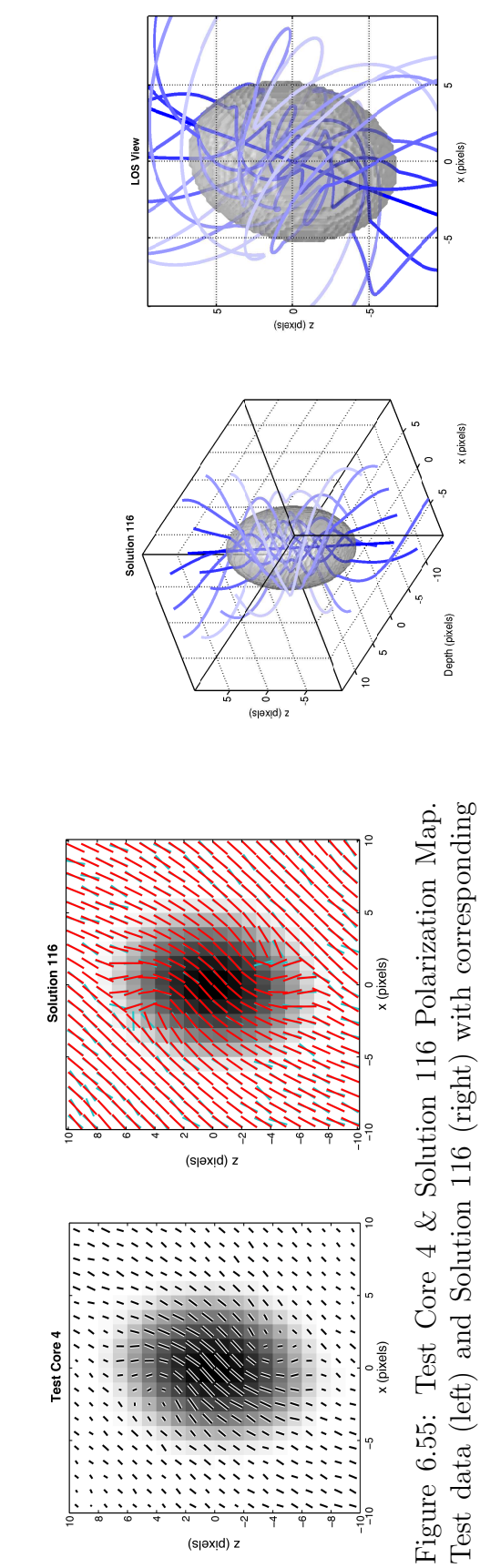

Figure 6.55: Test Core 4 & Solution 116 Polarization Map. Test data (left) and Solution 116 (right) with corresponding polarization vectors (red) overlain on the test data vectors (blue).

Figure 6.56: Solution 116 Residuals. Intensity (left) and χ_{pol} (right). Intensity residuals are presented as a fraction of $\bar{I}_{data}$=7.44 $\times 10^{-3}$ Jy beam^{-1}.

Figure 6.57: Three-Dimensional Structure of Solution 116.

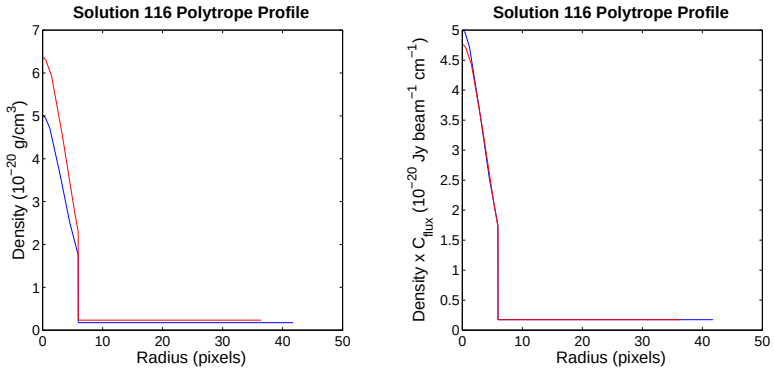

Figure 6.58: Solution 116 Polytrope Density Profiles. Scaled density profiles from the Solution 116 (red) and the seed model (blue) POLY transformations.

the original (4.75 to the seed value of 5 Jy beam^{-1} cm^{-1}). Although the Solution 116 core truncated at the correct radius, the polytropic index γ selected a value of 1.4, with a K of 0.083 and truncation pressure P_{out} at 0.24. The majority of the solutions appear to be clustered around these values, with a few outliers with $\gamma\sim$1.1 and $\sim$0.95, corresponding to the highest F1 values in the set.

The core shape was tightly constrained, with the entire solution set selecting solutions around the seed scale parameters of 0.8 and 1. As with Scenario 3C, the knee solution swapped the values for the a and b parameters and the RotateA angles have absorbed the 90° rotation relative to the seed model caused by the swap.

Examination of the RotateA parameters for the solution set as a whole shows PA selecting degenerate values of approximately 20° and 200°, i selecting values of approximately 30° and 150° and ϕ selecting values around 45° and 135°. In the i-PA slice of the parameter space, the solutions are again grouped in the three clusters mentioned previously (two clusters with $PA\sim$20°, one with 200°).

6.1.4.2 Scenario 4B: noTwistPoly (γ frozen)

This scenario was implemented to specifically test whether the S-shape of the polarization vectors could be adequately described without a twist. We applied a noTwistBE model with default parameters, excluding γ from the fit. The merged trade-off surface (Figure 6.59

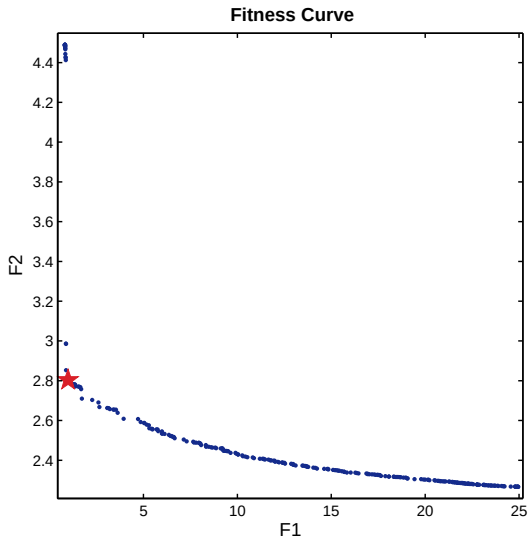

Figure 6.59: Test Core 4 Scenario B Trade-Off Curve. Solution 159 is indicated with a red star.

shows a clear knee at (0.987, 2.80), which selects Solution 159. We display its polarization maps, residuals, and three-dimensional views in Figures 6.60–6.62.

When viewing multiple projections of the parameter space, the distribution of solutions tended to fall into a nearly rectangular shape, without much clustering. Examination of all eight constituent solution sets shows that five of the runs tended to form clusters in the solution space tended to form clusters, while three did not. Four of the five runs that showed clustered parameters were from F-niching mode, with the fifth run (and the remaining three) in X-niching.

Examination of the Solution 159 polarization map (Figure 6.60) shows that, superficially at least, the intensity map appears to be reproduced. The fractional intensity residuals (Figure 6.61, left) show that the solution had an approximately 5–6% enhancement at the top left and bottom right edges compared to the test dataset. The model polarization vectors showed a pattern characteristic of an hourglass field oriented at approximately 50° (counter-clockwise) to the z-axis, which does not adequately describe the χ_{pol} angle outside of the top left and bottom right corners of the map, and a band running from the top right of the map to the bottom left (Figure 6.61, right).

Scenario 4B - noTwistPoly (γ frozen) Solution 159

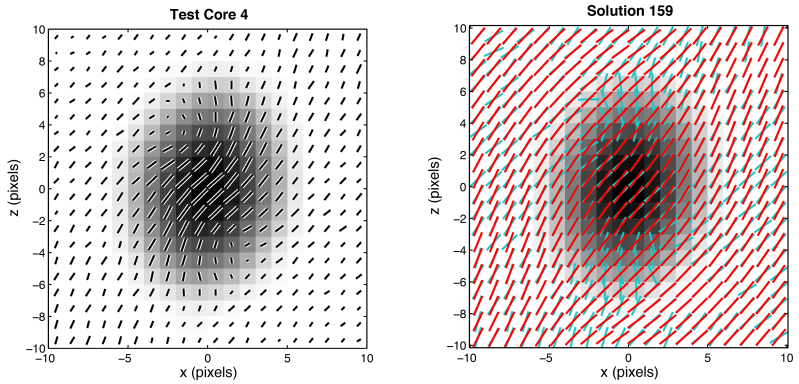

Figure 6.60: Test Core 4 & Solution 159 Polarization Maps. Test data (left) and Solution 159 (right) with corresponding polarization vectors (red) overlain on the test data vectors (blue).

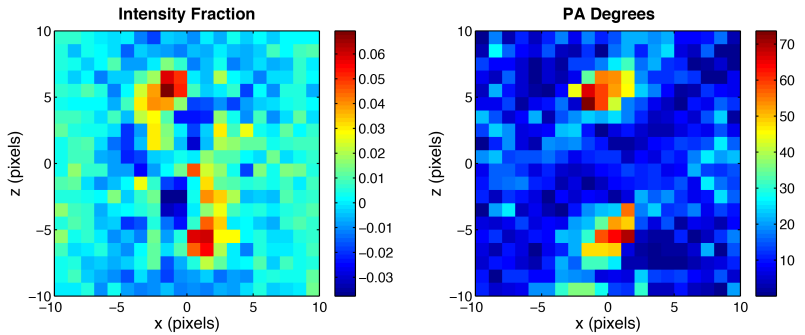

Figure 6.61: Solution 159 Residuals. Intensity (left) and χ_{pol} (right). Intensity residuals are presented as a fraction of $\bar{I}_{data}$=7.44 $\times$ 10^{-3} Jy beam^{-1}.

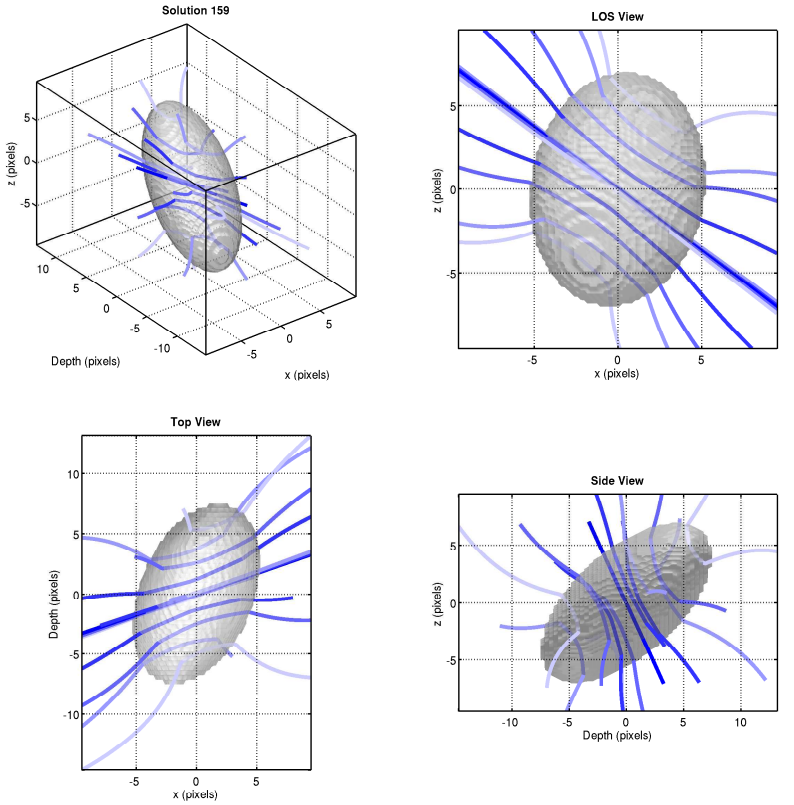

Figure 6.62: Three-Dimensional Structure of Solution 159.

The density scale and velocity dispersion were largely unconstrained, with the solutions occupying an almost rectangular region of the solution space, between $4.5 \times 10^{-21} < \rho_0 < 2.1 \times 10^{-20}$ g cm^{-3} and $0.46 < \sigma_0 < 1.2$ km s^{-1}. The knee solution itself appeared to lock onto the correct area of the parameter space, at 0.951×10^{-20} g cm^{-3} and 0.841 km s^{-1}. C_{flux} values typically ranged from 0.77 to 1.6 Jy beam^{-1} g^{-1} cm^2, with the knee solution selecting 0.8 Jy beam^{-1} g^{-1} cm^2.

The POLY parameters for the knee solution, with the exception of ρ_c, are well-fitted to the seed model values. Once the polytrope density profiles were scaled into Jy beam^{-1} cm^{-1} the large discrepancy in the profile's central density was reduced to nearly match the seed model. The overall distribution of the four non-frozen parameters was not well-constrained, with K taking a range of values from 0.03 to 0.24, and ρ_c from approximately 3-9$\times\rho_0$. Truncation pressure varied from approximately 0.13 to 0.35$\times$ and external density from 0.1 to 0.2$\times\rho_s$.

The results showed that PolCat was unable to reproduce the shape in this circumstance, with most of the cores selecting disks severely flattened parallel to the field direction. The knee model itself selected a shape elongated perpendicular to the field (Figure 6.62). In the shape map for the merged set (Figure 6.63, left), this solution falls in the lower wing, where $b < c < a$, with $(a, b, c) = (1.56, 0.69, 0.92)$. When we examined the best intensity fitness solution, we found that it selected a shape with $(a, b, c) = (1.27, 1.00, 0.78)$, which is the approximate shape of Test Core 4, rotated 90° about the x-axis. This is the same behaviour of the best F1 solution of Scenario 3C.

We find that the polarization pattern for a core with a symmetrically twisted magnetic field cannot be replicated with a non-twisted field model. Additionally, the knee solution for this scenario was also flattened perpendicular to the field direction, a situation similar to the knee solution of Scenario 3B.

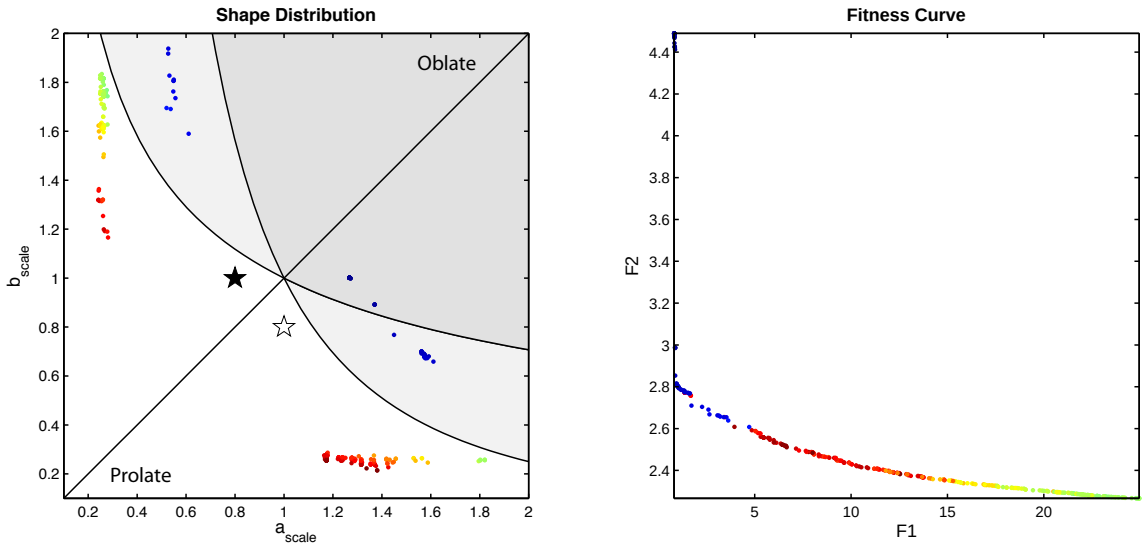

Figure 6.63: Scenario 4B Shape Map. Points coloured by c value (left), with corresponding Fitness Curve with the solutions coloured the same way for reference (right). The black star represents the seed values of a and b, and the white star represents the symmetrically equivalent values.

6.1.4.3 Scenario 4C: basic5Component (γ frozen)

In this case we were specifically testing whether we could reproduce the distinctive LinearTwistS S-pattern with a LinearTwistA transformation. To that end, we applied a basic5BE (frozen $\gamma = 1$) template to Test Core 4. The resulting merged trade-off surface is shown in Figure 6.64. The trade-off surface has an obvious knee, and we have made the selection of Solution 27 for analysis.

The polarization map for Solution 27 appears to replicate the shape of the intensity map accurately from Figure 6.65. However, the corresponding fractional residual map (Figure 6.66, left) shows that the model is too bright by approximately 7–8% $\bar{I}_{data}$ in a narrow band running through the centre at an angle of approximately 30°–40° to the horizontal, and too faint at the top and bottom of the map by approximately 4–5% $\bar{I}_{data}$. The polarization vectors and χ_{pol} residuals (Figure 6.66, right) show that the LinearTwistA twist is unable to account for the deflection in polarization angle at the top and bottom of the core caused by the symmetric twist.

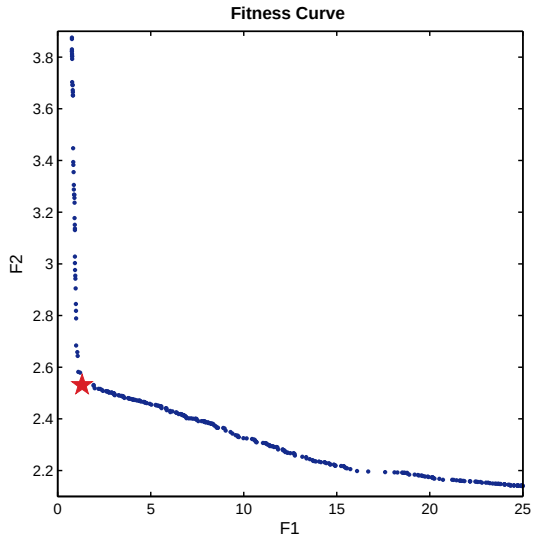

Figure 6.64: Test Core 4 Scenario C Merged Trade-Off Surface. The red star indicates Solution 27.

From the three-dimensional views of the model (Figure 6.67), the field is very tightly twisted. An examination of the entire merged solution set shows that the c_{twist} parameter took a range of values between 14.5 and 100. The solutions with F1 less than 7 had c_{twist} values between 54–100, resulting in cores with fields more twisted than we can consider physical.

The shape map for the merged set (Figure 6.68) did not cluster around the seed a or b values (or equivalent symmetry values) and were instead spread in a long line from approximately $(0.6, 1.4)$ to $(1.4, 0.6)$. However, on this line, several solutions did get close. The knee solution falls almost exactly on the $a = c < b$ line, at $(a, b, c) = (1.15, 0.757, 1.15)$, making an oblate spheroid with the short axis perpendicular to the field.

6.1.4.4 General Observations

The basic fit with the LinearTwistS model selected a c_{twist} value slightly smaller than the seed model. However, comparison of the three-dimensional seed model views to those of the Scenario 4A knee model shows little noticeable difference between the appearance of the magnetic fields. We note that the reduced chi-squared for χ_{pol} (recorded as χ^2_{PA} in Table

Scenario 4C - basic5Component (γ frozen) Solution 27

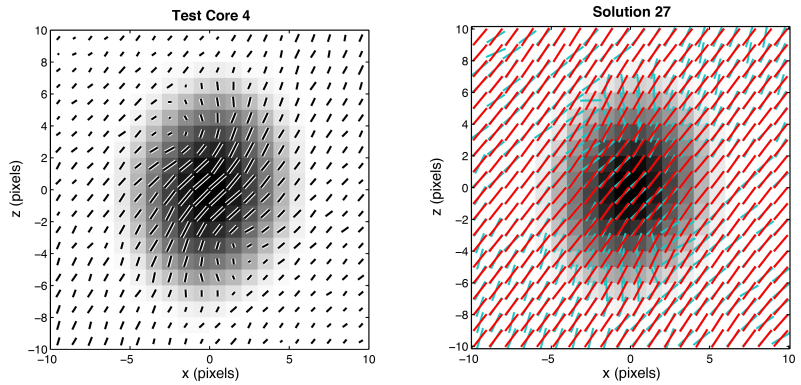

Figure 6.65: Test Core 4 & Solution 27 Polarization Maps. Test data (left) and Solution 27 (right) with corresponding polarization vectors (red) overlain on the test data vectors (blue).

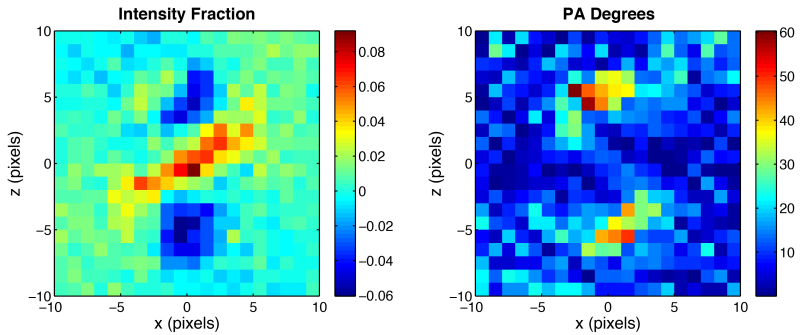

Figure 6.66: Solution 27 Residuals. Intensity (left) and χ_{pol} (right). Intensity residuals are presented as a fraction of $\bar{I}_{data}$=7.44 $\times$ 10^{-3} Jy beam^{-1}.

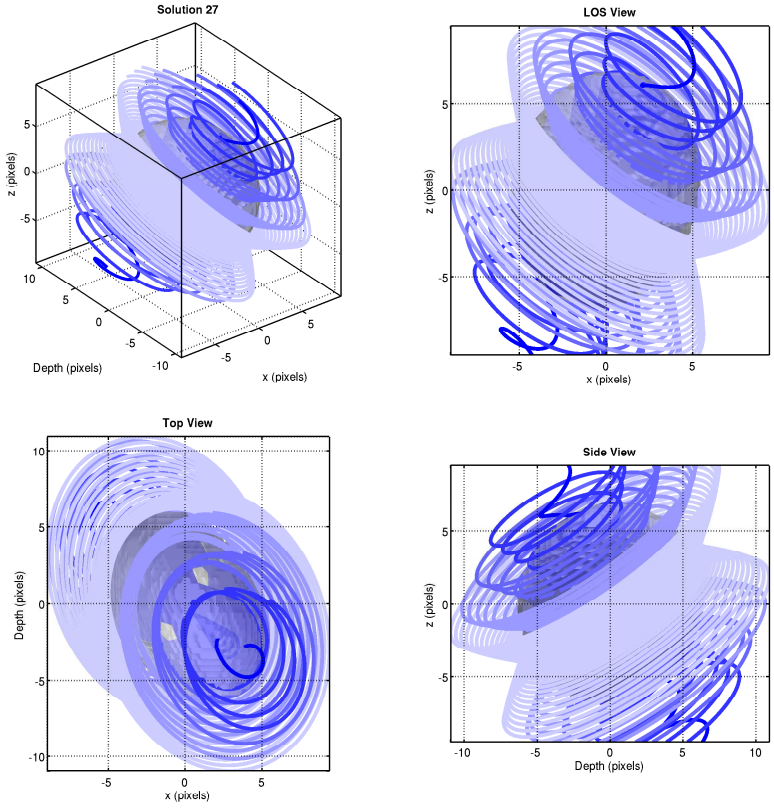

Figure 6.67: Three-Dimensional Structure of Solution 27.

	Seed	Scenario A	Scenario B	Scenario C
	–	# 116	# 159	# 27
F1	(0.555)	0.641	0.987	1.31
F2	(0.952)	0.949	2.80	2.53
χ^2_I	(1.23)	1.62	4.317	6.27
χ^2_{PA}	(0.907)	0.900	7.859	6.41
ρ_0 (g cm^{-3})	1×10^{-20}	2.44×10^{-20}	9.51×10^{-21}	7.93×10^{-21}
σ_0 (km s^{-1})	0.8	0.798	0.841	0.452
c_{twist}	10	7.58	–	94.84
K	0.1	0.0832	0.106	0.225
γ_{poly}	1	1.39	1*	1*
ρ_c	5	2.61	6.35	4.97
ρ_{out}	0.1	0.102	0.104	0.114
P_{out}	0.35	0.245	0.335	0.310
a_{scale}	0.8	1.01	1.56	1.15
b_{scale}	1	0.799	0.692	0.757
ϕ	45°	132.6°	129.1°	233.8°
i	30°	28.6°	-15.4°	-155.4°
PA	20°	20.2°	306.6°	207.6°
Δx (pix)	0	-0.001	0.002	-0.009
Δz (pix)	0	-0.002	-0.001	0.012
C_{flux} †	1	0.748	0.818	1.28

Table 6.5: Test Core 4 Results
*Parameter Frozen to Value
†Jy beam^{-1} g^{-1} cm^2

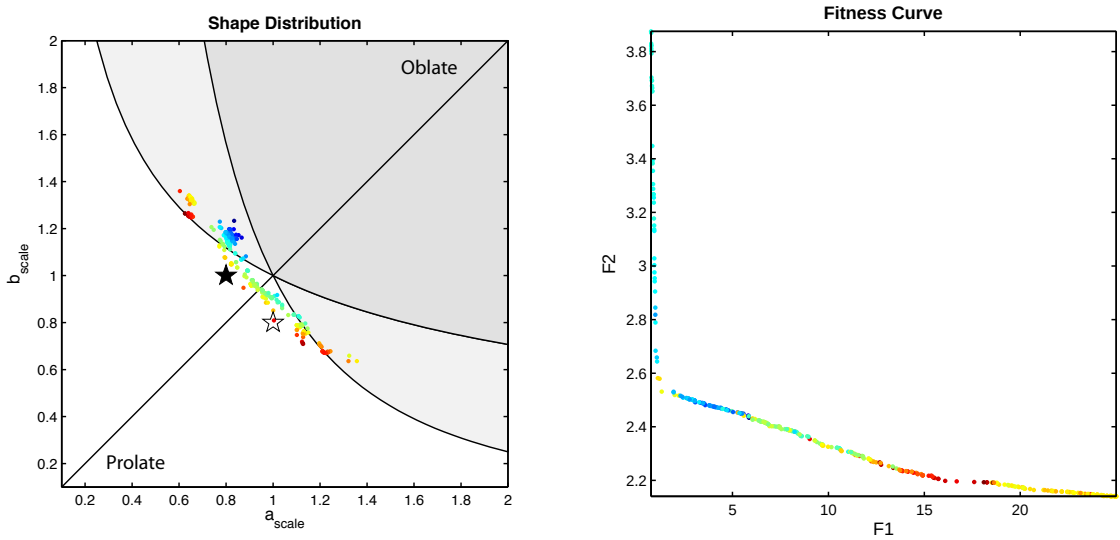

Figure 6.68: Scenario 4C Shape Map. Solutions coloured by c value (left), with corresponding Fitness Curve coloured the same way for reference (right). The black star represents the seed values of a and b, and the white star represents the symmetrically equivalent values.

6.5) shows a smaller value than the seed model. This may indicate that we have a similar situation to the Test Core 1 results, where the noise in the dataset may have caused changes to the polarization pattern characteristic of a slightly different model.

One obvious conclusion from the Test Core 4 results is that the polarization pattern LinearTwistS transformation cannot be replicated without a twist, or even by a model with a LinearTwistA field. Attempting to use either incorrect geometry produces model polarization maps that describe the LinearTwistS map inadequately. In addition, trying to use a LinearTwistA transformation to fit a model generated with LinearTwistS results in cores with fields that are far too twisted to be physical.

6.1.5 Discussion

One common finding for every scenario was that the scaling parameters C_{flux}, ρ_0, and POLY parameter ρ_c were poorly constrained individually, but better-constrained as $C_{flux} \times \rho_0 \times \rho_c$. Polytrope profiles that matched the seed profiles poorly became properly aligned when scaled by C_{flux}. As this replicates the step performed to scale the polarization maps into Jy beam^{-1},

this result is not entirely unexpected. Overall, the selection of C_{flux} for a particular model appears to be motivated by the amount the density profile must be scaled to match the level of emission, and the C_{flux} and ρ_0 value for each solution are tightly connected. However, at present we cannot take the approach of combining these into one parameter as we still require density to be separate for scaling purposes. Nevertheless, it does make a convincing argument for revisiting PolCat's scaling method, and suggesting an approach where either ρ_0 or C_{flux} are set and excluded from the fit.

The polarization position angle objective appears to constrain the RotateA i and PA parameters better than the intensity map, although i is constrained more tightly when the intensity map is generated from a solution that is not radially symmetric. For a perfectly symmetric density profile, the polarization vectors will reproduce accurate PA, but the model selection i will be affected by noise.

It is possible that scale parameters a and b add further degeneracy into rotation angle ϕ due to the scale parameters being interchangeable when the core is rotated 90° about the z-axis. Theoretically, in addition to the angles ϕ, 180°-ϕ, 180°+ϕ, and 360°-ϕ we should also be seeing 90°-ϕ, 90°+ϕ, 270°-ϕ, and 270°+ϕ corresponding to models with a and b values switched relative to the seed model. However, our selection of 45° for the seed model ϕ value may possibly be masking this. Overall, the test results show that the 90° rotation about the z-axis implied by flipped a and b parameters are absorbed into the RotateA parameters. Further tests with a variety of seed RotateA parameters are needed to explore the full degeneracy in this system.

These test results appear to show that removing polytropic index γ from the fit has mixed results. While there appears to be some marginal improvement in some parameters, the results also show that removal causes other parameters to become even less constrained.

Results from fitting twisted fields with non-twisted models (Sections 6.1.3.2, 6.1.4.2) show that if a significant twist is present in the data, the polarization pattern cannot be reproduced with a non-twisted field. Similarly, it appears that the characteristic S-shape of

the LinearTwistS vectors cannot be reproduced with a LinearTwistA transformation. The results suggest that choosing the wrong twist symmetry for a dataset will likely result in solution sets filled with unphysical models. However, since we generated each of our test datasets with the same c_{twist} and rotation parameters, more testing is required before we can prove this definitively for models with smaller or larger field twists at different orientations. However, our current results suggest that PolCat can definitively detect the magnetic field's twist symmetry.

6.2 SCUPOL Legacy Catalogue Data

Here we discuss fits to the DR21-M, OMC1, and RCr A regions. Our selection of DR21-M and OMC1 are mainly motivated by their regular shapes and relatively ordered field vectors. We also selected RCrA, despite its more disordered field vectors and bean-like shape, due to the polarization pattern appearing to have the approximate S-shape typical of a symmetrically twisted field. Each model's merged solution set is composed of the results of eight separate fits to the data, split evenly between X- and F-niching modes.

In the tables summarizing our results, we have recorded raw, uncorrected density scales from the PolCat fit as ρ_0, and corrected density scales as ρ_0^* (§5). The raw ρ_0 values have been included in the tables for completeness; any discussion of density scales and core mass computations in the body of the text will use the FCF^*-corrected density scale ρ_0^*.

6.2.1 DR21-Main

DR21 Main has the most ordered field of any core in the current sample, with orderly field vectors showing a clear two-dimensional hourglass when its B-vectors are traced (Kirby, 2009). For the purposes of our modelling, we designated the cropped dataset for this region "dr21-2."

Figure 6.69 shows the data cropped to the size we use in the fit. As with the test datasets,

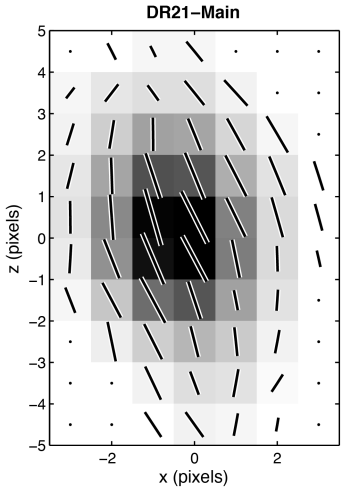

Figure 6.69: Cropped DR21-M Dataset. Vectors are scaled by $\sqrt{P_{flux}}$.

we have performed a total of eight fits to each model with the runs split evenly between X- and F-niching modes. Upon completion the runs were merged into a single set to map the Pareto front as efficiently as possible. We fit three templates to this dataset: noTwistPoly (§4.4.1), basic5Component (§4.4.2), and basic5Component_MOD1 (§4.4.4). The results are summarized in the following sections.

6.2.1.1 Model 1: noTwistPoly

The trade-off curve produced by merging the eight runs with the noTwistPoly template is presented in Figure 6.70. Solutions that best balance the objective functions are usually located near the "knee" of the trade-off surface; however, there is no convincing knee in this case. Post-Merge, the trade-off surface is nearly linear, making the location of the "knee" difficult to find as there is no sharp change in curvature. In such cases, we would usually pick solutions from the middle of the curve to try and find an acceptable balance between the two objectives. However, as the intensity fitness value F1 ranges between ∼3–24.5, choosing a solution in this manner yields a model core with an extremely poor fit to the DR21-M intensity map (F1∼10). As we cannot expect a reasonable model of DR21-M to be a poor match in intensity, we opt to choose our "knee" solution after pre-selecting a region of the

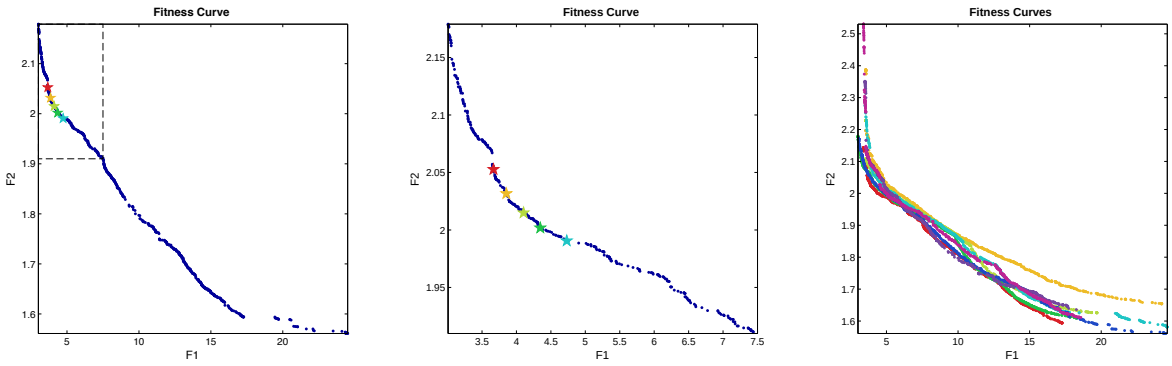

Figure 6.70: DR21-M: noTwistPoly Trade-off Surfaces. Left: merged surface from the noTwistPoly runs. Centre: Merged trade-off surface zoomed in on the rectangular region with the bottom right corner at (7.5, 1.91). The parameters of the solutions indicated with stars are summarized in Table 6.6 in order of increasing F1 value. Right: Trade-off surfaces from all eight constituent runs.

fitness curve that contains reasonable intensity models.

The Pareto front appears to undergo a sharp turn downwards at the point $(7.5, 1.91)$. At this point the intensity residuals begin degrading past the point usability for the model. The rectangle in the left side of Figure 6.70 shows the part of the curve bounded by this point, which serves as the axis limits for the plot on the right. With these new limits, we can see that the region of the curve between $(3.6, 2.05)$ and $(5, 2)$ forms a broad knee-like region. Examination of trade-off surfaces from all eight constituent runs (Figure 6.70, right) shows that this was the approximate knee region for the the runs as a whole.

The choice of any particular solution within this region is not extremely important, as all of the solutions in the knee area fall inside the exact same cluster in each projection of the parameter space. Indeed, averaging the individual parameters for every solution within the knee region shows standard deviation on each individual Ferret parameter to be reasonably well-constrained. However, for parameters such as ρ_0 and K, where the corresponding Ferret parameters are fit logarithmically, the standard deviation on the true values were of course much larger. Parameter values from five solutions spaced across the knee region, and shown as coloured stars in 6.70, are shown in Table 6.6. An examination of the polytrope profiles associated with each solution has shown that they are all consistent in terms of peak shape,

	# 203	# 37	# 142	# 104	# 44
F1	3.67	3.85	4.10	4.35	4.73
F2	2.05	2.03	2.01	2.00	1.99
ρ_0 (g cm^{-3})	1.11×10^{-20}	1.06×10^{-20}	1.08×10^{-20}	1.07×10^{-20}	1.06×10^{-20}
σ_0 (km s^{-1})	0.951	0.946	0.947	0.952	0.953
K	0.351	0.348	0.350	0.353	0.349
γ_{poly}	0.864	0.875	0.874	0.870	0.872
ρ_c	9.61	9.58	9.55	9.57	9.53
ρ_{out}	0.194	0.196	0.193	0.195	0.194
P_{out}	0.0945	0.0946	0.0945	0.0948	0.0946
a_{scale}	0.789	0.791	0.790	0.788	0.789
b_{scale}	1.466	1.468	1.489	1.473	1.469
ϕ	80.5°	77.8°	77.4°	79.5°	79.4°
i	146.7°	147.0°	147.5°	145.8°	145.6°
PA	255.5°	255.7°	255.9°	256.2°	256.1°
Δx	-0.389	-0.398	-0.398	-0.390	-0.381
Δz	0.072	0.045	0.008	-0.001	-0.014
C_{flux}*	1.07	1.08	1.08	1.08	1.08

Table 6.6: DR21-M Knee Solution Comparison. Parameters from five solutions approximately equally spaced along the knee region.
*Jy beam^{-1} g^{-1} cm^2

truncation radius, and external and central densities. As such, for simplicity in analysis we have chosen solution # 142 (middle solution in Figure 6.70) to represent the knee.

Figure 6.72 shows residuals for Solution 142. For all models in the set, the region of poorest intensity fit is along the southeastern[1] edge of the core. Comparing the polarization maps of the source and the knee model (Figure 6.71), we can see that there is a faint dip in brightness along the southeastern edge of the data intensity map, as though the material had been pushed slightly up and to the right. Overall, the intensity residual maps shows that the residuals values typically within 10% of the mean data intensity.

The χ_{pol} residuals show that the area of worst fit is at the northeastern corner of the map, where the source vectors are the most disordered. Overall, the position angle residuals typically fall around $\sim$15° or less, with the greatest congruence occurring on the edges of the core, as can also be seen in Figure 6.71. There appears to be a small, consistent misalignment

[1]Astronomical images are displayed with North pointing up and East to the left.

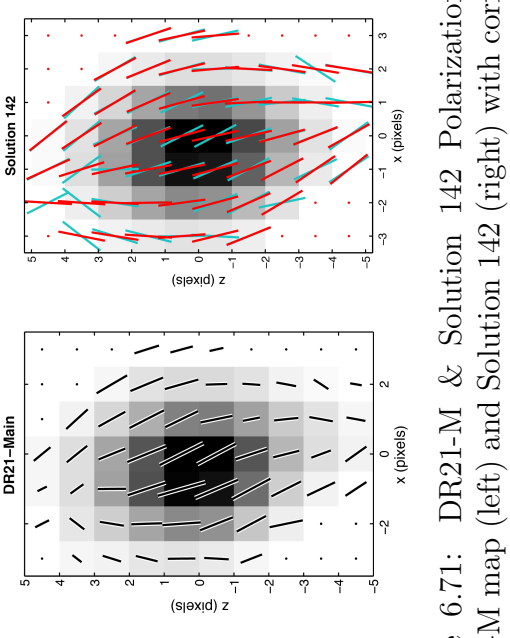

Figure 6.71: DR21-M & Solution 142 Polarization Maps. DR21-M map (left) and Solution 142 (right) with corresponding polarization vectors (red) over the DR21-M vectors (blue).

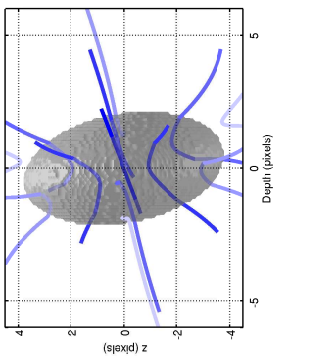

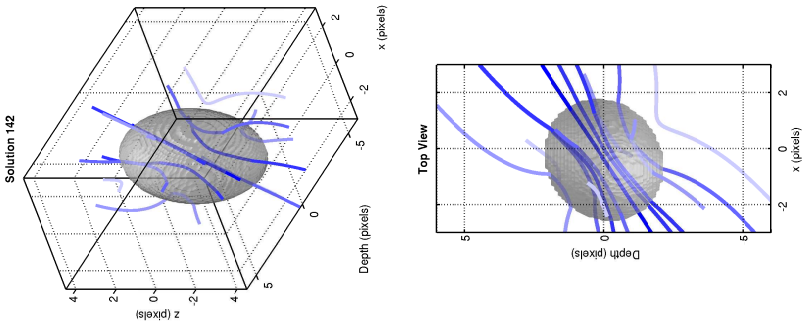

Figure 6.73: Three-Dimensional Structure of Solution 142. The density isosurface represents $\rho_s = 1.38 \times 10^{-18}$ g cm^{-3}.

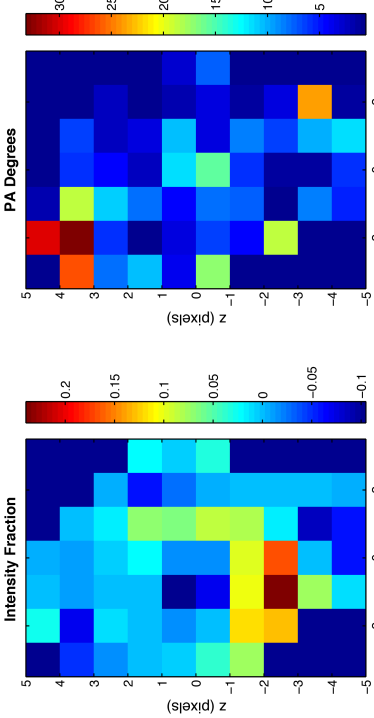

Figure 6.72: Solution 142 Residuals. Intensity (left) and χ_{pol} (right). Intensity residuals presented as a fraction of $\bar{I}_{data}$=3.43 Jy beam^{-1}.

DR21-M - noTwistPoly Solution 142

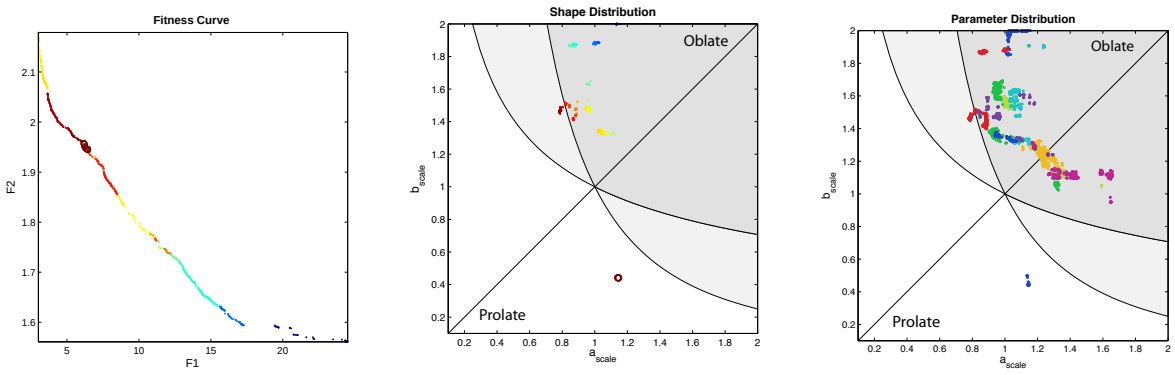

Figure 6.74: DR21-M: noTwistPoly Shape Maps. Left: Figure 6.70 with each solution colour-coded according to $c = 1/ab$ value. Centre: Corresponding shape map (§4.3.4). The empty circles on the graph had c values much larger than the majority and were thresholded to better show the value distribution. Right: Shape map for all eight constituent runs

between the source and model vectors towards the core centre. This behaviour is present in all models in the set, including the solution with the best F2 value at $(24.5, 1.56)$.

From the results of the rotation transformation and the three-dimensional core model (Figure 6.73), accounting for the degeneracy in the orientation angles, the core is oriented with a PA of $\sim 75°$ to the z-axis, and the magnetic field symmetry axis is inclined $\sim 60°$ to the line of sight.

If DR21-M had no twist to the magnetic field, we would expect the core to have contracted preferentially parallel to the magnetic field direction. Overall, we can see from the shape map for the merged solution set (Figure 6.74, centre) the solutions that have the lowest intensity fitness (F1) appear to favour triaxial cores with the shortest axis parallel the initial magnetic field, with the best solutions for intensity closest to the a=b (true oblate) line. The best solutions for position angle (F2) appear to favour cores with the shortest c value and longest b. Although the majority of the cores in the solution set fall in the oblate portion of the plot, the solutions that comprise the knee lie mostly at the edge of the $a = c < b$ curve, with the result that they are approximately prolate perpendicular to the field direction. The cluster of elongated-z cores in the bottom half of the figure correspond to a small cluster of solutions just inside of the zoomed-in region mentioned previously. Looking at the spread

of solutions from all eight runs (Figure 6.74, right) shows that the knee solutions are almost exclusively from a single run. The majority of the other seven runs shows a "W"-like spread across the a=b line in the oblate region of the plot.

We compute the mass by performing a rough summation of the three-dimensional density multiplied by the physical volume of one grid voxel. For the knee region, we compute masses of approximately 10 700 $M_\odot$ within the core truncation radius, and 20 100 $M_\odot$ for the cube as a whole.

We do not rule out this model as a possible geometry for DR21-M. However, the shape of the core is not what we would expect from gravitational contraction in the presence of a uniform magnetic field. The knee model has chosen an approximately prolate geometry with the long axis aligned perpendicular to the field direction. As a result there is an equivalent amount of contraction along the field lines as there is perpendicular to them. We would generally expect the both symmetry axes perpendicular to the magnetic field to be larger than the axis lying along the magnetic field. We move on to exploring the results of adding a twisted component to the magnetic field geometry.

6.2.1.2 Model 2: basic5Component

The merged solution set for the basic5Component runs (Figure 6.75, left) has two sharp, well-defined knees over a much smaller range of intensity fitness values than the noTwistPoly runs. The first knee occurs at $(3.15, 1.9)$ (Solution 133), and the second falls at $(4.1, 1.82)$ (Solution 258). Upon examination of the constituent trade-off surfaces (Figure 6.75, right), it becomes apparent that this first knee (and the section of the curve above it) are part of a single run, and that the other 7 runs have knees at approximately the same F1 value as the second knee. As such, we will examine solutions from both. We have summarized their parameters in Table 6.7. Solution 133 polarization map, residuals, and three-dimensional structure are shown in Figures 6.76–6.78. The corresponding figures for Solution 258 are Figures 6.79–6.81.

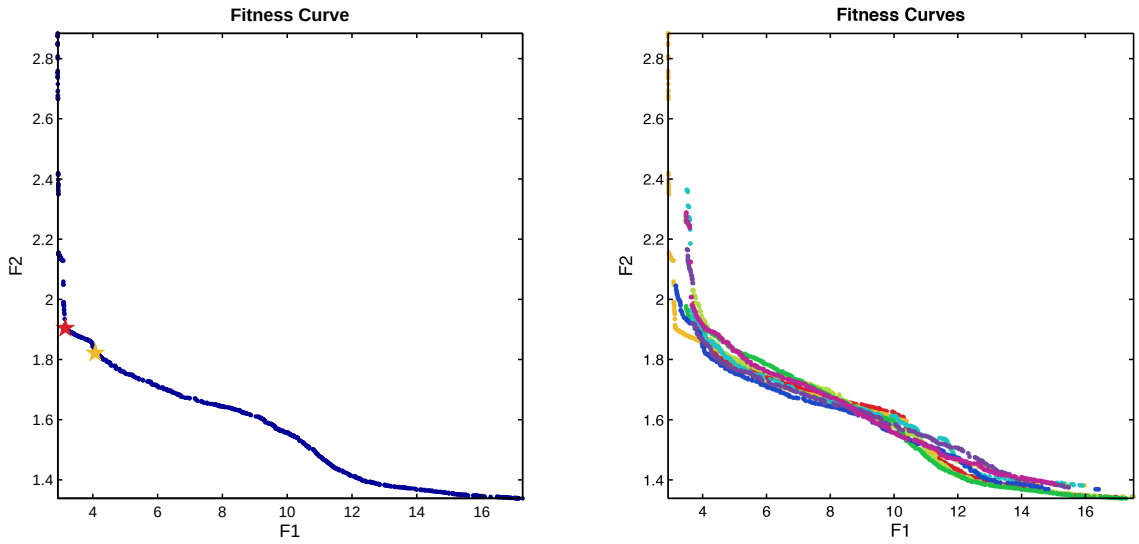

Figure 6.75: DR21-M: basic5Component Trade-off Surfaces. The merged solution set (left), with stars representing Solutions 133 (red) and 258 (orange) along with its eight constituent runs (right)

An examination of the intensity residuals shows a smaller range of values than for the noTwist case, with Solution 133 showing a similar enhancement along the lower left edge. Solution 258 does not show this behaviour, but shows two diagonal bands of negative residuals at the top and bottom of the core where the model was not able to accommodate the data. The χ_{pol} residuals for Solution 142 of the noTwistPoly model and both solutions 133 and 258 show a similar distribution of residuals, with the largest discrepancy at the top and bottom. Solutions 133 and 258 do show a similar misalignment of approximately 15° in a band beginning from the lower left edge of the map towards the centre, whereas the noTwist model only shows this behaviour in the centre.

A three dimensional plot of Solution 133 (Figure 6.78), shows the core to be significantly flattened perpendicular to the field direction, with the magnetic field inclined ∼50° to the line of sight. A similar analysis of Solution 258 (Figure 6.81) shows that its field is inclined ∼56° to the line of sight, with the core flattened along the field direction. All solutions in the merged set have values for the twist constant c_{twist} at ∼0.02–0.1, which produces such a minimal twist that it has a negligible effect on the model. To explore whether this is due to a

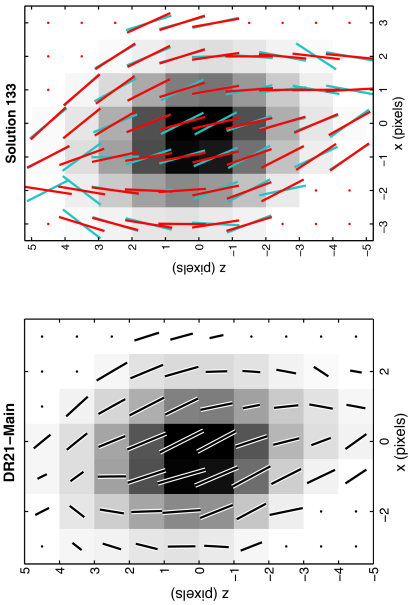

Figure 6.76: DR21-M & Solution 133 Polarization Maps. DR21-M map (left) and Solution 133 (right) with corresponding polarization vectors (red) over the DR21-M vectors (blue).

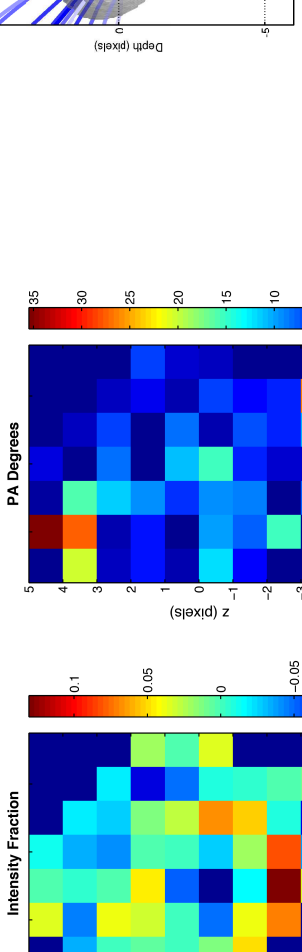

Figure 6.77: Solution 133 Residuals. Intensity (left) and χ_{pol} (right). Intensity residuals are presented as a fraction of $\bar{I}_{data}$=3.43 Jy beam^{-1}.

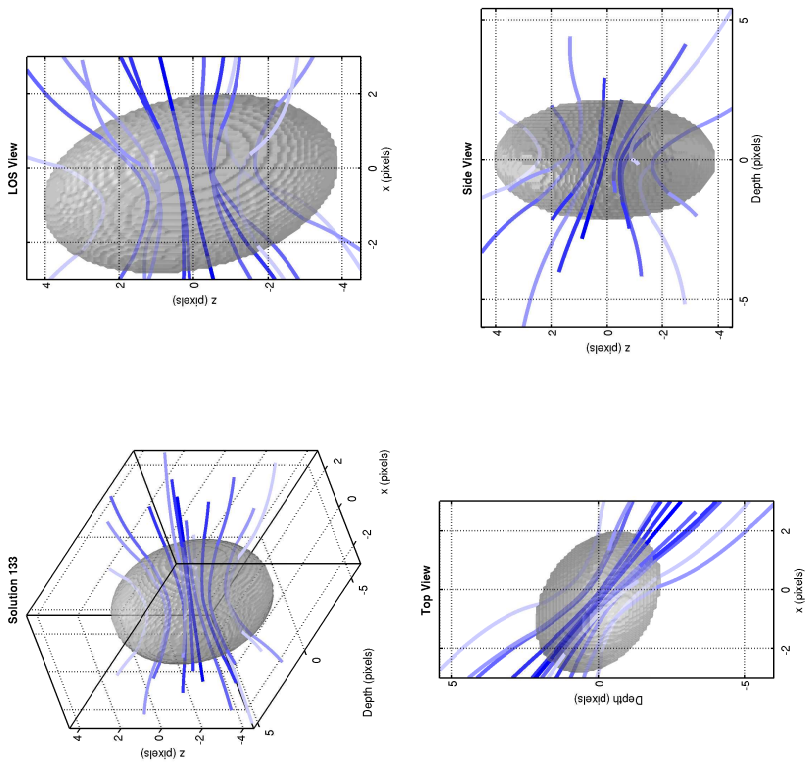

Figure 6.78: Three-Dimensional Structure of Solution 133. The density isosurface represents ρ_s=7.45 $\times$ 10^{-19} g cm^{-3}.

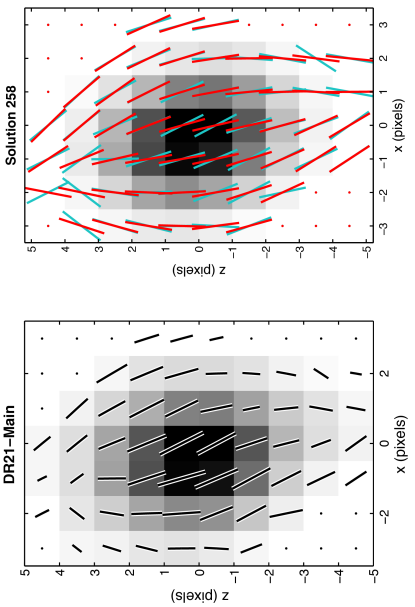

Figure 6.79: DR21-M & Solution 258 Polarization Maps. DR21-M map (left) and Solution 258 (right) with corresponding polarization vectors (red) over the DR21-M vectors (blue).

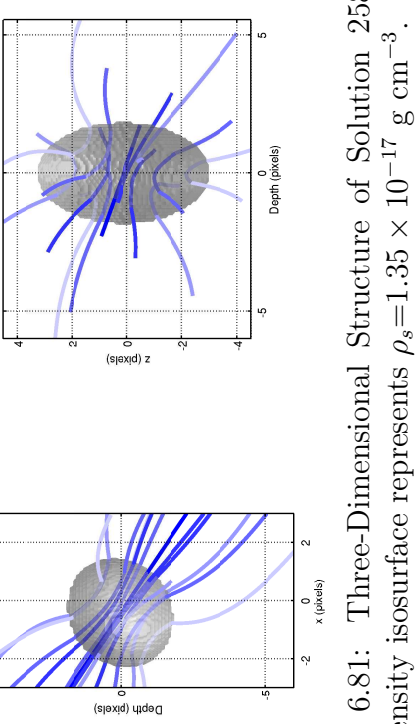

Figure 6.81: Three-Dimensional Structure of Solution 258. The density isosurface represents ρ_s=1.35 $\times$ 10^{-17} g cm^{-3}.

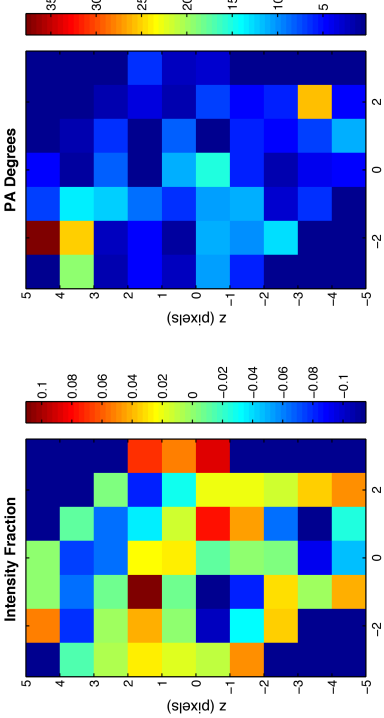

Figure 6.80: Solution 258 Residuals. Intensity (left) and χ_{pol} (right). Intensity residuals presented as a fraction of $\bar{I}_{data}$=3.43 Jy beam^{-1}.

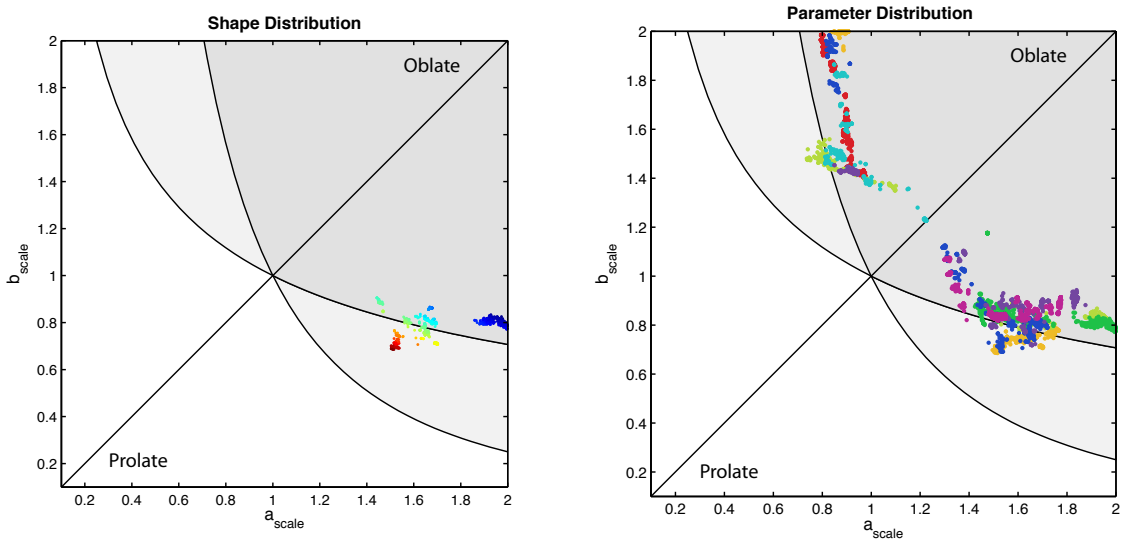

Figure 6.82: DR21-M: basic5Component Shape Maps. (§4.3.4) Merged set (left) and all constituent runs (right)

twist not actually being present in the core field or whether this is an effect of the logarithmic mapping of the c_{twist} parameter, we have applied another model where the twist constant is allowed to vary linearly. The results of fitting with the new model will be discussed in the following section.

The shape plot for the merged set (Figure 6.82) shows a similar distribution of solutions to the noTwistPoly case, reflected across the $a = b$ line. Examination of the rotation transformation components between this merged set and the noTwistPoly set of the last section shows a difference of $(n+1)\pi/2$ between the preferred ϕ parameters of the two sets, which is consistent with this result. The solutions of the first knee are clustered within the bottom wing of the shape map, whereas the solutions that comprise the second are clustered along the $b = c > a$ line, again showing preference for prolate cores with their long axes perpendicular to the field direction. When we examine the shape map for all runs (Figure 6.82, right), we see the solutions spread out across the spheroid line in a "W"-shape as with the noTwistPoly model. The main difference between these runs and the noTwist runs is that the majority of these solutions appear to be clustered on the edges of the W, which are closer to the $a = c$ and $b = c$ curves.

Integrating the mass within the truncation radius, we obtain a corrected mass of ∼8900 $M_\odot$ for the first knee, and ∼64 900 $M_\odot$ for the second. We note that the C_{flux} for Solution 258 is ∼1/10 that of Solution 133, therefore it is likely that the high density of this solution is compensating for low C_{flux}.

Comparing the polytrope profiles of the solutions from the two knees, we find that the central density of the solution at the second knee is approximately six times of that at the first knee. We also note that the two cores truncate at slightly different pixel radii, which is consistent with the appearance of their polarization maps. Once we multiply the polytrope profile by the C_{flux} value, we see that the central values in Jy beam^{-1} cm^{-1} are much closer in value, meaning the main component that separates the models at the two knees is the difference in C_{flux} and ρ_0.

6.2.1.3 Model 3: basic5Component_MOD1

This model differs from the basic5Component model in that LinearTwistA's c_{twist} parameter is fit linearly, POLY parameters ρ_{out} and P_{out} are fit logarithmically, and the limits on ρ_c are loosened to the range 1–320. This last attribute allows for a larger initial volume of gas to be contracted to form the final core. This template should generate a twisted field if the low c_{twist} of the basic5Component model results was an artifact of the logarithmic fit.

Overall, the intensity fitness values are on par with those from the previous two models, with the location of the primary knee being in approximately the same location in the fitness space. This model also shows a slight double-knee feature, where the trade-off surface makes a sudden dip at approximately $(8, 1.75)$ into a section that also shows knee behaviour, although at too high an F1 value to be useful. Further analysis shows that the merged set is largely comprised of a single run (henceforth the primary run), which also has the double-knee appearance. We select Solution 113 for in-depth analysis, and summarize its parameters in Table 6.7. The Solution 113 polarization map, residuals, and field structure are shown in Figures 6.84–6.86.

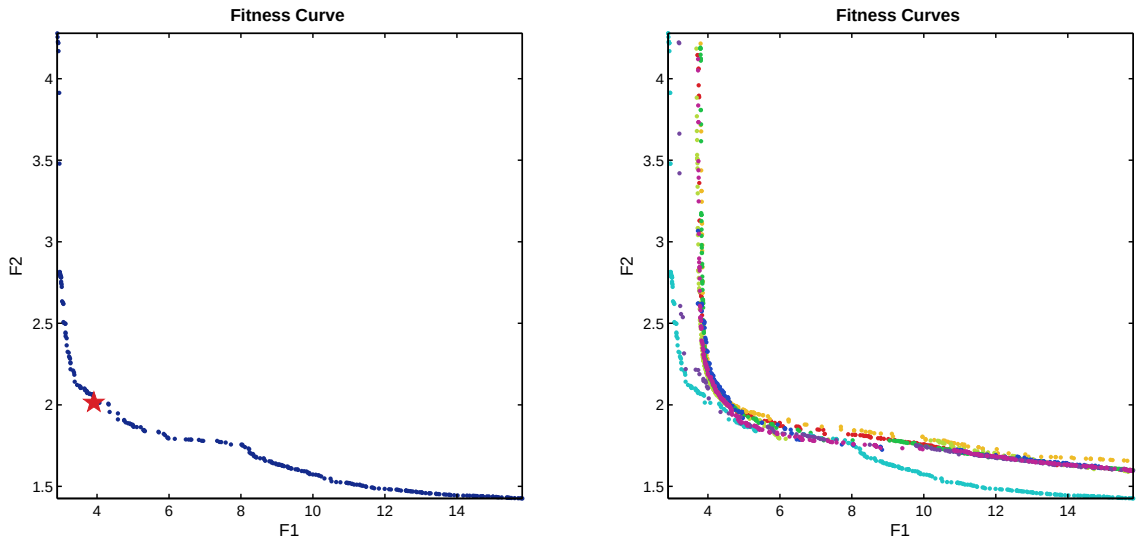

Figure 6.83: DR21-M: basic5Component_MOD1 Trade-off Surface. Left: Merged solution set with red star indicating Solution 113. Right: All eight constituent runs. The solution sets in the right figure have maximum values of F1=25 and F2=14.7; the figure has been zoomed to show the same limits as the merged set.

Residuals for intensity (Figure 6.85, left) show the residuals to be within 10–15% of the mean data value, with the model map having values mostly higher than the data. The χ_{pol} residuals again show the largest discrepancy at the northeast and southwest corners of the map and approximately 15° misalignment in the vectors in the centre region.

Examination of the shape plot (Figure 6.87) for the merged set shows the solutions split between a cluster on the $a = c$ line, as with the noTwist runs (and basic5Component runs by symmetry), and two clusters in the prolate region mirrored on either side of the $a = b$ line. This behaviour is also present in the shape plot for the primary run. Comparison to the fitness curve shows the solutions that comprise the $a = c$ cluster lie on the second dip of the fitness curve, which also have a much higher initial density scale: $\sim 7.0 \times 10^{-20}$ g cm^{-3} versus ~ 1–4×10^{-21} g cm^{-3} for the area of the curve with F1 < 8.

The range of ρ_c values extended almost to the full extent of its limits, ranging between approximately 45–320. The knee solution selected a ρ_c of 89.2, which was typical of solutions with the lowest F1 fitness values. Within the truncation radius, we find a mass of 10 400

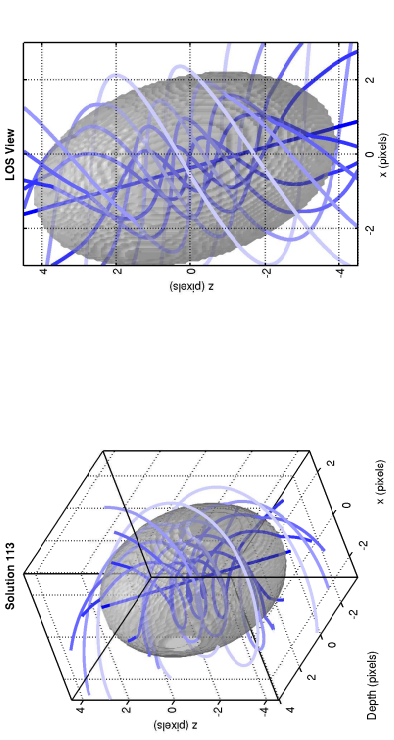

Figure 6.86: Three-Dimensional Structure of Solution 113. The density isosurface represents ρ_s=7.02 $\times$ 10^{-19} g cm^{-3}.

DR21-M - basic5Component_MOD1 Solution 113

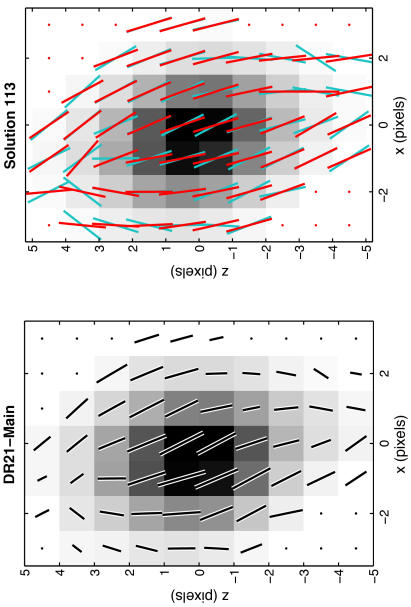

Figure 6.84: DR21-M & Solution 113 Polarization Maps. DR21-M map (left) and Solution 113 (right) with corresponding polarization vectors (red) over the DR21-M vectors (blue).

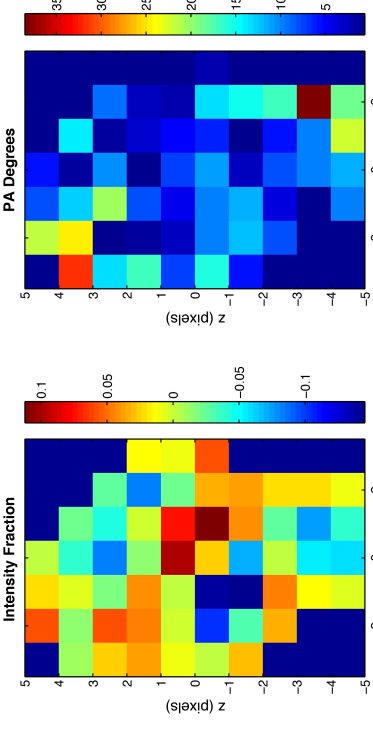

Figure 6.85: Solution 113 Residuals. Intensity (left) and χ_{pol} (right). Intensity residuals presented as a fraction of $\bar{I}_{data}$=3.43 Jy beam^{-1}.

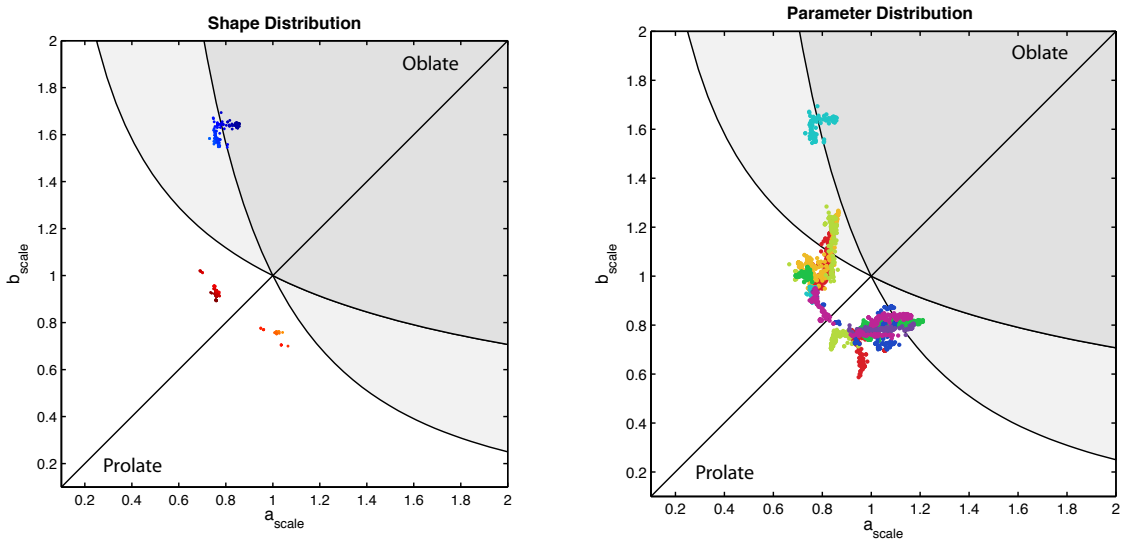

Figure 6.87: DR21-M: basic5Component_MOD1 Shape Maps. Merged data coloured by $c = (ab)^{-1}$ value (left), and all eight runs (right) with each run in a different colour.

$M_\odot$, with a mass of 18 900 $M_\odot$ for the cube as a whole, consistent with the noTwistPoly results, and Solution 133 of the basic5Component results.

An interesting result is that the presence of a twist in the field led PolCat to favour models prolate along the field direction over the perpendicular cores favoured by the low twist runs. This is consistent with the core being squeezed and confined by the helical field, as in the models of Fiege and Pudritz (2000d).

6.2.1.4 General Observations

When we examine all three trade-off surfaces, we can see that while all models are consistent in terms of F1, the F2 values vary wildly. The basic5Component model appears to have the advantage, with the location of the primary knee closest to the origin. However, as the twist on the magnetic field in these models is minuscule to the point of negligibility, it is effectively a noTwist model. We note that with the logarithmic c_{twist} parameter, the twist is never allowed to completely vanish (i.e. $c_{twist} > 0$ always). Therefore, it is possible that the very slight twist is responsible for the improvement. Another possibility is that the basic5Component runs simply found better values for the parameters shared with noTwistPoly. Removing the

	noTwistPoly	basic5Component		basic5Component_MOD1
	# 142	# 133	# 258	# 113
F1	4.10	3.15	4.08	3.91
F2	2.01	1.90	1.82	2.01
χ^2_I	848	428	691	450
χ^2_{PA}	4.06	3.62	3.32	4.06
ρ_0 (g cm^{-3})	1.08×10^{-20}	2.01×10^{-20}	3.58×10^{-19}	2.32×10^{-21}
ρ_0^* (g cm^{-3})	2.16×10^{-18}	4.02×10^{-18}	7.16×10^{-17}	4.64×10^{-19}
σ_0 (km s^{-1})	0.95	0.74	0.96	0.94
c_{twist}	–	0.06	0.03	6.14
K	0.35	0.33	1.91	0.32
γ_{poly}	0.87	1.09	1.16	0.91
ρ_c	9.55	4.60	1.62	89.2
ρ_{out}	0.193	0.302	0.159	0.363
P_{out}	0.094	0.030	0.082	0.025
a_{scale}	0.790	1.509	1.457	0.755
b_{scale}	1.489	0.690	0.883	0.955
ϕ	77.4°	182.2°	0.7°	33.5°
i	147.5°	-141.2°	33.0°	-1.5°
PA	255.9°	256.5°	256.7°	164.6°
Δx (pix)	-0.398	-0.411	-0.414	-0.406
Δz (pix)	0.017	0.088	0.135	0.143
$C_{flux}{}^{\dagger}$	1.08	1.28	0.151	1.14

Table 6.7: DR21-Main: Model Parameter Summary
†Jy beam^{-1} g^{-1} cm^2

twist parameter from the list and generating a noTwistPoly model from Solution 133's other parameters yields fitness values of $(3.15, 2.07)$ with reduced χ^2 of $(414, 4.30)$. Therefore, the source of this difference is likely a combination of the two possible reasons stated previously.

All three models showed a misalignment in the polarization vectors at the core centre. However, as the size of the map is small, we suggest that this may be due to some fine structure present in the core that is lost at the current resolution.

The characteristic model of the noTwistPoly template showed a core with nearly prolate geometry, with the long axis of the core oriented at 90° to the field symmetry axis. This was a behaviour we observed in Test Core Scenarios 3B (§6.1.3.2) and 4B (§6.1.4.3), where a test core with a twisted field was fit with a non-twisted field model.

A mass for DR21-M of 20 000 $M_\odot$ with a mean density of 4.4×10^{-19} g cm^{-3} determined by Kirby (2009) was computed over an area of 1 pc in radius around the core, which is much larger than our grid. To obtain mass values for proper comparison, We extended the grid to a larger size, setting the density outside the original grid to ρ_{out}, and summed the mass in the enlarged cube within a radius of 1 pc on the plane of the sky. Using this method, we obtain masses of approximately 1) 31 900 $M_\odot$ with a mean density ($\bar{\rho}$) of 3.85×10^{-19} g cm^{-3}, 2) 26 800 $M_\odot$ with a $\bar{\rho}$ of 3.23×10^{-19} g cm^{-3} for Solution 133 and 2.36×10^5 $M_\odot$ with a $\bar{\rho}$ of 2.87×10^{-18} g cm^{-3} for Solution 258 , and 3) 30 100 $M_\odot$ with a $\bar{\rho}$ of 3.67×10^{-19} g cm^{-3}. These masses are range from 1.1–9.4× the Kirby (2009) estimate.

The limits on C_{flux} shift we use are based on Fiege et al. (2004), and were derived from the conditions in the G11.11-0.12 filament in Johnstone et al. (2003), and may be of a different range in the DR21-Main core. Following the analysis of Johnstone et al. (2003) we substituted the effective beam size of our maps and the temperature value of ∼25 K deduced by Kirby (2009) into the C_{flux} equation ((equation (4.28))$^{-1}$) and found that the conditions in DR21-M require C_{flux} to be ∼5.14–7.08 Jy beam^{-1} g^{-1} cm^2 for these conditions. To correct our fits using this C_{flux}, we require the pixel values of the I (and Q and U) maps to remain constant. If we factor out the scaling from equations (4.24), (4.25), and (4.26) we

find that, in general, the quantity $C_{flux} \times \rho_0$ must remain constant for this to be true. As such, we can make the expansion:

$$C_{flux} \times \rho_0 = \left(C_{flux} \times \frac{C'_{flux}}{C_{flux}} \right) \times \left(\frac{C_{flux}}{C'_{flux}} \times \rho_0 \right) = C'_{flux} \times \rho'_0, \tag{6.5}$$

where C'_{flux} is the new C_{flux}, and $\rho'_0 = \rho_0 \times C_{flux}/C'_{flux}$ is the corrected density scale. The C_{flux}-corrected densities and their corresponding masses are therefore on the order of $20 - 30\%$ of the values found by Richardson et al. (1989) and Kirby (2009). We suggest one possible source of discrepancy may be due to the size of our three-dimensional model along the line of sight. The extent of the cloud along the line of sight may be larger than accounted for in the depth of our grid. actually be more intervening material along the line of sight outside the bounds of the cube that is not counted because of the cube's size.

6.2.2 OMC1

We have cropped the OMC1 map shown in Figure 5.4 to exclude the fainter southern core (Orion S (Coppin et al., 2000)) for our PolCat fits. The result is shown in Figure 6.88. For this dataset we applied the same three templates we applied to DR21-M: noTwistPoly (§4.4.1), basic5Component (§4.4.2), and basic5Component_MOD1 (§4.4.4). The results are summarized in the following sections.

6.2.2.1 Model 1: noTwistPoly

The fitness curve produced from merging all eight runs with the noTwistPoly template is shown in Figure 6.89. The curve shows a sharp bend at $(14.3, 6.61)$, and we select Solution 255 near the bend for analysis. We summarize its parameters in Table 6.8.

The intensity map (Figure 6.90) shows poor agreement with the data. The dark central region of the model map shows a more extended morphology than the compact central region of OMC1. The fractional intensity residuals (Figure 6.91, left) confirm this, showing that

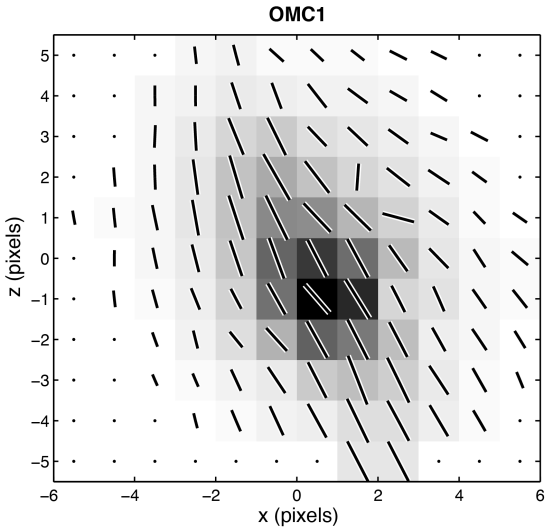

Figure 6.88: Cropped OMC1 Dataset. Vectors are scaled by $\sqrt{P_{flux}}$.

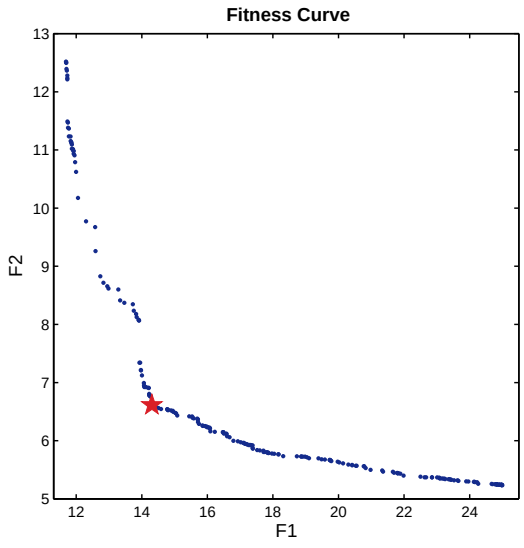

Figure 6.89: OMC1: noTwistPoly Trade-Off Curve. Solution 255 indicated by a red star.

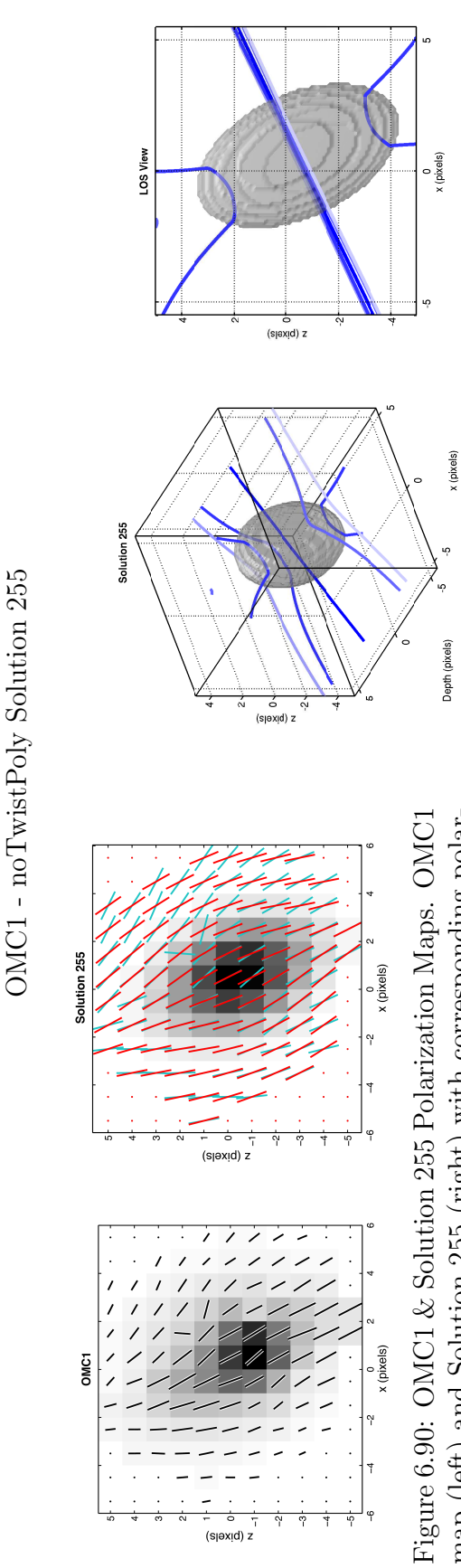

Figure 6.90: OMC1 & Solution 255 Polarization Maps. OMC1 map (left) and Solution 255 (right) with corresponding polarization vectors (red) over the OMC1 vectors (blue).

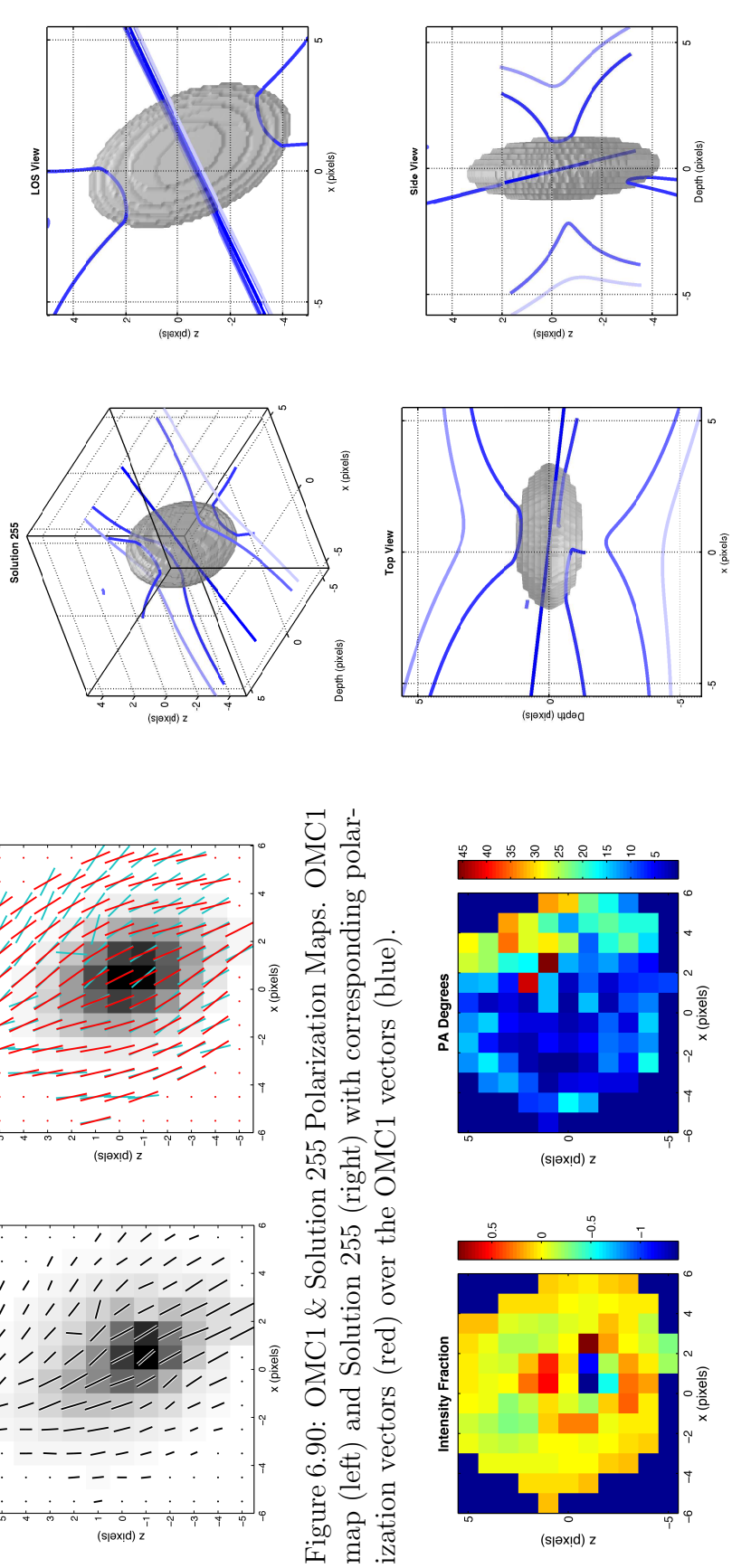

Figure 6.92: Three-Dimensional Structure of Solution 255. The density isosurface represents ρ_s=2.46 $\times$ 10^{-16} g cm^{-3}.

Figure 6.91: Solution 255 Residuals. Intensity (left) and χ_{pol} (right). Intensity residuals presented as a fraction of $\bar{I}_{data}$=12.4 Jy beam^{-1}.

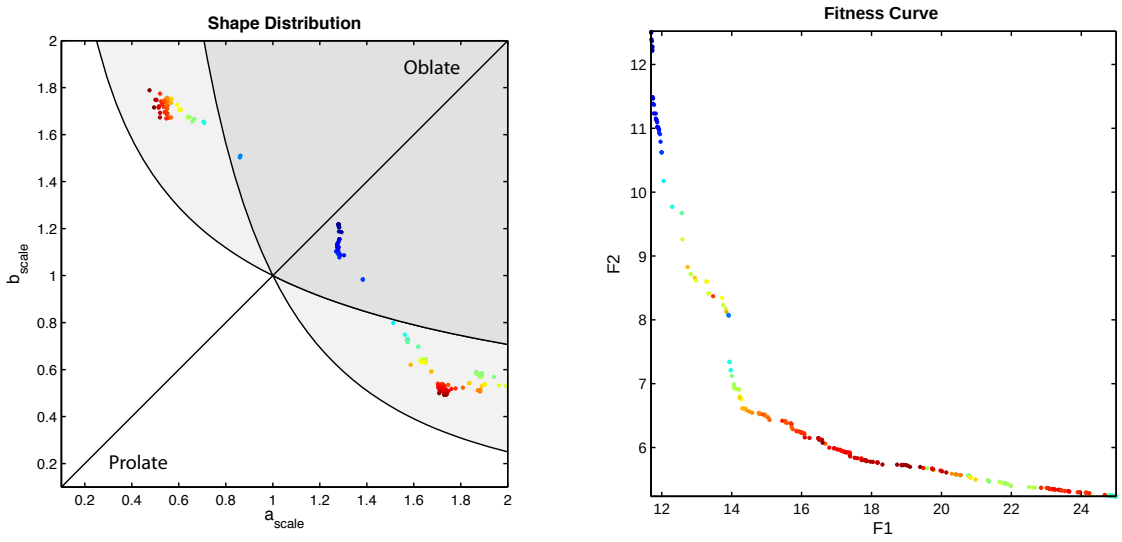

Figure 6.93: OMC1: noTwistPoly Shape Map. Solutions coloured by $c = (ab)^{-1}$ value. The solutions in fitness curve (right) are coloured identically for comparison.

the peak model emission fails to account for the brightest pixels in the OMC1 map, and the pixels in the model map surrounding this region are too bright.

The vectors in Figure 6.90 and the χ_{pol} residuals (Figure 6.91, right) show a large-scale misalignment of field vectors on the western edge of the core. This misalignment is present for all solutions in the set, including the solution with the best F2 value.

The three-dimensional views of Solution 255 (Figure 6.92) show the core to be a very flattened pellet-like shape with its shortest axis perpendicular to the field, and the field pointing approximately 84° to the line of sight at a PA equivalent to ∼65°. The distribution of core shapes (Figure 6.93) follows a broad arc, starting at the top wing, arcing through the oblate region, and down into the bottom wing. The knee solution itself falls in the top wing, where $a < c < b$.

The range of density scales spans two orders of magnitude from 10^{-17}–10^{-15} g cm^{-3}, and the velocity dispersion σ_0 shows a range of values from approximately 0.65–1 km s^{-1}. The range of C_{twist} values falls between approximately 0.4–2 Jy beam^{-1} g^{-1} cm^2. Polytrope central densities were also poorly constrained, spanning a range of values from approximately 4–10. Polytropic index γ selected a range of values between 0.64–2.8, with the solutions

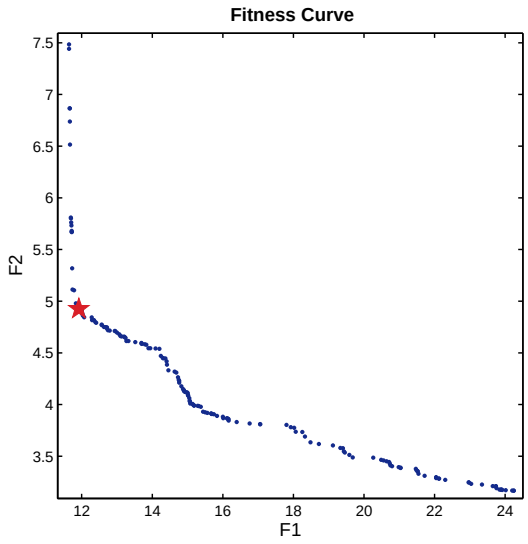

Figure 6.94: OMC1 basic5Component: Trade-off Curve. Red star indicates Solution 210.

comprising the knee falling in a cluster between $\gamma = 0.64$–0.75 with K values of approximately 2. Integrating the mass within the truncation radius gives a core mass estimate of 3400 $M_\odot$, and 5980 $M_\odot$ for the model cube as a whole.

Overall, this particular geometry appears unlikely. As magnetic fields do not exert force on material moving parallel to the field, we would expect that for a uniform initial field the core would be flattened along the field direction. The fact that the model core is flattened perpendicular to the field direction to such a large extent is an unlikely geometry. We conclude that noTwistPoly is insufficient to model this region, and we turn to models that include a twist.

6.2.2.2 Model 2: basic5Component

The merged basic5Component solution set is shown in Figure 6.94. The trade-off curve shows a clear knee at approximately $(5, 12)$; an improvement over the noTwistPoly results. We select Solution 210 at $(11.9, 4.93)$ for analysis and summarize its parameters in Table 6.8.

While the central region of Solution 210's intensity map (Figure 6.95) is less extended than

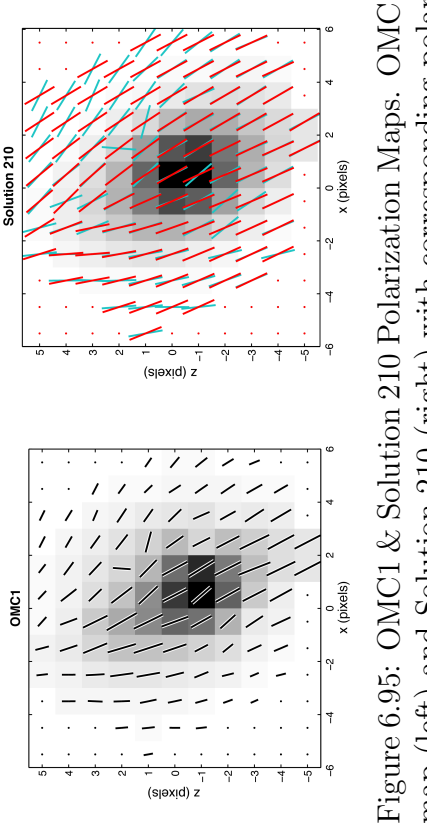

Figure 6.95: OMC1 & Solution 210 Polarization Maps. OMC1 map (left) and Solution 210 (right) with corresponding polarization vectors (red) over the OMC1 vectors (blue).

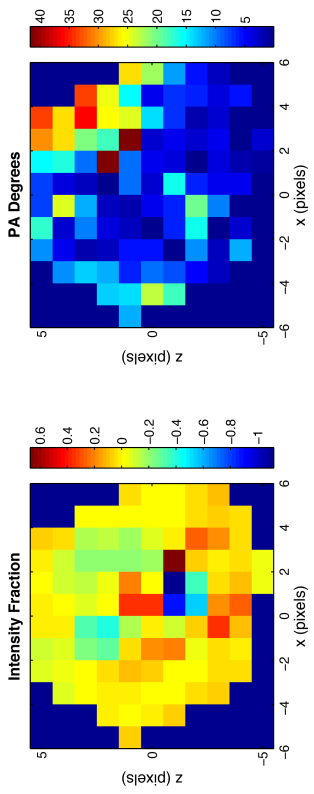

Figure 6.96: Solution 210 Residuals. Intensity (left) and χ_{pol} (right). Intensity residuals presented as a fraction of $\bar{I}_{data}$=12.4 Jy beam^{-1}.

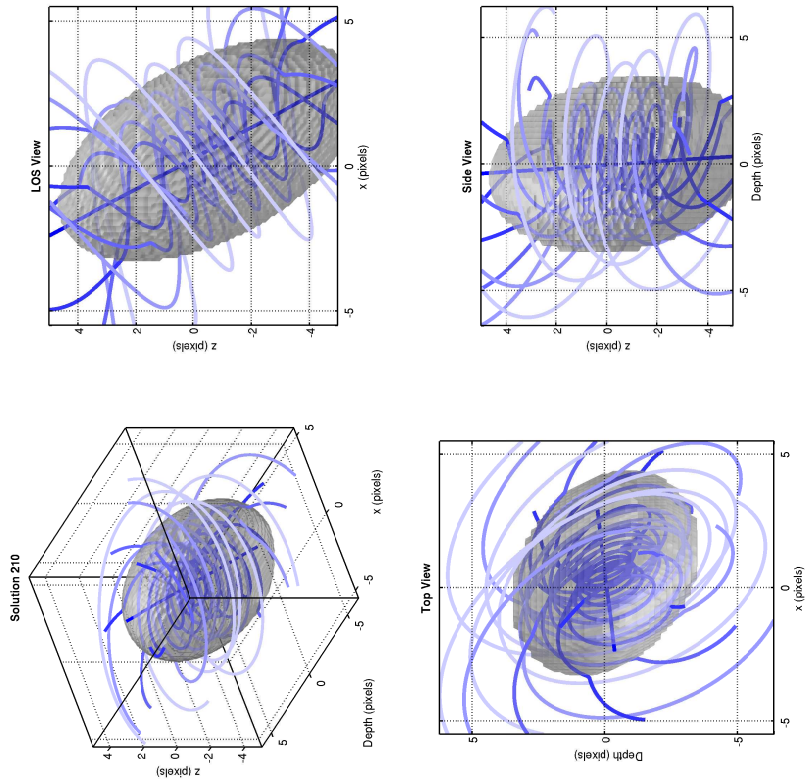

Figure 6.97: Three Dimensional Structure of Solution 210. The density isosurface represents ρ_s=1.45 $\times$ 10^{-17} g cm^{-3}.

OMC1 - basic5Component Solution 210

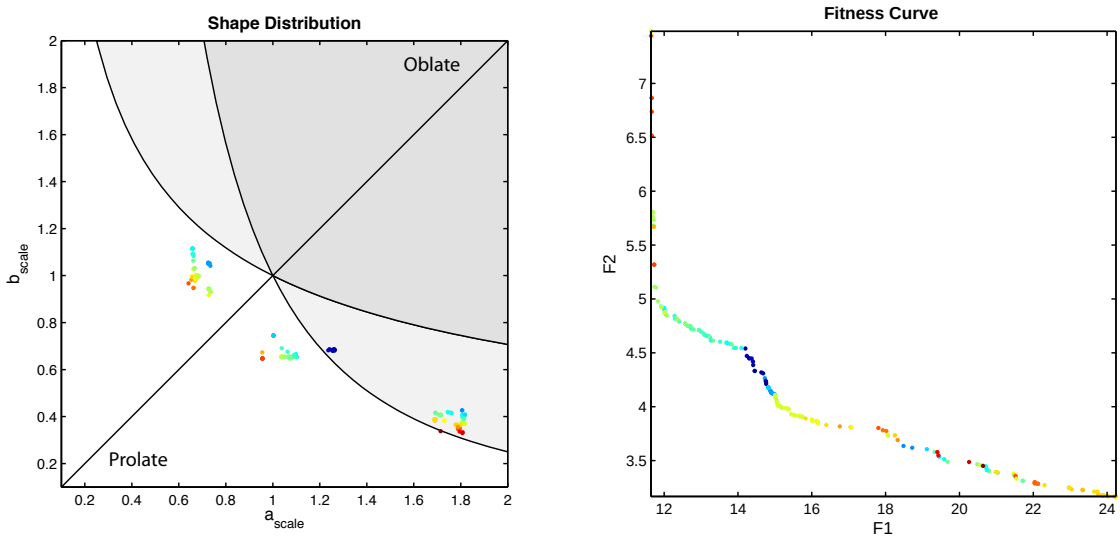

Figure 6.98: OMC1: basic5Component Shape Map. Solutions coloured by $c = (ab)^{-1}$ value. The solutions in fitness curve (right) are coloured the identically for comparison.

the noTwistPoly knee solution, and appears to be a better match, the fractional intensity residuals (Figure 6.96, left) do not show much difference in the residual pattern. However, they do show minor improvement in the range of values. There is still a misalignment in the polarization vectors on the western edge of the core, but examination of the χ_{pol} residuals (Figure 6.96, right) shows that the misalignment is less severe than the noTwistPoly models. The largest area of misalignment is now the northwest edge rather than the entire western half.

The three-dimensional views of Solution 210 (Figure 6.97) show a much larger, rounder core than the noTwistPoly knee models. Interestingly, the core has chosen a prolate shape, with the long axis parallel to the poloidal field direction. The twist shown is significant, with a c_{twist} of approximately 5.21. The core's z-symmetry axis is oriented at an angle of 86.5° to the line of sight, and at a PA 30° to the vertical. We can see from the shape map for the merged solution set (Figure 6.98) that the majority of the solution set selected prolate core shapes. The cluster of high a value solutions in the lower wing correspond to solutions with c_{twist} on the order of $\sim 10^{-0.75}$. In this case, the core and field geometry is consistent with the prolate core predictions of Fiege and Pudritz (2000b,c).

The density scales ρ_0 fell into the same range of values as the noTwistPoly solution set, with ρ_c taking values between 0.25–2. However, the velocity dispersion was better constrained, with a range of values between 0.73–0.82 km s^{-1}. The C_{flux} constant ranged from 1.13–1.66 Jy beam^{-1} g^{-1} cm^2. The polytropic index γ was split into two groups in the parameter space. The majority of the solutions had $\gamma \approx 0.9$, and solutions with low c_{twist} with $\gamma \approx 1$–1.3. Computing the core mass within the truncation radius yields a mass estimate of 1300 M$_\odot$, with a mass of 1960 M$_\odot$ for the entire model cube.

6.2.2.3 Model 3: basic5Component_MOD1

The basic5Component_MOD1 (or omc1_2a, is it was previously named) was developed through a number of experiments on OMC1. The main attributes that distinguish it from basic5Component are 1) c_{twist} is fit linearly, 2) ρ_c is allowed to vary between 1 and 320, and 3) ρ_{out} and P_{out} are fit logarithmically. The merged trade-off surface (Figure 6.99) from all eight runs shows significant improvement in χ_{pol} over the basic5Component set, with he knee region at about (12.6, 3.91). We select Solution 75 for analysis and summarize its parameters in Table 6.8 with the results of the previous two templates.

Comparing the OMC1 and Solution 75 polarization maps (Figure 6.100, we can see that this model has very nearly replicated the intensity profile. The central region is compact, and changes swiftly to diffuse emission before truncating. The F1 value is slightly worse than the basic5Component case, although the range of fractional intensity residuals (Figure 6.101, left) is narrower. The polarization vectors are in better agreement, with the χ_{pol} residuals (Figure 6.101, right) showing a further reduction in the misalignment along the north-western edge of the map.

We note from Figure 6.102 that the core selected a truncation radius such that the edges of the core surface fell into the masked pixels when projected along the line of sight (top right figure in Figure 6.102). Therefore we must be skeptical of the validity of the truncation. The angle the magnetic field makes with the line of sight is approximately 80°, and the PA

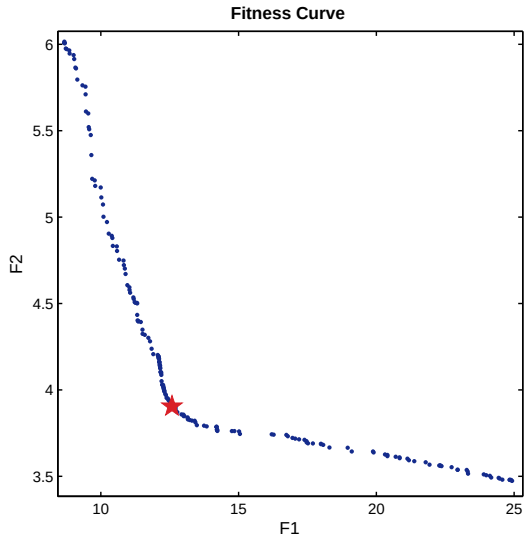

Figure 6.99: OMC1 basic5Component_MOD1: Trade-off Curve. Red star indicates Solution 75.

is equivalent to the basic5Component knee value. From the shape map (Figure 6.103) we can see that the majority of the solution set selected prolate cores, although as b increases and a decreases the less plausible they become. Solution 75 sits at the very bottom of the cluster at $a = 0.7$ and $b = 1$.

The density scales ranged from approximately 10^{-17}–10^{-16} g cm^{-3}, a slightly narrower than the previous two models. The central density had a wide range of values, from approximately 50–290$\times\rho_0$. The polytropic indices for the entire set were clustered very tightly around $\gamma = 1$. The knee solution selected a value of ρ_c of 194.5, and a γ of 0.972. The C_{flux} scale typically fell with in the range 0.5–1.3 Jy beam^{-1} g^{-1} cm^2. We compute the mass of the model cube to be 2340 M$_\odot$, neglecting computing the mass within the truncation radius as it falls outside the bounds of our grid.

6.2.2.4 General Observations

Dust temperature in the OMC1 region is typically taken to be 20–30 K. However, the dust temperature characteristic of Orion-KL, which is the extracted region, has been noted as 70 K (Coppin et al., 2000). A dust temperature range from 20–70 K would produce a range of

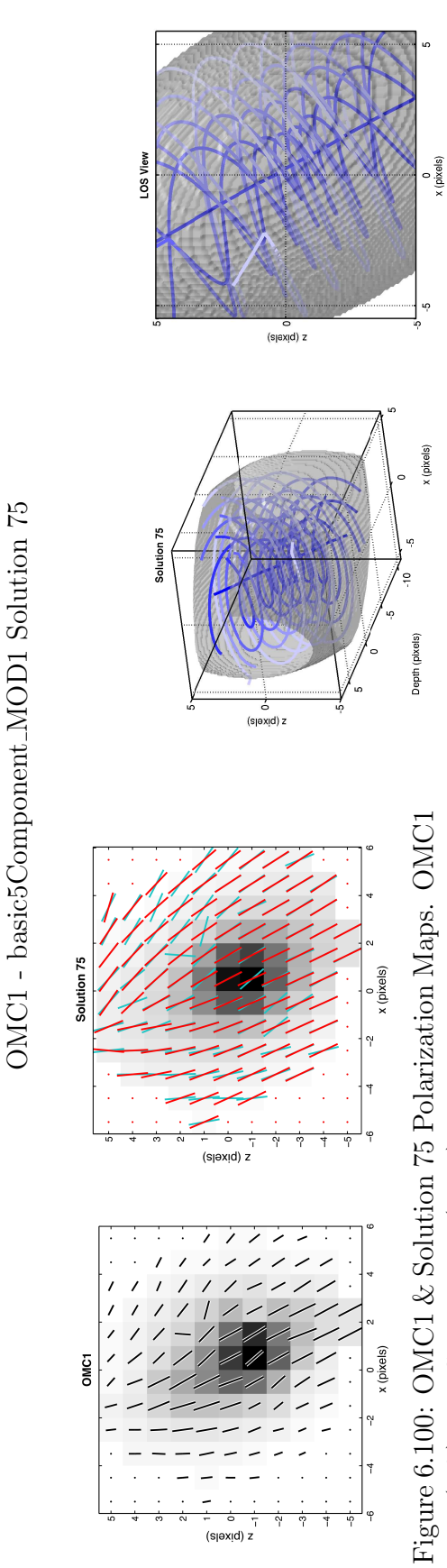

Figure 6.100: OMC1 & Solution 75 Polarization Maps. OMC1 map (left) and Solution 75 (right) with corresponding polarization vectors (red) over the OMC1 vectors (blue).

Figure 6.101: Solution 75 Residuals. Intensity (left) and χ_{pol} (right). Intensity residuals presented as a fraction of $\bar{I}_{data}$=12.4 Jy beam^{-1}.

Figure 6.102: Three-Dimensional Structure of Solution 75. The density isosurface represents ρ_s=3.81 $\times$ 10^{-18} g cm^{-3}.

	noTwistPoly	basic5Component	basic5Component_MOD1
	# 255	# 210	#75
F1	14.3	11.9	12.6
F2	6.61	4.93	3.91
χ^2_I	10885	5511	7886
χ^2_{PA}	43.7	24.3	15.3
ρ_0 (g cm^{-3})	2.60×10^{-18}	3.58×10^{-18}	9.39×10^{-20}
ρ_0^* (g cm^{-3})	5.21×10^{-16}	7.15×10^{-16}	1.88×10^{-17}
σ_0 (km s^{-1})	0.723	0.751	0.799
c_{twist}	–	5.21	9.92
K	1.98	0.247	0.309
γ_{poly}	0.684	0.894	0.972
ρ_c	6.74	3.57	194.5
ρ_{out}	0.0305	0.133	7.78×10^{-04}
P_{out}	0.162	0.0103	1.27×10^{-03}
a_{scale}	0.564	1.04	0.703
b_{scale}	1.75	0.656	0.998
ϕ	272.5°	54.6°	150.2°
i	5.9°	-176.5°	-170.1°
PA	244.8°	151.9°	151.2°
Δx (pix)	0.589	0.555	0.602
Δz (pix)	-0.452	-0.533	-0.631
$C^\dagger_{flux}$	0.428	1.31	1.05

Table 6.8: OMC1: Model Parameter Summary
†Jy beam^{-1} g^{-1} cm^2

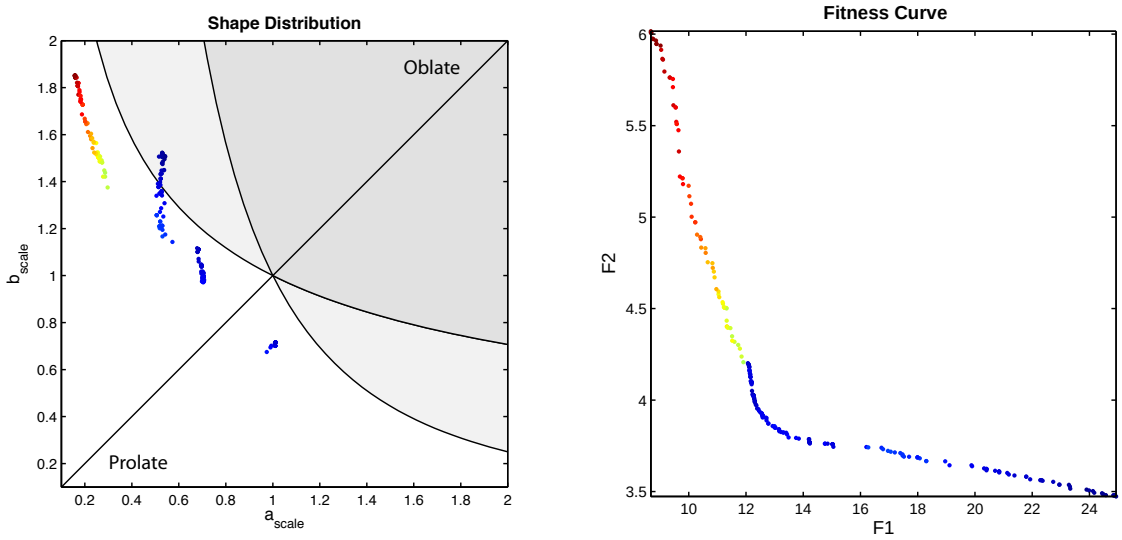

Figure 6.103: OMC1: basic5Component_MOD1 Shape Map. Solutions coloured by $c = (ab)^{-1}$. The solutions in the fitness curve (right) are coloured identically for comparison.

C_{flux} values between 5.18–25.2 Jy beam^{-1} g^{-1} cm^2. These values of C_{flux} would correct the estimates of the total mass of the knee model cubes to approximately 100–500 M$_\odot$.

The polytrope density profiles we are using to fit OMC1 appear to be a poor match to the intensity profile of the core. The overall appearance of OMC1 is a bright, compact central region, which transitions sharply into a more diffuse outer region before being truncated by the external envelope. The template that came closest to reproducing the intensity profile in the central region was the basic5Component_MOD1 template. The most significant difference between this template and the basic5Component template was that the limits on the POLY central density ρ_c were loosened from 1–10$\times\rho_0$ to 1–320$\times\rho_0$. This much larger central density allowed the profile to fall off more sharply than the profiles of §6.2.2.1 and §6.2.2.2. However, it appears that the fainter emission in the northern part of the core is bent slightly towards the west, and the southern portion is bent slightly towards the east, extending down into a faint tail connecting to the faint southern core that we have cropped from the image. This suggests that we may obtain a better fit to the intensity map if we include a bend transformation (see §4.3.10).

The core shape was completely different between the noTwist model and the basic5

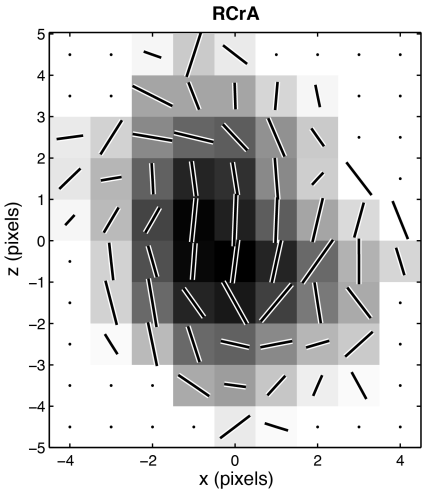

Figure 6.104: Cropped RCrA Dataset. Vectors are scaled by $\sqrt{P_{flux}}$.

models, with the twisted cores taking on a prolate geometry consistent with the Fiege and Pudritz (2000b,c) model. The noTwist model geometry selected shapes that contradicted the expected oblate core shape from an object undergoing gravitational contraction in a uniform magnetic field. We can therefore dismiss the noTwist model geometry for OMC1 on physical grounds and its poor fit to the data.

6.2.3 RCrA

RCra has an interesting field pattern, as the E-field vectors of the map seem to have an overall "S-shape." We run fits with the noTwistPoly and basic5Component templates as before, but also the basic5wLinTwistS template (§4.4.3). The latter template is essentially basic5Component with the LinearTwistS transformation substituted for the LinearTwistA component. We apply this template due to LinearTwistS's propensity for creating S-shaped polarization patterns. (§6.1.4). Figure 6.104 shows the cropped dataset we use for our fits. We tabulate the knee solution parameters in Table 6.9.

We note that RCrA's intensity profile is nearly bean-shaped. As such, our simple intensity profile will not be able to replicate it exactly.

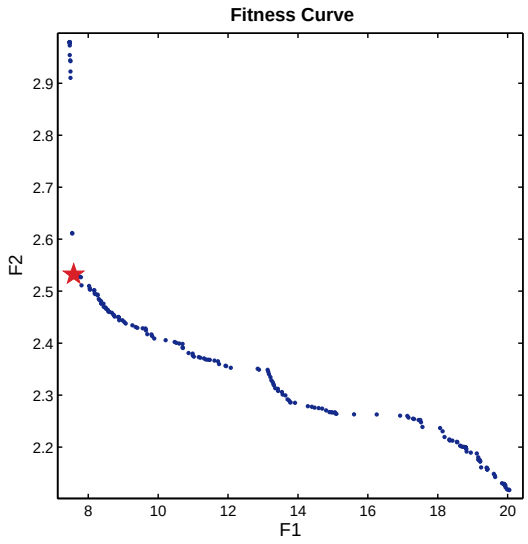

Figure 6.105: RCrA: noTwistPoly Trade-Off Curve. Red star indicates Solution 59.

6.2.3.1 Model 1: noTwistPoly

The merged trade-off surface for the noTwistPoly template (Figure 6.105) runs shows a sharp knee at $(7.58, 2.53)$, where the curve changes direction by approximately 140° from vertical. We select Solution 59 from near the bend for analysis and summarize its parameters in Table 6.9.

Comparing the model intensity map to the data (Figure 6.106), the model map appears to be an adequate match to RCrA. The fractional intensity residuals (Figure 6.107, left) appear to confirm this, with the difference between the model's smooth, ellipsoid shape and RCrA's bean-like intensity distribution manifesting itself as a 2x2 square of over-bright model pixels (between (0, 0.5) and (1,1.5) in pixel coordinates).

While the χ_{pol} residuals are reasonably small in the central regions, we can see that the polarization pattern in Figure 6.106 (right) is not a good match. Additionally, Figure 6.108 shows that the core's magnetic field is oriented almost parallel to the line of sight ($< 10°$). This is a similar field orientation to the case that instigated the intersection penalty P_{int} (§4.1.5), as aligning the field in this way allows greater control over the model polarization vectors with minimal alterations. Examination of the shape map (Figure 6.109) shows that

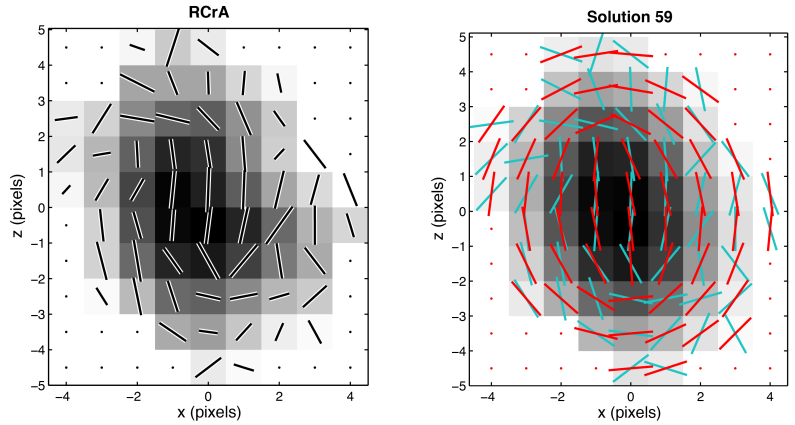

Figure 6.106: RCrA & Solution 59 Polarization Maps. RCrA map (left) and Solution 255 (right) with corresponding polarization vectors (red) over the RCrA vectors (blue).

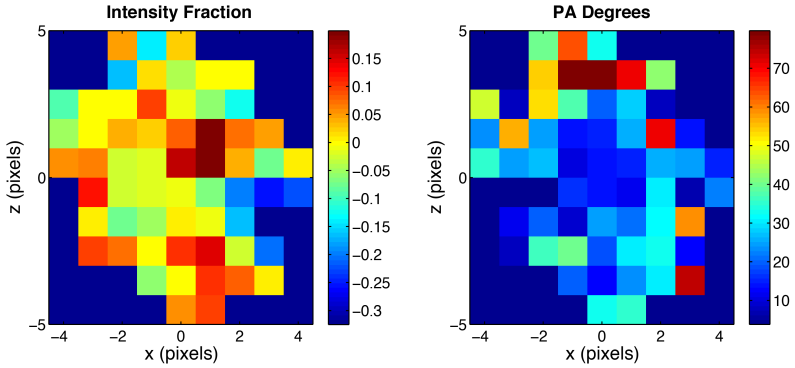

Figure 6.107: Solution 59 Residuals. Intensity (left) and χ_{pol} (right). Intensity residuals presented as a fraction of $\bar{I}_{data}$=0.998 Jy beam^{-1}.

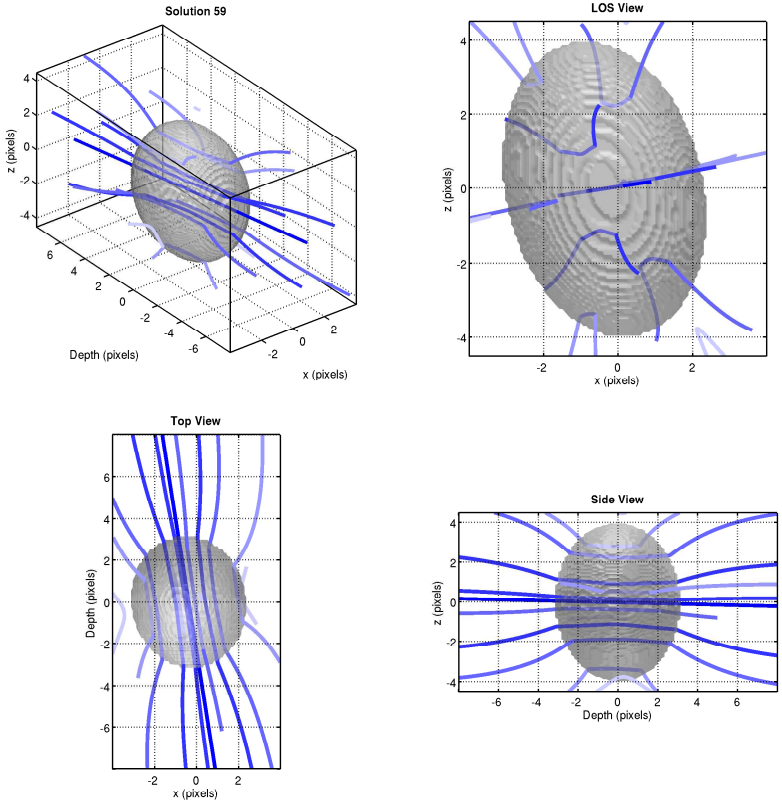

Figure 6.108: Three-Dimensional Structure of Solution 59. The density isosurface represents $\rho_s = 2.23 \times 10^{-17}$ g cm^{-3}.

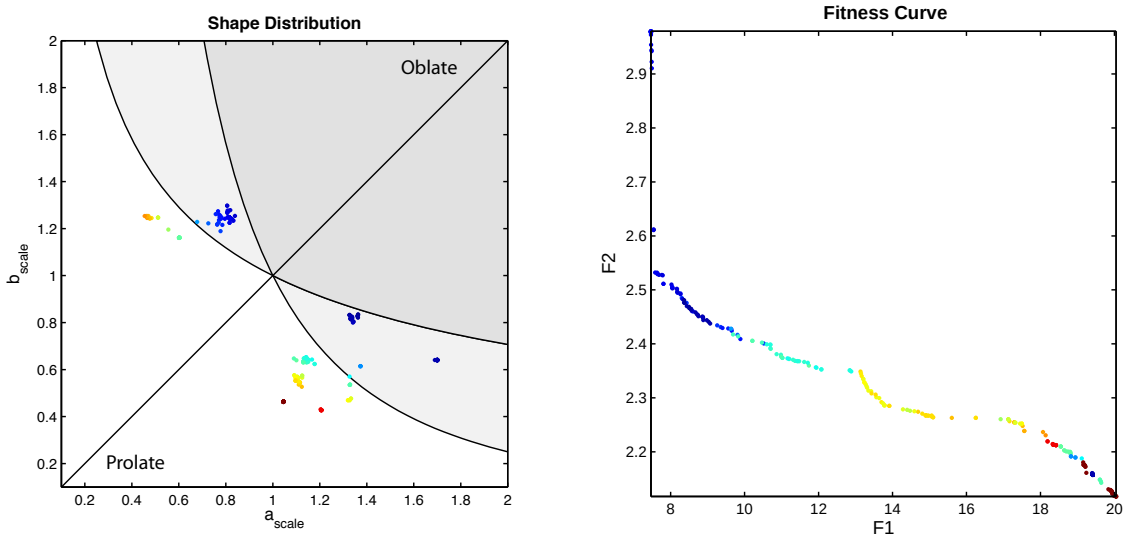

Figure 6.109: RCrA: noTwistPoly Shape Map. Coloured according to $c = (ab)^{-1}$ value. Shape map (left) with the fitness curve (right).

the solutions near the knee and with the lowest F1 values tend to sit in the two wings of the plot, where c falls in between a and b. The range of density scale values falls between 0.5–9.5 $\times 10^{-17}$ g cm^{-3}, with velocity dispersion σ_0 in the range of 0.4–0.9 km s^{-1}.

The noTwist model provides an adequate fit to the intensity map, but cannot reproduce the polarization vectors. We rule out this model and turn our attention to models containing a twisted field component.

6.2.3.2 Model 2: basic5Component

The merged fitness curve for the basic5Component template is shown in Figure 6.110. We select Solution 150 for analysis and summarize its parameters in Table 6.9.

Figure 6.111 shows the model polarization map with model vectors in red and data vectors in blue. The model polarization pattern has a different appearance than the data pattern. The model pattern does show some similarity to the noTwistPoly knee model with the southern vectors perpendicular to the vectors in the centre. However, the northern portion of the Solution 150 pattern are oriented in the same direction as those in the centre of the region. The fractional intensity residuals (Figure 6.112) show the same 2x2 pixel

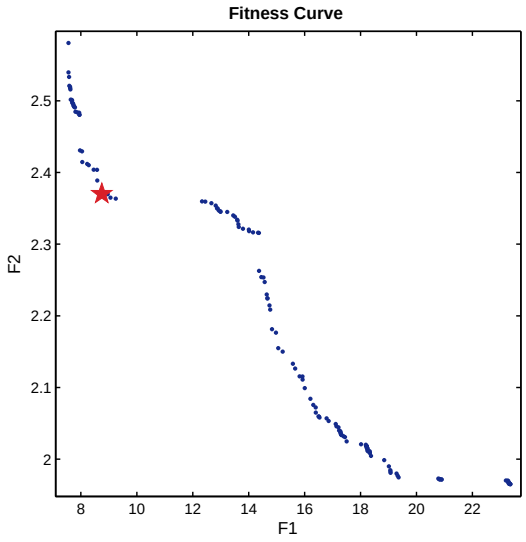

Figure 6.110: RCrA: basic5Component Trade-off Surface. Red star indicates Solution 150.

enhancement as noTwistPoly, where the inner edge of the RCrA "bean" shape differs from an ellipsoidal core.

We can see from the three-dimensional views of Solution 150 (Figure 6.113), that the core shape is that of a very thin disk with the magnetic field normal to the shortest axis, and the magnetic field exhibits a very low c_{twist}. Examination of the shape map for the solution set shows that this solution is in a cluster of solutions near the highest possible a and b values for the solution set. The geometry of the model suggests significant collapse along the direction of the poloidal field, which is expected as the poloidal field supports the gas orthogonal but not parallel to it. The field exhibits only a slight twist, and the overall polarization pattern is qualitatively different from that of the data. We rule this model out for its failure to reproduce the correct polarization pattern.

6.2.3.3 Model 3: basic5wLinTwistS

The merged trade-off surface from the basic5wLinTwistS template solution set is displayed in Figure 6.114. This trade-off surface shows significant improvement in F2, with the knee region occurring around $(8.9, 1.7)$. We select Solution 185 for analysis and summarize its

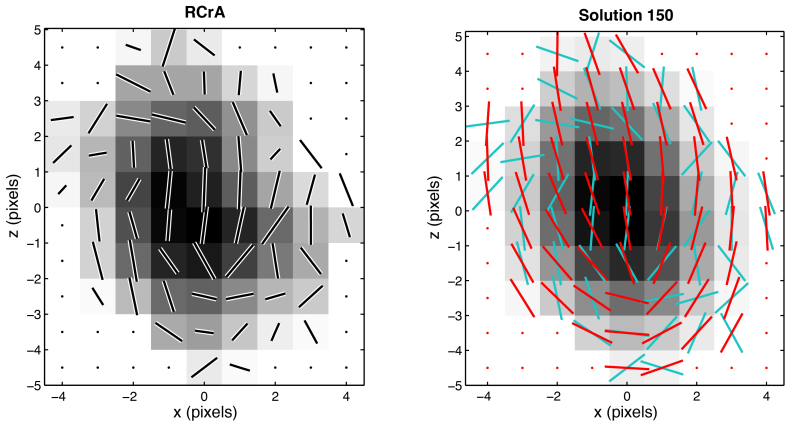

Figure 6.111: RCrA & Solution 150 Polarization Maps. RCrA map (left) and Solution 150 (right) with corresponding polarization vectors (red) over the RCrA vectors (blue).

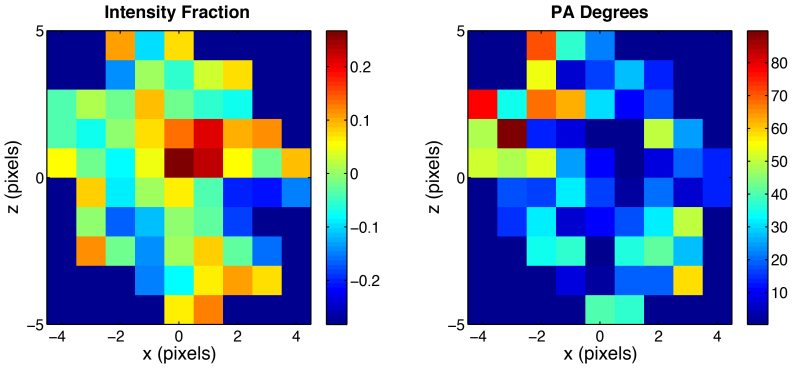

Figure 6.112: Solution 150 Residuals. Intensity(left) and χ_{pol} (right). Intensity residuals presented as a fraction of $\bar{I}_{data}$=0.998 Jy beam^{-1}.

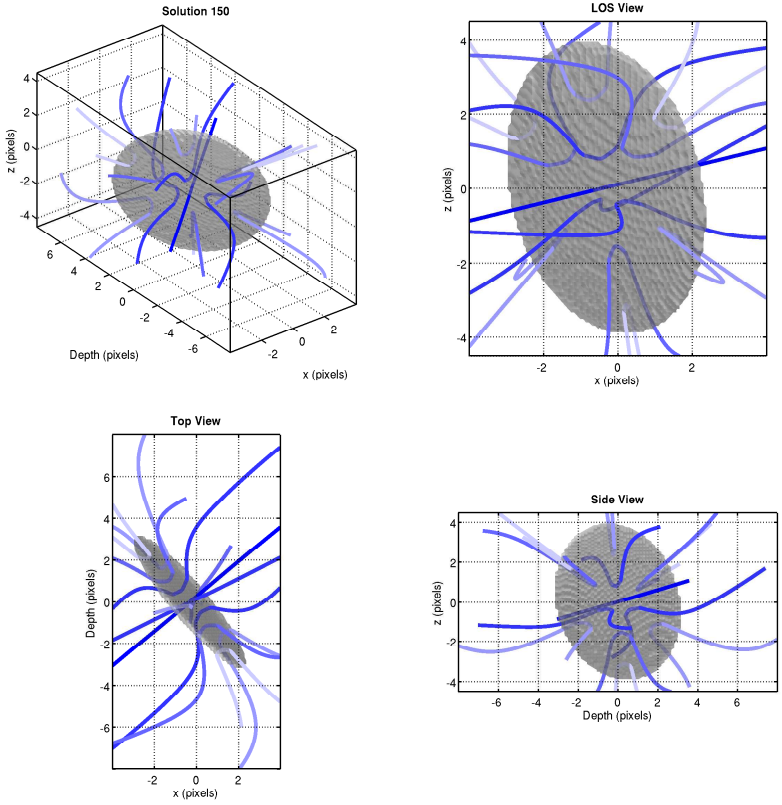

Figure 6.113: Three-Dimensional Structure of Solution 150. The density isosurface represents $\rho_s = 4.67 \times 10^{-17}$ g cm^{-3}.

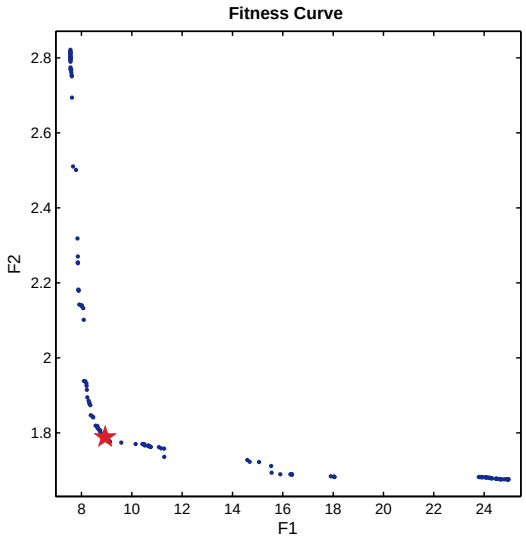

Figure 6.114: RCrA: basic5wLinTwistS Trade-Off Surface. Red star indicates solution 185.

parameters in Table 6.9.

We can see from the polarization map for Solution 150 (Figure 6.115) that, unlike the knee solutions from the other two templates, the polarization vectors at the centre of the core show near-perfect alignment with the data, and better agreement with the overall field pattern than either of the others. The fractional intensity residuals (Figure 6.116, left) also show the 2x2 enhanced pixel feature, and its largest points of discrepancy are along the edges of the map. The χ_{pol} residuals (Figure 6.116, right) show that the only vector misalignments greater than 30° lie in small clusters in the northeast and southwest edges.

We can see from the three-dimensional views of the solution (Figure 6.117) that the knee solution has a significant field twist ($c_{twist} = 11.74$) and a shape prolate along the core's z-symmetry axis, with $a = 1.01$ and $b = 0.758$. The cluster around these values in the shape map is composed entirely of solutions in the knee region of the fitness curve.

We favour this model over the other presented, due to its qualitative agreement with the data. We note that the core is prolate, like OMC1, but the symmetry of the field is opposite.

RCrA - basic5wLinTwistS Solution 185

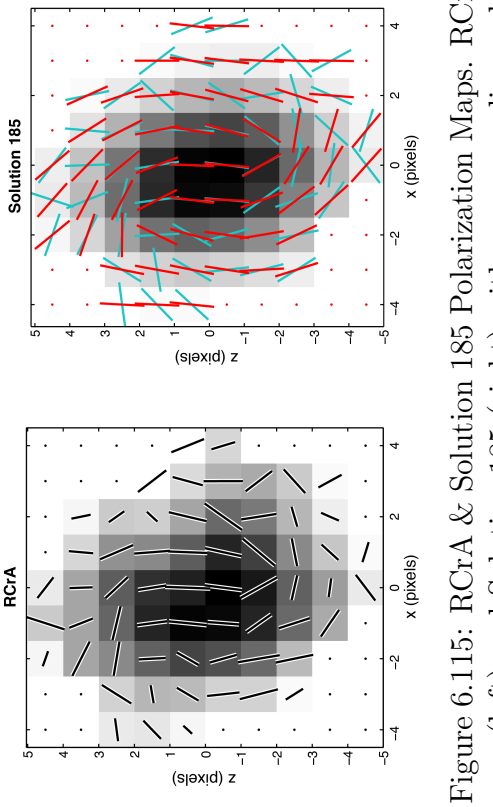

Figure 6.115: RCrA & Solution 185 Polarization Maps. RCrA map (left) and Solution 185 (right) with corresponding polarization vectors (red) over the RCrA vectors (blue).

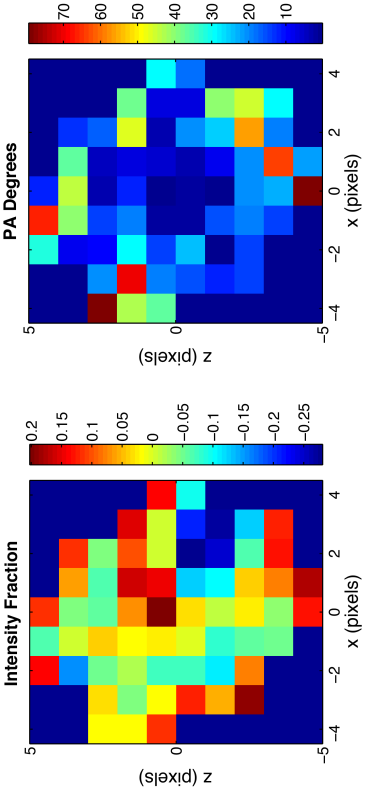

Figure 6.116: Solution 185 Residuals. Intensity (left) and χ_{pol} (right). Intensity residuals presented as a fraction of I_{data}=0.998 Jy beam^{-1}.

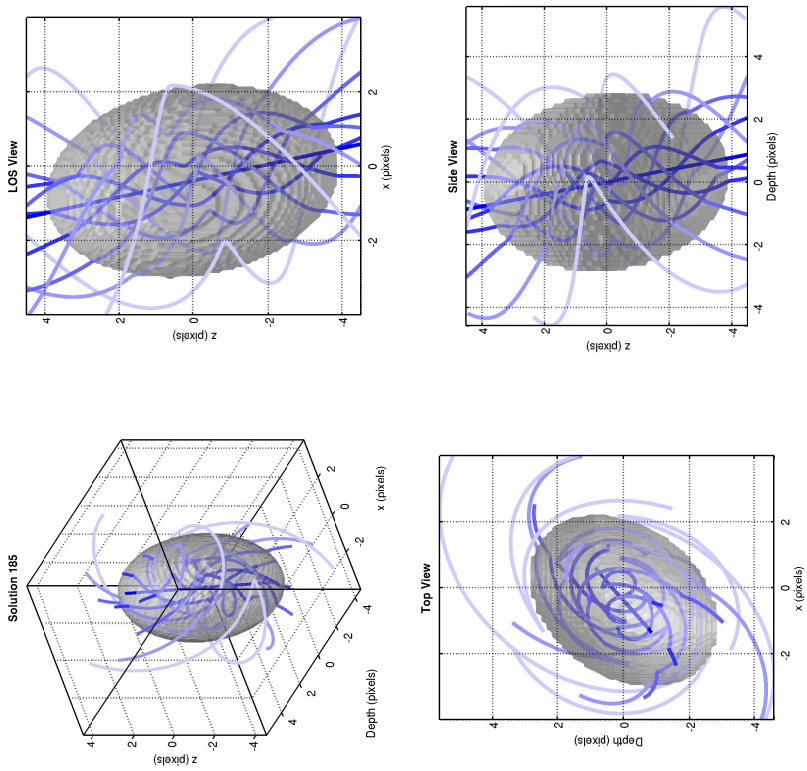

Figure 6.117: Three-Dimensional Structure of Solution 185. The density isosurface represents $\rho_s = 1.95 \times 10^{-17}$ g cm^{-3}.

	noTwistPoly	basic5Component	basic5wLinTwistS
	# 59	# 150	# 185
F1	7.58	8.75	8.94
F2	2.53	2.37	1.79
χ^2_I	85.8	99.3	98.3
χ^2_{PA}	6.41	5.62	3.20
ρ_0 (g cm^{-3})	5.71×10^{-20}	1.60×10^{-19}	5.88×10^{-20}
ρ_0^* (g cm^{-3})	1.14×10^{-17}	3.19×10^{-17}	1.18×10^{-17}
σ_0 (km s^{-1})	0.538	0.647	0.559
c_{twist}	–	0.416	11.74
K	0.0833	0.0221	0.0251
γ_{poly}	1.06	1.07	1.12
ρ_c	2.58	3.84	4.15
ρ_{out}	0.104	0.0520	0.184
P_{out}	0.741	0.356	0.358
a_{scale}	0.816	1.94	1.01
b_{scale}	1.24	1.98	0.758
ϕ	274.4°	353.4°	56.4°
i	81.0°	141.4°	169.2°
PA	261.3°	256.3°	347.7°
Δx (pix)	-0.363	-0.318	-0.392
Δz (pix)	-0.0117	0.0249	0.0177
$C^\dagger_{flux}$	0.589	0.652	0.494

Table 6.9: RCrA: Model Parameter Summary
†Jy beam^{-1} g^{-1} cm^2

6.2.3.4 General Observations

Overall, the basic5wLinTwistS template showed the best fit to the magnetic field, although the intensity fitness was slightly worse than the noTwistPoly model. We note that the noTwistPoly and basic5wLinTwistS knee models selected approximately the same shape, with Solution 59 having Scale constants $(0.816, 1.24, 0.987)$ and Solution 185 having $(1.01, 0.758, 1.31)$. However, we rule out the noTwistPoly model as a valid fit to the dataset. The polarization pattern was very different than the target dataset, and required the field to be closely aligned with the line of sight, a situation that is less than desirable.

We rule out the basic5Component model as the polarization pattern was not in good agreement with the data. However, we note that the solution set selected models with low c_{twist}. It is therefore possible that we are seeing the same situation as we observed in DR21-Main; where the logarithmic fit of the c_{twist} parameter is limiting the results by making the parameter search more difficult.

Although the basic5wLinTwistS knee model did show some misalignment along the north-eastern and southwestern edges of the core, the field vectors aligned almost perfectly in the centre; something neither the noTwistPoly nor the basic5Component models replicated. Additionally, the overall pattern of the polarization vectors of Solution 185 (Figure 6.115) follows the pattern of the data vectors more closely than the results of fitting with the other two templates.

Nutter et al. (2005) identified several clumps inside of this region (which are the origin of its bean-like shape) and computed envelope masses for each. The region we have extracted for our fits includes the clumps designated SMM1A–1C and SMM2. Adding up the component masses of the clumps, we obtain a mass estimate for our region of 7.5–12.3 $M_\odot$. For each solution in Table 6.9, we obtain masses within the core truncation radius of 13.5 $M_\odot$ (Solution 59), 9.4 $M_\odot$ (Solution 150), and 12.2 $M_\odot$ (Solution 185), which are in agreement with this range. Mass values for the density cube as a whole were typically twice the mass of the core inside the truncation radius.

However, this changes when we account for dust temperatures to make corrections to C_{flux}. The mass range of the SMM1A clump in Nutter et al. (2005) was calculated based on an assumed dust temperature of 11–15 K, whereas SMM1B-C and SMM2 were assumed to have temperatures of 30 K. To directly compute the assumed C_{flux} for RCrA, we take an in-between value of 20 K (Curran and Chrysostomou, 2007), producing a C'_{flux} of 5.18 Jy beam^{-1} g^{-1} cm^2. This corrects the masses from $\sim$10 M$_\odot$ to $\sim$1 M$_\odot$, which is extremely low. However, we note that we use a shorter distance to RCrA than Nutter et al. (2005), who use the 170 pc value found by Knude and Høg (1998). If we were to use this distance, our physical grid size would increase, and therefore the core volume would also increase. For an identical map to be produced (in pixels), the density scale estimate would not change. Therefore we suggest that the missing mass after C_{flux} correction may be accounted for at this larger distance. The method Nutter et al. (2005) used to determine the masses was proportional to the square of the distance. For a distance of 130 pc this would put the mass estimate for RCrA between 4.4–7.2 M$_\odot$.

6.2.4 Discussion

One common trend in the data, is that without the intersection fitness penalty, the current polytropic model has difficulty modelling diffuse emission in the outer regions of the core without predominately selecting cylinders oriented along the line of sight. While interesting, more research is needed to determine whether this effect is real or a numerical artifact. In the future, we will investigate models that allow for a more compact central region with diffuse edges. One possibility would be to model a composite polytrope, a compact polytropic core in an envelope with a different polytropic index, such as those posited in (Curry and McKee, 2000). These models would be more realistic, as the constant external density of POLY produces a sharp boundary at the limits of the grid. A more realistic model of the external envelope would allow the density of the external medium to fall off along the line of sight.

Our results question the usefulness of logarithmic fits. As we found with the DR21-M

results, applying a logarithmic fit to the twist parameters aided congruence between individual runs, but tended to favour smaller c_{twist} values, despite the data suggesting that a larger twist was required. The log transformation causes a disproportionally large volume of the parameter space to represent models with very low values. This appears to make the search more difficult. A possible fix would be to change the mapping function from X(P)=log(P) to X(P)=log(P+1). Such mapping would allow for congruence about the zero of the parameter, ie X(0)=0. The same problem has been noted in an X-ray spectroscopic modelling project, and this potential fix is being examined there (J. Fiege, private communication).

A trend across all of the datasets was that the C_{flux} values were poorly constrained. Although we would expect some correlation with the density scale ρ_0, we find that this is not the case. The C_{flux} values vary largely between runs, even on the same dataset. We find that PolCat typically selects C_{flux}, ρ_0, and POLY profile central density ρ_c values such that $C_{flux} \times \rho_0 \times \rho_c$ is well-constrained. This is an artifact of how the models are scaled; the peak intensity of the model maps has a scale typical of the product of these parameters.

We note that molecular clouds and their cores have clumpy, turbulent substructure that simple geometrical models cannot replicate. However, this substructure is inherently chaotic, and there would be little to learn from modelling random density fluctuations. We prefer to focus on the overall structure of cores and their fields. Nevertheless, the presence of substructure is a significant source of our high χ^2 value for intensity. The variations due to substructure tend to be much larger than the uncertainty in the I maps. This is not generally the case with Q and U, due to their much lower intensities, and therefore smaller χ^2 values. This large discrepancy between the intensity and polarization quantities is the prime motivation for treating our fits as multi-objective (see §4.1.5).

One interesting result with each of the three SCUPOL datasets was that the knee solutions tended to select scale parameters such that the cores were prolate perpendicular to the field direction, that is, the z-stretch, $c = (ab)^{-1}$ of the cores tended to have values between a and b. Conversely, when the model had a significant twist the core shapes tended to be

elongated along the poloidal field direction (prolate parallel to the core's z symmetry axis). This finding is consistent with the Fiege and Pudritz (2000b,c) filament model, where the toroidal field squeezes the core inwards.

In each of the three observational cases examined we were able to identify a field geometry that performs much better than the other geometries tested. Of course, these results are preliminary and our sample size is small, but our apparent ability to differentiate between three-dimensional field geometries holds promise for future research in this direction.

Chapter 7

Conclusions

This thesis has documented a new method to model magnetized molecular cloud cores, embodied in our new PolCat software, plus a series of numerical experiments to characterize our method. We also applied PolCat to several intensity and polarization maps from the SCUPOL Legacy Catalogue, to obtain intriguing initial results suggesting that these cores may be threaded by twisted magnetic fields. We have learned some important lessons from this research which will serve to illuminate the path forward as we apply our method to a larger selection of cores.

7.1 Data

In all cases, we found our determination of the core mass to be strongly affected by the assumed C_{flux} value, and therefore the observational dust temperature. Adjusting the raw PolCat results for both SCUBA FCF and new C_{flux} values resulted in masses typically smaller than observationally determined values, although applying the SCUBA FCF correction alone produced masses that are typically in agreement. Overall, there is too much variation in the possible scaling of the problem for us to trust density and mass estimates obtained from our code at present. We note that accurate mass determination is often difficult in this field due to the uncertainties in the dust temperature and emission properties.

Our difficulties are a reflection of these uncertainties.

7.1.1 DR21-Main

We fit DR21-M with three model templates: noTwistPoly, basic5Component, and basic5Component_MOD1. The latter two templates consist of identical transformation components, but use different parameter ranges and change how some parameters are fit.

Fits with the four-component noTwistPoly model produced a merged trade-off surface with nearly negligible curvature. The core geometry for this model was flattened equally along the core's x- and z-symmetry axes, which is not in agreement with gravitational contraction in the presence of a magnetic field aligned along the core's z-symmetry axis. We note that this behaviour is consistent with the results of fitting twisted fields with a non-twisted model (§6.1.3.2 and §6.1.4.2), which suggests that the non-twisted field model is insufficient to model this core.

The results from the basic5Component fits showed a similar geometry to noTwistPoly, exhibiting a low field twist. However, fits with the basic5Component_MOD1 model, where the twist parameter was allowed to vary linearly, selected significant c_{twist}. We suggest that basic5Component favouring minimally twisted fields is an artifact of the logarithmic fit of the c_{twist} parameter, which seems to degrade our ability to search the parameter space.

All three model templates showed adequate fits to the observed intensity and polarization angle of DR21-M, although the polarization maps showed a small misalignment with the vectors at the core centre. The core shapes corresponding to these twisted field geometries were different than the cores with "straight" fields, selecting chiefly prolate geometries aligned with the poloidal field direction. The result that selecting a significantly twisted field simultaneously selected a prolate core geometry is interesting in relation to the prediction of the (Fiege and Pudritz, 2000d) prolate molecular cloud core model.

7.1.2 OMC1

We fit OMC1 with the same three model templates as DR21-M. We find that the non-twisted polytrope with an hourglass field geometry fits the data poorly. In addition, this geometry results in core shapes with their shortest axis aligned perpendicular to the field direction, which unphysical for gravitational contraction from a uniform field geometry. Both models with a twist transformation component selected significant twisted field geometries with the cores' long axes aligned with the poloidal field direction, again consistent with the prolate core models of (Fiege and Pudritz, 2000d).

Due to OMC1 having a bright, compact central region and more diffuse outer region, we find that the default range of the ρ_c parameter in the basic5Component model was insufficient to model its intensity profile. The loosening the limits on the central profile density ρ_c from 1-10 to 1-320 significantly improved the overall range of intensity residuals. Our final model adequately describes the intensity structure and polarization map, using a very centrally concentrated polytrope and a twisted magnetic field.

7.1.3 RCrA

We fit the RCrA region with three different geometries: a polytrope with a non-twisted magnetic field, a polytrope with an asymmetrically twisted magnetic field (the basic5Component template), and a polytrope with a symmetrically twisted magnetic field (LinearTwistS transformation, §4.3.7).

We find that a non-twisted magnetic field geometry cannot match the observed polarization pattern, although the non-twisted field model was able to produce an adequate fit to the intensity map. Correspondingly, a fit to the basic5Component template also produced cores with inadequate polarization patterns. However, we note that these models had a low twist parameter, which may be an artifact of fitting c_{twist} logarithmically, as our findings from the DR21-Main results suggest. More testing without a logarithmic parametrization is required before we may rule definitively.

Of the three potential geometries that we applied to this dataset, we favour the results from the basic5wLinTwistS model template. The resulting core was prolate with a significantly twisted field, and with its long axis aligned to the poloidal magnetic field direction. It provided the best reproduction of the polarization pattern of the three geometries we applied.

7.2 Core Geometries

We find from our test results that cores fit with incorrect model templates show poor agreement with the input polarization map, possibly accompanied by unphysical core geometries. From our Test Core 3 and Test Core 4 results (§6.1.3 and §6.1.4), we find that PolCat is able to not only detect the presence of a twisted field, but also rule out non-twisted field models when the source data has a twisted field. PolCat can also detect the symmetry of the field twist.

The orientation angles obtained from the RotateA transformation are highly degenerate, as PolCat cannot distinguish between a field tilted towards or away from the line of sight. Overall the χ_{pol} objective constrains the i and PA angles better than intensity, but its assessment of i can be affected by noise. If the core is triaxial, the intensity map adds additional constraint on i that helps compensate for the effects of polarization angle noise.

While cores with their magnetic fields oriented close to or along the line of sight are a valid possible geometry, we must judge results favouring this geometry with skepticism. We have found that, overall, models oriented in this manner are very sensitive to the details of the field geometry due to projection effects; minor changes to the field can have large changes to the polarization pattern at this orientation. In fact, without the penalty function P_{int} (§4.1.5, equation (4.36)) we find that for difficult fields the solution set often favours elongated cylinders that intersect with the front and back of the model cube. While these results are interesting, more testing is required to determine whether these results are ever

physical, or always a numerical artifact.

An interesting result is the effect the presence of a significant twist has on the geometry of the model. The difference between a significantly twisted field model and a non-twisted model fit to the same dataset generally shows a 90° change in rotation PA. A model core with a helical field typically has a prolate geometry with the long axis parallel to the poloidal field direction. The non-twisted model typically either shows an oblate geometry with the short axis parallel to the field, or a geometry with the short axis perpendicular to the field. The latter is typically unphysical due to how gravitational contraction behaves in the presence of a magnetic field. When this geometry occurred in our test data, it was characteristic of a non-twisted model fit to a twisted field geometry (§6.1.3.2 and §6.1.4.2). We have only examined three cores in our analysis, but it is intriguing that all three are best fit by prolate core models threaded by a twisted magnetic field.

7.2.1 Curvature of the Trade-Off Surface

When we examine the trade-off surfaces for the test data, we find that, in general, fits to test cores with the same model template produced trade-off surfaces with a sharply curved knee. Fitting with templates with geometries different from the generating seed model produced more sparsely-populated trade-off surfaces with weaker curvature. Fits to the data generally showed similar behaviour, with weak curvature for poorly fitting solutions and strong, obvious bends for better-fitting models. This suggests that analyzing the curvature of the trade-off surface may provide an additional assessment of the quality of models with a particular geometry.

7.3 Polytrope Parameters

Overall, we find from our tests that our fits tended to select γ within ± 0.2–0.3 of each other for a particular dataset. This can often produce significant differences in profile, as

the solutions with polytropic index $\gamma > 1$ tend to truncate naturally. However, the shape of the profiles within the truncation radius were still very similar, as the fits appeared to select constant K, and external pressure P_{out} values to ensure that the core was truncated at the correct pixel (or physical) core radius, regardless of what the seed values for those parameters might be. Differences in core profile when scaled to the same central density value were minimal and likely not discernible in the context of our polarization maps because of their low resolution.

Results from our fits showed that ρ_c typically varied widely between the solutions in a set for a particular run. The selection of the precise value of the central density of the polytrope profile appeared to be correlated to the solution's C_{flux} and ρ_0 values. Two profiles that were largely discrepant in peak density usually lined up when scaled into units of Jy beam^{-1} cm^{-1}, which replicates the step prior to integration into polarization maps (see §4.1.4). Thus, we reproduce the observed intensity structure, despite some difficulty constraining the profiles central density.

7.4 Scaling

While PolCat was able to obtain well-constrained estimates to the C_{flux} value for the knee solutions of the test datasets, the results from multiple runs showed that the parameter was largely unconstrained. While we might expect the C_{flux} values to show some correlation with the preferred density scales over multiple runs on the same object — as the quantity $C_{flux} \times \rho_0$ controlled how the dimensionless model scaled into Jy beam^{-1} for the fit — we found this was not the case, although the quantity $C_{flux} \times \rho_0 \times \rho_c$ as a whole showed much better constraint. In fact, as this quantity defines the magnitude of the peak intensity of the simulated polarization maps, much of the variation in C_{flux} from solution to solution appears to be compensating for the ρ_0 value. This was evident in Solution 258 in Section 6.2.1.2, where the solution had low C_{flux} and high density compared to Solution 133 from

the same solution set. We conclude that PolCat is not sensitive to the C_{flux} factor. We suggest that, going forward, we use a fixed estimate for C_{flux} based on equation (4.28) for best results from the program. Fixing C_{flux} to a core-specific estimate will reduce the scaling problem to the two competing density scales, ρ_0 and ρ_c.

We suspect that our default limits on the density scale ρ_0 may be too wide (and the central polytrope density ρ_c limits too narrow) for ρ_0 to truly represent the initial density of the cloud. Additionally, the fiducial SCUBA FCF value we use to convert the SCUPOL Legacy maps is estimated from an average. Our analysis could be improved using flux-calibrated data.

7.5 Final Statement

We are confident in fits to the core geometries produced by PolCat, but not our density and C_{flux} scales. We make this assessment based on how we handle our dimensionless computation of the model, with scaling into physical units not occurring until the final step of polarization map computation. While the choice of density scale affects the conversion into dimensionless units, correcting the density scale simply amounts to rescaling our model. The scaling constants have no effect on the overall shape of the intensity profile and no effect on the polarization angle.

Future developments to the code will involve adding several different density models. We also plan to develop models with cylindrical geometries to model filaments, and develop multi-core models for datasets with multiple cores with shared or connected envelopes, such as the complicated structure of cores seen in the SCUPOL Legacy OMC1 dataset.

We plan to apply PolCat to a large sample of molecular cloud cores from the SCUPOL Legacy Catalogue to obtain a large library of potential density and field geometries. We will also seek data from other telescopes. We plan to make PolCat freely available to the submillimetre astronomy community.

Other future developments will be to develop a molecular outflow modelling package that will interface with PolCat to allow for simultaneous fits to outflows and central cores, to explore the relationship between magnetic fields in cores and the larger turbulent outflow structures. The TADPOL survey (Hull et al., 2014) provides 1 mm polarization data in addition to CO velocity data, which will allow for simultaneous fits to both the core regions and the outflows.

Appendix A

Coordinate Transformation Proof

Maxwell's equations describe how electric and magnetic fields behave. Inside media, they take the form

$$\nabla \times \mathbf{H} = \boldsymbol{\varepsilon} \frac{\partial \mathbf{E}}{\partial t} + \mathbf{J} \tag{A.1}$$

$$\nabla \times \mathbf{E} = -\boldsymbol{\mu} \frac{\partial \mathbf{H}}{\partial t} \tag{A.2}$$

$$\nabla \cdot (\boldsymbol{\varepsilon} \mathbf{E}) = \rho \tag{A.3}$$

$$\nabla \cdot (\boldsymbol{\mu} \mathbf{H}) = 0 \tag{A.4}$$

For the case of light travelling through homogeneous materials, solving the equations inside of the material is straightforward, but for the case of light propagating through complex, non-homogeneous materials, the problem becomes more difficult, such as the case where the electric and magnetic permittivity constants, ε and μ vary spatially (Ward and Pendry, 1996). There are several approaches to computing how electric and magnetic fields behave in these materials, including plane wave expansions or representing the fields on a discrete mesh, each with its own computational challenges (Ward and Pendry, 1996). However, it is also possible to use coordinate transformations to determine the way light behaves in complex systems due to the fact that Maxwell's equations take the same form in both systems. Therefore, we can

solve the equations for the case of a uniform, homogeneous medium, and apply a coordinate transformation that deforms it to take on the desired properties, with the effective changes being absorbed into ε and μ for the complex medium (Ward and Pendry, 1996; Pendry et al., 2006). This technique is generally referred to as "transformation optics" and is generally used to design complex media that control the path of light passing through, such as in the development of invisibility cloaks (Pendry et al., 2006). However, instead of performing the complex derivation as performed in Ward and Pendry (1996) and Pendry et al. (2006), it is far simpler to express the transformations in terms of the Jacobian matrix $\boldsymbol{\mathcal{J}}$.

The transformations required for Maxwell's equations to take the same form across the coordinate systems are expressed in terms of the Jacobian matrix as

$$\boldsymbol{E}' = (\boldsymbol{\mathcal{J}}^T)^{-1}\boldsymbol{E} \tag{A.5}$$

$$\boldsymbol{H}' = (\boldsymbol{\mathcal{J}}^T)^{-1}\boldsymbol{H} \tag{A.6}$$

$$\boldsymbol{\varepsilon}' = \frac{\boldsymbol{\mathcal{J}}\boldsymbol{\varepsilon}\boldsymbol{\mathcal{J}}^T}{\det \boldsymbol{\mathcal{J}}} \tag{A.7}$$

$$\boldsymbol{\mu}' = \frac{\boldsymbol{\mathcal{J}}\boldsymbol{\mu}\boldsymbol{\mathcal{J}}^T}{\det \boldsymbol{\mathcal{J}}} \tag{A.8}$$

$$\boldsymbol{J}' = \frac{\boldsymbol{\mathcal{J}}\boldsymbol{J}}{\det \boldsymbol{\mathcal{J}}} \tag{A.9}$$

$$\rho' = \frac{\rho}{\det \boldsymbol{\mathcal{J}}}. \tag{A.10}$$

The proof that follows is based on lecture notes by Steven G. Johnson at MIT (Johnson, 2007) freely available over the internet at `http://math.mit.edu/~stevenj/18.369/coordinate-transform.pdf`.

We can express equation (A.1) in Einstein summation notation as follows

$$\partial_a H_b \epsilon_{abc} = \epsilon_{cd}\frac{\partial Ed}{\partial t} + J_c \tag{A.11}$$

where $\partial_a = \partial/\partial x_a$ and summation occurs over repeat indices. Making the substitution of E

and H to E' and H' using (A.5) and (A.6), represented by

$$E_d = \mathcal{J}_{ld} E'_l \tag{A.12}$$

$$H_b = \mathcal{J}_{jb} H'_j \tag{A.13}$$

in Einstein summation notation we get

$$\partial_a \mathcal{J}_{jb} H'_j \epsilon_{abc} = \varepsilon_{cd} \mathcal{J}_{ld} \frac{\partial E'_l}{\partial t} + J_c. \tag{A.14}$$

If we expand the partial derivative on the left side of the equation we get $(\partial_a \mathcal{J}_{jb}) H'_j \epsilon_{abc} + \mathcal{J}_{jb} \partial_a H'_j \epsilon_{abc}$, however, due to summation and the presence of the levi-civita symbol, the left-most term cancels and we are left with the rightmost term. Making the further substitution that $\partial_a = \mathcal{J}_{ia} \partial'_i$ and multiplying both sides by $\mathcal{J}_{kc}$, equation (A.14) becomes

$$\mathcal{J}_{kc} \mathcal{J}_{jb} \mathcal{J}_{ia} \partial'_i H'_j \epsilon_{abc} = \mathcal{J}_{kc} \varepsilon_{cd} \mathcal{J}_{ld} \frac{\partial E'_l}{\partial t} + \mathcal{J}_{kc} J_c. \tag{A.15}$$

However, $\mathcal{J}_{kc} \mathcal{J}_{jb} \mathcal{J}_{ia} \epsilon_{abc}$ is equal to $\epsilon_{ijk} \det \boldsymbol{\mathcal{J}}$. Translating (A.15) back into vector notation and rearranging we obtain

$$\nabla' \times \mathbf{H}' = \frac{\boldsymbol{\mathcal{J}} \boldsymbol{\varepsilon} \boldsymbol{\mathcal{J}}^T}{\det \boldsymbol{\mathcal{J}}} \frac{\partial \mathbf{E}'}{\partial t} + \frac{\boldsymbol{\mathcal{J}} \mathbf{J}}{\det \boldsymbol{\mathcal{J}}}. \tag{A.16}$$

Therefore, in order for equation (A.1) to take the same form across the coordinate transformation, equations (A.7) and (A.9) must also be true.

The exact same proof can be used to prove (A.8), so we shall not delve into further detail. To prove (A.10), we expand again in Einstein notation

$$\rho = \partial_a \varepsilon_{ab} E_b = \mathcal{J}_{ia} \partial'_i \varepsilon_{ab} \mathcal{J}_{jb} E'_j \tag{A.17}$$

If we insert the identity operator $\mathbf{I} = \mathcal{J}_{ak}^{-1}\mathcal{J}_{ka}$ between ∂_i' and ε_{ab} we obtain

$$\rho = \mathcal{J}_{ia}\partial_i'\mathcal{J}_{ak}^{-1}\mathcal{J}_{ka}\varepsilon_{ab}\mathcal{J}_{jb}E_j' = \mathcal{J}_{ia}\partial_i' \det\boldsymbol{\mathcal{J}}\,\mathcal{J}_{ak}^{-1}\varepsilon_{kj}'E_j'. \tag{A.18}$$

$$= (\partial_a \det\boldsymbol{\mathcal{J}}\,\mathcal{J}_{ak}^{-1})\varepsilon_{kj}'E_j' + (\det\boldsymbol{\mathcal{J}}\,\partial_i'\varepsilon_{kj}'E_j'). \tag{A.19}$$

In Einstein notation, $\det\boldsymbol{\mathcal{J}}\boldsymbol{\mathcal{J}}^{-1}$ is

$$\partial_a \det\boldsymbol{\mathcal{J}}\,\mathcal{J}_{ak}^{-1} = \partial_a\epsilon_{anm}\epsilon_{kij}\mathcal{J}_{in}\mathcal{J}_{jm}/2 \tag{A.20}$$

and taking into account $(\partial_a\mathcal{J}_{jb})\epsilon_{abc} = 0$ as used in the previous proof, (A.20) is also 0. Therefore (A.18) reduces to

$$\rho = \det\boldsymbol{\mathcal{J}}\,\partial_i'\varepsilon_{kj}'E_j' \Longrightarrow \frac{\rho}{det\boldsymbol{\mathcal{J}}} = \nabla'\cdot(\boldsymbol{\varepsilon}'\mathbf{E}'). \tag{A.21}$$

Therefore, (A.10) is also true.

We can extend this technique to create a model of a magnetized cloud core if we assume the charge density moves with the mass density to take up the same configuration. Fiege (2005) applied a variation of this technique to create a model of a magnetized filament by applying a coordinate transformation to a uniform mass density and magnetic field. The resulting field is assumed to have been dragged along with the gas into the new configuration, replicating the effect of flux-freezing (Fiege, 2005). One definite advantage of this technique is the ability to create a complex, three-dimensional model of a core or filament with a magnetic field structure arising naturally from the deformation of the cloud into the desired density configuration.

Appendix B

SCUPOL Data Corrections

If the SCUPOL Legacy Catalogue maps were not converted into Jy beam^{-1} prior to the fit, we may correct the results in the following fashion. The magnitude of the intensity maps will be too low by a factor of the numerical value of FCF^*, the flux conversion factor to Jy beam^{-1}. As a result, our model maps will be too low by this factor as well. So as $I^*_{data} \mapsto FCF^* \times I_{data}$ (where I^*_{data} is the scaled intensity map), so must $I^*_{model} \mapsto FCF^* \times I_{model}$.

Referring back to our polarization map computation (§4.1.4), model I, Q, and U are dependent on the total mass density ρ. The code treats this as a dimensionless structure multiplied by a constant density scale, i.e. $\rho = \rho_0\tilde{\rho}$ as discussed in section §4.1.1. As our surface density to Jy beam^{-1} conversion factor C_{flux} is a function of cloud temperature (see §4.1.3), we can hold it constant while absorbing the correction factor $CORR = FCF^*/(1$ Jy beam^{-1} V$^{-1}) = 200$ into the density scale in the following way. First

$$I^*_{model} = CORR \times I_{model}. \tag{B.1}$$

The scaling of I_{model} is determined by two constants: C_{flux} and ρ_0. We can therefore define

the quantity $\tilde{I}_{model}$ such that $I_{model} = C_{flux}\rho_0\tilde{I}_{model}$. Inserting this definition into (B.1)

$$I^*_{model} = C_{flux}(CORR \times \rho_0)\tilde{I}_{model} \tag{B.2}$$

$$= C_{flux}\rho^*_0\tilde{I}_{model}, \tag{B.3}$$

where ρ^*_0 represents the corrected density scale.

For Stokes Q and U the conversion is much the same:

$$Q^*_{model} = C_{flux}\langle\alpha\rangle(\rho_0 \times CORR)\tilde{Q}_{model} \tag{B.4}$$

$$= C_{flux}\langle\alpha\rangle\rho^*_0\tilde{Q}_{model} \tag{B.5}$$

where $\tilde{Q}_{model}$ represents $Q/(C_{flux}\rho_0)$, and the expression for U takes the same form (explanation of $\langle\alpha\rangle$ in §2.5).

While this means that the maps must be corrected, in our standard two-objective fitting mode only the intensity fitness values are affected by uncertainties in the CORR calibration factor. Polarization position angle depends only on the q and u quantities (§4.1.4). As our chosen fitness functions are only dependent on ratios, CORR cancels out, having a null effect on the results. Thus a fit to a raw SCUPOL Legacy map with intensity maps and densities corrected in post-processing would be valid.

We do note that, as ρ_0 is included in our radial scale for conversion to dimensionless coordinates, this would change the spatial extent of the density profile in our descaled grid. However, as the spatial extent of the profile is controlled by the K parameter in the POLY model, we find that to generate the exact same profile with the corrected density, a correction must be applied to K as well. We leave solving the exact relationship between K and K^* for future work.

Appendix C

Glossary of Symbols

a, a_{scale}
: PolCat parameter representing stretch on the x-axis (Scale transformation). §4.3.4.

a_{grain}
: Dust grain cross-section. §2.3.1.

A (Sinebend parameter)
: PolCat parameter representing amplitude of Sinebend transformation. §4.3.11 ONLY.

b, b_{scale}
: PolCat parameter representing stretch on the y-axis (Scale transformation). §4.3.4.

B
: Magnitude of the magnetic field. §2.1.3.

B (Sinebend parameter)
: PolCat parameter representing the coefficient that converts vertical distance into radians. §4.3.11 ONLY.

$\mathbf{B}$
: Magnetic field vector. §2.1.3.

$\mathcal{B}$
: Net magnetic energy. §2.1.3.

$B_\nu(T_j)$
: Planck function. §2.5.

B_ϕ
: Component of the magnetic field in the $\hat{\phi}$-direction (toroidal). §1.

c
: Stretch on the z-axis as a result of Scale transformation parameters a and b: $c = (ab)^{-1}$. §4.3.4.

c_j
: Fraction of total mass density per mean molecular mass of grain species j. §2.5.

cm
: Centimetres, cgs unit of distance.

c_s
: Isothermal sound speed. §2.1.1.

c_{twist}
: PolCat parameter representing the amount of twist in the LinearTwistA, LinearTwistS, PowerTwistA, and PowerTwistS transformations. §4.3.6, §4.3.7, §4.3.8, 4.3.9.

$C_{+,j}$
: Convenience constant. §2.5.

$C_{\mathrm{ext},j}$
: Effective extinction cross-section of dust grain species j. §2.5.

C_{flux}
: Constant absorbing grain emission terms in polarization map computation in units of Jy beam^{-1}g^{-1} cm^2. §4.1.4.

CO
: Carbon monoxide. §2.2.

$C_{\parallel,j}$
: Absorption cross-section parallel to dust grain axis of symmetry. §2.5.

$C_{\perp,j}$
: Absorption cross-section perpendicular to dust grain axis of symmetry. §2.5.

$C_{\mathrm{pol},j}$
: Effective polarization cross-section for dust grain species j. §2.5.

CS
: Carbon monosulfide. §2.2.

C_{shift}
: Offset in simulated polarization map computation. §4.1.4.

D_i
: Data values. §3 and §4.1.5 ONLY.

erg
: cgs unit of energy.

E
: Electric field. §2.7.

f_i
: Fitness criteria (multi-objective). §3 ONLY.

F1
: Also F_I. PolCat I fitness, mean deviation of model from data as a fraction of mean data value. §4.1.5, §6.

F2
: Also F_{PA}. χ_{pol} fitness value, square root of reduced χ^2 function. §4.1.5, §6.

FCF
: Flux Conversion Factor. §4.1.4, §5.

FCF*
: Flux Conversion Factor required to convert SCUPOL Legacy Catalogue maps into Jy beam^{-1} in units of Jy beam^{-1} V^{-1}. §5.

F_I
: Also F1, PolCat I fitness, mean deviation of model from data as a fraction of mean data value. §4.1.5, §6.

F_j
: Reduction in dust grain alignment of species j due to turbulent magnetic field component (constant). §2.5.

F_{PA}
: Also F2. χ_{pol} fitness value, square root of reduced χ^2 function. §4.1.5, §6.

$F_{P_{frac}}$
: P_{frac} fitness value, reduced χ^2 function. §6.

$F_{P_{flux}}$
: P_{flux} fitness value, reduced χ^2 function. §6.

FWHM
: Full-Width at Half Maximum, width of profile at half its maximum value. §2.2.

F^{α}
: Solution in multi-objective problem. §3.2 ONLY.

G
: Gravitational constant, $\sim$6.67 $\times$ 10^{-8} cm^3 g^{-1} s^{-2}. §2.1.1.

g
: Grams, cgs unit of mass.

$g(\rho)$
: Empirical grain alignment function (simulates polarization hole). §4.1.4.

$\mathbf{H}$
: Magnetizing field. $\mathbf{B} = \boldsymbol{\mu}\mathbf{H}$. §2.7.

H_2
: Molecular hydrogen. §2.2.

i
: PolCat parameter representing RotateA transformation angle of rotation about the positive x-axis (inclination). §4.3.3.

I
: [1]Intensity of emission (Stokes I) in Jy beam^{-1} (flux density). §2.5.
[2]Moment of inertia, §2.1.3 ONLY.

$\ddot{I}$
: Second derivative of the moment of inertia with respect to time. §2.1.3 ONLY.

Jy
: Jansky, unit of flux density, equal to 10^{-26} watts per square metre per Hertz.

Jy beam^{-1}
: Janskys per beam, unit of flux density equal to 10^{-26} Watts per square metre per Hertz of the telescope beam.

$\mathbf{J}$
: Current density. §2.7.

$\boldsymbol{\mathcal{J}}$
: Jacobian matrix. §2.7.

$\mathcal{J}_{ij}$
: Element of Jacobian matrix. §4.1.2.

k
: Boltzmann's constant: 1.38×10^{-16} erg K^{-1}.

km
: Kilometre. Unit of distance equal to 100 000 cm.

K
: PolCat parameter representing the constant in the polytropic equation of state. §2.6.1, §4.3.2.

K
: Kelvin. Unit of temperature.

L
: Region size. §2.1.2.

m_{twist}
: PolCat parameter representing the exponent in the PowerTwistA and PowerTwistS transformations. §4.3.8, §4.3.9.

M
: Mass (general).

$M_\odot$
: "Solar masses": unit of mass equal to the mass of the sun. §2.1.1.

M_J
: Jeans mass, the mass contained within a sphere of diameter λ_J. §2.1.1.

n_j
: Number density of dust grain species j. §2.5.

NH_3
: Ammonia. §2.2

pc
: Parsec. Unit of distance equal to 3.08×10^{13} km (3.08×10^{18} cm).

P
: Pressure (general).

PA
: PolCat parameter representing RotateA transformation angle of rotation about the positive y-axis (Position Angle). §4.3.3.

$\mathrm{P_{dist}}$
: Penalty on fitness functions. Scales with distance of $(\Delta x, \Delta z)$ from non-masked pixels. §4.1.5.

P_{ext}
: External pressure.

$\mathrm{P_{fit}}$
: Penalty on fitness functions. Acts as a threshold. §4.1.5.

P_{flux}
: Intensity of polarized emission in Jy beam^{-1}. §4.1.4.

P_{frac}
: Fraction of polarized emission. §2.5.

$\mathrm{P_{int}}$
: Penalty on fitness functions. Prevents core surface from intersecting with the front and back of the model cube. §4.1.5.

P_{out}
: PolCat parameter representing external pressure of the POLY transformation as a fraction central pressure. §4.3.2.

q
: Simulated Stokes Q in units of surface density. §2.5.

Q
: Stokes Q in Jy beam^{-1}, flux density of polarized emission at 0° or 90°. §2.5.

r
: Radius (general).

$\mathbf{r}$
: Radial vector (general).

r_0
: Radial scale for scaling PolCat model grid into "dimensionless" units, equal to $\sqrt{\sigma_0^2/(4\pi G\rho_0)}$. §4.1.1.

r_0 (Bend variable)
: Radius of curvature of the bend on the $z = 0$ line of the Bend transformation. §4.3.10 ONLY.

R_j
: Rayleigh reduction factor of dust species j: characterizes degree of grain alignment with local magnetic field. §2.5.

s
: Seconds. Unit of time.

T
: Temperature (general).

$\mathcal{T}$
: Time-averaged kinetic energy. §2.1.1.

T_d
: Dust temperature in K. §4.1.4.

T_{gas}
: Gas temperature. §2.3.1.

T_j
: Temperature of dust grain species j. §2.5.

u
: Simulated Stokes U in units of surface density. §2.5.

U
: Stokes U in Jy beam^{-1}, flux density of polarized emission at 45° or 135°. §2.5.

V
: Volts, unit of electrical potential.

$\mathcal{W}$
: Time-averaged gravitational potential energy. §2.1.1.

x_i
: Generalized coordinate notation, $x_1 = x$, $x_2 = y$, $x_3 = z$ (general).

X_i
: Parametric model. §3 and §4.1.5 ONLY.

z_0 (Bend parameter)
: PolCat parameter representing the start height of the Bend transformation. §4.3.10 ONLY.

z_0 (Sinebend parameter)
: Polcat parameter representing the phase-shift constant of the sinebend. §4.3.11 ONLY.

$\langle\alpha\rangle$
: Weighted mean of α_j. §2.5.

α (Bend parameter)
: PolCat parameter representing angle of bend in the Bend transformation. §4.3.10 ONLY.

α_j
: Convenience constant absorbing the effective polarization cross-section $\times C_{+,j}$ for dust grain species j. §2.5.

β_g
: PolCat parameter representing the exponent in $g(\rho)$. §4.1.4.

γ
: PolCat parameter representing the polytropic index of the POLY transformation. §2.6.1, §4.3.2.

γ_B
: Angle between magnetic field and the plane of the sky. §2.5.

γ_g
: PolCat parameter representing the constant in $g(\rho)$. §4.1.4.

δ_{ij}
: Kronecker delta, equals 1 if $i = j$ and 0 otherwise. §4.1.3.

Δr_0 (Bend parameter)
: PolCat parameter representing an offset between the maximum cylindrical radius of the coordinate system and the radius of curvature of the $z = 0$ line of the Bend transformation. §4.3.10.

Δx
: PolCat parameter representing x-axis displacement in the Shift transformation. §4.3.5.

Δz
: PolCat parameter representing z-axis displacement in the Shift transformation. §4.3.5.

$\boldsymbol{\varepsilon}$
: Absolute dielectric permittivity tensor. §2.7.

κ_{850}
: Emissivity at 850 μm. §4.1.4

λ_J
: Jeans length, the wavelength of the perturbation which will cause a thermally supported uniform isothermal cloud to collapse. §2.1.1.

$\boldsymbol{\mu}$
: Magnetic permeability tensor. §2.7.

μm
: Micrometre/micron, unit of length, 10^{-6} m (10^{-4} cm).

ν
: Degrees of freedom in parametric model. §4.1.5.

π
: Mathematical constant relating a circle's circumference to its diameter.

ρ
: Mass density (general).

ρ_0*
: FCF*-corrected ρ_0. §5.

ρ_0
: PolCat parameter representing initial cloud density in g cm^{-3}. §4.1.1.

ρ_c
: [1]PolCat parameter representing central density as a fraction of ρ_0 in the POLY transformation. §4.3.2.
[2] Central density (general).

ρ_{charge}
: Charge density. §2.7.

ρ_{grain}
: Grain density. §2.3.1.

ρ_{out}
: PolCat parameter representing external density of the POLY transformation as a fraction of the density at the truncation radius ρ_s. §4.3.2.

ρ_s
: Density at core surface.

σ
: Velocity dispersion. §2.1.2.

σ_0
: PolCat parameter representing initial cloud velocity dispersion in km s^{-1}. §4.1.1.

$\sigma_{P_{flux}}$
: Uncertainty in the polarized intensity P_{flux}. Variance is $\sigma^2_{P_flux}$. §5.

$\sigma_{P_{frac}}$
: Uncertainty in the fraction of polarized emission P_{frac}. Variance is $\sigma^2_{P_{frac}}$. §5.

σ_i
: Uncertainty in data point (i.e. pixel) i. §3.1, §4.1.5.

σ_I
: Uncertainty in intensity (Stokes I) map. Variance is σ^2_I. §5.

σ_{nt}
: Non-thermal component of the 1D velocity dispersion. §2.1.2.

σ_{PA}
: Uncertainty in polarization position angle χ_{pol}. Variance is σ^2_{PA}. §5.

σ_Q
: Uncertainty in Stokes Q map. Variance is σ^2_Q. §5.

σ_U
: Uncertainty in Stokes U map. Variance is σ^2_U. §5.

Σ
: Density integrated along the line of sight (surface density)

Σ_2
: $\rho(\cos^2\gamma_B/2-1/3)$ integrated along the line of sight. §2.5.

ϕ (RotateA parameter)
: PolCat parameter representing RotateA transformation angle of rotation about the positive z-axis. §4.3.3.

ϕ (Bend and Sinebend parameter)
: PolCat parameter representing the angle of rotation required to align the plane of operation with the x-axis in Bend and Sinebend. §4.3.10, §4.3.11 ONLY.

Φ

Gravitational potential. §2.6.1.

Φ_0

Scaling constant to convert Φ into dimensionless units. §4.1.1.

Φ_j

Polarization reduction factor of dust grain species j. §2.5.

χ^2

Chi-squared function. §3.1.

χ_{pol}

Position angle of electric field component of polarized emission. §2.5.

χ^2_ν

Reduced chi-squared function. §4.1.5.

ψ_B

Angle between north on the sky and the plane-of-sky projection of the magnetic field. §2.5.

ω_T

Angular velocity (thermal). §2.3.1.

Bibliography

Bally, J. (1989, September). The structure and kinematics of star forming clouds. In B. Reipurth (Ed.), *European Southern Observatory Conference and Workshop Proceedings*, Volume 33 of *European Southern Observatory Conference and Workshop Proceedings*, pp. 1–32. 1, 6

Bally, J., N. J. Cunningham, N. Moeckel, M. G. Burton, N. Smith, A. Frank, and A. Nordlund (2011, February). Explosive Outflows Powered By the Decay of Non-Hierarchical Multiple Systems of Massive Stars: Orion Bn/Kl. *The Astrophysical Journal 727*(2), 113. 86

Binney, J. and M. Merrifield (1998). *Galactic Astronomy*. Princeton, NJ: Princeton University Press. 11, 13

Binney, J. and S. Tremaine (1987). *Galactic Dynamics*. Princeton, NJ: Princeton University Press. 1, 7, 8

Bonnor, W. B. (1956). Boyle's Law and gravitational instability. *Monthly Notices of the Royal Astronomical Society 116*, 351. 22

Carroll, B. W. and D. A. Ostlie (2007). *An Introduction to Modern Astrophysics* (2nd ed.). Pearson Addison-Wesley. 1, 7, 12

Chandrasekhar, S. and E. Fermi (1953, July). Magnetic Fields in Spiral Arms. *The Astrophysical Journal 118*, 113. 14, 16

Clark, S., A. McCall, A. Chrysostomou, T. Gledhill, J. Yates, and J. Hough (2000, December). Polarization models of young stellar objects - II. Linear and circular polarimetry of R Coronae Australis. *Monthly Notices of the Royal Astronomical Society 319*(2), 337–349. 14, 87

Coppin, K. E. K., J. S. Greaves, T. Jenness, and W. S. Holland (2000). Structure, star formation and magnetic fields in the OMC1 region. *Astronomy and Astrophysics 356*, 1031–1038. 86, 159, 167

Crutcher, R., C. Heiles, and T. Troland (2003). Observations of Interstellar Magnetic Fields. In E. Falgarone and T. Passot (Eds.), *Turbulence and Magnetic Fields in Astrophysics*, Volume 614 of *Lecture Notes in Physics, Berlin Springer Verlag*, pp. 155–181. 15, 16

Curran, R. L. and a. Chrysostomou (2007, December). Magnetic fields in massive star-forming regions. *Monthly Notices of the Royal Astronomical Society 382*(2), 699–716. 14, 87, 88, 181

Curry, C. L. and C. F. McKee (2000, January). Composite Polytrope Models of Molecular Clouds. I. Theory. *The Astrophysical Journal 528*(2), 734–755. 181

Draine, B. (2003, September). Interstellar Dust Grains. *Annual Review of Astronomy and Astrophysics 41*(1), 241–289. 3, 13

Dyson, J. E. and D. A. Williams (1997). *The Physics of the Interstellar Medium* (2nd ed.). New York, NY: Taylor & Francis Group. 11

English, J., J. D. Fiege, T. Wiegert, B. Koribalski, W. Kerzendorf, and K. C. Freeman (2010). The DiVA's Mask: Iconifying Galaxies and Revealing HII Anomalies. In D. L. Block, K. C. Freeman, and I. Puerari (Eds.), *Galaxies and their Masks*, pp. 105–112. New York, NY: Springer New York. 34

Fiege, J. D. (2005). Computational Intelligence Techniques for Submillimetre Polarization Modeling. In A. Adamson, C. Aspin, C. J. Davis, and T. Fujiyoshi (Eds.), *Astronomical Polarimetry: Current Status and Future Directions*, Volume 343, pp. 171–175. 3, 27, 195

Fiege, J. D. (2010). Qubist User's Guide: Optimization, Data-Modeling, and Visualization with the Qubist Global Optimization Toolbox for MATLAB. 4, 29, 34, 35

Fiege, J. D., D. Johnstone, R. O. Redman, and P. A. Feldman (2004). A GENETIC ALGORITHM–BASED EXPLORATION OF THREE FILAMENT MODELS : A CASE FOR THE MAGNETIC SUPPORT OF THE G11.11 - 0 . 12 INFRARED-DARK CLOUD. *The Astrophysical Journal 616*, 925–942. 3, 46, 47, 79, 158

Fiege, J. D., B. McCurdy, P. Potrebko, H. Champion, and A. Cull (2011, October). PARETO: A novel evolutionary optimization approach to multiobjective IMRT planning. *Medical physics 38*(9), 5217–29. 34

Fiege, J. D. and R. Pudritz (2000a). Polarized Submillimeter Emission from Filamentary Molecular Clouds. *The Astrophysical Journal 544*, 830. 4, 17, 18, 19, 20, 37, 41, 45

Fiege, J. D. and R. E. Pudritz (2000b, January). Helical fields and filamentary molecular clouds - I. *Monthly Notices of the Royal Astronomical Society 311*(1), 85–104. 3, 10, 23, 165, 171, 183

Fiege, J. D. and R. E. Pudritz (2000c, January). Helical fields and filamentary molecular clouds - II. Axisymmetric stability and fragmentation. *Monthly Notices of the Royal Astronomical Society 311*(1), 105–119. 165, 171, 183

Fiege, J. D. and R. E. Pudritz (2000d, May). Prolate Cores in Filamentary Molecular Clouds. *The Astrophysical Journal 534*(1), 291–308. 10, 24, 156, 185, 186

Fonseca, C. and P. Fleming (1993). Genetic algorithms for multiobjective optimization:

formulation, discussion and generalization. In *Proceedings of the Fifth International Conference on Genetic Algorithms*, San Mateo, CA, USA, pp. 416 – 23. 30, 31

Fonseca, C. and P. Fleming (1998). Multiobjective optimization and multiple constraint handling with evolutionary algorithms. I. A unified formulation. *IEEE Transactions on Systems, Man, and Cybernetics - Part A: Systems and Humans 28*(1), 26–37. 30

Goldberg, D. E. (1989). *Genetic Algorithms in Search, Optimization, and Machine Learning.* Artificial Intelligence. Addison-Wesley. 30, 33, 34

Greaves, J. S., W. S. Holland, N. R. Minchin, A. G. Murray, and J. A. Stevens (1999). Submillimetre polarization and constraints on dust grain alignment. *Astronomy and Astrophysics 344*, 668–674. 3

Heiles, C. and R. Crutcher (2005). Magnetic Fields in Diffuse HI and Molecular Clouds. In R. Wielebinski and R. Beck (Eds.), *Cosmic Magnetic Fields*, Volume 664 of *Lecture Notes in Physics, Berlin Springer Verlag*, pp. 137. 14, 15, 16, 17

Heiles, C., A. A. Goodman, C. F. McKee, and E. G. Zweibel (1993). Magnetic fields in star-forming regions - Observations. In E. H. Levy and J. I. Lunine (Eds.), *Protostars and Planets III*, pp. 279–326. 15, 16

Hennebelle, P. and E. Falgarone (2012, November). Turbulent molecular clouds. *The Astronomy and Astrophysics Review 20*(1), 55. 2, 8, 9, 10

Holland, J. H. (1975). *Adaptation in natural and artificial systems: An introductory analysis with applications to biology, control, and artificial intelligence.* University of Michigan Press. 31

Holland, W. S., E. I. Robson, W. K. Gear, C. R. Cunningham, J. F. Lightfoot, T. Jenness, R. J. Ivison, J. A. Stevens, P. A. R. Ade, M. J. Griffin, W. D. Duncan, J. A. Murphy,

and D. A. Naylor (1999, March). SCUBA: a common-user submillimetre camera operating on the James Clerk Maxwell Telescope. *Monthly Notices of the Royal Astronomical Society 303*(4), 659–672. 78, 79

Hull, C. L. H., R. L. Plambeck, W. Kwon, G. C. Bower, J. M. Carpenter, R. M. Crutcher, J. D. Fiege, E. Franzmann, N. S. Hakobian, C. Heiles, M. Houde, A. M. Hughes, J. W. Lamb, L. W. Looney, D. P. Marrone, B. C. Matthews, M. W. Pillai, Thushara; Pound, N. Rahman, G. Sandell, I. W. Stephens, J. J. Tobin, J. E. Vaillancourt, N. H. Volgenau, and M. C. H. Wright (2014). TADPOL: A 1.3 mm Survey of Dust Polarization in Star-forming Cores and Regions. *Astrophysical Journal Supplement*. In Press. 84, 191

Johnson, S. G. (2007). Coordinate Transformation & Invariance in Electromagnetism. `http://math.mit.edu/~stevenj/18.369/coordinate-transform.pdf`. 25, 193

Johnstone, D., J. D. Fiege, and R. Redman (2003). The G11.11-0.12 Infrared-Dark Cloud: Anomalous Dust and a Nonmagnetic Isothermal Model. *The Astrophysical Journal 588*, L37–L40. 46, 158

Joint Astronomy Centre (2005). SCUBA Flux Conversion Factors. `http://www.jach.hawaii.edu/JCMT/continuum/calibration/sens/gains.html`. 80

Kirby, L. (2009, April). Dr21 Main: a Collapsing Cloud. *The Astrophysical Journal 694*(2), 1056–1066. 85, 86, 142, 158, 159

Knude, J. and E. Høg (1998). Interstellar reddening from the Hipparcos and Tycho catalogues. I. Distances to nearby molecular clouds and star forming regions. *Astronomy and Astrophysics 338*, 897–904. 87, 181

Larson, R. (1981). Turbulence and star formation in molecular clouds. *Monthly Notices of the Royal Astronomical Society 194*, 809–826. 8, 9

Lazarian, A., A. A. Goodman, and P. C. Myers (1997, November). On the Efficiency of Grain Alignment in Dark Clouds. *The Astrophysical Journal 490*(1), 273–280. 13, 14

Lee, H. and B. Draine (1985). Infrared Extinction and Polarization Due to Partially Aligned Spheroidal Grains: Models for the Dust Toward the BN Object. *The Astrophysical Journal 290*, 211–228. 12, 14, 17, 18

Matsumura, S., T. Oka, K. Tanaka, M. Nagai, K. Kamegai, and T. Hasegawa (2012, September). Discovery of the Pigtail Molecular Cloud in the Galactic Center. *The Astrophysical Journal 756*(1), 87. 64

Matthews, B. C., C. A. McPhee, L. M. Fissel, and R. L. Curran (2009, May). THE LEGACY OF SCUPOL: 850 μm IMAGING POLARIMETRY FROM 1997 TO 2005. *The Astrophysical Journal Supplement Series 182*(1), 143–204. 4, 14, 78, 79, 85, 88

McKee, C. F. and E. C. Ostriker (2007, September). Theory of Star Formation. *Annual Review of Astronomy and Astrophysics 45*(1), 565–687. 6, 8, 9, 10, 15, 16, 22, 23

McKee, C. F., E. G. Zweibel, A. A. Goodman, and C. Heiles (1993). Magnetic Fields in Star-Forming Regions - Theory. In E. H. Levy and J. I. Lunine (Eds.), *Protostars and Planets III*, pp. 327. 10

Menten, K. M., M. J. Reid, J. Forbrich, and A. Brunthaler (2007, November). The distance to the Orion Nebula. *Astronomy & Astrophysics 474*(2), 515–520. 86

Mestel, L. and L. Spitzer Jr. (1956). Star formation in magnetic dust clouds. *Monthly Notices of the Royal Astronomical Society 116*, 503. 10

Mouschovias, T. C. (1976, June). Nonhomologous contraction and equilibria of self-gravitating, magnetic interstellar clouds embedded in an intercloud medium: Star formation. I Formulation of the problem and method of solution. *The Astrophysical Journal 206*, 753. 24

Murray, A. G., R. Nartallo, C. V. Haynes, F. Gannaway, and P. A. R. Ade (1997, August). An Imaging Polarimeter for SCUBA. In A. Wilson (Ed.), *The Far Infrared and Submillimetre Universe.*, Volume 401 of *ESA Special Publication*, pp. 405. 79

Myers, P. and A. Goodman (1988). Evidence for Magnetic and Virial Equilibrium in Molecular Clouds. *The Astrophysical Journal 326*, L27–L30. 9

Nutter, D. J., D. Ward-Thompson, and P. André (2005, March). The pre-stellar and protostellar population of R Coronae Australis. *Monthly Notices of the Royal Astronomical Society 357*(3), 975–982. 87, 180, 181

Ostriker, E. C., J. M. Stone, and C. F. Gammie (2001, January). Density, Velocity, and Magnetic Field Structure in Turbulent Molecular Cloud Models. *The Astrophysical Journal 546*(2), 980–1005. 17

Ostriker, J. (1964, October). The Equilibrium of Polytropic and Isothermal Cylinders. *The Astrophysical Journal 140*, 1056. 23

Pence, W. D., L. Chiappetti, C. G. Page, R. a. Shaw, and E. Stobie (2010, November). Definition of the Flexible Image Transport System (FITS), version 3.0. *Astronomy & Astrophysics 524*, A42. 81

Pendry, J. B., D. Schurig, and D. R. Smith (2006, June). Controlling electromagnetic fields. *Science (New York, N.Y.) 312*(5781), 1780–2. 25, 193

Poidevin, F., D. Falceta-Gonçalves, G. Kowal, E. de Gouveia Dal Pino, and A. M. Magalhães (2013, November). MAGNETIC FIELD COMPONENTS ANALYSIS OF THE SCUPOL 850 μm POLARIZATION DATA CATALOG. *The Astrophysical Journal 777*(2), 112. 6

Press, W. H., S. A. Teukolsky, W. T. Vetterling, and B. P. Flannery (2007). *Numerical Recipes 3rd Edition: The Art of Scientific Computing* (Third ed.). Cambridge University Press. 29

Richardson, K. J., G. Sandell, and K. Krisciunas (1989, October). Small-scale structure in the DR 21/DR 21 (OH) region - A high resolution continuum study at millimetre and submillimetre wavelengths. *Astronomy and Astrophysics 224*, 199–205. 86, 159

Rogers, A. and J. D. Fiege (2011, February). Gravitational Lens Modeling With Genetic Algorithms and Particle Swarm Optimizers. *The Astrophysical Journal 727*(2), 80. 34

Shu, F. H. (1977, June). Self-similar collapse of isothermal spheres and star formation. *The Astrophysical Journal 214*, 488. 23

Tomisaka, K. (1991, July). The equilibria and evolutions of magnetized, rotating, isothermal clouds. V - The effect of the toroidal field. *The Astrophysical Journal 376*, 190. 24, 25

Tomisaka, K., S. Ikeuchi, and T. Nakamura (1988a, March). The equilibria and evolutions of magnetized, rotating, isothermal clouds. I - Basic equations and numerical methods. *The Astrophysical Journal 326*, 208. 24, 25

Tomisaka, K., S. Ikeuchi, and T. Nakamura (1988b, December). The Equilibria and evolutions of magnetized, rotating, isothermal clouds. II - The extreme case: Nonrotating clouds. *The Astrophysical Journal 335*, 239. 24, 25

Tomisaka, K., S. Ikeuchi, and T. Nakamura (1989, June). The equilibria and evolutions of magnetized, rotating, isothermal clouds. III - Critical mass. *The Astrophysical Journal 341*, 220. 24, 25

Tomisaka, K., S. Ikeuchi, and T. Nakamura (1990, October). The equilibria and evolutions of magnetized, rotating, isothermal clouds. IV - Quasi-static evolution. *The Astrophysical Journal 362*, 202. 24, 25

Ward, A. and J. Pendry (1996). Refraction and geometry in Maxwell's equations. *Journal of Modern Optics 43*(4), 773–793. 25, 192, 193

Wardle, M. and A. Konigl (1990). A Model for the Magnetic Field in the Molecular Disk at the Galactic Center. *The Astrophysical Journal 362*, 120–134. 17, 18

Weintraub, D. A., A. A. Goodman, and R. L. Akeson (2000, May). Polarized Light from Star-Forming Regions. *Protostars and Planets IV*, 247. 14

Yu, X. and M. Gen (2010). *Introduction to Evolutionary Algorithms*. Decision Engineering. London: Springer London. 30, 35